SIMULATION OF FULL-SCALE COMBUSTION INSTABILITIES IN SMALL-SCALE RIGS USING ACTIVELY CONTROLLED BOUNDARY CONDITIONS

A Dissertation
Presented to
The Academic Faculty

by

Yong Jea Kim

In Partial Fulfillment
of the Requirements for the Degree
Doctor of Philosophy in the
School of Aerospace Engineering

Georgia Institute of Technology
December 2017

SIMULATION OF FULL-SCALE COMBUSTION INSTABILITIES IN SMALL-SCALE RIGS USING ACTIVELY CONTROLLED BOUNDARY CONDITIONS

Approved by:

Dr. Ben T. Zinn, Advisor
School of Aerospace Engineering
Georgia Institute of Technology

Dr. Krishan K. Ahuja
School of Aerospace Engineering
Georgia Institute of Technology

Dr. Jechiel Jagoda
School of Aerospace Engineering
Georgia Institute of Technology

Dr. Tim Lieuwen
School of Aerospace Engineering
Georgia Institute of Technology

Dr. Ari Glezer
School of Mechanical Engineering
Georgia Institute of Technology

Date Approved: November 6, 2017

ACKNOWLEDGEMENTS

I would like to express my sincere appreciation to my advisor, Dr. Ben T. Zinn, for his support and guidance. His patience and advice enabled me to accomplish this research work. I also thank Dr. Jechiel Jagoda for his support and help. He served on the thesis committee and has helped with various administrative matters. I would like to thank my thesis committee members, Dr. Krishan K. Ahuja, Dr. Tim Lieuwen, and Dr. Ari Glezer, for reviewing the thesis and providing valuable comments. The thoughtful and pertinent feedback I have received from my committee has added to the quality of this dissertation.

I would like to thank Dr. Yedidia Neumeier and Dr. Manuj Dhingra for their support and help. The experience and learning from the works with them was valuable for me to accomplish this research work. I also thank Dr. David Scarborough for his kind advice and encouragement. I would like to thank to the project team members, Dr. Mathew Quinlan and Alex Damião, for their help and encouragement.

I would like to thank all my colleagues in the Ben T. Zinn Combustion Laboratory for their friendship and support during my years in the lab. I have enjoyed my interactions with graduate and undergraduate students and research engineers in the lab, and the conversations with them encouraged me and provided clues to the progresses in the research.

On a personal note, I would like to thank my family for always being there for me and their endless love and support.

The financial support of the Air Force Office of Scientific Research is gratefully acknowledged.

TABLE OF CONTENTS

Page

LISTS OF TABLES

Page

LISTS OF FIGURES

Page

NOMENCLATURE

Abbreviation	Description
ACS	Active Control System
BC	Boundary Condition
CFL	Courant–Friedrichs–Lewy number
CI	Combustion Instability
C.S.	Control Surface
C.V.	Control Volume
D	Dimension
Eq.	Equation
Eqs.	Equations
FFT	Fast Fourier Transform algorithm
FTBS	Forward-Time Backward-Space
LHS	Left Hand Side
RHS	Right Hand Side
1-D	One-Dimension

Symbol	Description
$\bar{a}$	Speed of sound, $[m/s]$
A	Cross-sectional area of the annular combustor, $[m^2]$
A^*	Cross-sectional area of the throat of the exhaust nozzle, $[m^2]$
c	Speed of sound, $[m/s]$
c_p	Specific heat of the mixture gas (per mass), $[J/(kg \cdot K)]$

Symbol	Description
dS	Infinitesimal area of the control surface, $[m^2]$
dV	Infinitesimal volume of the control volume, $[m^3]$
f_s	Sampling frequency, $[1/s]$
f	Right going wave, $[N/m^2]$
f	Frequency $[1/s]$
g	Left going wave, $[N/m^2]$
h	Enthalpy (per mass), $[J/kg]$
h_f	Formation enthalpy of the mixture gas (per mass), $[J/kg]$
$h_{f,l}$	Formation enthalpy of the species l (per mass), $[J/kg]$
h_s	Sensible enthalpy (per mass), $[J/kg]$
h_t	Total enthalpy (per mass), $[J/kg]$
$h_{t,s}$	Stagnation enthalpy (excluding formation enthalpy) (per mass), $[J/kg]$
i	Time index
k	Wave number, $k = \omega/c = 2\pi/\lambda$
M	Mach number of tangential flow
$\bar{M}$	Mach number of tangential mean flow
$\hat{n}$	Unit vector normal to the control surface
p	Pressure. $[N/m^2]$
p'	Acoustic pressure, $[N/m^2]$
$\hat{P}$	Complex amplitude of the acoustic pressure, $[N/m^2]$
t	Time coordinate, current time, $[s]$
T	Temperature, $[K]$
v'	Acoustic velocity, $[m/s]$

Symbol	Description
$\vec{V}$	Flow velocity, $[m/s]$
$\bar{\vec{V}}$	Mean flow velocity, $[m/s]$
$\bar{V}$	Tangential mean flow velocity in 1-D case, $[m/s]$
$\hat{V}$	Complex amplitude of the acoustic velocity, $[m/s]$
x	Space coordinate, $[m]$
Y_l	Mixture ratio of the species l (mass fraction)
z	Acoustic impedance, $z = p'/v'$, $[N \cdot s/m^3]$
Z	Complex acoustic impedance, $Z = \hat{P}/\hat{V}$, $[N \cdot s/m^3]$
ρ	Density, $[kg/m^3]$
τ_s	Sampling time, $[s]$
γ	Ratio of the specific heats, $\gamma = c_p/c_v$
ω	Circular frequency of the oscillations, $[rad/s]$
Δt	Time step size, $[s]$
Δx	Spatial grid size, $[m]$
$(\cdot)'$	Perturbed property
$\overline{(\cdot)}$	Mean (or steady state) property
$\widehat{(\cdot)}$	Normalized property: e.g., $\hat{f}_1$, $\hat{g}_1$, $\hat{p}'$, $\cdots$. or unit vector: e.g., $\hat{x}_1$, $\hat{x}_2$, and $\hat{n}$. or complex amplitude with a large capital number: e.g., $\hat{P}$, $\hat{V}$.
$\widetilde{(\cdot)}$	Estimated (approximated) quantity

SUMMARY

The objective of this Ph.D. study was to develop an experimental approach that would allow the investigation of the causes of detrimental combustion instabilities (CIs) that often hinder the development of various propulsion and power generation systems (e.g., rockets, ramjets, air breathing engines, and gas turbines) in small-scale rigs that can simulate the flow, thermal, and acoustic environments inside the full-scale engines. The availability of such capabilities would significantly reduce the cost of and time required for developing *stable* propulsion systems.

The onset of CIs has hindered the development and performance of combustion systems employed in industrial, power generation and propulsion systems for many decades. In an effort to solve this problem, many investigations to date sought to elucidate the *feedback mechanisms* that drive these CIs. Ideally, the experimental setup used in such studies should simulate the operating conditions (e.g., combustor and reactant supply systems' pressures and temperatures, and acoustic environments), geometry, and scale of the unstable system in order to properly reproduce in the small-scale rig the combustion process and acoustic oscillations that occur in the unstable full-scale engine. This, in turn, would assure that all the parameters affecting the feedback mechanism are reproduced in the laboratory rig. Clearly, investigating the instability in an unstable "full-scale" engine would satisfy these requirements. However, investigating CIs in full-scale engine tests is not practical because of the exorbitant cost of such tests, the large space required to house the full-sized engine, and the inability to equip full-scale engines with diagnostic systems that could measure, e.g., the temporal and spatial

dependence of the mean and acoustic pressures, velocities, temperatures, compositions, and reaction rates. Because of these difficulties, most studies of CIs to date were performed in “small-scale” setups that were geometrically similar to but smaller than the full-scale engines combustors. While testing with these small-scale setups reduced the cost of testing and produced important results, the acoustic modes excited in the small-scale setups had considerably higher frequencies that did not simulate the lower frequency oscillations that are excited in the unstable full-scale engines.

The above discussion indicates that in order to study the driving of CIs in full-scale engines in small-scale rigs, the latter must simulate the acoustic environments, the combustion processes, and the interactions between these processes in the unstable full-scale engine. This study has investigated the use of a small-scale rig equipped with a *real time active acoustic boundary control* (see figure below) to simulate the acoustic environment of the full-scale engine in the small-scale rig. The proposed approach, for the study of the driving mechanism of *longitudinal* CIs, is described in the figure below. It describes the proposed approach for experimentally studying the processes taking place in region (I)~(II) of an unstable full-scale engine in a small-scale rig. To attain this goal, the active control system (ACS) needs to generate an acoustic impedance at location (II) of the small-scale rig that equals to the acoustic impedance at the corresponding location in the full-scale unstable engine. If this is accomplished, the acoustic oscillations in the region between locations (I) and (II) in the small-scale rig and the full-scale engine would be identical.

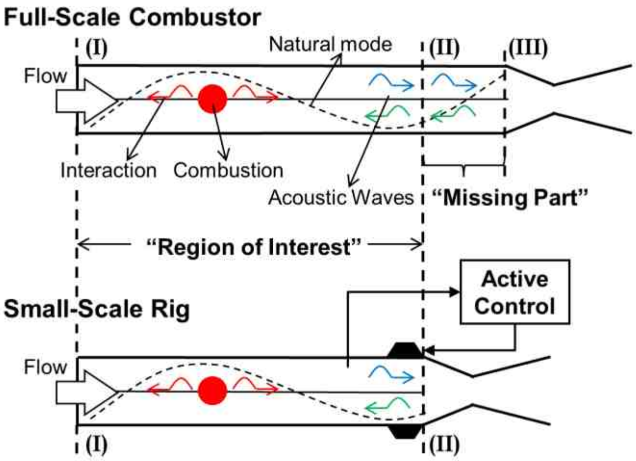

Description of the proposed experimental approach that allows an actively controlled small-scale rig to simulate *longitudinal* combustion instability in the full-scale combustor

As described in Chapter 2, this study has developed an ACS that enables a small-scale rig to simulate the acoustic oscillations in full-scale engines experiencing *longitudinal* CIs. It consists of the following three modules: 1) A *wave separation module* that uses measured acoustic pressures and a *real time wave separation* algorithm, developed using the *method of characteristics*, to determine the properties of the right and left going waves in the actively controlled, small-scale rig; 2) A *simulation module* that numerically determines in *real time* the properties of the right and left going waves in the "missing part" of the full-scale engine (see figure above), using input from the *wave separation module*, and determines in *real time the acoustic boundary condition* (BC) that must be established at location (II) of the small-scale rig in the above figure; and 3) An *actuator (speaker) module*, that uses input from the *simulation module* and determines the control current to the actuator at location (II) that "generates" the needed acoustic BC at that location in the small-scale rig. This is accomplished by determining the control current to the actuator (a speaker in this study) by modelling the speaker as a mechanical *spring-mass-damper* system forced by the *acoustic pressure* and the *electromagnetically induced force by the input current*.

The performance of the developed ACS was successfully demonstrated in numerical simulations and experiments. The experimental efforts developed a small-scale, actively controlled, rig equipped with speakers on its left and right hand sides. The left speaker was used to generate acoustic oscillations in the rig that simulated the driving of the CI by the combustion process, and the right speaker was actively controlled to simulate the acoustic field in the full-scale system. This experimental setup was used to demonstrate that the ACS could excite a travelling acoustic wave CI within the small-scale rig by actively "generating" a non-reflecting acoustic BC at the right boundary (II) of the rig. This rig was also used to demonstrate that the developed ACS could simulate a standing acoustic wave CI in a full-scale engine (i.e., the longer tube in the figure above) within the small-scale rig. Additionally, this rig was used to demonstrate that standing acoustic waves CI in full-scale engines having different lengths could be simulated in the developed, actively controlled, small-scale rig.

Finally, as discussed in Chapter 3, this study also developed a theoretical model that determines in *real time* the acoustic BC that must be generated by the ACS at the boundaries of a small-scale rig that simulates *transverse* (*tangential*) CI in an annular combustor similar to those used in gas turbines and jet engines. In this case, the small-scale rig consists of a small section of the annular combustor and the "missing part" of the full-scale engine consists of what has been "left over" after the small-scale sector-rig has been removed from the annular combustor (see figure below). The developed model assumed that reactants are supplied to the annular combustor by several nozzles (injectors) that stabilize a “concentrated” combustion region in their vicinity, and that the combustion products leave the combustor through exhaust nozzles located downstream of the combustion regions. The developed model accounts for the presence of a tangential mean flow in the annular combustor. To determine the BCs that needed to be established at the boundaries of the actively controlled, small-scale rig, the developed model accounts for the effects of the periodic combustion processes and flows through the reactants supply and exhaust nozzles in the “missing part” of the engine, and for the presence of a tangential mean flow in the annular combustor.

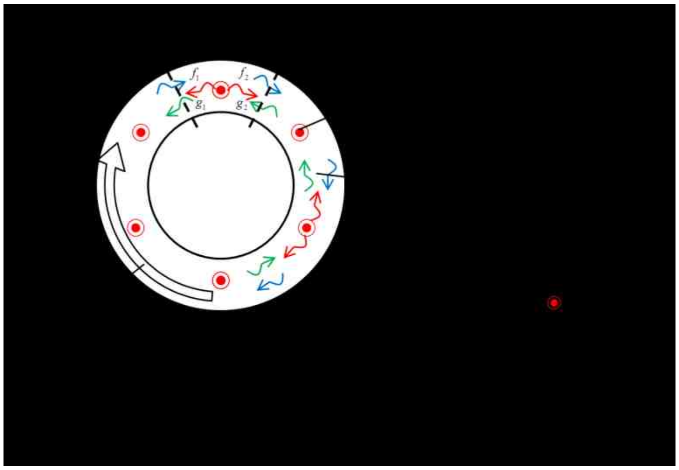

Description of the proposed approach that allows an actively controlled small-scale sector rig to simulate *tangential* combustion instability in the full-scale annular combustor

The developed model was numerically validated and used to investigate the effects of the exhaust nozzle, combustion process, and tangential mean flow component upon the characteristics of *tangential* CIs in an annular combustor. Specifically, the numerical simulations studied the interactions of initial travelling and standing acoustic waves disturbances with the exhaust nozzle and combustion process, and the effect of the tangential mean flow upon the characteristics of standing and travelling acoustic modes CIs.

Initially, numerical solutions of the developed model shed light on the damping and driving of the oscillations provided by the exhaust nozzle flow and a combustion process that is only "sensitive" to the local pressure perturbations, respectively, and the dependence of these processes upon the presence of a tangential mean flow in the annular combustor. They showed that in the *absence* of the tangential mean flow, initially travelling or standing acoustic wave disturbances are damped by the exhaust nozzle until a standing acoustic wave with its pressure node aligned with the exhaust nozzle is established in the annular combustor. This study also showed that a "pressure sensitive" (only) combustion process would amplify an initially travelling or standing wave disturbance, resulting in the establishment of a standing acoustic wave whose pressure anti-node is aligned with the combustion region. The amplitude of this CI continues to grow (to infinity) in the absence of nonlinear and/or damping processes that would limit the growth of wave.

It was also shown that when a tangential mean flow is *present* in the annular combustor, initial disturbances are continuously damped by the exhaust nozzle until their amplitudes are reduced to zero. However, when the driving by the pressure sensitive combustion process exceeds the exhaust nozzle damping, all initial disturbances are continuously amplified until, eventually, their amplitudes go to infinity, when there is a tangential mean flow in the annular combustor.

The developed model was also used to study how a combustion process that depends upon the steady (tangential) flow velocity component and (acoustic) velocity perturbation affects the characteristics (e.g., temporal variations of the spatial waveforms) of the ensuing CIs. Numerical solutions of the developed model showed when an initial disturbance is introduced into the annular combustor in the *absence* of a tangential mean flow, the (nonlinear) dependence of the combustion process upon the acoustic velocity *magnitude* produces a higher frequency component in the developed CI that oscillates with twice the frequency of the initial disturbance. They also showed that the *presence* and direction of the mean tangential flow component critically affect the characteristics of *tangential* (*spinning*) instabilities, due to the nonlinear dependence of the combustion process upon the acoustic velocity and the tangential mean flow. Specifically, this study showed that when a tangential mean flow component is *present* in the annular combustor, an initially standing wave disturbance gradually transforms itself into a *spinning* wave that rotates around the annular combustor in the direction of the tangential mean flow component. This finding is in agreement with previous experimental observations that have not been explained to date.

CHAPTER 1.

INTRODUCTION

The objective of this study was to develop a real time, active boundary control approach that would allow simulations of longitudinal and tangential combustion instabilities (CIs) in full-scale engines in small-scale laboratory rigs that could be used to study these CIs more thoroughly and at significantly lower cost.

1.1. Background and Motivation

The onset of combustion instabilities (CIs) has hindered the development and performance of combustion systems employed in industrial, power generating and propulsion systems for many decades, shortening components lifetime and causing systems failures. CIs manifest themselves as organized, large amplitude, pressure, velocity, and reaction rate oscillations in the combustion system [1, 2]. An example of pressure oscillations measured in an unstable combustor is shown in Figure 1.

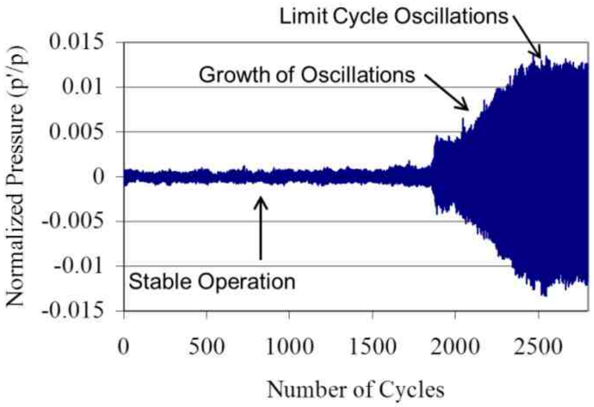

Figure 1. An example of pressure oscillations in an unstable laboratory combustor, from Lieuwen and Zinn [3, 4].

CIs are driven by *feedback processes* in which the combustion process and flow oscillations (e.g., vortex shedding and acoustic oscillations) interact with each other. Figure 2 presents an example of such a feedback process [2]. More specifically, CIs are excited when combustion process heat release oscillations drive acoustic pressure and velocity oscillations. These acoustic oscillations may, in turn, produce, e.g., periodic vortex shedding, mixing and reactants flow rates oscillations that enhance the combustion process heat release oscillations, thus producing a feedback process that supplies energy to the acoustic oscillations. Simultaneously, acoustic energy is lost from the oscillations by, for example, convection of acoustic energy out of the combustor (e.g., through the nozzle), viscous dissipation, and heat transfer. If the magnitude of the “driving” processes exceeds the magnitude of these “damping” processes, the energy of the oscillations increases with time. In this case, the oscillations are amplified until constant amplitude, limit cycle, oscillations are established in the combustor [3, 4] as shown in Figure 1. At the limit cycle, the time averages of the acoustic energies supplied and removed by the driving and damping processes, respectively, are equal and no net energy is added to the oscillations.

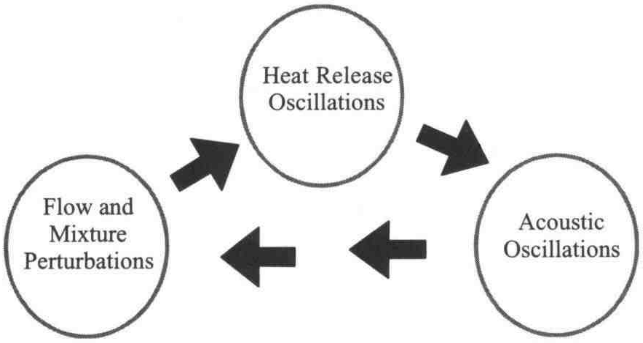

Figure 2. An example of a feedback cycle responsible for driving combustion instability, from Lieuwen and Yang [2].

The driving effectiveness of the feedback process generally depends upon two characteristic time constants: the period of the oscillations and the characteristic time constant of the feedback process. In a typical feedback process, each physical process affects another process after a time delay; e.g., the time lag of the combustion process, the relaxation time of the injection system, the chamber pressure relaxation time and so on. The sum of the time delays for the involved physical processes provides the total time delay for the completion of one feedback cycle, which represents its characteristic time constant. The feedback process drives CI only when the period of the instability is related to the time constant of the feedback process by a specific relationship as demonstrated by the example below. Notably, CIs generally excite a natural acoustic mode of the combustor whose period satisfies the required *"time relationship"*.

To illustrate the importance of the magnitude of the characteristic time constant of the feedback process, consider the simple combustor shown in Figure 3. It shows a combustible mixture of fuel and air injected into the combustor at its left boundary by a constant pressure supply system, thus generation a mean flow through the combustor. For simplicity, it is assumed that a concentrated combustion process occurs near the injector, see Figure 3-(i). Suppose that oscillations with a frequency, f_{osc}, occur near the injector that produce local chamber pressure oscillations as shown in Figure 3-(ii). This produces injector pressure drop oscillations that experience a minimum when the chamber pressure is at a maximum and vice versa. The oscillatory pressure drop across the injector produces an oscillatory injection rate after a certain time delay (i.e., the line relaxation time). The injection rate oscillations produce burning rate oscillations after a combustion time lag and, finally, the combustion heat release rate oscillations produce pressure, temperature, and velocity oscillations in the chamber after a time delay, which approximately equals the chamber relaxation time. The sum of the line relaxation time, the combustion time lag, and the chamber relaxation time provides a characteristic time constant for the feedback process, τ_{fb}, which is the total time delay for the completion of one feedback cycle. If in the example shown in Figure 3-(ii) the sum of these time delays is close to a half period of the local chamber pressure oscillations, i.e., $\tau_{fb} \approx \frac{1}{2} T_{osc} = \frac{1}{2} \frac{1}{f_{osc}}$, the combustor oscillations are amplified (driven) by the energy supplied by the oscillatory combustion process. If this condition is satisfied, when the local chamber pressure is at its minimum the reactants injection rate is at its maximum. At this instant, the injector supplies a "maximum energy packet" of reactants that releases its "maximum energy" and, thus, creates maximum driving of the combustor oscillations about a half a period of the oscillations later when the local chamber pressure is at its maximum, see Figure 3-(ii), thus enhancing the combustor oscillations. This example shows that a feedback process having a time constant, τ_{fb}, can drives the combustor oscillations only at selected frequencies; i.e., $f_{osc} \approx \frac{1}{2} \frac{1}{\tau_{fb}}$. If the frequency of one of the natural acoustic modes of the combustor satisfies this condition, i.e., $f_n \approx f_{osc} \approx \frac{1}{2} \frac{1}{\tau_{fb}}$, the combustion process (through the feedback process) may excite large amplitude oscillations of this natural acoustic mode of the system.

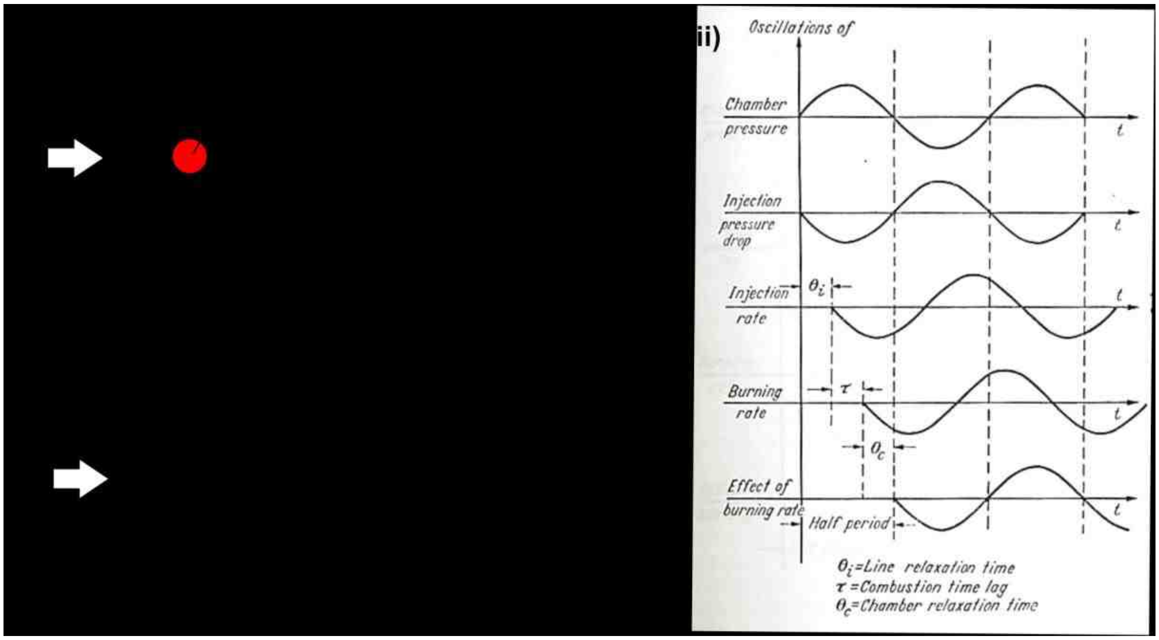

Figure 3. An example of time and spatial relationships for driving combustion instability; (i) an example of an unstable combustor, (ii) a schematic of the time dependence of the various oscillating quantities, showing relevant time delays, from Crocco and Cheng [1], (iii) locations of the combustion process relative to the structure of the excited acoustic pressure oscillations: (a) maximum driving, (b) driving, (c) no effective driving by the concentrated combustion process**.**

The driving of CI also depends upon the location of the oscillating combustion process relative to the structure of the excited acoustic mode pressure oscillations as shown in Figure 3-(iii). Let's assume that a natural acoustic mode oscillations with a frequency, $f_{n,1}$, and a feedback process having time constant, τ_{fb}, of the concentrated combustion process satisfy the above discussed time condition; i.e., $f_{n,1} \approx f_{osc} \approx \frac{1}{2}\frac{1}{\tau_{fb}}$. If the concentrated combustion process occurs at a node of the natural acoustic mode pressure oscillations, location (c) in Figure 3-(iii), this mode cannot be driven by the feedback process because the combustion process "experience" no pressure oscillations at the node, thus "preventing" the excitation of the feedback process. In this case, another natural acoustic mode of the combustor with a different frequency, $f_{n,2}$ ($f_{n,2} \neq f_{n,1}$), may be excited, if the oscillatory combustion process is not located at a the pressure node of this mode and the above discussed time condition is satisfied. On the other hand, when the concentrated combustion process is located at a pressure anti-node, i.e., location (a) in Figure 3-(iii), maximum driving of the pressure oscillations through the feedback process may occur. A combustion process located between a node and an anti-node of the acoustic pressure oscillations, e.g., location (b) in Figure 3-(iii), may still interact with the combustion process in a manner that will drive an instability.

The above discussion shows that the onset of CI and its frequencies depend upon the *temporal and spatial conditions* for driving the oscillations through a feedback process. The *temporal condition* relates the time delays of the involved physical and combustion processes and the periods of the natural acoustic modes of the system. The *spatial condition* relates the location of the combustion process heat release “relative” to the structure of the unstable mode. These conditions depend upon the design and operating conditions of the combustor and the characteristics of the unstable mode. Thus, combustion systems with different configurations and operating conditions are susceptible to CI having different frequencies and mode structures (e.g., tangential or longitudinal modes), because the parameters that affect these temporal and spatial conditions depend upon the system design and operating conditions. For example, changing the injection system design changes the line relaxation time and changing the fuel changes the time lag of the combustion process as different fuels (e.g., solid, liquid, and gaseous fuels) have different characteristic combustion times. Also, reducing the size of the combustion chamber increases the frequencies of its natural acoustic modes.

All of these modifications alter the feedback mechanism and may excite different CI modes at different frequencies.

Investigations of the mechanisms that drive CI generally consisted of combinations of experimental, theoretical, and numerical studies. These generally seek to elucidate the feedback process that drives the CI, see Figure 2. Ideally, the experimental setups used in such studies should be capable of simulating all the phenomena, e.g., thermodynamic operating conditions, mixing processes, combustion process, and acoustic oscillations that occur in the unstable full-scale engine to assure that all the parameters affecting the feedback mechanism are reproduced in the laboratory rig. Clearly, investigating the instability in the unstable, *full-scale* engine, would satisfy these requirements. However, investigating CI in the full-scale engine tests is not practical because of the exorbitant costs of such tests [5] and the inability to equip full-scale engines with diagnostic systems that could measure, e.g., the temporal and spatial dependence of the mean and acoustic pressures, temperatures, velocities, and reaction rates.

Because of the above described problems of investigating CI in full-scale engine combustors, most studies of CI to date were performed in *small-scale* setups that were geometrically similar to but smaller than the full-scale engine combustor. While testing with these small-scale setups reduced the cost of testing and produced important results [6, 7], the acoustic modes excited in the small-scale setups had higher frequencies and could not simulate the lower frequency oscillations that are excited in the unstable full-scale engines.

Next, we will discuss the problems associated with small-scale rigs that are used to study longitudinal and transverse (tangential) CIs. The former involves excitation of oscillations whose properties vary along the direction of the axis of the combustor and the latter involves the excitation of oscillations in transverse planes of the combustor whose properties vary in planes perpendicular to the combustor's axis. The problems associated with the study of these CIs will be discussed with the aid of Figure 4-(a) for longitudinal CI and Figure 4-(b) for transverse (tangential) CI. Figure 4-(a) shows a "full-scale" combustor that experiences longitudinal CI on top and a small-scale rig that is used to study this CI on the bottom. Such a small-scale rig is generally developed by reducing the length and diameter of the full-scale engine while maintaining other design parameters, such as mean flow Mach number (i.e., nozzle area ratio), injectors design, reactants combination, and fuel/air mixture ratio the same as in the full-scale engine on top of Figure 4-(a). The frequencies and driving/damping of the modes excited in the full-scale engine and the small-scale rig are determined by the combustion processes, the combustor's length and diameter (because it affects damping), the gas temperature, and the acoustic boundary conditions (BCs) at the combustor's inlet (where the injectors or fuel nozzles are located) and the outlet (where the exhaust nozzle is located). As discussed above, since CIs are excited when a certain relationship (e.g., the temporal/spatial conditions) is satisfied between the characteristic combustion time and the period of the acoustic mode, this relationship may be satisfied for different mechanisms or different modes in the small-scale rig and full-scale engine. For example, since the small-scale rig is shorter than the full-scale engine, the natural acoustic modes of the small-scale rig have higher frequencies and shorter wavelengths than the full-scale engine; i.e., $f_{n,small-scale} > f_{n,full-scale}$ and $\lambda_{n,small-scale} < \lambda_{n,full-scale}$. Consequently, the CIs' feedback processes in the small-scale rig and the full-scale rig should satisfy the following temporal conditions: $f_{n,small-scale} \approx \frac{1}{2}\frac{1}{\tau_{fb,small-scale}}$ and $f_{n,full-scale} \approx \frac{1}{2}\frac{1}{\tau_{fb,full-scale}}$. However, since the natural acoustic modes of the small-scale rig and the full-scale rig are different, the time constants of the feedback processes of the oscillatory combustion processes may significantly differ from one another (i.e., $\tau_{fb,small-scale} \neq \tau_{fb,full-scale}$). Additionally, the fundamental mode (e.g., $f_{1,small-scale}$) may be excited in the small-scale rig while the first harmonic of the fundamental mode (e.g., $f_{2,full-scale}$) will be excited in the full-scale engine because the frequencies of these two modes are close (e.g., $f_{1,small-scale} \approx f_{2,full-scale}$). However, since these modes have different spatial structures, their interactions with the oscillatory combustion processes may be significantly different. When these occur, the results obtained in the small-scale rig study may not elucidate the physics of the instability in the full-scale engine. This discussion indicates that in order for a small-scale rig to simulate (longitudinal) instabilities in a full-scale engine, it must simulate the acoustic environment experienced by the combustion process in the full-scale engine. As discussed below, this could be achieved by active control of the small-scale rig's acoustic boundary condition (BC).

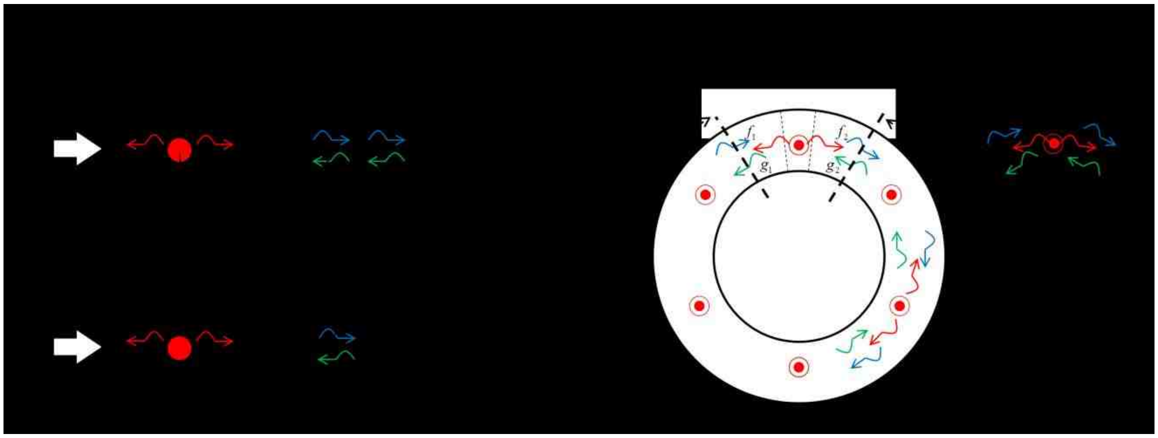

Figure 4. Descriptions of full-scale combustors and small-scale rigs: (a) case of longitudinal instability, (b) case of tangential instability.

Similar problems are encountered when attempting to simulate full-scale tangential instabilities, similar to those encountered in annular gas turbine combustors [8, 9], in a small-scale laboratory rig, see Figure 4-(b). In this case, the direction of the acoustic motions is normal to the direction of the mean flow from the injectors to the combustor's exit. Furthermore, the full-scale combustor employs several fuel nozzles while the small-scale rig may have only one (as shown in Figure 4-(b)), two or three fuel nozzles. Clearly, as in the above discussed longitudinal instability case, the small-scale "tangential" rig cannot simulate the acoustic environment in the unstable full-scale engine because of its smaller dimensions and, additionally, the need to account for the driving provided by all the fuel nozzles in the full-scale engine. Specifically, the onset and frequency of CI in the full-scale engine depend on the temporal and spatial variations of the state variables encountered by the multiplicity of combustion processes generated by all the fuel nozzles. Furthermore, the onset of CI in the full-scale engine and small-scale rig depends upon the acoustic damping in each system. To study tangential CIs, the small-scale rig could consist of a "segmented combustor", see Figure 4-(b), that is formed by “truncating” the full-scale annular combustor. Consequently, the small-scale rig would likely have a single fuel nozzle whose “single” combustion process would interact with acoustic oscillations excited by one or more natural acoustic mode whose frequencies are most likely much higher than the frequency of the instability in the full-scale annular combustor. In this small-scale rig, the driving is “supplied” by a “single combustion process” in contrast to the driving provided by the system of fuel nozzles in the full-scale combustor. Therefore, the small-scale rig cannot simulate the driving provided by all the injectors in the full-scale engine. Figure 4-(b) describes these problems. It indicates that the small-scale rig could simulate the CI of the full-scale engine only if the effects of the phenomena occurring in the “missing part” (shown in Figure 4-(b)) of the annular combustor could be simulated in the small-scale combustor by active control of the acoustic BCs at both ends of the small-scale rig. Specifically, the actively controlled BCs at the both ends of the small-scale rig would have to account for the effects of acoustic wave propagation/reflection and combustion processes in the “missing part” of the engine.

1.2. Simulating “Full-Scale” Combustion Instabilities in Small-Scale Laboratory Rigs

The above discussions indicate that in order to study the driving of CI in a full-scale engine in a small-scale rig, the latter must simulate the acoustic environment, the combustion process, and the interactions between these processes as encountered in the unstable, full-scale, engine.

1.2.1. Simulating Longitudinal Combustion Instabilities in Small-Scale Rigs

To demonstrate how to attain these goals, using active acoustic BC control, we will first discuss the case of longitudinal CIs with the aid of Figure 5, which shows a schematic of the full-scale engine on top and the actively controlled small-scale rig on the bottom. To illustrate how a small-scale rig might be able to simulate the acoustic environment in the unstable full-scale engine, we drew a vertical line (i.e., the thick dashed line (II)) at the location where the full-scale engine would be "cut off" in order to construct the small-scale rig. An acoustic wave generated in the combustion region in the unstable full-scale engine would propagate to the right, past the dashed line (II). When this wave reaches the exhaust nozzle, "part of the wave" will be transmitted through the nozzle and a "part" will be reflected off the nozzle and propagate back into the combustion chamber. Consequently, incident and reflected acoustic waves will be present at the location of the dashed line (II). The properties of these waves determine the magnitude and phase of the acoustic impedance (i.e., $z = p'/v'$) at that location. This acoustic impedance represents the effect of the acoustics in the combustor section to the right of the dashed line and the nozzle (i.e., the region between the dashed lines (II) and (III)) upon the oscillations in the combustor section to the left of the dashed line (i.e., the region between the dashed lines (I) and (II)). Consequently, if the acoustic impedances at the location of the dashed line (II) in the full-scale engine and the small-scale rig are the same, the acoustic environments to the left of the dashed line (II) in both setups will be the same. Finally, to assure that the small-scale rig simulates the driving in the full-scale engine, the small-scale rig must also simulate the mean flow Mach number in the full-scale engine and employ the same injectors' design, propellants, and mixture ratio as in the full-scale engine.

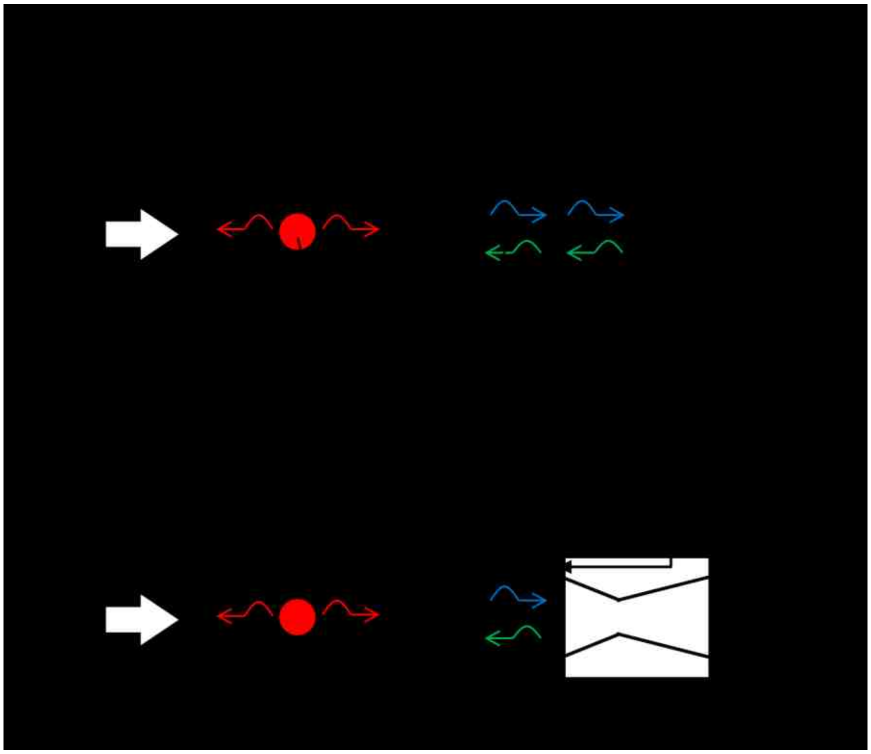

Figure 5. Proposed approach for using a small-scale rig with real time active boundary control to simulate the acoustic environment in an unstable full-scale engine experiencing an axial (longitudinal) combustion instability.

It is proposed that the small-scale rig employ actively controlled actuators (e.g., speakers) installed at its (right) exit to generate the acoustic impedance that is present at that location in the full-scale engine (i.e., the dashed line (II) in Figure 5). Such actuators could be installed on the sidewalls of the small-scale combustor rig near the exit plane to allow the combustion products to flow out of the rig.

In order to determine the acoustic BC (e.g., acoustic pressure and velocity, or impedance) at the boundary of the small-scale rig (i.e., location (II) in Figure 5), which needs to equal, e.g., the acoustic pressure and velocity (or the ratio of them, i.e., impedance) at the corresponding location in the full-scale engine, the proposed active control system (ACS) will have to perform the following tasks:

i. Determine the *right and left going waves* in the small-scale rig (i.e., region (I)~(II) in Figure 5) using the measured acoustic pressures, by performing "*wave separation*". This determines the *right going* acoustic wave arriving at the right boundary of the small-scale rig (i.e., location (II) in Figure 5).

ii. Numerically simulate in real time the acoustic waves propagation and reflection in the "missing part" of the full-scale engine (i.e., region (II)~(III) in Figure 5), and determine the properties of the reflected, *left going* acoustic wave arriving at location (II).

iii. Using the determined properties of the *right and left going* acoustic waves (obtained in steps *i.* and *ii.* above), determine the acoustic pressure and velocity at the boundary of the small-scale rig (i.e., location (II) in Figure 5).

iv. Use the actuator (e.g., speaker) at the boundary of the small-scale rig to generate the determined acoustic BC, i.e., acoustic pressure and velocity at the small-scale rig's boundary (determined in step *iii.*).

Such an active control system (ACS) was developed as part of this study and is discussed in detail in Chapter 2.

1.2.1.1. Related Studies

The developments and applications of *"active control approaches"*, which manipulate the acoustic impedance at the boundary of the rig using actively controlled actuator, were studied by several researchers. Guicking and Karcher [10] first suggested this concept to generate non-reflecting (or fully absorbing) BC at the termination of an impedance tube and implemented an ACS for noise absorption purposes. Paschereit at al. [11-13] investigated the application of a related "*impedance tuning approach*" to a combustion system under non-reacting and reacting flow conditions. Other related studies dealing with, e.g., noise absorption and resonator wave simulation, also showed that *impedance tuning approaches* can be used to control the impedance at a given location in a small-scale rig to create non-reflecting BCs that simulate anechoic terminations [10, 14] or maintain a predetermined reflection coefficient [11-13, 15]. Among these, the studies by Guicking and Karcher [10] and Paschereit at al. [11-13] are discussed herein as they influenced this study.

Guicking and Karcher [10] demonstrated active control of a one-dimensional acoustic wave reflection off a boundary. Specifically, the objective of their study was to develop a methodology for manipulating the acoustic impedance of a boundary using an actuator (e.g., a loud speaker in their study) to establish a fully absorbing (or, non-reflecting) acoustic BC.

Their experimental setup is shown in Figure 6-(a). It consisted of an impedance tube equipped with a loud speaker at each end. The speaker at the right boundary was used to excite a harmonic sound wave at a given frequency in the tube, and the speaker at the left boundary actively controlled the acoustic impedance (and, thus, the reflection coefficient) there. In order to generate the control signal, a *"wave separator"* algorithm was developed and first used to "manipulate" the acoustic pressures measured by two microphones (by adding, subtracting, and time-delaying), to "split" the acoustic wave field into *incident and reflected waves*, for pure harmonic excitations. A signal describing the incident wave was then fed into the amplifier (for the speaker), and the gain and phase of the amplifier signal were "manually tuned" until a non-reflecting acoustic BC was established at the left boundary where the actively controlled speaker was installed. Notably, this "manual tuning" process was necessary because their ACS could not determine "non-reflecting" acoustic impedance and did not have a speaker model that could be used to determine the command signal to speaker, as was done in this study (and discussed in Chapter 2).

This "empirical" ACS, using a wave separator, was applied to generate non-reflecting acoustic BC for harmonic oscillations at different frequencies. The result of their study is shown in Figure 6-(c). It shows the frequency dependence of the obtained reflection coefficient, $|r|$, (i.e., the ratio of the amplitude of the reflected wave to that of the incident wave) in the 100~800 Hz frequency range (see the solid line). Notably, it was close to zero over the investigated frequency range, thus demonstrating the effectiveness of the developed ACS for this specific application; i.e., establishing $|r| \cong 0$ at a boundary (while $|r| = 0$ at the ideal "non-reflecting" boundary). In their study, the use of the wave separator allowed the ACS to use the incident wave only without *"interference"* from the reflected wave, which was generated by the speaker, thus preventing unstable operation of the ACS (i.e., rapid amplification of the reflected wave), which could be driven by a *feedback path* involving the measurement system, the control system, and the speaker. It should be also noted that when the control was attempted without the use of a wave separator, with the use of only one measured acoustic pressure (see M_1 microphone in Figure 6-(b)), the *"feedback instability"* became significant and the ACS was not able to establish non-reflecting BC at frequencies above 400 Hz as described by the dashed line in Figure 6-(c).

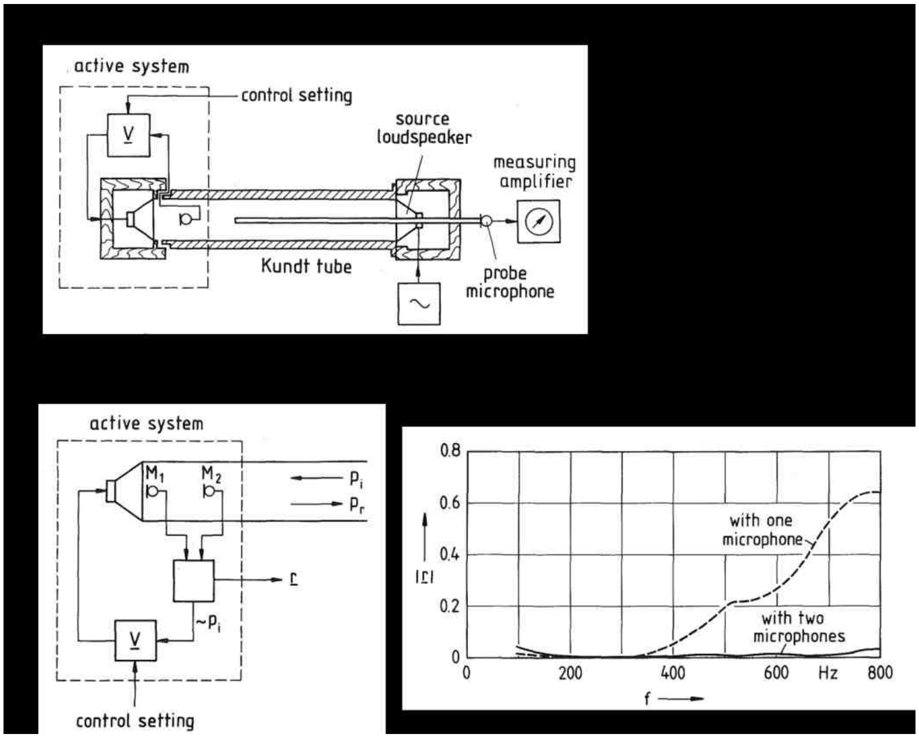

Figure 6. Active impedance control for one-dimensional sound, from Guicking and Karcher [10]: (a) experimental setup, (b) active impedance control with two feedback microphones (and a wave separator), (c) reflection coefficients obtained for harmonic excitations, with the wave separator (with two-microphones - solid line) and without wave separator (with one-microphone - dashed line).

These results suggest that it should be possible to actively manipulate the acoustic BC (or, acoustic impedance) by actively controlling an actuator (e.g., speaker) at the boundary of the rig. Also, a *wave separator*, which identifies the *right and left going waves* from two measured acoustic pressures in the rig, is crucial to the successful operation of such an active control approach. This study suggested that for an active control of an acoustic BC in a rig, the ACS would require capabilities for determining (i) the properties of the rightward and leftward moving waves in the rig, (ii) the acoustic pressure and velocity at the actively controlled boundary, and (iii) a “speaker model” that determines the required command current to the speaker that "generates" the desired acoustic BC.

Paschereit at al. [11-13] also used an active control scheme to manipulate the acoustic BC in a swirl stabilized, lean premixed, combustor, see Figure 7-(a). The objective of their studies was to investigate whether longitudinal CIs in full-scale combustors having different lengths may be investigated in the same test rig during *early engine design phases* before the final design and fabrication of the full-scale combustor.

To actively control the acoustic BC, they measured acoustic pressures using microphones located at several locations along the rig and used a *"wave separator"* to characterize the *right and left going waves* in the combustor. This wave separator was developed in *frequency domain*, based on the *"wave separator"* algorithm developed by Guicking and Karcher [10]. The commands for the acoustic impedance (i.e., $Z = \hat{P}/\hat{V}$) at the reference plane, where the actively controlled actuators, i.e., speakers, were located, as shown in Figure 7, were "predetermined" using pre-calculated frequency domain solutions of the acoustic motions in the full-scale combustor at each frequency. In order to apply this approach to general acoustic pressure signals consisting of several frequencies components, the measured signals were decomposed, and the wave separator was separately applied to each frequency component. These results were then used to determine acoustic BC at each frequency at the reference plane (i.e., the location of the actuators), and the results were synthesized to generate the time varying control signal to the actuator. Their study demonstrated that the ACS was able to generate fully reflecting and non-reflecting acoustic impedances at the boundary of the combustor (i.e., the location of the actively controlled actuators) under reacting and non-reacting flow conditions.

(a) Schematic set up of the atmospheric test rig

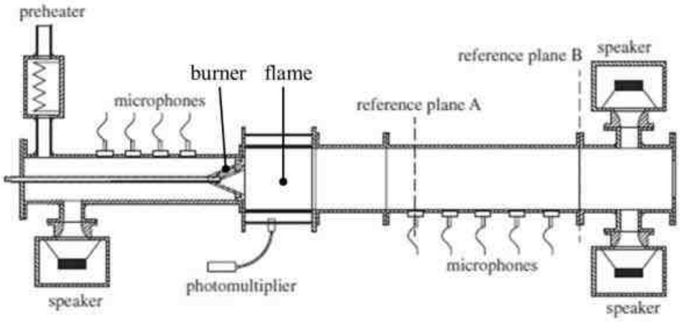

(b) Application of the active control scheme

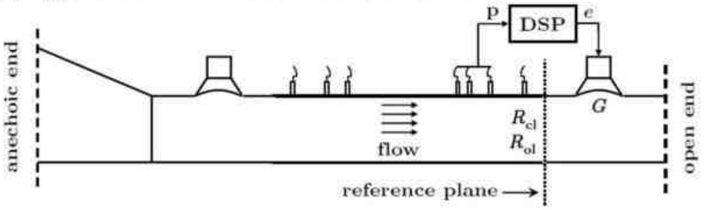

Figure 7. Impedance tuning of a premixed combustor using active control, from Bothien, Moeck, and Paschereit [11-13]: (a) schematic set up of the atmospheric test rig, (b) application of the active control scheme.

Paschereit at al.’s [11-13] results also suggest that it should be possible to use an active control approach to manipulate the acoustic BC of a small-scale combustor rig in order to allow it to simulate longitudinal CIs in different lengths’, full-scale, combustors. Notably, Paschereit at al.’s ACS also used a *wave separator* and *“apriori”* determined the actively controlled acoustic impedance BC in *frequency domain*. Additionally, their ACS could actively control multi-frequencies oscillations by employing signal decomposition and synthesis processes, which require relatively long computational periods and complex algorithms. This suggests that there is a need for another signal analysis approach that would enable active control of acoustic BCs in “real time”. Also, since their studies simulated only longitudinal CIs in full-scale combustors, it has been assumed that no combustion process is present in the “missing part” of the combustor, which allowed *“apriori”* determination of the actively controlled acoustic impedance at the boundary using the solutions of the full-scale combustor’s acoustics. Notably, this approach would not work, if combustion is present in the “missing part” of the full-scale engine and should be considered in the determination of the actively controlled, acoustic, (impedance) BC. Additionally, to simulate tangential CIs in a full-scale engine (where combustion occurs in the “missing part” of the full-scale engine; see Figure 4-(b)) in a small-scale rig, it may not be possible to *“apriori”* determine the actively controlled acoustic impedance BCs at the boundaries of the small-scale rig using frequency domain solutions that account for the effects of the acoustic oscillations, tangential mean flow, and combustion in the “missing part” of the full-scale combustor. Determining the actively controlled acoustic BCs in this case would require a model that describes the interactions among the combustion process, tangential mean flow, and acoustic waves in the “missing part” of the full-scale combustor, and could be solved in real time. The development of such a model is described in Chapter 3 of this thesis.

As discussed in the previous studies, to identify the rightward and leftward moving acoustic waves in the small-scale rig from the acoustic pressures measurements in real time, a *“wave separation”* module that uses two (or more) acoustic pressure measurements is required. Analysis of the acoustic field using acoustic pressures measured by two or more acoustic pressure sensors distributed along the rig has been extensively studied. For example, Chung and Blaser [16, 17] developed a transfer function method that determines the acoustic properties of a duct. They successfully decomposed a broadband stationary random acoustic wave in a duct into its complex incident and reflected components (for a complex reflection coefficient) using a transfer function relationship between the acoustic pressures at two locations in the tube. However, in order to develop a *"real time"* ACS, the wave separator needs to rapidly identify the rightward and leftward moving acoustic waves at least before the right going wave arrives at the reference plane (i.e., the boundary of the small-scale rig where the actively controlled actuator is installed), thus requiring a very short calculation time. For this reason, the transfer function method developed by Chung and Blaser [16, 17] is not directly applicable to the present study because it uses a relatively "slow" FFT to analyze the measured acoustic pressure signals [18, 19]. This indicates that in order to develop a "real time" ACS, a "real time" approach for determining the properties of the rightward and leftward moving waves using two measured acoustic pressures will have to be developed. The development of such an approach is described in Chapter 2 of this thesis.

The general features of the active control approaches used by Paschereit at al. [11-13] and Guicking and Karcher [10] are described in Figure 8. It shows that their ACS uses two (or more) transducers to measure the acoustic pressures in the small-scale rig. Next, the frequency spectra of the measured pressure signals are determined and fed into an array of the "wave separators" that determine the properties of the rightward and leftward moving waves at each frequency. These solutions are "modified" to satisfy *"apriori"* determined acoustic impedances that must be established at the small-scale rig's boundary by each frequency component present in the measured signal. The determined impedance BCs at the various frequencies are then synthesized to determine the acoustic BC that needs to be established by the actively controlled speaker. Finally, to determine the control current to the actively controlled speaker, the ACS requires the use of a “speaker model” that relates the acoustic pressure and velocities at the speaker’s diaphragm to the control current to the speaker. Notably, the ACS developed by Guicking and Karcher did not have such a model and they accomplished their objective by “manual” control of the current fed to the speaker, while Paschereit at al.’s ACS employed a speaker model, which is shown in Figure 8.

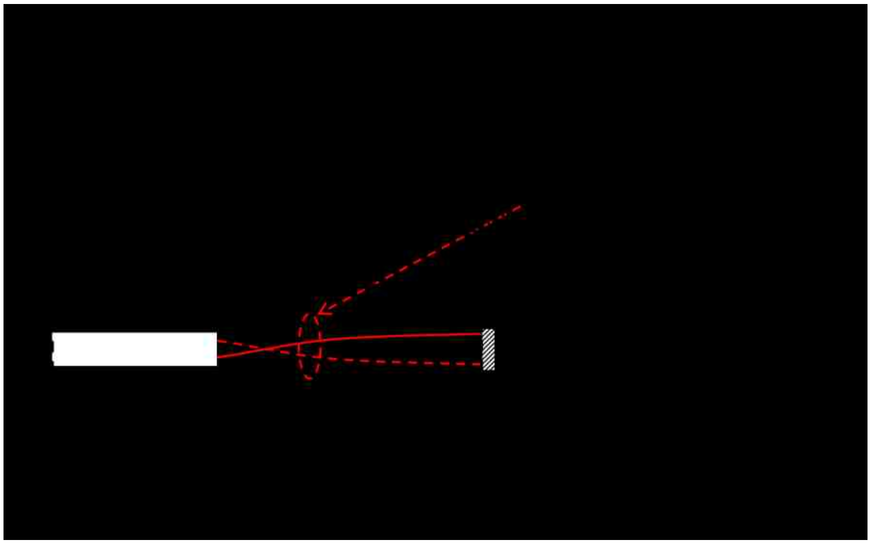

Figure 8. A schematic of the active control system used by previous investigators (Guicking and Karcher [10] and Paschereit at al. [11-13]) to simulate longitudinal oscillations in “full-scale” engines in a small-scale rig.

As discussed above, the ACS used in the earlier studies (described in Figure 8) used wave separators formulated in *frequency domain* to characterize the acoustic field inside the rig, and *“apriori”* determined the acoustic impedance at each frequency component present in the rig. Such *frequency domain* approaches are useful for developing a stable ACS because selective suppression of noise in unwanted frequency ranges can be attained. Also, as shown in Figure 8, the ACS “prescribed” *apriori* determined acoustic impedances at the location of the control actuator (shown as the red dashed circle) that were determined using frequency based analyses of the full-scale system acoustics (for example, see the red colored solution of the pressure amplitude near the boundary). Thus, before the operation of the ACS and the small-scale rig, the frequency domain solution of the full-scale system acoustics is required, and the acoustic impedances at the control actuator of the small-scale rig need to be determined *apriori* using this solution of the full-scale system acoustics.

1.2.1.2. Active Control Approach Developed in this Study

Since, as discussed above, the active acoustic BC control approaches that have been developed to date, see Figure 8, do not meet the performance goals of the ACS that would be required to simulate full-scale engines' CIs in a small-scale rig, this study has developed a new ACS that is shown in Figure 9. It consists of:

1. Two transducers to measure the acoustic pressures at two locations in the small-scale rig,
2. A *"wave separation"* module that determines the properties of the *rightward* and *leftward* moving acoustic waves in the rig in "real time",
3. A simulation module that determines in "real time" the properties of the rightward and leftward moving waves in the *"missing part"* of the full-scale combustor and determines the acoustic BC that must be "generated" at the boundary of the small-scale rig (i.e., location (II)),
4. A speaker model module that determines the control current to the speaker that would generate the required acoustic BC, and
5. An actuator (i.e., a speaker in this study) that actively generates the required acoustic BC at the boundary of the small-scale rig (i.e., location (II)).

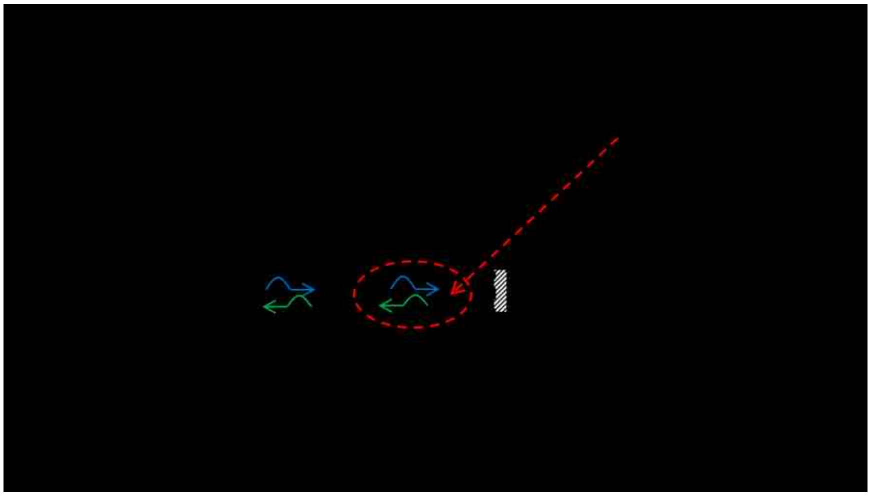

Figure 9. A schematic of the active control approach developed in this study to simulate full-scale engines', longitudinal, combustion instabilities in a small-scale rig.

To identify the rightward and leftward moving acoustic waves in the small-scale rig from the two acoustic pressures measurements in real time, a "wave separation" module was developed in this study. To meet the objectives of this study, the developed wave separation module needs to identify the rightward and leftward moving acoustic waves in a time shorter than the time required for the right going wave to arrive at the boundary of the small-scale rig where the actively controlled actuator is installed. In addition, since the right going wave identified by the wave separation module is used as an input to a "real time" simulation that determines the subsequent behavior of the combustion and acoustic processes in the "missing part" of the full-scale combustor, the wave separation module must use a "*time domain*" formulation, which significantly differs from the *"frequency domain"* approaches used by the previous investigators. For these reasons, this study has developed and used a relatively simple wave separation algorithm that analyzes the measured acoustic pressure signals without the use of, e.g., FFT, coherence calculations, etc. that require significant computation times. Therefore, the wave separation algorithm developed in this study “operates” in *time domain,* which requires short calculation times and, thus, provides “real time” active control. Additionally, the developed *time domain* wave separation algorithm is compatible with the real time, “time marching”, simulations of the combustion and acoustic processes in the “missing part” of the full-scale engine that are performed by the “simulation module”, see Figure 9.

Also, the developed *time domain* wave separation algorithm eliminates the need for the time consuming decomposition and synthesis processes that have been employed in the previous studies. Therefore, the developed *time domain* based ACS can handle active control scenarios involving general time varying signals; i.e., transient or stationary oscillating signals.

In summary, the main difference between the active control approach developed in this study and the previously used approaches to determine the actively controlled, acoustic, BC in the small-scale rig is the approach used to characterize the acoustic processes in the “missing part” of the full-scale combustor. Specifically, the previously developed approaches *“apriori”* determined the acoustic impedances that must be satisfied at the boundary of the small-scale rig by analyzing the acoustics (in the “missing part”) of the full-scale combustor. In contrast, this study determines the actively controlled, acoustic, BCs by analyzing the oscillations in the small-scale rig and the “missing part” of the full-scale combustor using a *“real time”* simulation. As shown in Figure 9 and discussed in Chapter 2, the simulation module numerically simulates in real time the acoustic processes in the “missing part” of the full-scale combustor (see the red dashed circle) and determines the acoustic BC at the actively controlled boundary of the small-scale rig. When combustion processes occurs in the “missing part” of the full-scale combustor, the simulation module of the ACS must simulate the combustion and acoustic processes and their interactions in the “missing part” of the full-scale combustor in real time using an appropriate model (which was also developed in this study and discussed in Chapter 3).

1.2.2. Simulating Tangential Combustion Instabilities in Small-Scale Rigs

This study also investigated the possible use of a small-scale “tangential” rig for investigating tangential CIs in full-scale engines. The proposed approach is described in Figure 10. It shows a small-scale rig consisting of a sector of the full-scale annular combustor located in the space between the two dashed lines (I) and (II). When a tangential CI occurs in the full-scale engine, it excites two travelling acoustic waves that move in opposite directions across the dashed lines (I) and (II) that enclose a small-scale segment of the full-scale engine in Figure 10. In this case, the wave that moves in the clockwise direction across the right dashed line (II) would move around the annular combustor before re-entering the segment across the left dashed line (I). As the two waves move around the engine, outside the “enclosed” segment, they are damped by, e.g., viscous and heat transfer processes and exhaust nozzles, and amplified by interactions with the combustion processes associated with the different fuel nozzles. In this case, actively controlled actuators located at the two ends (i.e., at the locations of the dashed lines (I) and (II)) of the small-scale rig would need to simulate the effect of all the processes taking place in the “removed” or “missing” part of the engine upon the processes in the small-scale rig between the two dashed lines (I) and (II). Specifically, these actuators will actively generate acoustic impedances at locations (I) and (II) of the small-scale rig that would equal to the acoustic impedances at the corresponding locations of the two dashed lines (I) and (II) in the full-scale annular combustor.

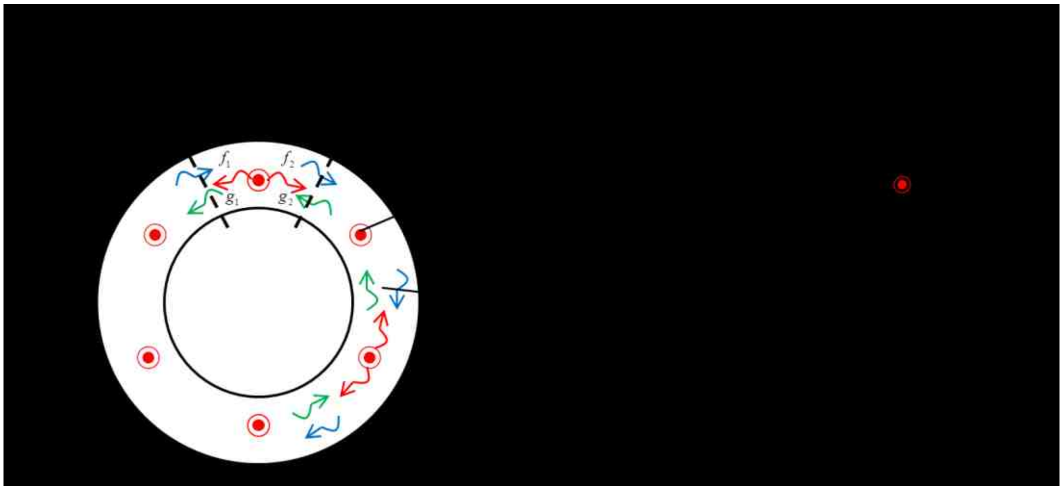

Figure 10. A schematic of the proposed small-scale rig with actively controlled acoustic boundary conditions (on the right) that simulates a tangential combustion instability in the full-scale annular combustor (on the left)

Notably, in the case of tangential CIs in a full-scale annular combustor (e.g., see Figure 10), multiple driving/damping sources (i.e., combustion processes, exhaust nozzles, and fuel/oxidizer nozzles) and propagating acoustic waves are present in the full-scale combustor, which differs from the scenarios encountered when trying to simulate axial (longitudinal) CIs in a small-scale rig, as discussed in Section 1.2.1. Clearly, the acoustic impedances that will have to be “established” at the two boundaries at locations (I) and (II) of the small-scale rig will have to account for the acoustic waves propagation and the damping and driving of the waves by the combustion processes, exhaust nozzles, and fuel/oxidizer nozzles that occur in the “missing part” of the full-scale combustor. As discussed in Chapter 3, this study has developed a real time approach for determining these actively controlled impedances that uses a model that describes the acoustic motions and their interactions with the combustion processes (including injectors and exhaust nozzles flows) and a tangential mean flow in the “missing part” of the full-scale annular combustor.

1.2.2.1. Proposed Active Control Approach for Simulating Tangential CI in a Small-Scale Rig

Figure 11 describes the approach proposed in this study for simulating the tangential CI in a full-scale annular combustor in a small-scale rig. It consists of a small-scale sector combustor rig equipped with an ACS installed at its boundaries at location (I) and (II). The wave separation module diagnoses the acoustic field inside the small-scale rig and identifies the properties of the waves crossing the boundaries of the small-scale rig (i.e., at the dashed lines (I) and (II)). Using a developed model, the real time simulation module estimates the changes experienced by the outgoing waves as they propagate through the “missing part” of the full-scale annular combustor (i.e., the region enclosed by red dashed lines in Figure 11) and interact with the concentrated combustion regions, exhaust nozzles, and fuel/oxidizer supply systems. For example, a wave crossing the left dashed line (I) in Figure 11 and moving in the counterclockwise direction will interact with several concentrated combustion processes, exhaust nozzles, and fuel/oxidizer supply systems before crossing the dashed line (II) on the right. Similarly, a wave travelling in the clockwise direction will experience similar interactions. The simulation module also estimates the acoustic impedances at the boundaries of the small-scale rig (i.e., the locations (I) and (II)) using the information provided by the wave separation module and the simulation module that determine the properties of the waves leaving and re-entering the small-scale rig at locations (I) and (II) at all times. Once determined, these acoustic impedances will have to be established at the boundaries of the small-scale rig (i.e., the locations (I) and (II)) by actuators (e.g., speakers) that will be driven by control signals generated by models of these actuators. Applying this approach, it would be possible to simulate in the small-scale rig the acoustic environment occurring at the dashed lines (I) and (II) in an unstable, full-scale, annular combustor.

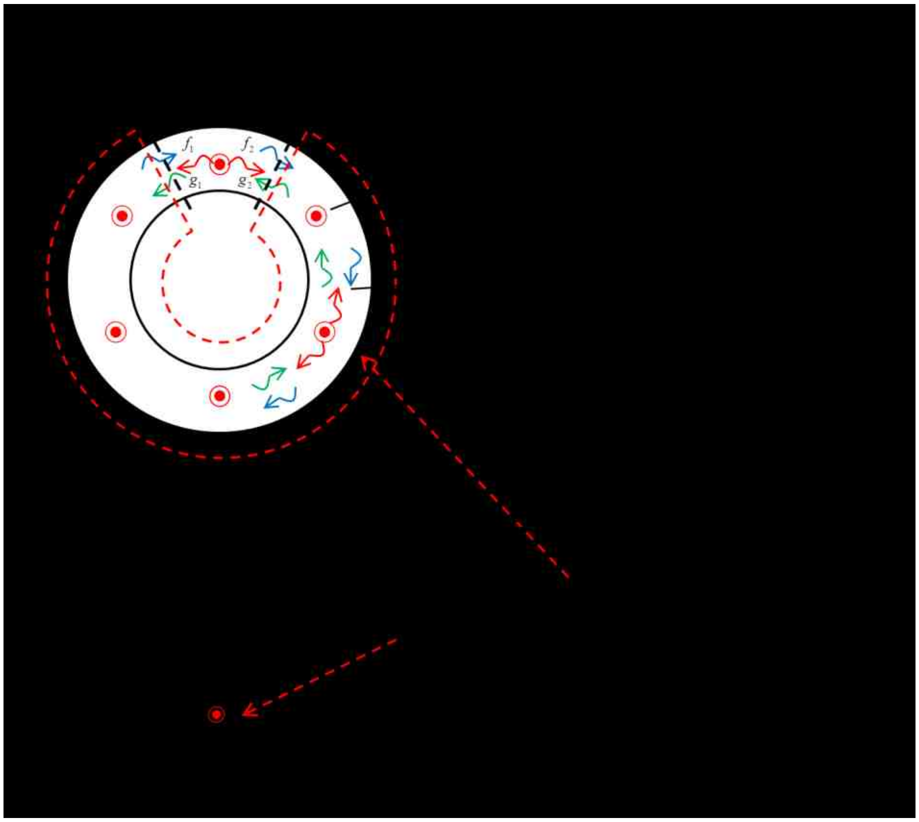

Figure 11. Description of a proposed active control approach for simulating a tangential combustion instability in a full-scale annular combustor in a small-scale rig.

1.3. Objectives of this Investigation

The overall objective of this study was to develop a real time, active boundary control approach that would allow simulations of longitudinal and tangential CI in full-scale engines in small-scale laboratory rigs. The following goals will have to be met to attain the overall objective of this study:

a. Develop a real time active control system (ACS) that consists of: (i) a *wave separation* module that determines the properties of the rightward and leftward propagating waves in the small-scale rig by analyzing (at least) two measured acoustic pressures; (ii) a simulation module that simulates the propagation, amplification, and damping of the acoustic waves in the "missing part" of the full-scale engine (e.g., see Figure 5 and Figure 10). This information is used to determine the acoustic BCs that need to be established at the boundaries of the small-scale rig; and (iii) an actuator module that uses the output of the simulation module (i.e., the acoustic BC) and models of the actuators (e.g., speakers) to determine the control signals to the actuators. These efforts are described in details in Chapter 2 of this thesis.
b. Develop the proposed ACS and investigate its performance in a small-scale rig that simulates the acoustics of longitudinal CIs in full-scale engines (e.g., see Figure 5). These efforts are also described in Chapter 2 of this thesis.
c. Develop a model that could be used to determine the time dependence of actively controlled BCs of a small-scale rig that simulates tangential CIs in a full-scale annular combustor (e.g., see Figure 10). Additionally, use the developed model to investigate the dependence of tangential CIs upon the characteristics of the combustion process, exhaust nozzle damping, the impedances of the reactants supply system, and the presence of a mean tangential flow component. These efforts are described in Chapter 3 of this thesis.

d. Propose follow up research efforts that will further expand the work performed under this study. These are described in Chapter 4 of this thesis.

CHAPTER 2.

DEVELOPMENT OF A REAL TIME ACTIVE ACOUSTIC BOUNDARY CONTROL APPROACH FOR SMALL-SCALE RIGS

As discussed in Chapter 1, in order to study the causes of combustion instabilities (CIs) in a full-scale engine in a small-scale rig, the acoustic environments in the unstable, full-scale, engine combustor must be reproduced in the small-scale rig. However, since the small-scale rig and the full-scale engine have different dimensions, the frequencies and amplitudes of the acoustic modes excited by CIs in these facilities are different. This chapter describes the results of a study that investigated the use of an active control system (ACS) to resolve this issue. Specifically, the objective of this study has been to determine whether actively controlled acoustic boundary conditions (BCs) could be applied to excite axial oscillations in a small-scale (short) rig that simulate the acoustic oscillations excited in a longer, full-scale, engine that experiences axial CIs. These efforts involved development of the necessary rigs, and the hardware and software of the ACS. The results of these studies are described in the remainder of this chapter.

2.1. Problem Statement

2.1.1. Simplified Problem

Since the objective of this study was to develop a specific active control system (ACS), this research was performed on a “simplified”, one-dimensional, cold flow, setup, which was developed for this purpose. The investigated problem is described in Figure 12. Figure 12-(a) describes a full-scale engine experiencing an axial instability that is driven by an oscillatory combustion process, which is described as a red ball near the left end of the combustor where the reactants are supplied. As stated earlier, the goal of this study is to determine whether the unstable oscillations in the full-scale engine could be simulated in the shorter rig shown in Figure 12-(b). To accomplish this, the shorter rig has been retrofitted with an ACS at its right boundary (i.e., at location II). The objective of this ACS is to reproduce the acoustic impedance at location II in the full-scale engine shown in Figure 12-(a) at the right boundary of the small-scale rig.

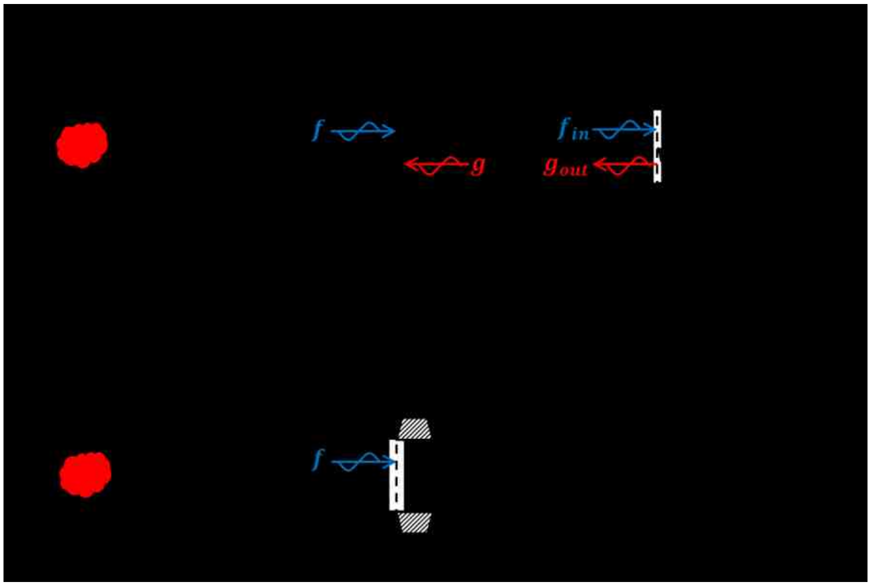

Figure 12. Schematics of the full-scale engine and the small-scale rig "simulator" with active control.

This would require, however, that the full-scale engine and small-scale rig "employ" a combustion process to drive the acoustic oscillations, which would introduce unnecessary complexities into this study. Also, an exhaust nozzle (see Figure 12) will be required to discharge the generated combustion products, which, in turn, will create a mean flow in the rig. These exhaust nozzle flow and mean flow will affect the acoustic boundary conditions (BCs) that will have to "set up" by the ACS in the small-scale rig.

Finally, the presence of an exhaust nozzle flow and mean flow will require the development of "complex" actuator that will have to be shielded (e.g., insulated or cooled) from the hot mean flow. However, for the purpose of investigating whether the ACS is able to simulate the oscillations in the full-scale engine in a small-scale rig by actively controlling the acoustic BCs of the small-scale rig, the incorporation of an exhaust nozzle would introduce unnecessary complexities into this study.

The above observations suggested that the objective of this study could be pursued using the cold flow setups described in Figure 13. It shows the "full-scale engine" on top and the actively controlled small-scale rig on the bottom. The objective of the study is to demonstrate that the actively controlled rig could simulate the longitudinal acoustic resonances of the full-scale engine on top in the small-scale rig on the bottom; i.e., the acoustic field in the actively controlled rig of length L_2 (i.e., region I~II) would be identical to the acoustic field in region I~II in the full-scale engine, see Figure 13.

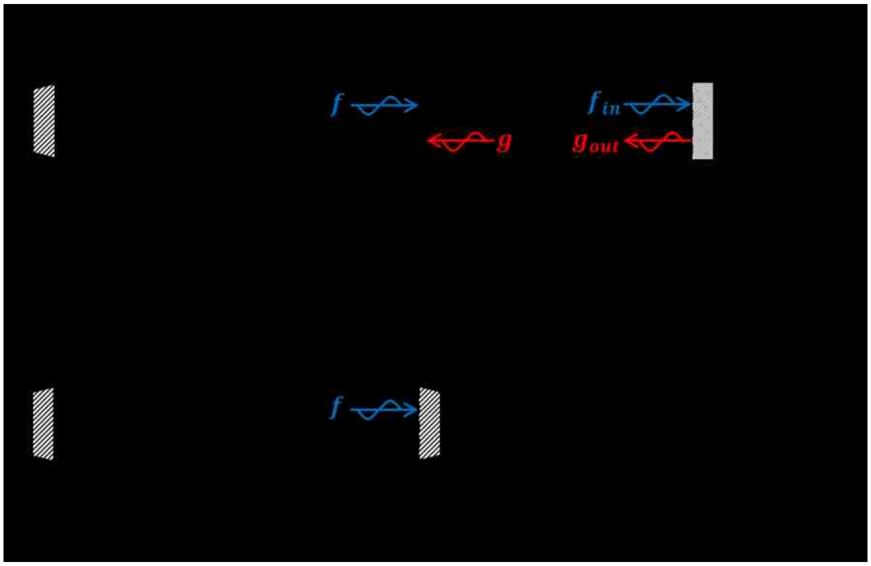

Figure 13. Description of the simplified one-dimensional cold flow setup used to develop the active control system.

To achieve this objective, the ACS should be able to simulate both travelling and standing wave type CIs that are encountered in unstable, full-scale, engines in the small-scale rig. This could be accomplished by experimentally demonstrating the developed ACS can determine the acoustic BC that must be established at the actively controlled boundary (at location II) of the small-scale rig that properly accounts for the effects of the acoustic oscillations in the "missing part" of the full-scale engine (i.e., in region II~III; see Figure 13).

If, for example, such capabilities could be demonstrated for "full-scale" engines having different lengths (and, thus, having different lengths of the "missing part" of the engine), then longitudinal resonances in different lengths' full-scale engines could be simulated using the same small-scale rig, as demonstrated later in this chapter. It is also noteworthy that, the ACS should be able to simulate any "portion" of the resonant standing wave oscillations in the full-scale engine within the small-scale rig. For example, as shown in Figure 13, the ACS should be also able to simulate the oscillations between, e.g., locations (1) and (2) in the full-scale engine (note that the distance between locations (1) and (2) also equals L_2, the length of the small-scale rig), in the small-scale rig.

2.1.2. Description of the Developed Active Control System (ACS)

To meet this study's objectives, the developed small-scale rig was equipped with a speaker at its left boundary and an ACS employing a speaker as an actuator at its right boundary, see Figure 14. The objective of the speaker on the left boundary is to drive an oscillation at a resonant frequency of the "full-scale" engine (i.e., the longer rig on the top of Figure 13 and Figure 14) in the small-scale rig, thus simulating the combustion process that drives resonant acoustic oscillations in unstable, full-scale, engine (as shown in Figure 12). The objective of the ACS is to establish the acoustic BC at location II of the small-scale rig that is the same as the acoustic condition (e.g., acoustic pressure and velocity, or impedance) at location II in the full-scale rig on top, see Figure 14 . If this would be accomplished, the acoustic fields in region I~II in the small-scale and full-scale rigs would be the same.

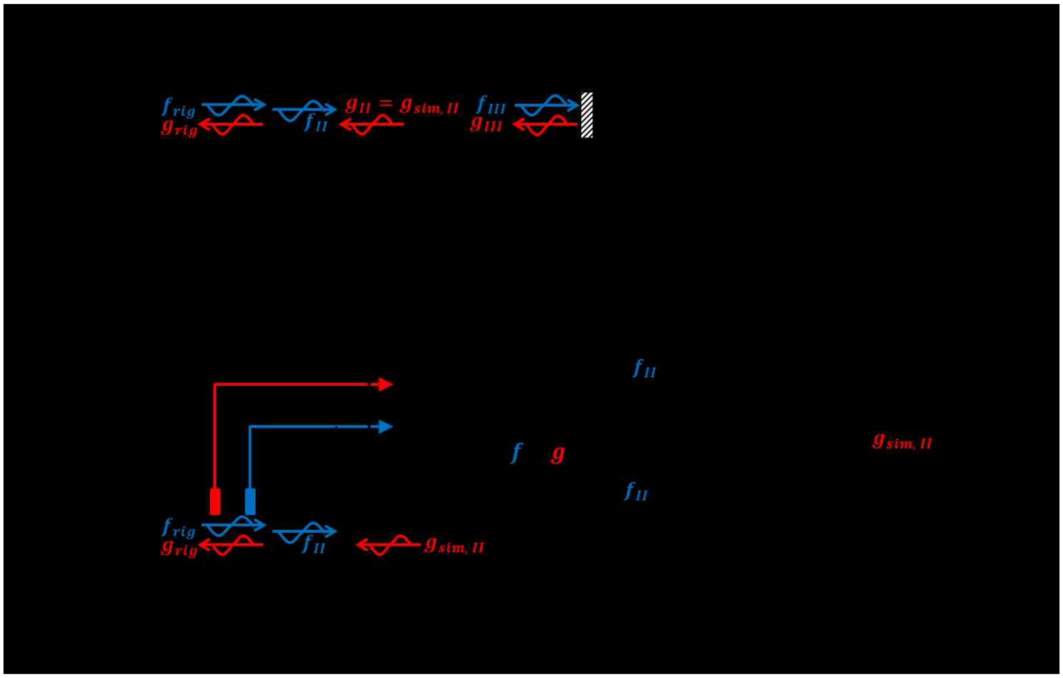

Figure 14. Schematics of the developed, actively controlled, small-scale rig simulator (bottom) and the corresponding "full-scale rig" (top).

To achieve these objectives, the ACS must first diagnose the acoustic field inside the small-scale rig (i.e., region I~II in Figure 14). To accomplish this, the acoustic pressures inside the small-scale rig are measured with pressure transducers, which are installed on the wall of the rig. The ACS analyses the measured acoustic pressures (minimally at two locations) and characterizes the properties of the acoustic waves leaving and entering the rig; i.e., it performs *"wave separation"* analysis that determines the *right going wave*, f_{rig}, and the *left going wave*, g_{rig}, of the excited acoustic field, see Figure 14. The right going wave, f_{rig}, propagates toward the right boundary of the rig (i.e., location II) where it "leaves" the rig, see f_{II} in Figure 14. Thus, the "wave separation module" of the ACS in Figure 14 determines the properties of f_{rig} and f_{II} and provides this information to the "simulation module" of the ACS.

Next, the ACS must simulate the acoustic waves' propagations/reflections in the "missing part" in the full-scale engine; i.e., region II~III in Figure 14. In the full-scale engine, the right going wave, f_{II}, continues to propagate into the "missing part" of the "full-scale engine" until it arrives at the right boundary of the engine (i.e., location III), see f_{III} in Figure 14. This right going wave, f_{III}, is then reflected off the boundary at location III to generate the left going wave, g_{III}. This left going wave, g_{III}, propagates back towards location II, see g_{II} on top of Figure 14. The ACS simulates these waves' propagation and reflection processes in region II~III, to "estimate" the properties of the left going wave, g_{II} at location II in the full-scale engine that equals $g_{sim,II}$ at location II at the right boundary of the small-scale rig; i.e., $g_{sim,II}$ is the estimation of g_{II}, see bottom of Figure 14. This analysis is performed by the "simulation module" of the ACS in Figure 14.

Next, the ACS determines the acoustic BC at the location of the actuator (i.e., location II) by using the results provided by the wave separation and simulation modules. At location II in the full-scale rig (see top of Figure 14), the acoustic pressure, p', and velocity, v', are related to the right going wave, f_{II}, and the left going wave, g_{II}; i.e., $p'_{II} = f_{II} + g_{II}$ and $v'_{II} = \frac{1}{\rho c}(f_{II} - g_{II})$ [20-22]. On the other hand, the ACS determines the acoustic BC at the right boundary (location II) of the small-scale rig by combining the right going wave, f_{II}, and the estimated left going wave, $g_{sim,II}$ to obtain i.e., $\widetilde{p'}_{II} = f_{II} + g_{sim,II}$ and $\widetilde{v'}_{II} = \frac{1}{\rho c}\left(f_{II} - g_{sim,II}\right)$, see bottom of Figure 14. Notably, p'_{II} and v'_{II} are the acoustic pressure and velocity at location II in the full-scale engine while $\widetilde{p'}_{II}$ and $\widetilde{v'}_{II}$ are the acoustic pressure and velocity estimated by the "simulation module" of the ACS to determine the "needed" acoustic BC (at location II) of the small-scale rig, which is also determined by the "simulation module" of the ACS in Figure 14.

Finally, the actuator (i.e., a speaker in this study) of the ACS is used to establish the estimated acoustic pressure, $\widetilde{p'}_{II}$, and velocity, $\widetilde{v'}_{II}$, at the right boundary of the small-scale rig. To accomplish this, the actuator must receive a control command from the ACS that describes the time dependence of the input current to the speaker. The model of the speaker that was used to calculate this input current to the speaker using the estimated acoustic pressure and velocity at location II, see "speaker model module" in Figure 14, will be discussed later.

2.2. Development of the Actively Controlled Small-Scale Laboratory Rig Simulator

The roles of the modules of the ACS (i.e., the "wave separation", "simulation", and "speaker model" modules) are described in the previous section and Figure 14. In this section, the development of these modules is discussed.

2.2.1. The Wave Separation Module

This section describes how the *wave separation* module determines the properties of the right and the left going waves in the small-scale rig from measured acoustic pressures. A one-dimensional acoustic field can be represented by a combination of a *"right going wave"* and a *"left going wave"*. By determining the properties of the right and the left going waves, the acoustic field in the small-scale rig can be characterized.

As discussed in Chapter 1, Chung and Blaser [16, 17] showed that one-dimensional acoustic field can be accurately analyzed by a transfer function method employing FFT and coherence analyses. However, this and related approaches require a relatively "long" period of time to "collect" and "analyze" a large arrays of sampled data [18, 19]. For example, in this study, the ACS measured the acoustic pressures and performed the required calculations (using the three modules discussed in Section 2.1.2.) to determine the control signal at a sampling frequency, $f_s = 10\ kHz$ (or with a sampling time, $\tau_s = 1/f_s = 0.1\ msec$). If a FFT analysis is used to determine the frequency content of the signal in the 1 Hz to 5 kHz ($= f_s/2$) range with resolution of 1 Hz, 1 sec period of time is required to collect 10000 samples of data, and a "long" calculation time is necessary to integrate 10000 samples of the data at each frequency. The duration of these processes is too long (i.e., more than 1 sec) for the proposed real time active control approach (that requires a computation time less than 0.1 msec). Therefore, a different signal analysis approach was developed in this study to reduce the measured acoustic pressures analysis period. Specifically, the developed wave separation algorithm employs simple formulas whose solution requires relatively small amount of data and very short "calculation time" compared with commonly used approaches such as FFT and coherence calculations. This approach allows the wave separation module to rapidly identify the right and the left going waves in the small-scale rig *before* the right going wave arrives at the right boundary of the small-scale rig where the actively controlled actuator is installed (i.e., location II in Figure 14), thus enabling "real time" active control.

In this study, a time domain approach was used to develop the *wave separation algorithm* rather than a frequency domain approach that has been used in related studies [10-14]. This approach allows the wave separation algorithm to handle "all" time varying signals, including transient and stationary, oscillatory signals. The developed wave separation algorithm has been also incorporated into the simulation module that analyses the acoustics in the missing part of the engine; i.e., the module that performs the real time numerical simulation of the acoustics in the missing part of the engine using a *"time marching"* approach.

2.2.1.1. The Wave Separation Algorithm

The wave separation algorithm essentially employs the well-known *"method of characteristics"* [21, 22]. The right and the left going waves propagations are described using *"characteristic lines"* in the (x, t) plane, as shown in Figure 15, where the abscissa is the space coordinate, x, and the ordinate is the time coordinate, t. In this *characteristic plane* (x, t), waves propagating at a constant speed of sound, c, are represented as straight lines. For example, when the medium is stationary (i.e., the mean flow velocity is $\bar{V} = 0$), a right going wave is represented as a line having a positive slope, $\frac{1}{c}$, and a left going wave is represented by a line having a negative slope, $\frac{1}{-c}$; e.g., see the *characteristic lines* R1 and L1 in Figure 15.

The objective of the wave separation module is to determine the properties of the acoustic pressures and velocities at any location in the small-scale rig from the measurements of acoustic pressures at (a minimum of) two locations in the rig. For example, the wave separation module may need to determine the properties of the right going wave, f_3, at location x_3 from the two acoustic pressures, p'_1 and p'_2, measured at locations x_1 and x_2, respectively, see Figure 15.

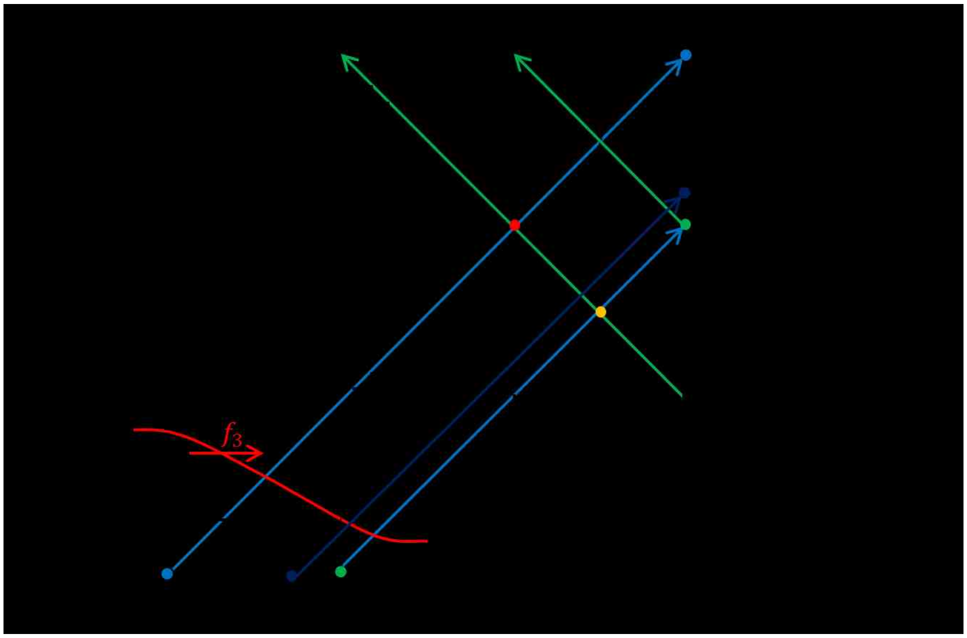

Figure 15. Characteristics of acoustic waves and the wave separation algorithm.

An acoustic pressure measured at a certain location and time can be represented by the sum of a right going wave and a left going wave at that location and time. For example, the acoustic pressures, p'_1 measured at location x_1 at time t and p'_2 measured at location x_2 at time $t-\tau$, are described by the expressions in Eq. (2-1) below, where t is the current time and τ is the time required for an acoustic wave to propagate from location x_1 to location x_2, see Figure 15.

$$\begin{aligned} p_1'(t) &= f_1(t) + g_1(t) \\ p_2'(t-\tau) &= f_2(t-\tau) + g_2(t-\tau) \end{aligned} \qquad \textbf{(2-1)}$$

where, $p'_2(t-\tau)$ was measured earlier (i.e., at time $t-\tau$) and stored by the ACS.

The properties of the right and left going waves are constant along their corresponding characteristic lines; i.e., $f = constant$ on line R1 and $g = constant$ on line L1. Using these properties and Figure 15, the following relationships are obtained:

$$\begin{aligned} f_3(t+2\cdot\tau) &= f_1(t) \\ f_3(t) &= f_2(t-\tau) \\ g_1(t) &= g_2(t-\tau) \end{aligned} \tag{2-2}$$

The first relationship in Eq. (2-2) states that the right going wave at location x_3 and time $t + 2 \cdot \tau$, $f_3(t + 2 \cdot \tau)$, is equal to the right going wave at location x_1 and time t, $f_1(t)$, since the right going wave is constant along the characteristic line R1; see Figure 15. Similarly, the second and third relationships in Eq. (2-2) can be derived using the characteristic lines R2 and L1, respectively.

Using Eqs. (2-1) and (2-2) and Figure 15, the change in magnitude of the right going wave between the characteristic lines R1 and R2, can be derived. Specifically, subtracting $p'_2(t-\tau)$ from $p'_1(t)$ provides the following expression for the change in magnitude, Δp_f, of the right going wave:

$$\begin{aligned} p_1'(t) - p_2'(t-\tau) &= f_1(t) + g_1(t) - f_2(t-\tau) - g_2(t-\tau) \\ &= f_1(t) - f_2(t-\tau) \\ &\equiv \Delta p_f \end{aligned} \tag{2-3}$$

because $g_1(t) = g_2(t-\tau)$ from the last relationship in Eq. (2-2).

Substituting the first and second expressions in Eq. (2-2) into Eq. (2-3) and manipulating the resulting expression yields the following relationship:

$$\begin{aligned} \Delta p_f &= p_1'(t) - p_2'(t-\tau) \\ f_3(t+2\cdot\tau) &= f_3(t) + \Delta p_f \end{aligned} \tag{2-4}$$

where the value, $f_3(t)$, of the right going wave at location x_3 and time t is known because it has been determined at earlier time $t - 2 \cdot \tau$. Equation (2-4) essentially shows that using the two measured acoustic pressures at locations x_1 and x_2 and times t and $t - \tau$, respectively, and the stored value of the right going wave (i.e., $f_3(t)$), the right going wave at location x_3 at 2τ time later (i.e., $f_3(t + 2 \cdot \tau)$) can be obtained.

While Eq. (2-4) is general and can be used when *"continuous"* descriptions of the measured pressures are available, in practice the measured pressures are discretized at a certain sampling rate given by, e.g., $\tau_s = \frac{1}{f_s}$, where f_s is the sampling frequency. The ACS measures acoustic pressures and performs the required operations (e.g., wave separation, simulation, etc.) at every discretized time instant, τ_s. In this case, the current time t can be described by a time index i that satisfies the relationship, $t = i \cdot \tau_s$, and the next time step t_{next} is given by $t_{next} = t + \tau_s = (i + 1) \cdot \tau_s$, where i is an integer. In the developed ACS, the "times" in Eq. (2-4) are replaced by their *"digital"* descriptions using the time index i as shown in Eq. (2-5) below, where m is the number of digital time steps required for an acoustic wave to propagate from location x_1 to location x_2; i.e., $\tau \approx \tau_s \cdot m$, where m is a positive integer.

$$\begin{aligned} \Delta p_f &= p_1'(i \cdot \tau_s) - p_2'(i \cdot \tau_s - \tau_s \cdot m) \\ f_3(i \cdot \tau_s + 2 \cdot \tau_s \cdot m) &= f_3(i \cdot \tau_s) + \Delta p_f \end{aligned} \tag{2-5}$$

Omitting, for convenience, τ_s from the above equations yields the following simplified expressions in a *"discrete form"*:

$$\begin{aligned} \Delta p_f &= p_1'(i) - p_2'(i - m) \\ f_3(i + 2 \cdot m) &= f_3(i) + \Delta p_f \end{aligned} \tag{2-6}$$

While on the surface either Eq. (2-4) or (2-6) could be used to perform wave separation, the application of these equations in practice is problematic because of numerical stability issues. From a numerical point of view, these equations are similar to those obtained when applying the first-order upwind scheme (using the spatial grid Δx and the temporal grid Δt) with $CFL = c\Delta t/\Delta x = 1$ to the solution of 1-D convection equations, which also describes the wave equations [23, 24]. Equation (2-7) below provides an example of a 1-D convection equation, a first-order upwind scheme (Forward-Time Backward-Space (FTBS) [24]) for its numerical solution, and the definition of the CFL number.

$$\frac{\partial f}{\partial t} + c\frac{\partial f}{\partial x} = 0$$

$$f(x, t+\Delta \mathrm{t}) = f(x,t) - c\frac{\Delta t}{\Delta x}\left(f(x,t) - f(x-\Delta x, t)\right) \qquad \textbf{(2-7)}$$

where, $CFL = c\dfrac{\Delta t}{\Delta x}$

Figure 16 below describes the relationships between the used (known) data and the estimated data determined by the wave separation algorithm (using Eq. (2-6)) and the first-order upwind scheme shown in Eq. (2-7), respectively, by showing the domains of dependence of both schemes [23-26]. Specifically, the wave separation algorithm uses the known values of $p'_1(i)$, $p'_2(i-m)$, and $f_3(i)$ (shown as black points) to calculate an "estimated" value of $f_3(i + 2 \cdot m)$ (shown as a red point). On the other hand, the first-order upwind scheme uses the known values of $f(x - \Delta x, t)$ and $f(x, t)$ (shown as black points) to calculate $f(x, t + \Delta t)$ (shown as a red point), which describes the wave at the next time step. It can be shown that if the wave separation algorithm is applied to solve the 1-D convection equation to determine the propagation of only right going waves, the algorithm becomes equivalent to the first-order upwind scheme with $CFL = 1$.

For numerical stability, this numerical scheme requires a $CFL \leq 1$ (note that $CFL = 1$ is only marginally stable) [24, 25]. The numerical scheme with $CFL = 1$ employs a grid size, Δx, and a time step size, Δt, that satisfy the relationship, $CFL = c\Delta t/\Delta x = 1$; see the shaded triangle in Figure 16-(b). To assure numerical stability, it requires that $CFL < 1$. This, in turn, requires that the time step size, Δt, be reduced to yield $CFL = c\Delta t/\Delta x < 1$ for the given grid size, Δx. Thus, a stable first-order upwind scheme (Forward-Time Backward-Space (FTBS)) determines the estimated data point at the next time step, $f(x, t + \Delta t)$, inside the shaded triangular region or on the line between $f(x, t + \Delta t)$ (when $CFL = 1$ and shown as a red point), and $f(x, t)$ (shown as a black point); see Figure 16-(b). Similarly, as shown in Figure 16-(a), the data points needed for applications of the wave separation algorithm are located “on” the boundaries of the domains of dependence (shaded regions), which results in $CFL = 1$ and a marginally stable algorithm. Notably, a numerical scheme having $CFL < 1$ is stable because an error introduced at a certain time step t is subsequently suppressed by the numerical scheme. On the other hand, when $CFL = 1$, an error introduced at a certain time step t is not amplified nor suppressed as the calculation proceeds. Thus, since errors are continuously introduced in experiments, they are accumulated and amplified as the calculation proceeds when $CFL = 1$. Consequently, when Eq. (2-6) is applied to analyze noisy experimental data, this algorithm becomes unstable, and the solution diverges.

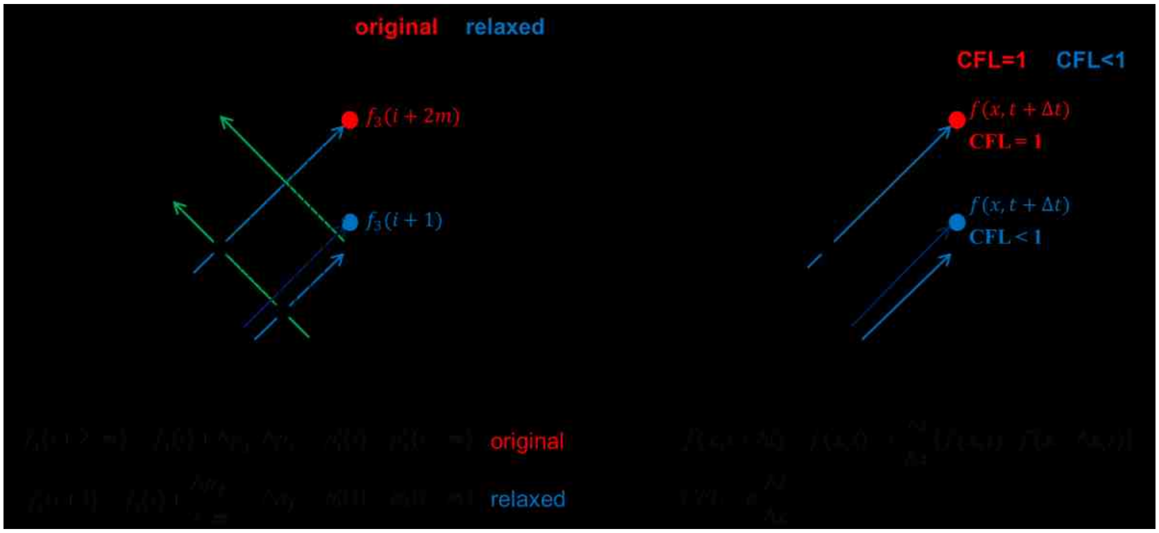

Figure 16. Domains of dependence; (a) original (Eq.(2-6)) and relaxed (Eq. (2-8)) wave separation algorithm, (b) first-order unwind scheme (Eq. (2-7)) (Forward-Time Backward-Space (FTBS)) for solving 1-D convection equation with CFL=1 and CFL<1.

To illustrate this point, Eq. (2-6) was applied to analyze the behavior of a given, “pure”, right going travelling wave field. Adding noise to an assumed, “exact”, solution for the pressures, p'_1 and p'_2, the right going wave at location x_3 was estimated and compared with the exact value provided by the known (assumed) travelling wave. The results are shown in Figure 17. Figure 17-(a) shows that the solution (described by the red curve) becomes unstable and slowly diverges from the exact solution (represented by the black curve). This example shows that the wave separation algorithm employing Eq. (2-6) produces erroneous solution when $CFL = 1$, even though the scheme is marginally stable in this case.

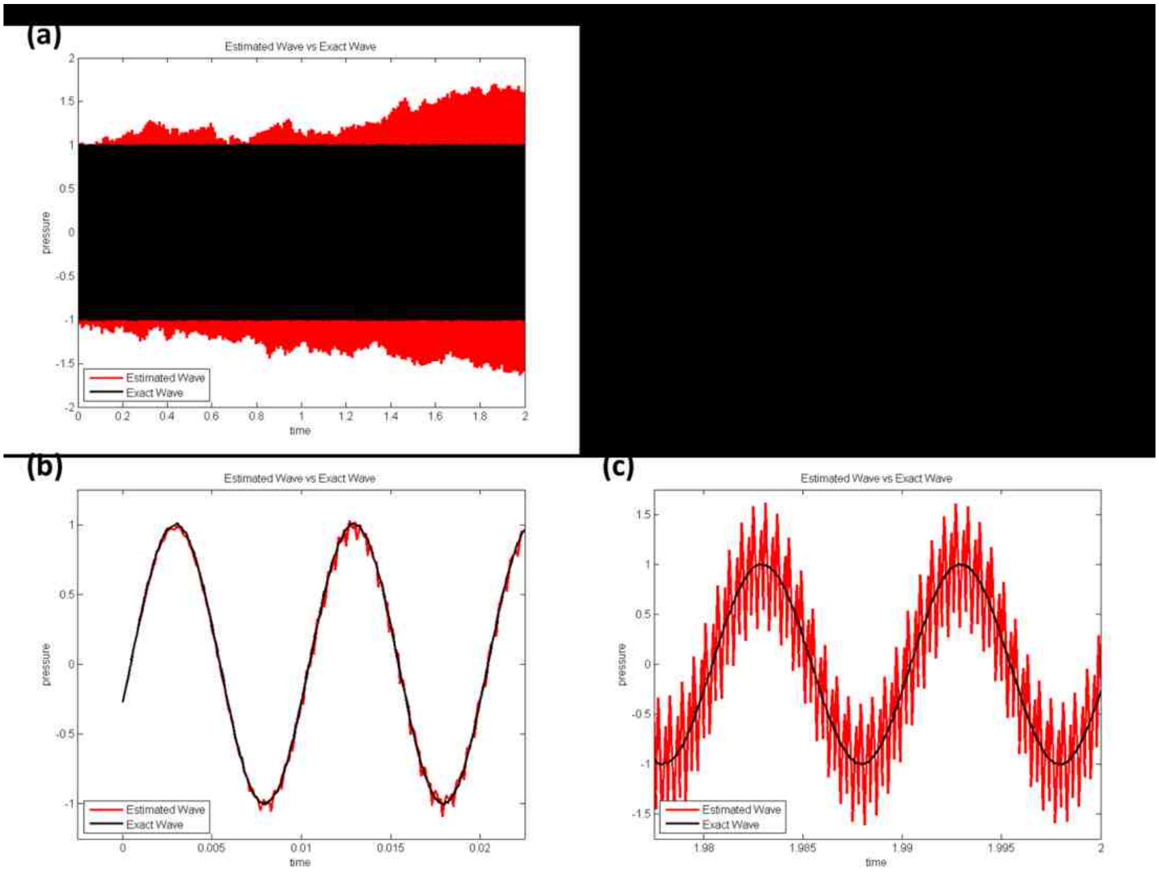

Figure 17. Example of numerical test (with 100 Hz right going travelling wave) of the original algorithm (Eq. (2-6)); (a) whole result: exact wave (black line) and estimated wave (red line), (b) result shortly after the start of the calculation, (c) result near 1.5 sec.

Also, as shown in Eq. (2-6), the information at each time step does not depend on the information at “adjacent” time steps (i.e., $i \pm 1$). In fact, Eq. (2-6) shows that it only depends on the information at time indices located $2 \cdot m$ time steps apart; e.g., $f_3(i + 2 \cdot m)$ depends on $f_3(i)$. In the domain of dependence in Figure 16-(a), the value of $f_3(i + 2 \cdot m)$ (depicted as a red point) depends on $f_3(i)$ but not on the values of $f_3(\cdot)$ at any intermediate time steps such as $f_3(i + 1)$, $\dots f_3(i + 2 \cdot m - 1)$ (depicted as open circles). Specifically, $f_3(i + 2 \cdot m)$ depends on $f_3(i)$, $f_3(i)$ depends on $f_3(i - 2 \cdot m)$, and $f_3(i - 2 \cdot m)$ depends on $f_3(i - 4 \cdot m)$, etc. On the other hand, $f_3(i + 2 \cdot m - 1)$

depends on $f_3(i-1)$, $f_3(i-2\cdot m-1)$, $f_3(i-4\cdot m-1)$, etc. Consequently, the estimations at adjacent time steps, e.g., $f_3(i+2\cdot m)$ and $f_3(i+2\cdot m-1)$ (or, equivalently $f_3(i)$ and $f_3(i-1)$), do not depend upon each other. As the calculation proceeds, estimations at adjacent time steps accumulate errors independently, and the estimated signal eventually has higher frequency oscillation errors that are related to τ_s. This growth of high frequency oscillations errors in time is shown in Figure 17-(b) (in the initial period) and Figure 17-(c) (near the end of the calculation).

The discussed algorithm can be stabilized by adding a *"relaxation"* to the numerical scheme. Equation (2-6) shows that the magnitude of the right going wave at location x_3 changes by an "exact" amount, Δp_f, between the time steps i and $i+2\cdot m$. This "exact" difference, Δp_f, could be "relaxed" using an *approximated slope*, $\frac{\Delta p_f}{2\cdot m}$, representing the change Δp_f between the time steps i and $i+2\cdot m$, see Figure 15 and Figure 18. If the distance between the two acoustic pressure sensors is sufficiently smaller than the excited acoustic wave length (i.e., $\Delta x \ll \lambda$), as required for proper use of the two microphones technique, then the actual right going wave (the red curve in Figure 18) and its linear approximation (the dashed line in Figure 18) are very close to each other.

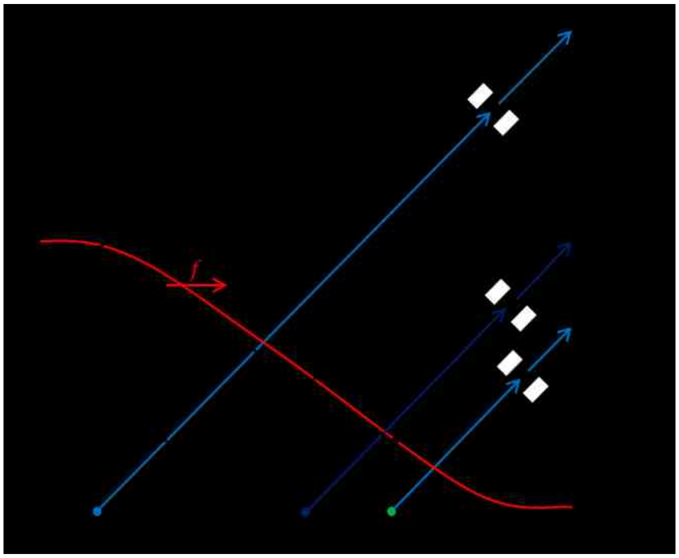

Figure 18. Relaxation of the rigorous algorithm using the approximated slope, $\Delta p_f/(2m)$.

Using the approximated (linear) slope, $\frac{\Delta p_f}{2 \cdot m}$, the right going wave at time step $i+1$, rather than at time step $i + 2 \cdot m$, can be estimated, while still applying the *method of characteristics*, as shown by Eq. (2-8) below.

$$\begin{aligned} \Delta p_f &= p_1'(i) - p_2'(i-m) \\ f_3(i+1) &= f_3(i) + \frac{\Delta p_f}{2 \cdot m} \end{aligned} \qquad \textbf{(2-8)}$$

Notably, the *relaxed or approximated* algorithm given in Eq. (2-8) does not experience the numerical stability problems associated with the use of Eq. (2-6). The *relaxed or approximated* algorithm is similar to a first-order upwind scheme for 1-D convection equation with $CFL < 1$. Thus, the estimation, $f_3(i+1)$ (shown as a blue point in Figure 16-(a)), by the wave separation algorithm is within the domain of dependence (i.e., inside the shaded region between the characteristic lines from $p'_1(i)$ to $f_3(i+2m)$ and from $p'_2(i-m)$ to $f_3(i)$), as is the case with the first-order upwind scheme with $CFL < 1$ whose solution at the next time step, $f(x, t+\Delta t)$ (shown as a blue point in Figure 16-(b)) is also within the domain of dependence (i.e., inside the shaded triangular region). Thus, the algorithm described in Eq. (2-8) provides the wave separation module of the ACS with a numerically stable solution approach.

Additionally, the use of Eq. (2-8) eliminates the high frequency oscillations errors that are related to the sampling period, τ_s. Using this scheme, the information at each time step depends on the previous time step, and the information and errors propagate to the next time step, not to time steps several time steps apart; e.g., $f_3(i+1)$ depends on $f_3(i)$. As the calculation progresses, the estimations at adjacent time steps do not accumulate errors independently, and errors in $f_3(i)$ affect errors in $f_3(i+1)$. Due to this dependence between the adjacent time steps, the algorithm estimates *approximated travelling wave solutions* devoid of high frequency oscillations errors. Thus, introducing *relaxation* to the original *rigorous* algorithm not only stabilizes the wave separation algorithm but also provides a "step-to-step" solution dependence, which was lacking in the *rigorous* algorithm and caused diverging solutions with high frequency errors.

While the *relaxed or approximated* algorithm described in Eq. (2-8) is stable, it introduces errors because it is an approximation of the "exact" relationship given in Eq. (2-6). These errors could be studied by evaluating the algorithm's frequency response by comparing the frequency dependence of its prediction for the amplitude and phase of a wave with known exact solutions. To investigate this problem, the developed algorithm (Eq. (2-8)) was used to predict the propagation of a known, harmonic, right going wave having a specific frequency and unit amplitude. The amplitude and phase of the calculated/estimated wave was obtained and compared with the unit amplitude and the phase of the given, harmonic, travelling wave. This numerical test was performed at each frequency in the 0 Hz to 1 kHz frequency range using Eq. (2-8). The calculated frequency dependences of the amplitude and phase of the estimated waves are shown in Figure 19. It shows, for example, that when the algorithm is applied to a harmonic 300 Hz right going wave with unit amplitude, the estimated right going wave has ~0.9 amplitude and ~0.5 Rad phase lead; see the dashed lines at 300 Hz in Figure 19-(a) and (b), respectively.

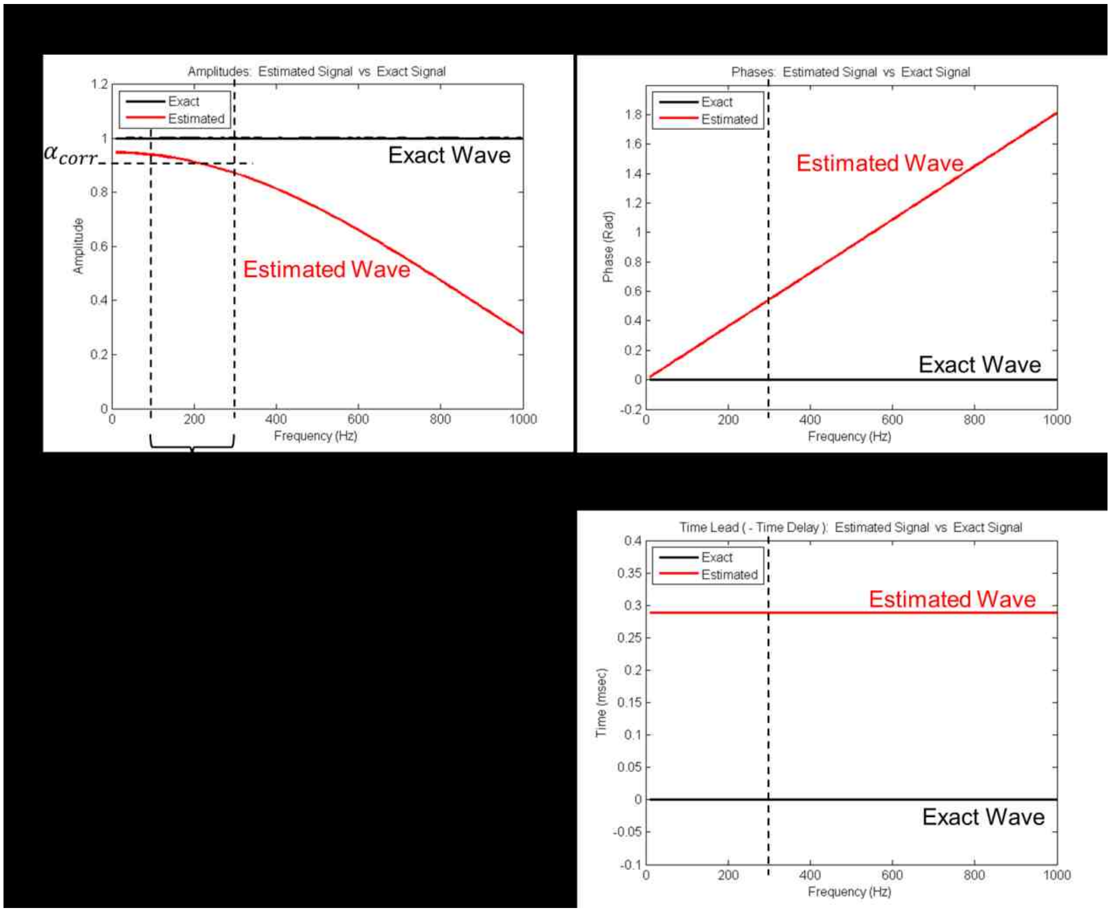

Figure 19. Frequency responses of the approximated wave separation algorithm; (a) amplitude vs frequency, (b) phase vs frequency, (c) time lead (negative time delay) vs frequency.

The amplitude plot in Figure 19-(a) shows that the amplitude of the estimated wave (red curve) is close to the exact solution (black line) at low frequencies. As the frequency increases, the amplitude of the estimated wave decreases and the deviation from the amplitude of the exact solution increases. For example, at 100 Hz and 300 Hz, the estimated amplitude is ~0.95 and ~0.9, respectively, while the amplitude of the exact solution is 1.0. Also, the decrease in the amplitude of the estimated wave is nearly linear in the high frequency region (i.e., 600 Hz ~ 1000 Hz range), and its slope is larger than the slope of the decrease in the estimated amplitude in the low frequency region (i.e., 100 Hz ~ 300 Hz range). This feature helps to stabilize the algorithm as it suppresses high frequency noise. Figure 19-(a) also shows that in the frequency range of interest (i.e., 100 Hz ~ 300 Hz), the algorithm produces reasonably accurate amplitudes and the calculated amplitude does not vary rapidly with the frequency. The phase plot in Figure 19-(b) shows that the algorithm introduces a *phase-lead* error that linearly increases with frequency.

Notably, both the amplitude and phase errors can be corrected in practice. Since the amplitude of the frequency response of the approximated algorithm in the frequency range of interest (100 Hz ~ 300 Hz) does not vary rapidly with frequency (varying from ~0.95 to ~0.9), the amplitude error can be minimized by multiplying the calculated solution by a "correction factor". For example, this correction factor, α_{corr}, could be chosen using an average value (e.g., 0.925) of the estimated amplitudes at 100 Hz and 300 Hz, by letting $1/\alpha_{corr}$=0.925 (see "$1/\alpha_{corr}$" in Figure 19-(a)). Multiplying this correction factor, α_{corr}, with the estimated amplitude could minimize the amplitude error, and this "corrected amplitude" using this amplitude correction approach varies from ~1.03 to ~0.97 from 100 Hz to 300 Hz.

Also, the phase-lead error shown in Figure 19-(b) could be corrected for because the phase at the current time was estimated by the algorithm at earlier time, which allows the ACS to store the history of the solutions up to the current state (or time). Consequently, the correct phase of the current state could be provided by one of the stored solutions. Additionally, since the phase error of the calculated solution linearly depends upon the frequency, it can be compensated for by introducing a "time delay". Figure 19-(b) shows that the phase-lead of the estimated wave (red line) relative to the exact wave (black line) is a straight line that linearly varies with the frequency. The time-lead of the estimated wave, which is obtained by dividing the phase-lead by the frequency, is a constant, ~0.3 msec; see Figure 19-(c). Thus, since (in this example) the wave separation algorithm provides the wave estimation ~0.3 msec early, this phase error can be accounted for by time delaying the solution by ~0.3 msec for all the frequency components.

The developed approximated wave separation algorithm that includes corrections for the amplitude and phase errors is given in Eq. (2-9) below, where $\widetilde{f}_3$ is the corrected, estimated, right going wave at location x_3, α_{corr} is the amplitude correction, and n_{corr} is the time delay correction that compensate for the phase error.

$$\begin{aligned} \Delta p_f &= p_1'(i) - p_2'(i-m) \\ f_3(i+1) &= f_3(i) + \frac{\Delta p_f}{2 \cdot m} \\ \widetilde{f}_3(i) &= \alpha_{corr} f_3(i - n_{corr}) \end{aligned} \qquad \textbf{(2-9)}$$

Notably, the developed wave separation algorithm described in Eq. (2-9) does not depend on the frequency of the oscillations; it only depends on the time dependence of the measured acoustic pressures (i.e., $p'_1(i)$ and $p'_2(i-m)$ in Eq. (2-9) above).

2.2.1.2. Investigation of the Developed Wave Separation Module

The developed wave separation algorithm has been tested both numerically and experimentally. In the numerical test of the algorithm, the propagation of a 1-D 190 Hz right going travelling wave was analyzed by the developed wave separation module. Using the pressures, p'_1 and p'_2, provided by the known (assumed) properties of the wave, the wave separation module calculated the right going wave at location x_3. This estimated right going wave was compared with the known exact solution p'_3 at location x_3. This numerical test is described in Figure 20-(a), and the calculated and known exact solutions are compared in the plot in Figure 20-(b). The black line is the exact wave solution, the red line is the estimated wave without phase and amplitude corrections, and the blue line is the estimated wave with phase correction (i.e., time delay) without amplitude correction. Figure 20-(b) shows that the wave separation algorithm estimates the right going wave with reasonable accuracy. The developed wave separation algorithm successfully captures the harmonic behavior of the exact solution. The amplitude errors of the estimated waves with and without phase corrections are within 10 % of the exact solution, and this amplitude error could be compensated for by introducing the amplitude correction factor (i.e., α_{corr} in Eq. (2-9)). The estimated wave without corrections (i.e., Eq. (2-8)) is shown as a red line in Figure 20-(b). It phase-leads (time-leads) the exact solution that is described by the black line, as discussed above in connection with the results presented in Figure 19-(b) and Figure 19-(c). Correcting for this phase-lead error using time-delay, n_{corr} in Eq. (2-9), the wave separation algorithm successfully estimates the phase of the exact solution; i.e., see the phase-match between the estimated solution (i.e., the blue line) and the exact solution (i.e., the black line) in Figure 20-(b).

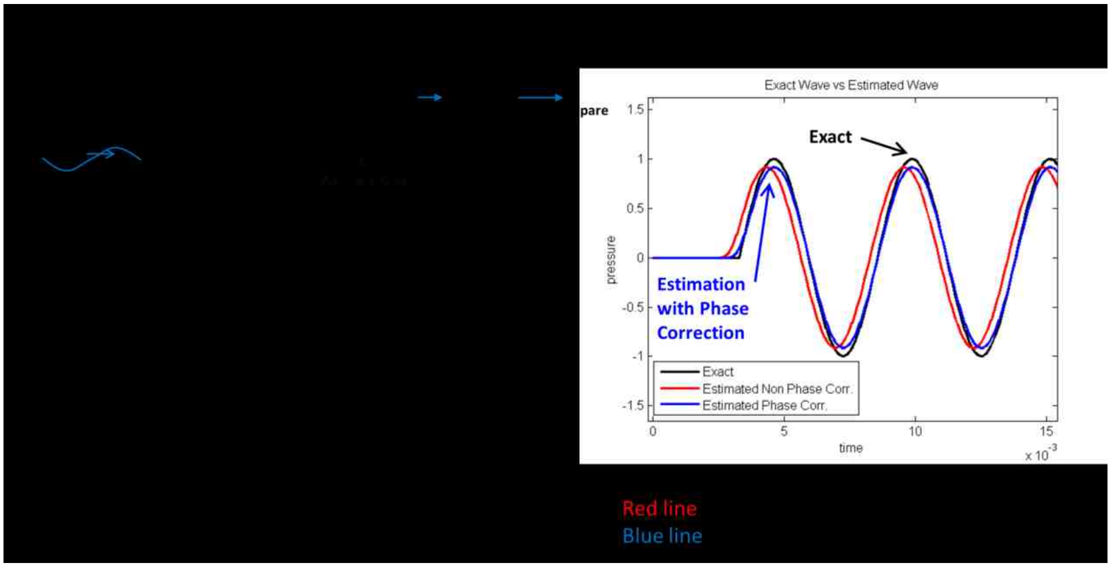

Figure 20. Numerical results of the evaluation of the performance of the developed wave separation algorithm; (a) setup of numerical validation, (b) comparison between the estimated wave and the exact wave.

The performance of the wave separation algorithm was experimentally studied in the impedance tube shown in Figure 21-(a). A 190 Hz right going travelling wave field was established by manually "tuning" the speakers at both ends of the tube. Using the measured acoustic pressures, p'_1 and p'_2, the developed wave separation module (i.e., Eq. (2-9)) estimated the right going wave at location x_3. The estimated right going wave was then compared with the measured acoustic pressure, p'_3 at location x_3. Figure 21-(b) shows that the measured and the estimated right going waves (shown as black and blue lines, respectively) at location x_3 are reasonably matched, indicating that the developed wave separation algorithm can successfully estimate the behavior of harmonic travelling waves. It also shows that the estimated right going wave is in phase with the measured right going wave and that its amplitude is reasonably close to the amplitude of the measured right going wave. The amplitude errors of the estimated waves are within ~7 % of the measured wave. As previously discussed in connection with the results presented in Figure 19-(a), since the amplitudes of the high frequency noise components are damped by the algorithm, the estimated signal is smoother than the measured signal; i.e., the blue curve describing the estimated right going wave is smoother than the black curve that describes the measured right going acoustic wave, see Figure 21-(b). Significantly, this characteristic makes the developed wave separation algorithm (and ACS) less susceptible to high frequency noise in applications. In additional tests, not discussed here, it has also been shown that the developed wave separation algorithm also works well in applications involving standing wave acoustic fields where the presence of the left going wave does not reduce the algorithm's effectiveness.

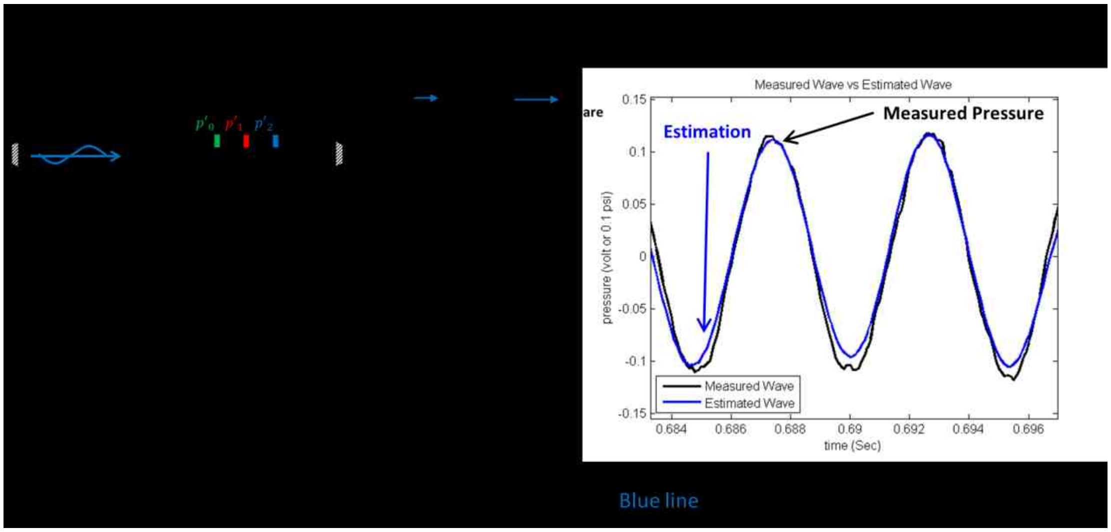

Figure 21. Experimental results of the evaluation of the performance of the developed wave separation algorithm; (a) setup of experimental validation, (b) comparison between the estimated wave and the measured acoustic pressure.

2.2.2. The Simulation Module

As discussed in Sections 2.1.2. and 2.2.1., the objective of the wave separation module is to determine the properties of the right and left going waves in the small-scale rig from the measured acoustic pressures. This determines the properties of the right going wave arriving at the right boundary of the small-scale rig (i.e., location II in Figure 14). In the full-scale engine, this right going wave passes through location II and propagates towards the right boundary of the full-scale engine (i.e., location III), where it is reflected off the boundary. The reflected, left going, wave propagates back towards location II (see Figure 14). The right and left going waves at location II determine the acoustic pressure and velocity, p' and v', at location II in the full-scale engine. These acoustic pressure, p', and velocity, v', at location II in the full-scale engine must be "generated" by the active control system (ACS) at the right boundary of the small-scale rig (i.e., location II in Figure 14). When the acoustic pressure and velocity at location II in the full-scale engine and the small-scale rig are the same, the oscillations in region I~II in the full-scale engine and the small-scale rig would be the same. Thus, to determine the characteristics of the acoustic conditions at location II of the small-scale rig, the "simulation module" of the ACS must simulate the acoustic processes taking place in the "missing part" of the full-scale engine; i.e., in region II~III of the full-scale engine in Figure 14. The acoustic boundary conditions (BCs) at location II of the small-scale rig are then determined using the right going wave provided by the wave separation module and the left going wave provided by the simulation module at the boundary of the small-scale rig (i.e., location II in Figure 14).

The remainder of this section describes how the simulation module of the ACS performs the following tasks:

i. Simulates the acoustics in the missing part (i.e., region II~III in Figure 14) of the full-scale engine using the right going wave (at location II in Figure 14) provided by the wave separation module, and

ii. Determines the acoustic pressure and velocity, p' and v', at the boundary (i.e., location II) of the small-scale rig in Figure 14.

2.2.2.1. Simulation of the Acoustics in the Missing Part of the Full-Scale Engine

As discussed earlier and shown in Figure 22, the "wave separation module" determines the properties of the *right going wave* and the *left going wave* inside the small-scale rig and calculates the *right going wave*, f_{II}, at the boundary of the small-scale rig (i.e., location II). Using this *right going wave*, f_{II}, as an input, the "simulation module" of the ACS numerically simulates in real time the propagations and reflection of this *right going wave*, f_{II}, in the missing part of the full-scale engine and determines the *left going wave*, $g_{sim,II}$, at the right boundary of the small-scale rig, (i.e., an estimation of the *left going wave*, g_{II}, that propagates back to location II in the full-scale engine); see waves, f_{II}, g_{II}, and $g_{sim,II}$ in Figure 22.

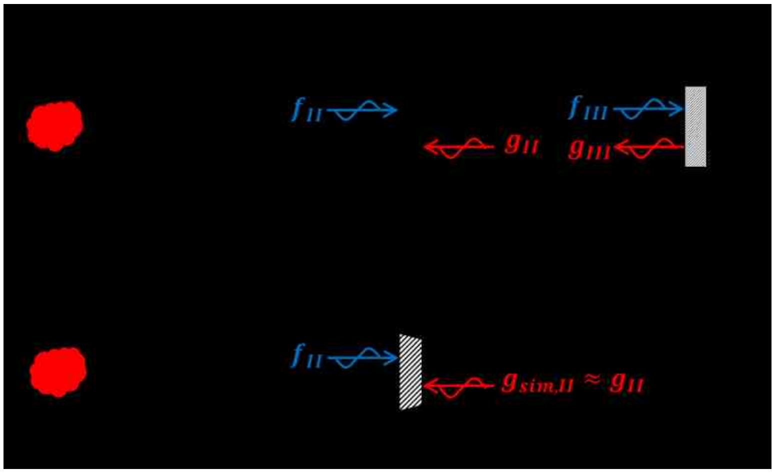

Figure 22. Acoustic wave phenomena in the full-scale system and the small-scale rig.

In Figure 22, the *right going wave*, f_{II} at the boundary of the small-scale rig (i.e., location II), would propagate to the right boundary of the full-scale engine (i.e. location III) during the time, $\frac{L_{removed}}{c}$, where c is speed of sound, as described in Eq. (2-10) below.

$$f_{III}(t) = f_{II}\left(t - \frac{L_{removed}}{c}\right) \tag{2-10}$$

When this *right going wave* arrives at location III, i.e., f_{III}, it is reflected off the boundary as a *left going wave*, g_{III}. The relationship between the incident wave and the reflected wave is determined by the BC at location III in the full-scale engine. In the "fully absorbing" (or non-reflecting) boundary (or an infinitely long tube) case, no reflected wave is generated. On the other hand, when the boundary at location III is a rigid wall, the reflected wave has the same amplitude as the incident wave and is in phase with it. For the open end case, the reflected wave has the same amplitude as the incident wave, but it is 180° out of phase. The time domain representations of these BCs are given in Eq. (2-11). In the more general case, the BCs are given by specifying the impedance BC, $Z = \hat{P}/\hat{V}$, where $\hat{P}$ and $\hat{V}$ are the complex amplitudes of the acoustic pressure p and velocity v at the location of interest. For example, for a travelling wave, $Z = \rho c$, for a rigid wall, $Z = \infty$, and for an open end, $Z = 0$. These complex impedance BCs need to be "transformed" into time domain representations to enable the simulation module to calculate the reflected wave at the boundary at each time step in a *time marching* approach. The general BCs in time domain can be represented as a relationship between the incident wave, f_{III}, and the reflected wave, g_{III}, as shown in Eq. (2-11) below.

$$\begin{aligned} &\text{non-reflecting boundary;} \quad g_{III} = 0 \\ &\text{rigid wall boundary;} \quad g_{III} = f_{III} \\ &\text{open end boundary;} \quad g_{III} = -f_{III} \\ &\text{general boundary;} \quad F\left(f_{III}, g_{III}, \ldots\right) = 0 \end{aligned} \qquad \textbf{(2-11)}$$

where $F(\cdots)$ is a functional relationship between f_{III} and g_{III} obtained in "separate" analysis and/or experiments.

The reflected wave, g_{III}, reaches location II (i.e., dashed line II in Figure 22) after a time delay, $\frac{L_{removed}}{c}$, resulting in the following relationship between the reflected wave, g_{III}, and the wave arriving at location II, g_{II}:

$$g_{II}(t) = g_{III}\left(t - \frac{L_{removed}}{c}\right) \qquad \textbf{(2-12)}$$

Equations (2-10), (2-11), and (2-12) describe the relationships between the propagating waves (i.e., f_{II}, f_{III}, g_{III}, and g_{II}) in the missing part (i.e., region II~III) in the full-scale engine; see the top of Figure 22. For the small-scale rig, shown at the bottom of Figure 22, the simulation module of the ACS numerically simulates these relationships using the *right going wave* at the boundary of the small-scale rig, f_{II} (provided by the wave separation module) and estimates the *left going wave* at the right boundary of the small-scale rig, $g_{sim,II}$, where $g_{sim,II}$ is the estimated value for g_{II} ($g_{sim,II} \approx g_{II}$).

Notably, if acoustic sources that add/remove energy from the acoustic field, such as combustion processes and acoustic liners, respectively, are present in the missing part of the full-scale engine (as shown in Figure 10 in Chapter 1), their effects upon the acoustic wave propagations and reflections in the missing part must be also determined by the simulation module of the ACS. An analysis describing how the effects of combustion processes and injector and exhaust nozzle flows in the missing part of the engine might be accounted for is presented in Chapter 3.

2.2.2.2. Determination of the Boundary Condition of the Small-Scale Rig

The wave separation module determines the *right going wave,* f_{II}, and the simulation module determines the *left going wave,* $g_{sim,II}$, at the boundary of the small-scale rig. These can be used by the simulation module of the ACS to establish the required acoustic BC at the right boundary of the small-scale rig by actively controlling an actuator, which was a speaker in this study.

The acoustic pressure and velocity at location II in the full-scale engine (corresponding to the right boundary of the small-scale rig) are given by the following expressions.

$$\begin{aligned} p'_{II} &= f_{II} + g_{II} \\ v'_{II} &= \frac{f_{II}}{\rho c} - \frac{g_{II}}{\rho c} \end{aligned} \qquad \textbf{(2-13)}$$

For the small-scale rig, the simulation module calculates the acoustic BC of the small-scale rig using the *right going wave,* f_{II}, and the *left going wave,* $g_{sim,II}$, which are obtained by the wave separation and simulation modules of the ACS, respectively; see Eq. (2-14) below.

$$\begin{aligned} \tilde{p}'_{II} &= f_{II} + g_{sim,II} \\ \tilde{v}'_{II} &= \frac{f_{II}}{\rho c} - \frac{g_{sim,II}}{\rho c} \end{aligned} \tag{2-14}$$

These pressure and velocity at the right boundary of the small-scale rig are needed to reproduce the acoustic field of the full-scale engine within the small-scale rig. If the wave separation module accurately identifies the *right going wave* f_{II} at the boundary of the small-scale rig (location II), and the simulation module accurately determines the *left going wave* $g_{sim,II}(\approx g_{II})$ at location II, then the acoustic pressure and velocity, Eq. (2-13), at location II in the full-scale engine and the acoustic pressure and velocity, Eq. (2-14), at the boundary of the small-scale rig (location II) would be close to each other; i.e., $(p'_{II}, v'_{II}) \approx (\widetilde{p}'_{II}, \widetilde{v}'_{II})$. In this case, the acoustic oscillations in the small-scale rig would be close to the acoustic oscillations in the region I~II in the full-scale engine.

In summary, the developed simulation module of the ACS simulates the acoustics in the "missing part" of the full-scale engine during the proposed experiments in real time. Notably, it employs a time domain analyses in the simulation in contrast to the frequency domain representations that have been employed in the related studies (Paschereit at al. and Mongeau at al. [11-13, 15]). These approaches pre-calculated the acoustic fields in the one-dimensional full-scale engine and *apriori* determined the impedance BC at the boundary of the small-scale rig, which was subsequently used by their frequency domain based ACS.

2.2.3. The Actuator (Speaker) Module

This section describes the development and application of the actuator (speaker) model, which was used by the ACS to determine the control current to the actuator (a speaker in this study). Figure 14 (in Section 2.1.2.) describes the manner in which the three developed ACS modules interacted with one another. It shows that the "wave separation module" calculates the value of f_{II} (the *right going wave* at location II) that is used by the "simulation module" to determine the time dependence of the acoustic pressure, $\widetilde{p}'_{II}$, and velocity, $\widetilde{v}'_{II}$, at the right boundary (at location II) of the small-scale rig that "corresponds" to p'_{II} and v'_{II} at location II of the full-scale engine. The calculated $\widetilde{p}'_{II}$ ($\approx p'_{II}$) and $\widetilde{v}'_{II}$ ($\approx v'_{II}$) are then supplied to the "actuator module" that uses these inputs to determine the command signal, which is a controlled electric current, I, to the speaker. This current "forces" the speaker to generate the required acoustic pressure and velocity at location II of the small-scale rig.

This study employed a speaker to actively control the acoustic BC and a current mode amplifier to ensure that the command and generated electric current match well. The use of the current mode amplifier reduces the influence of back-EMF (backwards electromotive force) and makes the model of the speaker more reliable.

2.2.3.1. Modelling the Speaker

The dynamics of the speaker's diaphragm was modeled as a spring-mass-damper system [20, 21]. As shown in Figure 23, the diaphragm is forced by the acoustic pressure and the force electromagnetically induced by the current; i.e., F_p and F_I, respectively.

Figure 23. Speaker model; a moving diaphragm described as a spring-mass-damper system forced by the acoustic pressure and driven by the force induced by the electric current.

The spring-mass-damper system model for the speaker is described by Eq. (2-15) below.

$$m \cdot \ddot{x} + c \cdot \dot{x} + k \cdot x - F_p = -F_I \qquad \textbf{(2-15)}$$

where

$$\begin{aligned} &F_I = \alpha \cdot I \, , \quad F_p = A \cdot p' \\ &\dot{x} = v' \end{aligned} \qquad \textbf{(2-16)}$$

and m, c, k, and A are the mass, damping constant, spring constant, and area of the diaphragm (speaker), respectively. α is a constant that relates the electric current, I, to the electromagnetic force, F_I, via the relationship, $F_I = \alpha \cdot I$.

The diaphragm of the speaker is subjected to an acoustic pressure force, F_p, and an electromagnetic force induced by the current, F_I. These set the diaphragm in motion with a velocity, $\dot{x}$ (x is the diaphragm displacement), that must be equal to the acoustic velocity, v', at its face; see Figure 23 and Eq. (2-16) above. Substituting Eq. (2-16) into Eq. (2-15) yields in the following expression:

$$m \cdot \dot{v}' + c \cdot v' + k \cdot \int v' - A \cdot p' + \alpha \cdot I = 0 \qquad \textbf{(2-17)}$$

Notably, the acoustic pressure and velocity in Eq. (2-17) above are provided by the simulation module of the ACS; see Eq. (2-14). The coefficients, m, c, k, A, and α in Eq. (2-17) have been experimentally determined using different lengths' impedance tubes equipped with the speaker at one end and having open or closed boundaries at their other end; see Figure 24.

Figure 24. Experimental setup for the determination of the coefficients, m, c, k, A, and α, of the speaker model.

For harmonic excitation at frequency, ω, the acoustic pressure and velocity, and the electric current in Eq. (2-17) can be expressed by the following relationships:

$$\begin{aligned} &p' = \mathrm{Re}[\hat{P}e^{-i\omega t}], \quad v' = \mathrm{Re}[\hat{V}e^{-i\omega t}] \\ &I = \mathrm{Re}[\hat{I}e^{-i\omega t}] \end{aligned} \tag{2-18}$$

where, $\hat{P}$, $\hat{V}$, and $\hat{I}$ are the complex amplitudes of the acoustic pressure and velocity at the diaphragm of the speaker, and the electric current to the speaker, respectively.

Substituting Eq. (2-18) into Eq. (2-17) and manipulating the resulting expression yields the following relationship:

$$(-i\omega\hat{V})\cdot m + (\hat{V})\cdot c + (\frac{1}{-i\omega}\hat{V})\cdot k - \hat{P}\cdot A + \hat{I}\cdot\alpha = 0 \tag{2-19}$$

As shown in Figure 24, the speaker was driven by a harmonic electric current, $\hat{I}$, at frequency, ω. The acoustic pressures in the tube were measured by the equally spaced pressure transducers (i.e., $\hat{P}_0$, $\hat{P}_1$, $\hat{P}_2$, and $\hat{P}_3$) to determine the complex amplitudes of the pressure and velocity ($\hat{P}$ and $\hat{V}$) at the speaker face. Substituting these complex amplitudes, $\hat{P}$, $\hat{V}$, and $\hat{I}$, and the frequency, ω, into Eq. (2-19) provides a relationship between coefficients, m, c, k, A, and α.

Performing such experiments with different lengths' tubes with open/closed ends at the left boundary of the tube and different frequencies, the following system of algebraic equations for the five unknowns, m, c, k, A, and α, was obtained:

$$\begin{gathered}
(-i\omega_1\hat{V}_1)\cdot m+(\hat{V}_1)\cdot c+(\frac{1}{-i\omega_1}\hat{V}_1)\cdot k-\hat{P}_1\cdot A+\hat{I}_1\cdot\alpha=0 \\
(-i\omega_2\hat{V}_2)\cdot m+(\hat{V}_2)\cdot c+(\frac{1}{-i\omega_2}\hat{V}_2)\cdot k-\hat{P}_2\cdot A+\hat{I}_2\cdot\alpha=0 \\
(-i\omega_3\hat{V}_3)\cdot m+(\hat{V}_3)\cdot c+(\frac{1}{-i\omega_3}\hat{V}_3)\cdot k-\hat{P}_3\cdot A+\hat{I}_3\cdot\alpha=0 \\
\vdots
\end{gathered} \tag{2-20}$$

Applying a *least squares method* into the above "overdetermined system of linear equations", Eq. (2-20), the coefficients, m, c, k, A, and α, of the speaker model were obtained.

2.2.3.2. Command Signal Calculation

It is convenient to rewrite Eq. (2-17) in a form in which the acoustic properties serve as inputs, and the electrical current appears as an output as shown by Eq. (2-21) below.

$$I = -\frac{1}{\alpha}\left(m \cdot \dot{v}' + c \cdot v' + k \cdot \int v' - A \cdot p'\right) \tag{2-21}$$

Since the acoustic pressure and velocity at the speaker's diaphragm are provided by the simulation module of the ACS (i.e., $\widetilde{p'}_{II}$ ($\approx p'_{II}$) and $\widetilde{v'}_{II}$ ($\approx v'_{II}$) at the boundary of the small-scale rig, see Eq. (2-14)), the command signal for the electric current (i.e., $I_{command}$) can be expressed as follows:

$$I_{command} = -\frac{1}{\alpha}\left(m \cdot \dot{\tilde{v}}'_{II} + c \cdot \tilde{v}'_{II} + k \cdot \int \tilde{v}'_{II} - A \cdot \tilde{p}'_{II}\right) \tag{2-22}$$

Notably, since the command signal, $I_{command}$, is determined by a linear model of the speaker and duct acoustics [20, 21], it would have to be modified for the applications in which nonlinearities become significant. This linear model was used in this study because its main objective was to investigate the performance of the developed ACS.

2.3. Investigation of the Performance of the Actively Controlled Small-Scale Cold Flow Rig

This section describes the results of experiments whose objective was to determine whether the developed ACS can be used to simulate the acoustic environments in unstable, full-scale, engines in a small-scale rig. This study employed the actively controlled, small-scale, rig shown in Figure 14 whose ACS executes the following sequence of steps in real time:

i. Uses the wave separation module to estimate the right going wave in the rig at the current time step.

ii. Uses the simulation module to simulate the acoustics in the missing part of the full-scale engine and calculate the acoustic BC that must be established at the actively controlled boundary of the small-scale rig setup at the next time step using stored data history.

iii. Uses the speaker model to generate the required command signal (current) to the speaker that generates the proper acoustic BC for the next time step.

For the ACS to function properly, all the estimations and calculations need to be completed within a time step, and the command signal should be available at the next time step. To accomplish these *real time operations*, the ACS was operated using the real time operation system (dSPACE DS1103 board) shown in Figure 25.

2.3.1. Experimental Setup

The performance of the developed ACS was investigated using the setup shown in Figure 25. The objective of this study was to determine whether the ACS could simulate one-dimensional acoustic fields encountered in longer (i.e., the "full-scale engines") rigs in the developed "small-scale" rig.

The developed experimental setup consisted of a 4 inch diameter tube equipped with an acoustic speaker having 8 ohm impedance at each end. The speaker at the left end was used to generate an acoustic field in the tube that simulated the sound generated by, e.g., a combustion process, and the speaker at the right end was actively controlled by the ACS. The objective of the control speaker was to excite one-dimensional acoustic oscillations in the rig that simulated those encountered in a longer, unstable, combustor.

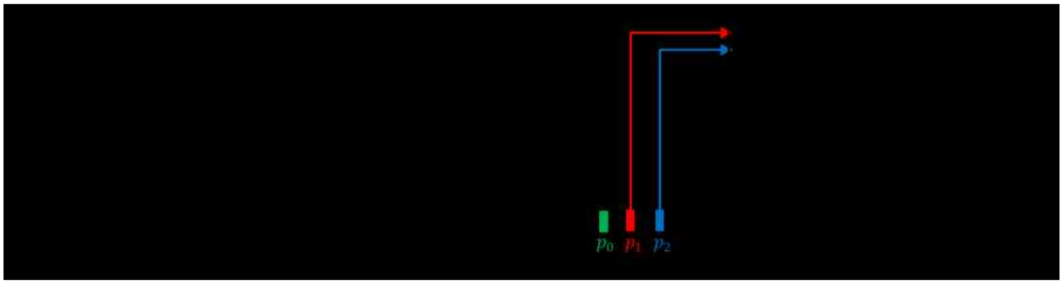

Figure 25. A schematic of the developed experimental setup.

Experiments were performed over a frequency range of 100 ~ 400 Hz that was higher than the resonant frequency of the speakers (~60 Hz), and lower than the first cut-off frequency (~1960 Hz) of the tube to avoid interference from speaker resonances and transverse acoustic modes oscillations during the experiments.

Four pressure sensors (Kistler type 211B5), installed equal distances (~12 cm) apart on the wall of the tube, were used to measure acoustic pressures, and two of them supplied the signals to the ACS. The measured signals and command signals were conditioned by analog filters (Krohn-Hite model 3364). The developed ACS was implemented with a real time operation system (dSPACE DS1103 board) using a 10 kHz sampling rate. A voltage mode amplifier (Samson servo200) and a function generator (Tektronix AFG3022) were used to drive the "driving speaker" at the left end of the tube and a current mode amplifier (AE Techron LVC608) was used to provide the command current signal to the "control speaker" at the right end of the tube.

2.3.2. Using the ACS to Simulate Travelling Wave Fields

Initial experiments investigated whether the developed ACS could excite one-dimensional travelling acoustic waves in the small-scale rig setup. In these experiments, the driving speaker (i.e., the left speaker in Figure 25) generated a 120 Hz sinusoidal signal, and the ACS was set to establish a right going travelling wave in the small-scale rig that may simulate a travelling, one-dimensional, acoustic wave that might be encountered in a full-scale (longer) rig having a non-reflecting BC at its right end. Since, in this case, the incident wave, f_{III}, is not reflected at the right boundary of the full-scale rig (see Figure 14 or Figure 22), the simulation module of the ACS "calculated" a zero amplitude reflected wave; i.e., $g_{III} = 0$.

The measured acoustic pressures at evenly spaced locations are shown in Figure 26 for tests conducted with two small-scale tube rigs having lengths of ~38.5 inch (case (a)) and ~55 inch (case (b)). Note that the 55 inch tube has a natural acoustic mode whose frequency is close to 120 Hz, which is the frequency at which the system was driven by the source speaker.

Figure 26 shows the time dependence of the acoustic pressure oscillations measured by the red, blue, and black colored transducers in Figure 25. The nearly equal time (or phase) shifts between the wave forms measured by the equally spaced transducers indicate that the ACS excited a traveling wave in both setups. However, the amplitudes measured by the different transducers slightly differed from one another, in contrast to the theoretical requirement that the amplitudes measured by the transducers at different locations equal one another. The differences between the determined amplitudes could have been caused by errors introduced by, e.g., pressure transducers calibrations, signal conditioners, amplifiers, real time data acquisition system components, and inadequacies of the models used in the wave separation, simulation, and speaker modules (such as inaccuracies of the assumed speed of sound and the approximations used for algorithm). The sensitivity of the accuracy of the amplitudes determination upon these factors needs to be further studied.

To determine the “deviation” of the travelling wave acoustic fields excited by the ACS from “ideal” travelling waves, the reflection coefficients of the excited acoustic waves were calculated using Eq. (2-23) below.

$$R = \frac{\left|g_{rig}\right|}{\left|f_{rig}\right|} = \frac{amplitude\ of\ the\ left\ going\ wave}{amplitude\ of\ the\ right\ going\ wave} \tag{2-23}$$

Using the measured acoustic pressures, the complex amplitudes were calculated using a FFT analysis. Using the complex acoustic pressures at different locations, the amplitudes of the right and left going waves, $\left|f_{rig}\right|$ and $\left|g_{rig}\right|$, in Eq. (2-23) above were calculated and used to determine the reflection coefficient, R, for the two experimental setups.

The reflection coefficients for the two setups (note that $R = 0$ for an “ideal” travelling wave) were found to be $R = \sim 0.10$ for case (a) and $R = \sim 0.17$ for case (b). These results show that while the incident right going waves were not completely “absorbed” by the actively controlled BC, the resulting acoustic fields show the characteristics of a travelling wave. Notably, in spite of the fact that in case (b) the system was driven near the tube’s natural acoustic mode frequency, the ACS accomplished its goal without the amplification of the excited wave in time due to resonance effects. These tests demonstrated that the developed ACS could excite acoustic oscillations closely approximating a travelling wave acoustic field in the small-scale rigs even near the tube’s natural acoustic mode frequency.

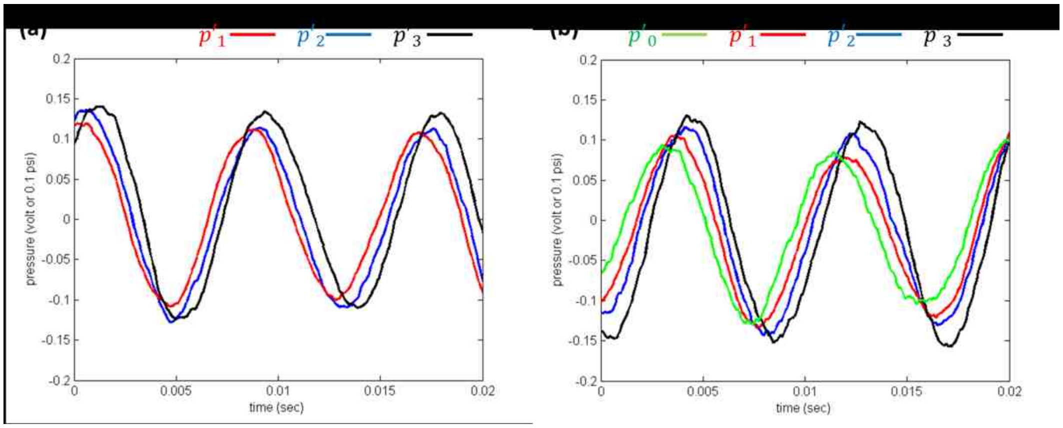

Figure 26. Experimental results showing the simulations of 120 Hz travelling acoustic waves in longer full-scale tube rigs in actively controlled small-scale rigs; (a) 38.5 inch tube, R=0.10, (~129 dB incident wave to the control speaker), (b) 55 inch tube, R=0.17, (~129 dB incident wave to the control speaker).

2.3.3. Using the ACS to Simulate Standing Wave Fields

In follow up tests, the application of the developed ACS to excite one-dimensional, standing, acoustic wave encountered in "full-scale" (i.e., longer) tubes in the developed small-scale rigs was investigated. Specifically, we investigated whether standing waves acoustic oscillations encountered in a "full-scale engine" having a rigid wall BC at its right end can be reproduced in a small-scale rig using the developed ACS.

Figure 27 describes the experimental setup with the "missing part" of the "full-scale rig" shown by the dashed line tube extension with a rigid wall boundary (i.e., a "virtual" rigid wall) on the right side. The driving speaker (the left speaker in Figure 25 and Figure 27) was supplied with a 120 Hz sinusoidal signal, and the ACS was set to excite a standing acoustic wave oscillations consisting of equal amplitude right and left going waves in the "full-scale engine". Specifically, the ACS was set to simulate a (standing) acoustic wave oscillations in a "full-scale engine" that is longer (on the right side) than the small-scale rig by $L_{missing\ part}$ and has a rigid wall at its right boundary, see Figure 27. In this study, the simulation module of the ACS used the length, $L_{missing\ part}$, of the "missing part" and a rigid wall reflection BC (yielding $g_{III} = f_{III}$, see Figure 14 and Figure 22) to determine $g_{sim,II}$ ($\approx g_{II}$), $\widetilde{p'}_{II}$ ($\approx p'_{II}$), and $\widetilde{v'}_{II}$ ($\approx v'_{II}$) at the right boundary of the small-scale rig.

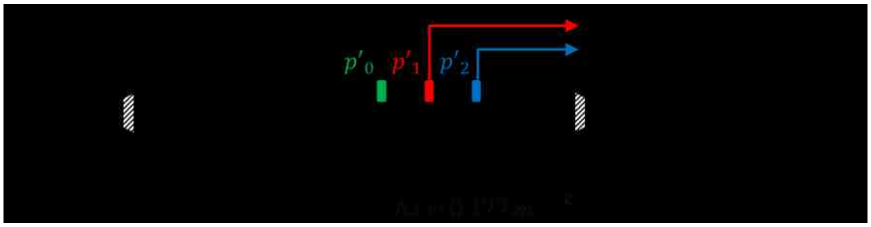

Figure 27. A schematic of the actively controlled small-scale rig setup with a virtual tube extension on its right side.

Figure 28 shows acoustic pressures measured at evenly spaced locations in tests performed in two different small-scale rig configurations consisting of a ~38.5 inch tube with a 16" virtual rigid wall extension in case (a) (see Figure 28-(a)) and a ~55 inch tube with a 10.7" virtual rigid wall extension in case (b) (see Figure 28-(b)). The locations and color/location relationships of the acoustic pressures measurements are described in Figure 27. Figure 28 shows that the waveforms measured at four different locations in the small-scale rigs are in-phase or out-of-phase each other. In Figure 28-(a), the measured acoustic pressure, p'_1, (measured by the red colored transducer shown in Figure 27) has the smallest amplitude and is out-of-phase with the acoustic pressures, p'_2 and p'_3, measured by the blue and black colored transducers, respectively. These results indicate that a pressure node was located between the red and blue colored transducers (i.e., the locations of p'_1 and p'_2) and close to the red colored transducer (i.e., the location of p'_1). Figure 28-(b) shows that the acoustic pressure p'_0 (measured by the green colored transducer) is out-of-phase with the acoustic pressures, p'_1, p'_2, and p'_3, measured by the red, blue, and black colored transducers, respectively. In this case, a pressure node is located between the green and red colored transducers (i.e., the locations of p'_0 and p'_1). Generally, an "ideal" standing wave acoustic field shows 0° or $180°$ phase differences between the acoustic measurements at different locations and has pressure nodes at locations where leftward and rightward moving waves having the same amplitude cancel one another. The results in Figure 28 agree reasonably well with the expected behavior of standing waves.

The reflection coefficients ($R = \frac{amplitude\ of\ the\ left\ going\ wave}{amplitude\ of\ the\ right\ going\ wave}$) for the two experiments (note that $R = 1$ for an "ideal" standing wave) were found to be $R = \sim 0.85$ for case (a) and $R = \sim 1.05$ for case (b). While the incident right going wave and the reflected left going wave do not have the same amplitudes, i.e., $R \neq 1$, the excited acoustic fields exhibit all the characteristics of standing waves. Notably, in case (b), the small-scale rig (~55" tube) was driven at 120 Hz, which is near the tube's natural acoustic mode frequency, yet the ACS was able to simulate the standing wave acoustic field of the "longer", full-scale, engine (of length ~55"+10.7") instead of exciting oscillations at the natural acoustic mode frequency of the small-scale rig without experiencing "amplitude amplification" due to resonance effects. These tests demonstrated that the ACS can simulate standing wave acoustic fields excited in "full-scale engines" in small-scale rigs.

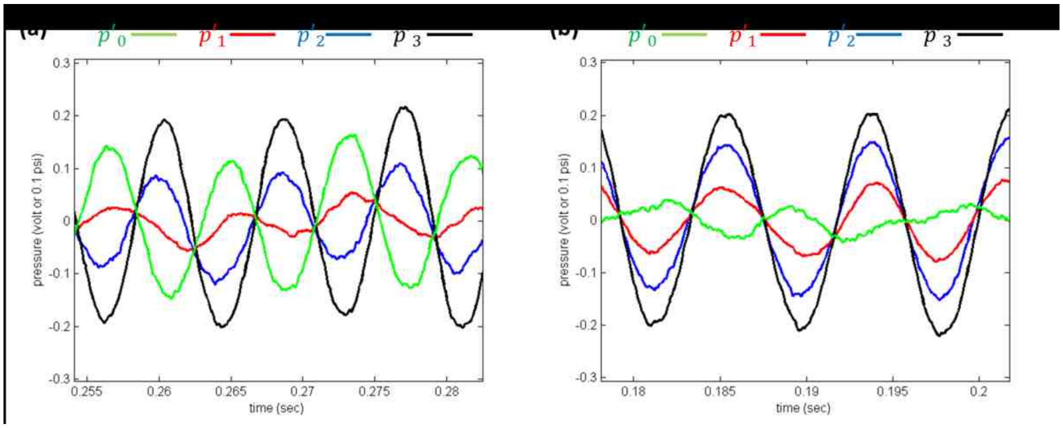

Figure 28. Experimental results showing the simulations of 120 Hz standing acoustic waves in longer full-scale tube rigs in actively controlled small-scale rigs; (a) 38.5 inch tube, 16" virtual rigid wall extension, R=0.85, (~132 dB incident wave to the control speaker), (b) 55 inch tube, 10.7" virtual rigid wall extension, R=1.05, (~132 dB incident wave to the control speaker), where the location of each colored pressure transducer is shown in Figure 27.

2.3.4. Using the ACS to Simulate Standing Waves in Full-Scale Engines

To get further insight into the performance of the developed, actively controlled, small-scale, rigs, their ability to simulate standing, longitudinal, acoustic waves CIs in full-scale engines (or longer tubes, in this study) was investigated in two "series" of experiments whose configurations are described on the bottom of Figure 29. Of particular interest is the "relationship" between the standing wave acoustic field excited by the ACS in the shorter, small-scale, rig and the oscillations in the longer, full-scale engine (or rig). As shown in Figure 29, these experiments used the previously discussed ~38.5" and ~55" experimental setups. In each series of experiments, the ACS was set to simulate, within the small-scale rig, the oscillations in longer tubes whose length was equal to the length of the small-scale rig plus an additional, virtual, length on its right side that varied between ~5.4" to ~18.7", as shown on the bottom of Figure 29. In all of these experiments, 120 Hz acoustic oscillations were excited in the small-scale rig by the speaker on its left end, and the speaker on the right was actively controlled to simulate the oscillations in the longer, full-scale, tube. The determined spatial dependences of the acoustic pressure amplitudes in the investigated configurations are shown on the top of Figure 29 where the vertical dashed (on the left) and solid (on the right) lines describe the locations of the right terminations of the investigated, ~38.5" and ~55" tube rigs, respectively, where the actively controlled speakers were installed.

Figure 29 describes the spatial dependences of the amplitudes of the acoustic pressures (i.e., the "acoustic pressures mode shapes") in domains consisting of the small-scale rig and the "missing part" of the "full-scale tube" (i.e., the virtual tube extension of the small-scale rig). Each plot shows the amplitudes of the four measured acoustic pressures (shown as circles) superimposed upon the calculated pressure mode shape (shown as a dashed or a solid curve) in the actively controlled small-scale rig and its "virtual extension" that was assumed to be terminated by a rigid wall. The plots in Figure 29-(a) and Figure 29-(b) describe the results obtained with the ~38.5" and ~55" actively controlled small-scale rigs, respectively, for each of the investigated configurations, which are shown below each figure. The measured acoustic pressures amplitudes, shown as circles in the figures, were obtained by applying FFT to the four acoustic pressure measurements, p'_i, that are related to their (complex valued) amplitudes, $\hat{P}_i$, by the following relationship:

$$p_i' = \mathrm{Re}[\hat{P}_i e^{-i\omega t}], \quad i = 0,1,2,3 \text{ (see transducer's locations in Figure 27)} \qquad \textbf{(2-24)}$$

where, p_i'; acoustic pressure measured at location i

$\hat{P}_i$; complex acoustic pressure amplitude at location i

The FFT analyses also showed that the phase differences between the (complex valued) acoustic pressure amplitudes at different locations are $0°$ or $180°$. Notably, pressure amplitudes having $180°$ phase difference with respect to other measured pressures (on the same plot) are presented as "negative" pressure amplitudes on the mode shape plots in Figure 29. Using the four measured complex valued pressure amplitudes (that describe the amplitude and phase), the complex amplitudes of the right and left going waves were calculated. At the location of transducer i, the complex amplitudes of the right and left going waves, $\hat{A}$ and $\hat{B}$, respectively, and the measured complex pressure amplitude, $\hat{P}_i$, satisfy the following relationship:

$$\hat{A}e^{ikx_i} + \hat{B}e^{-ikx_i} = \hat{P}(x_i) = \hat{P}_i, \quad i = 0,1,2,3 \text{ (see Figure 27)} \tag{2-25}$$

where, $\hat{A}$; complex amplitude of the right going wave
$\hat{B}$; complex amplitude of the left going wave
x_i; location i

By solving Eq. (2-25) above, the complex amplitudes of the right and left going waves, $\hat{A}$ and $\hat{B}$, were obtained. Using these, complex valued, right and left going waves, the acoustic pressure mode shape in the domain of the actively controlled small-scale rig and the "missing part" of the full-scale tube were determined (using Eq. (2-26) below), and are described by the dashed and solid curves in Figure 29-(a) and (b), respectively.

$$\hat{P}(x) = \hat{A}e^{ikx} + \hat{B}e^{-ikx} \tag{2-26}$$

These calculations were performed for all the experimentally investigated cases (i.e., the actively controlled small-scale rigs and virtual extensions) shown in Figure 29. The investigated test matrix consisted of the two small-scale rigs having lengths of ~38.5" and

~55” with each setup of actively controlled small-scale rig being virtually “extended” by four lengths of ~5.4”, ~10.7”, ~16”, and ~18.7”.

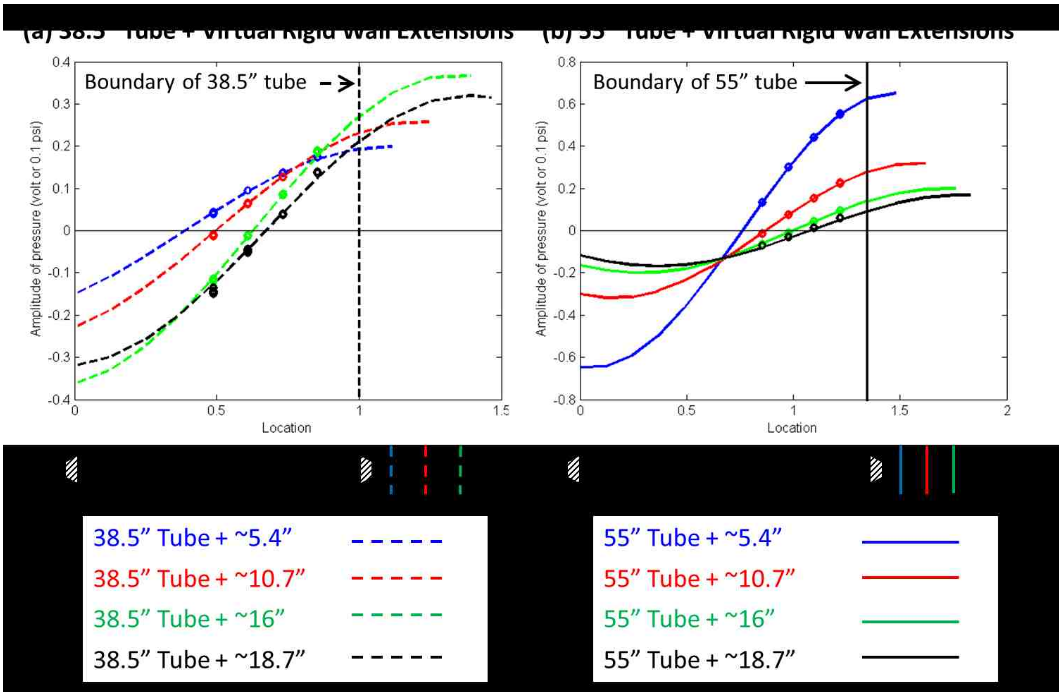

Figure 29. Measured acoustic pressure amplitudes (depicted as open circles) and calculated acoustic pressure mode shapes in the domain of the full-scale tubes (depicted as dashed and solid curves for cases (a) and (b), respectively); (a) 38.5 inch tube with ACS setups of ~5.4”, ~10.7”, ~16”, and ~18.7” virtual rigid wall extensions, (b) 55 inch tube with ACS setups of ~5.4”, ~10.7”, ~16”, and ~18.7” virtual rigid wall extensions, (from ~125 dB to ~ 139 dB incident wave to the control speaker).

Each of the calculated acoustic pressure mode shape in Figure 29 covers a domain that starts at the left side of the small-scale rig where the driving speaker is located and ends at the location of the right boundary of the simulated, full-scale, tube where the “virtual” rigid wall of the “missing part” of the tube is located. Figure 29-(a) and (b) show that as the length of the virtual extension (i.e., the distance between the locations of the right termination of the small-scale rig and the virtual rigid wall of the virtual tube extension) increases, the acoustic pressure node (i.e., $p' = 0$) moves to the right towards the boundary of the small-scale rig in each of the investigated, small-scale, configurations.

This occurred because increasing the length of the “missing part” of the full-scale tube while keeping the properties of the virtual rigid wall termination of the virtual tube extension on the right and the driving frequency of 120 Hz unchanged required that wavelength of the oscillations and the $\frac{dp'}{dx} = 0$ acoustic BC at the rigid wall on the right side remain unchanged for all the investigated cases. This, in turn, required that the excited acoustic mode shape shift to the right in step with the “rightward displacement” of the virtual, rigid, wall boundary location. Consequently, as location of the virtual rigid wall moved to the right, the acoustic pressure oscillations’ spatial profile, which included its pressure node, also moved to the right as shown in Figure 29-(a) and (b). These results show that the developed ACS can simulate, one-dimensional, standing wave, acoustic oscillations that occur in longer full-scale tubes having different lengths in an actively controlled, small-scale, rig.

The analysis performed in this study also determined the “acoustic velocity mode shape” in domains consisting of the actively controlled small-scale rig and the “missing part” of the full-scale tube using Eq. (2-27) below. These spatial profiles are described by the dashed and solid line curves in Figure 30-(a) and (b) for the ~38.5” and ~55” actively controlled rigs, respectively, for the shown virtual length “extensions” of ~5.4”, ~10.7”, ~16”, and ~18.7”.

$$\rho c \cdot \hat{V}(x) = \hat{A}e^{ikx} - \hat{B}e^{-ikx} \qquad \textbf{(2-27)}$$

where, ρ ; density of the air, c ; speed of sound

As the acoustic pressure mode shape, the acoustic velocity mode shape plots in Figure 30 show that as the location of the virtual rigid wall moved to the right, the acoustic velocity mode shape and its anti-node (i.e., where $\frac{dv'}{dx} = 0$) locations also shifted to the right, to assure that its acoustic velocity node (i.e., $v' = 0$) remained adjacent to the virtual rigid boundary that shifted to the right, as shown in Figure 30-(a) and (b).

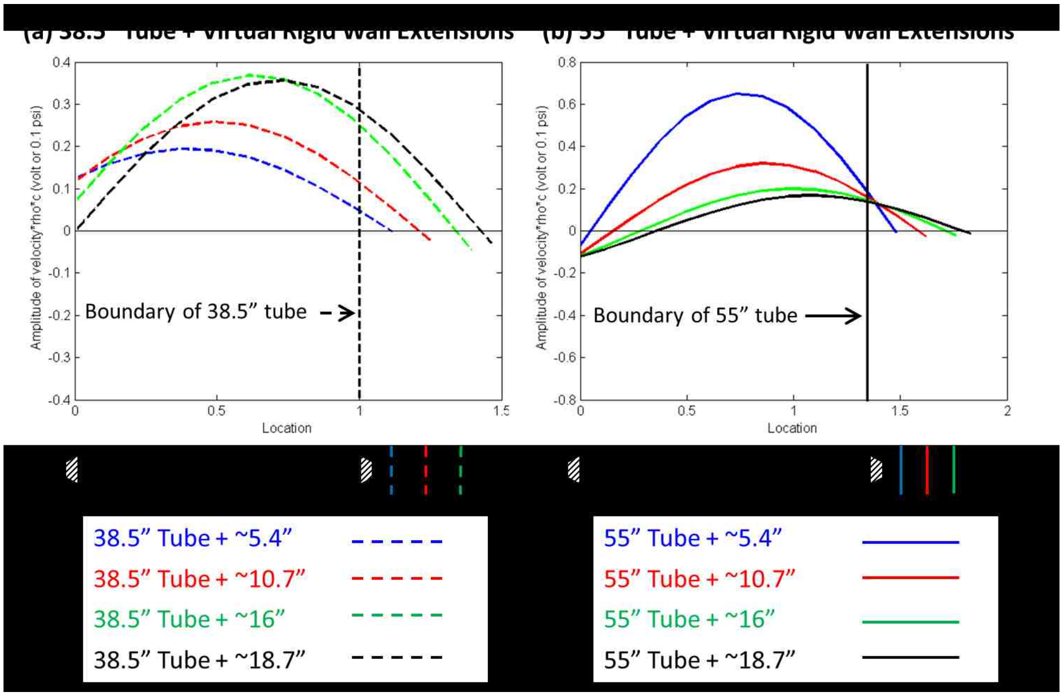

Figure 30. Calculated acoustic velocity mode shapes in the domain of the full-scale tubes (depicted as dashed and solid curves for cases (a) and (b), respectively); (a) 38.5 inch tube with ACS setups of ~5.4", ~10.7", ~16", and ~18.7" virtual rigid wall extensions, (b) 55 inch tube with ACS setups of ~5.4", ~10.7", ~16", and ~18.7" virtual rigid wall extensions, (from ~125 dB to ~ 139 dB incident wave to the control speaker).

To gain additional insight into the results presented in Figure 29 and Figure 30, these results are redrawn in a different "coordinate system" in Figure 31, where the virtual, rigid, wall boundary of each of the tested configurations is set at the right end of the "coordinate system". Notably, all the tested configurations are shown on the bottom of Figure 31, and the acoustic pressure and velocity modes shapes obtained in the tests using the ~38.5" and ~55" tube rigs are shown by dashed and solid lined plots, respectively. It should be noted that the "combined length" of the tested configurations (consisting of the length of the small-scale rig and the virtual tube extension) shown on the bottom of Figure 31 increases as one moved from the top to the bottom configuration. Consequently, the locations of the left terminations of the configurations and the acoustic pressure p' and velocity v' modes shapes' plots differ from one another.

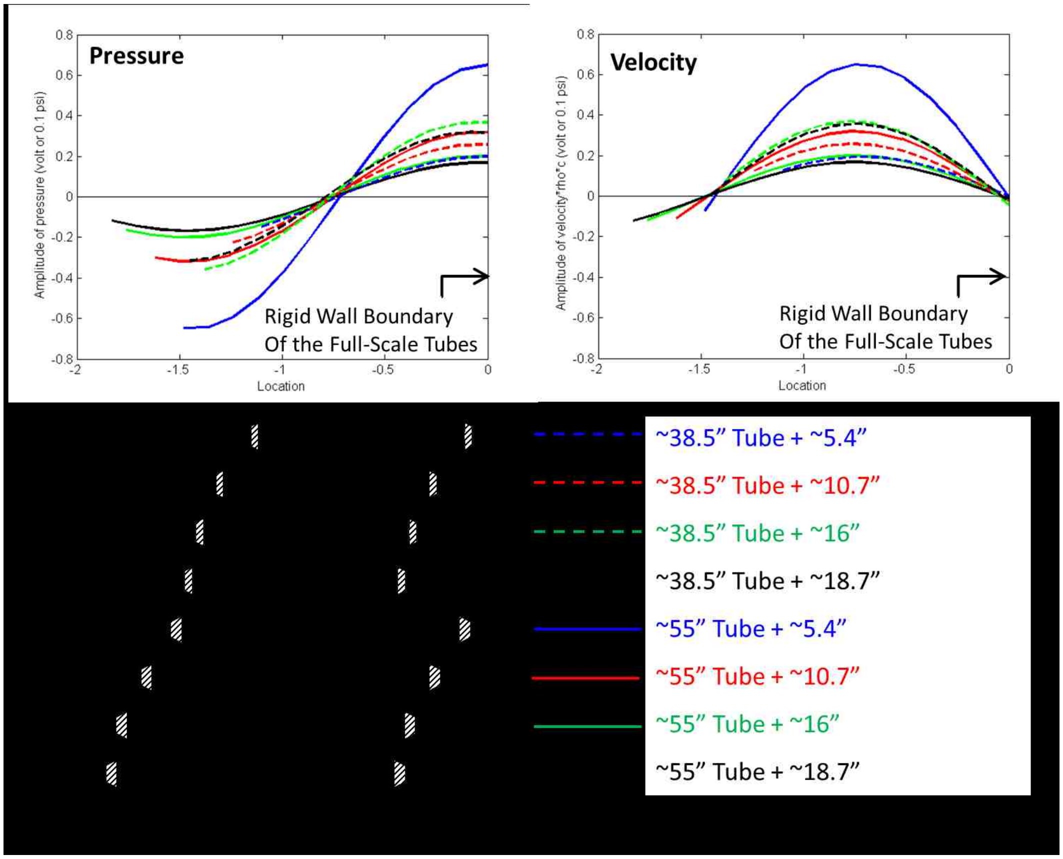

Figure 31. Collections of the calculated acoustic mode shapes aligned at the virtual rigid walls; (a) acoustic pressure mode shapes, (b) acoustic velocity mode shapes, (from ~125 dB to ~ 139 dB incident wave to the control speaker).

An examination of the acoustic pressure p' and velocity v' modes shapes in Figure 29 through Figure 31 shows that the developed ACS generated acoustic oscillations that properly accounted for the "virtual extension" of the small-scale rig and satisfied the "rigid wall" acoustic BC (i.e., $v' = 0$ and $\frac{dp'}{dx} = 0$) at the right end of the virtual tube extension. Additionally, Figure 31 shows that the acoustic mode shapes excited in all the investigated configurations (i.e., the ~38.5” and ~55” small-scale rigs being “extended” by four lengths by the ACS), have acoustic pressure nodes (i.e., $p' = 0$) and acoustic velocity anti-nodes (i.e., the maximums, $\frac{dv'}{dx} = 0$) approximately at the same locations.

These p' and v' plots also show that the magnitudes of the acoustic pressure gradient $\frac{dp'}{dx}$, acoustic velocity v', and its gradient $\frac{dv'}{dx}$ next to the locations of the “driving” speakers at the left ends of the small-scale rigs varied from one investigated configuration to another, even though the input voltages’ amplitudes to the driving speakers in all the tested configurations were the same. This happened because for each tested configuration the driving speaker was located at a different location on the structure of the excited oscillations; i.e., at a different distance from the location of the oscillations’ pressure node or anti-node (recall that the wavelength of the oscillations was fixed at all tests while the distance of the driving speaker from the virtual rigid wall on the right side varied form on test to another). Because the location of the driving speaker relative to the structure of the excited acoustic oscillations varied from one configuration to another, the effectiveness of the speaker’s driving was affected, which may have also affected the magnitude of the acoustic field excited at each configuration. Thus, as the location of the driving speaker got close to the location of the maximum amplitude oscillations (in this study, it occurred when the length of tested configuration of the full-scale engine approximately equaled half the wavelength of the driven 120 Hz oscillations), the speaker’s driving effectiveness increased and the magnitude of the excited oscillations in the actively controlled small-scale rig increased as shown in Figure 29 through Figure 31.

Figure 29 through Figure 31 also show that the excited acoustic pressure and velocity amplitudes were maximum in the configuration consisting of the ~55” small-scale tube rig (virtually) extended by ~5.4” whose profiles are described by the blue solid curves. An analytical investigation of the resonant frequencies of this tube, which included the application of an “empirical effective tube length” correction that accounts for the presence of a multi-dimensional acoustic field near the speaker’s diaphragm [20], showed that the effective “acoustic length” of the investigated “maximum amplitude” configuration equaled ~56.4”; i.e., $56.4'' \approx \sim 55'' + \sim 5.4'' - 4''$ where the subtracted 4” (4” is the diameter of the tube) is the above discussed length correction. This calculation also showed that the driving 120 Hz frequency equals one of the resonant frequencies of the (effectively) 60.4” length configuration that exhibited the largest amplitude oscillations. Thus, the largest amplitude acoustic oscillations excited in the actively controlled ~55” small-scale tube rig (virtually) extended by ~5.4” simulated a “resonating” standing wave acoustic field in a ~60.4” tube having a driving speaker and a rigid wall at its boundaries.

It is, however, noteworthy that at resonance, for a given “energy input”, the maximum amplitude oscillations are excited in the system. Furthermore, when the system is linear, “infinite amplitude” oscillations are excited for an infinitesimal energy supply at resonance. In this study, it was shown that for the same amplitude voltage input to the driving speaker, the amplitude of the excited oscillations depended upon the length of the simulated full-scale tube (or engine) and that maximum amplitude oscillations were excited when the resonant frequency of the simulated full-scale tube (i.e., sum of the small-scale rig and the “missing prat” of the full-scale tube) was close to the frequency of the driving voltage. However, to rigorously determine whether the actively controlled small-scale rig simulated a resonance of the full-scale tube, the "acoustic power input" through the driving speaker for all the investigated configurations needed to be determined in order to show that the energy input to the driving speaker was minimized when a resonance of the full-scale engine was simulated. While this writer believes that this was the case, this fact regretfully cannot be proved because the power input to the driving speaker was not measured in these experiments.

Notably, the small-scale rigs utilized in the above discussed experiments, each equipped with a driving speaker and an actively controlled speaker on their left and right boundaries, respectively, could only simulate the oscillations in the portion of the wavelength of the full-scale tube's (or engine's) oscillations immediately adjacent to the driving speaker at the left end of the rig. This scenario is described in Figure 32-(a) and (b) below where Figure 32-(a) describes the "full-scale" tube (or engine) whose oscillations are simulated in the small-scale rig shown in Figure 32-(b). The latter consists of the small-scale rig equipped with a driving and an actively controlled speakers at its left and right ends, respectively. In this arrangement, the small-scale rig can only simulate the oscillations in the section between locations I and II of the full-scale engine on top, as was done in the studies described in this chapter.

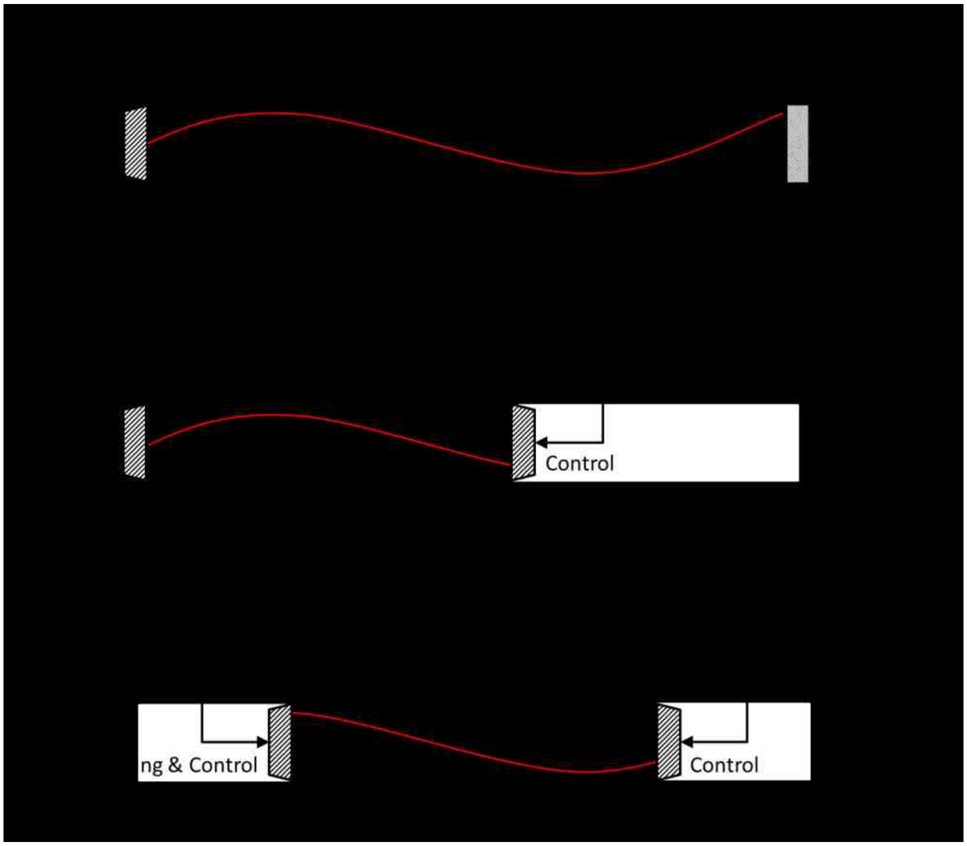

Figure 32. Simulating "different portions of the oscillations" of the full-scale engine in the small-scale rigs; (a) "full-scale rig", (b) small-scale rig with active control setup 1, (c) small-scale rig with active control setup 2.

Next, we would like to provide some suggestions for future research. One interesting study would consider how to modify the small-scale rig if we wanted to simulate the oscillations in a section between locations (1) and (2) in the full-scale engine shown in Figure 32-(a); note that the distance between locations (1) and (2) also equals L_2, the length of the small-scale rig. To accomplish this, we will have to equip the small-scale rig with actively controlled speakers at both ends as shown in Figure 32-(c). In this case, the left and right speakers will use ACSs to generate the acoustic impedances at locations (1) and (2) in the full-scale engine (on top) at the left and right ends of the small-scale rig, respectively. In this experiment, the ACS of the left speaker will simulate in real time the oscillations in region I~(1) and the ACS of the right speaker will simulate in real time the oscillations in region (2)~III of the full-scale engine, respectively. This, in principle, will assure that the small-scale rig will simulate the oscillations in the section between locations (1) and (2) of the full-scale engine above. Furthermore, this small-scale rig would enable experimental simulations in the small-scale rig of oscillations in any section of length L_2 in the full-scale engine. *Investigating the performance of the rig shown in Figure 32-(c) provides a very interesting future research topic that may significantly improve existing capabilities for experimentally investigating full-scale, axial, CIs in small-scale rigs.*

CHAPTER 3.

SIMULATION OF TANGENTIAL COMBUSTION INSTABILITIES IN ANNULAR COBUSTORS

As discussed in Chapter 1, the objective of this thesis is to develop a real time, active boundary control approach that would allow simulations of longitudinal and tangential combustion instabilities (CIs) that occur in full-scale engines in small-scale laboratory rigs; see Figure 5 and Figure 10 in Chapter 1. To achieve this objective, capabilities for performing real time simulations of the acoustic and combustion processes in the “missing part” of the full-scale engine combustor must be developed, as it is one of the three modules (i.e., the “wave separation”, “simulation”, and “actuator model” modules) of the active control system (ACS) that determine the control signal for the actuator. In Chapter 2, the “simulation module” of the ACS only simulated the acoustic waves propagations/reflections in the missing part of the combustor because the study in Chapter 2 focused on the simulation of longitudinal CIs when no combustion generally occurs in the missing part; see Figure 5 in Chapter 1. In contrast, when tangential CIs are excited in an engine, combustion processes, a tangential mean flow, and inflows and outflows through injectors and exhaust nozzles, respectively, are present in transverse planes of the combustor and interact with the acoustic motions there. Therefore, the simulation module of the ACS needs to account for all of these interactions in the “missing part” of the engine; see Figure 10 in Chapter 1. Thus, as discussed in Chapter 1, the use of ACS to simulate full-scale, tangential, CIs in a small-scale rig will require development of capabilities for simulating the interactions of the tangential mean flow, combustion process, injectors' inflows, and exhaust nozzles' outflows with the acoustics in the "missing part" of the engine. The development of such capabilities is described in this chapter.

The interactions between combustion (flame) and the flow and acoustic disturbances and their effects on the longitudinal and tangential (transverse) CIs have been investigated in several studies. For example, the detail unstable thermo-acoustic modes structures associated with flow instabilities and their responses to the acoustics in swirl stabilized combustor have been studied [27]. The flame response to transverse acoustic excitation has been analyzed in detail [28, 29]. In this study, to perform "real time" control, the developed CI model must simulate the important physics of the problem and be simple enough to allow rapid computational solution of the problem. The developed model describes tangential CI in an annular combustor, see Figure 33. It simulates the essential features of tangential CIs; i.e., periodic combustion, acoustic waves, the axial in/out mean flows through the injectors and exhaust nozzles, respectively, and a tangential mean flow component, see Figure 33. The developed model was numerically solved, and the results are described at the end of this chapter.

3.1. Problem Statement

Tangential CIs, whose acoustic motions are perpendicular to the direction of the mean flow from the injectors to the exhaust nozzles, are often encountered in liquid rocket motors and annular gas turbine combustors, see Figure 33-(a). It shows a liquid rocket motor that employs a large number of injectors on a circular injector plate and an annular gas turbine combustor that employs several fuel nozzles on its inlet plane. Such tangential CIs may manifest themselves as large amplitudes, standing or spinning, acoustic waves, which may travel in the clockwise or counterclockwise direction, see Figure 33-(a).

This study developed a “simplified” model of tangential CIs in an annular combustor because this geometry (shown in Figure 33-(b)) can be considered to be an “element” of a full-scale circular combustor (shown as an annular region within two black circular boundaries in Figure 33-(a)) or a representation of a full-scale annular gas turbine combustor (shown in the bottom of Figure 33-(a)).

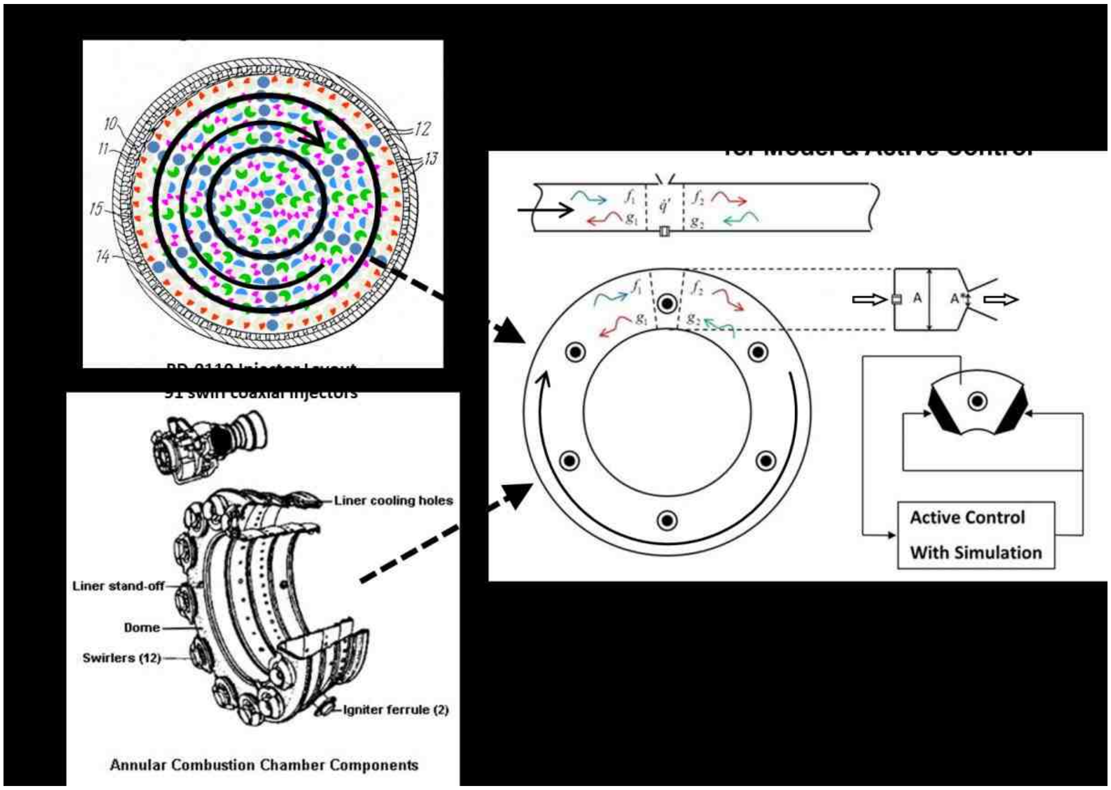

Figure 33. Examples of full-scale combustors experiencing tangential combustion instabilities: (a) rocket engine and annular gas turbine combustor, (b) simple annular combustor with several fuel nozzles (injectors), and exhaust nozzles.

The annular combustor modeled in this study is described in Figure 33-(b). During unstable operation, acoustic waves may propagate in the clockwise or counterclockwise direction and interact with combustion processes anchored to the fuel nozzles in the presence of a tangential mean flow component in the clockwise or counterclockwise direction. In such a combustor, the fuel nozzles (injectors) supply streams of liquid or gaseous fuel and oxidizer that subsequently may vaporize, mix, react, and release heat, thus generating a flow of hot combustion products that is discharged through the exhaust nozzles. All of these processes must be simulated by the model, since they affect the driving/damping of the CIs through a feedback process.

3.1.1. Simplified Problem

This section describes the development of a model of tangential CIs that simulates the interactions of the acoustic waves with the combustion processes, injectors and exhaust nozzles flows, and the tangential mean flow in an annular combustor, see Figure 34. The developed model assumed that the reactants are gases, the mixing processes are infinitely fast, the medium behaves as a thermally perfect gas, and the tangential component of the mean flow moves in the clockwise direction, see Figure 34. This tangential mean flow is shown to move from left to right as it crosses the combustion region in the top schematic in Figure 34.

We further assumed that the annular combustor volume could be separated into two types of regions; i.e., small “concentrated combustion” regions and larger “no combustion” regions in between, see Figure 34. For example, one of the several "concentrated combustion" regions is shown as a red dashed region, and one of "no combustion" regions is shown as a blue dashed region in Figure 34.

Specifically, it was assumed that the combustion process is concentrated in a small region whose scale is much smaller than the excited acoustic wavelength. The gaseous fuel and oxidizer enter the combustion regions through fuel nozzles (or injectors), mix, and react to release heat. The gaseous combustion products are discharged through exhaust nozzles; see the "combustion" region in Figure 34. These combustion processes, inflows, and outflows interact with the mean flow and the travelling acoustic waves that enter and leave the combustion regions through their right and left boundaries; see the interfaces between "combustion" and "no combustion" regions in Figure 34.

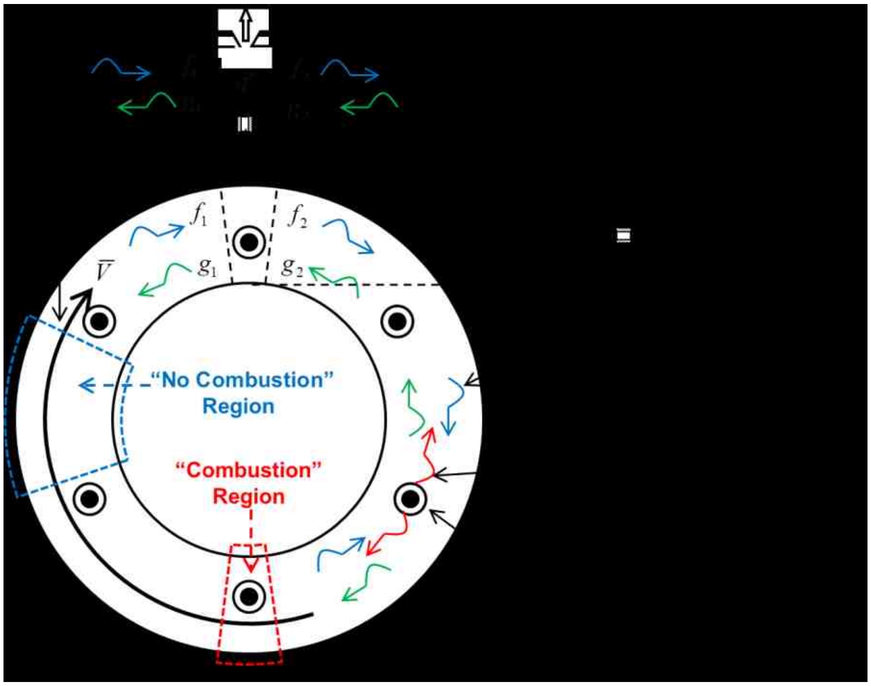

Figure 34. Simplified problem; annular combustor with concentrated combustion regions, linear acoustic waves propagations, injectors and exhaust nozzles, and tangential mean flow.

It has also been assumed that no combustion occurs in the regions outside the concentrated combustion regions, implying that no acoustic sources that drive the waves are present in these regions; see the “no combustion” region in Figure 34.

3.2. Derivations of the Model Equations

The modeled, concentrated, combustion region is described in Figure 35. It shows that the incoming acoustic waves f_1 and g_2 enter the control volume through the control surface s1 and s2, respectively. As these waves cross the volume, they interact with the combustion process, which amplifies or damps the waves, to produce the outgoing acoustic waves g_1 and f_2. In this one-dimensional description, the tangential mean flow in the clockwise direction, $\bar{\vec{V}}$, is aligned with the $\hat{x}_1$ direction. It affects the propagations of the right going (f_1, f_2) and the left going (g_1, g_2) waves and their interactions with the combustion process.

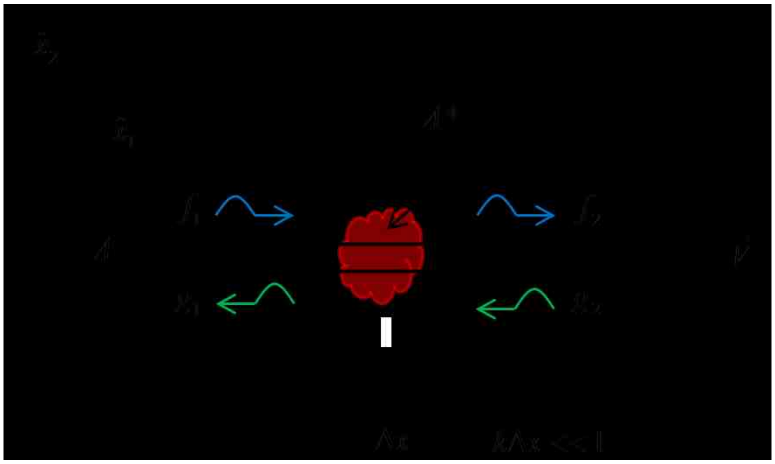

Figure 35. Interaction between acoustic waves and combustion process at the acoustically compact combustion region.

The fuel/oxidizer mixture is supplied by the injector at the bottom wall (s3 in Figure 35), the combustion process (red ball in Figure 35) occurs in the space enclosed by s1, s2, the injector (s3), and the exhaust nozzle (s4), and the gaseous combustion products are discharged through the choked nozzle in the upper wall (s4 in Figure 35). The objective of the developed model is to describe the interaction of these processes with the incoming (f_1, g_2) and outgoing (g_1, f_2) acoustic waves.

To simplify the presentation of the derivation of the model equations, only key steps of the derivation are presented in this discussion. A detailed derivation of the model is presented in APPENDIX A, and the definitions of the various variables are listed in NOMENCLATURE at the beginning of the thesis.

We start the development of the model by considering the following, general, three-dimensional, integral forms of the conservation equations for a reacting flow [30, 31]:

Mass:

$$0 = \frac{\partial}{\partial t}\iiint_{C.V.} \rho \, dV + \iint_{C.S.} \rho \vec{V} \circ \hat{n} \, dS \qquad \textbf{(3-1)}$$

Momentum:

$$\sum \vec{F}_{external} = \frac{\partial}{\partial t}\iiint_{C.V.} \rho \vec{V} \, dV + \iint_{C.S.} \left(\rho \vec{V}\right)\vec{V} \circ \hat{n} \, dS + \iint_{C.S.} p \, \hat{n} \, dS \qquad \textbf{(3-2)}$$

where, $\sum \vec{F}_{external}$ is the sum of the external forces acting on the control volume.

Energy:

$$\dot{Q}_{external} - \dot{W}_s = \frac{\partial}{\partial t}\iiint_{C.V.} e \, \rho \, dV + \iint_{C.S.} e \, \rho \vec{V} \circ \hat{n} \, dS + \iint_{C.S.} p \vec{V} \circ \hat{n} \, dS \qquad \textbf{(3-3)}$$

where, $\dot{Q}_{external}$ is the external heat added to the control volume; $\dot{W}_s$ is the shaft work; $e = u + p.e. + k.e.$ where u, $p.e.$, and $k.e.$ are the internal energy per unit mass, potential energy per unit mass, and kinetic energy per unit mass, respectively.

Species:

$$\dot{M}_l = \frac{\partial}{\partial t}\iiint_{C.V.} Y_l\, \rho\, dV + \iint_{C.S.} Y_l\, \rho\, \vec{v}_l \circ \hat{n}\, dS \qquad \textbf{(3-4)}$$

where, $\dot{M}_l$ is the mass production rate of species l in the control volume; i.e., $\dot{M}_l = \iiint_{C.V.} \dot{m}_l''' dV = \iiint_{C.V.} MW_l\, \dot{\omega}_l\, dV$

where MW_l is the molecular weight of species l; $\dot{\omega}_l$ is the molar production rate of species l per unit volume. Additionally, $\vec{v}_l = \vec{V} + \vec{V}_{l,diffusion}$ is the velocity of species l and $\vec{V}$ and $\vec{V}_{l,diffusion}$ are the mass averaged flow velocity and the diffusion velocity of species l, respectively.

Next, we derive the mean and small-perturbation conservation equations assuming that $\dot{Q}_{external} = 0$ (adiabatic system), $\dot{W}_s = 0$ (no shaft work), and $p.e. = 0$ (negligible potential energy). We also assumed that all the properties can be expressed as a sum of a steady state property and a small-perturbation; e.g., $p = \bar{p} + p'$, $\rho = \bar{\rho} + \rho'$, … where $\frac{p'}{\bar{p}}, \frac{\rho'}{\bar{\rho}}, \ldots \ll 1$. The assumed expressions for the properties are then substituted into the above conservation equations, and the resulting equations are separated into the following steady state conservation equations and small-perturbation conservation equations.

- <u>Steady state (or mean) conservation equations:</u>

Mass:

$$0 = \frac{\partial}{\partial t}\iiint_{C.V.} \bar{\rho}\, dV + \iint_{C.S.} \bar{\rho}\, \bar{\vec{V}} \circ \hat{n}\, dS \qquad \textbf{(3-5)}$$

Momentum:

$$\overline{\left(\sum \vec{F}_{external}\right)} = \frac{\partial}{\partial t}\iiint_{C.V.} \bar{\rho}\, \bar{\vec{V}}\, dV + \iint_{C.S.} \left(\bar{\rho}\, \bar{\vec{V}}\right) \bar{\vec{V}} \circ \hat{n}\, dS + \iint_{C.S.} \bar{p}\, \hat{n}\, dS \qquad \textbf{(3-6)}$$

Energy:
$$0=\frac{\partial}{\partial t}\iiint_{C.V.}\bar{h}_t\,\bar{\rho}\,dV-\frac{\partial}{\partial t}\iiint_{C.V.}\bar{p}\,dV+\iint_{C.S.}\left(\bar{h}_t\,\bar{\rho}\right)\bar{\vec{V}}\circ\hat{n}\,dS \tag{3-7}$$

Species:
$$\overline{(\dot{M}_l)}=\frac{\partial}{\partial t}\iiint_{C.V.}\bar{Y}_l\,\bar{\rho}\,dV+\iint_{C.S.}\bar{Y}_l\,\bar{\rho}\,\bar{\vec{v}}_l\circ\hat{n}\,dS \tag{3-8}$$

- <u>Small-perturbation conservation equations:</u>

Mass:
$$0=\frac{\partial}{\partial t}\iiint_{C.V.}\rho'\,dV+\iint_{C.S.}\bar{\rho}\,\vec{V}'\circ\hat{n}\,dS+\iint_{C.S.}\rho'\,\bar{\vec{V}}\circ\hat{n}\,dS \tag{3-9}$$

Momentum:
$$\begin{aligned}\left(\sum\vec{F}_{external}\right)'=&\frac{\partial}{\partial t}\iiint_{C.V.}\bar{\rho}\,\vec{V}'\,dV+\iint_{C.S.}p'\,\hat{n}\,dS+\frac{\partial}{\partial t}\iiint_{C.V.}\rho'\,\bar{\vec{V}}\,dV\\&+\iint_{C.S.}\left(\bar{\rho}\,\vec{V}'+\rho'\,\bar{\vec{V}}\right)\bar{\vec{V}}\circ\hat{n}\,dS+\iint_{C.S.}\left(\bar{\rho}\,\bar{\vec{V}}\right)\vec{V}'\circ\hat{n}\,dS\end{aligned} \tag{3-10}$$

Energy:
$$\begin{aligned}0=&\frac{\partial}{\partial t}\iiint_{C.V.}\left(\bar{h}_t\,\rho'+h_t'\,\bar{\rho}\right)dV-\frac{\partial}{\partial t}\iiint_{C.V.}p'\,dV\\&+\iint_{C.S.}\left(\bar{h}_t\,\bar{\rho}\right)\vec{V}'\circ\hat{n}\,dS+\iint_{C.S.}\left(\bar{h}_t\,\rho'+h_t'\,\bar{\rho}\right)\bar{\vec{V}}\circ\hat{n}\,dS\end{aligned} \tag{3-11}$$

Species:
$$\begin{aligned}(\dot{M}_l)'=&\frac{\partial}{\partial t}\iiint_{C.V.}\left(Y_l'\bar{\rho}+\bar{Y}_l\,\rho'\right)dV\\&+\iint_{C.S.}\bar{Y}_l\,\bar{\rho}\,\vec{v}_l'\circ\hat{n}\,dS+\iint_{C.S.}\left(Y_l'\bar{\rho}+\bar{Y}_l\,\rho'\right)\bar{\vec{v}}_l\circ\hat{n}\,dS\end{aligned} \tag{3-12}$$

Next, we manipulate the mean (or steady state) and small-perturbation energy equations to obtain equations that would allow to derive an integral form of the non-homogeneous wave equation that includes an acoustic source term representing the effect of the heat release by the combustion process upon the acoustic motions. The derivation of the mean and small-perturbation energy equations with source terms describing the effect of the heat release by the combustion process is presented in Section A.1.3. of APPENDIX A, where Eqs. (A-32) and (A-34) describe the mean and small-perturbation chemical heat release terms. These expressions were subtracted from the mean and small-perturbation energy equations (i.e., Eqs. (3-7) and (3-11)) to obtain the following expressions (see Section A.1.3. for the details of the derivations of Eqs. (A-36) and (A-37)):

$$
\begin{aligned}
&-\sum_l h_{f,l}\overline{(\dot{M}_l)} \\
&\quad = \frac{\partial}{\partial t}\iiint_{C.V.}\bar{\rho}\left(\bar{h}_s + \overline{k.e.}\right)dV - \frac{\partial}{\partial t}\iiint_{C.V.}\bar{p}\;dV \\
&\quad + \iint_{C.S.}\bar{\rho}\left(\bar{h}_s + \overline{k.e.}\right)\bar{\vec{V}} \circ \hat{n}\;dS
\end{aligned}
\qquad \textbf{(3-13)}
$$

$$
\begin{aligned}
&-\sum_l h_{f,l}(\dot{M}_l)' \\
&\quad = \frac{\partial}{\partial t}\iiint_{C.V.}\left\{\left(\bar{h}_s + \overline{k.e.}\right)\rho' + \left(h_s' + k.e.'\right)\bar{\rho}\right\}dV - \frac{\partial}{\partial t}\iiint_{C.V.}p'\;dV \\
&\quad + \iint_{C.S.}\bar{\rho}\left(\bar{h}_s + \overline{k.e.}\right)\vec{V}' \circ \hat{n}\;dS \\
&\quad + \iint_{C.S.}\left\{\left(\bar{h}_s + \overline{k.e.}\right)\rho' + \left(h_s' + k.e.'\right)\bar{\rho}\right\}\bar{\vec{V}} \circ \hat{n}\;dS
\end{aligned}
\qquad \textbf{(3-14)}
$$

Notably, the left hand sides (LHSs) of the above equations describe the mean and small-perturbation heat releases due to chemical composition changes. Since, as discussed in Section A.1.2., it has been assumed that the specific heat, $c_{p,l}$, of all species equal to one another, the small-perturbation sensible enthalpy, h'_s, for the gas mixture (in Eq. (3-14) above) varies only as the temperature perturbation, T', varies; i.e., $h'_s = c_p T'$ (where c_p is the specific heat of the gas mixture, see Eq. (A-27)).

Also, to derive a non-homogeneous wave equation having the effects of all the relevant acoustic sources appearing as inhomogeneous terms, the effects by the in/out flows through the injectors and exhaust nozzles have been separated out and expressed as source terms in the small-perturbation conservation equations. The derivations of these equations are in Section A.1.4., yielding the following expressions:

Mass:

$$\begin{aligned}
&\frac{\partial}{\partial t}\iiint_{C.V.}\rho'\,dV+\iint_{C.S.}\overline{\rho}\,\vec{V}'\circ\hat{n}\,dS+\iint_{C.S.}\rho'\,\overline{\vec{V}}\circ\hat{n}\,dS\\
&\quad=\dot{M}'_{injector}-\dot{M}'_{nozzle}\\
&\quad\equiv\tilde{S}_{mass}
\end{aligned}\qquad\textbf{(3-15)}$$

where,

$$\begin{aligned}
\dot{M}'_{injector}&=-\iint_{C.S.,s3}\overline{\rho}\,\vec{V}'\circ\hat{n}\,dS-\iint_{C.S.,s3}\rho'\,\overline{\vec{V}}\circ\hat{n}\,dS\\
\dot{M}'_{nozzle}&=\iint_{C.S.,s3}\overline{\rho}\,\vec{V}'\circ\hat{n}\,dS+\iint_{C.S.,s3}\rho'\,\overline{\vec{V}}\circ\hat{n}\,dS
\end{aligned}\qquad\textbf{(3-16)}$$

Momentum in $\hat{x}_1$ direction (i.e., tangential direction):

$$\begin{aligned}
&\frac{\partial}{\partial t}\iiint_{C.V.}\overline{\rho}\,\vec{V}'\,dV+\iint_{C.S.}p'\,\hat{n}\,dS+\frac{\partial}{\partial t}\iiint_{C.V.}\rho'\,\overline{\vec{V}}\,dV\\
&\qquad\qquad+\iint_{C.S.}\left(\overline{\rho}\,\vec{V}'+\rho'\,\overline{\vec{V}}\right)\overline{\vec{V}}\circ\hat{n}\,dS+\iint_{C.S.}\left(\overline{\rho}\,\overline{\vec{V}}\right)\vec{V}'\circ\hat{n}\,dS\\
&\quad=\left(\sum\vec{F}_{external,\hat{x}_1}\right)'\\
&\quad\equiv\tilde{S}_{force,\hat{x}_1}
\end{aligned}\qquad\textbf{(3-17)}$$

Energy:

$$\begin{aligned}
&\frac{\partial}{\partial t}\iiint_{C.V.}\left\{\left(\overline{h}_s+\overline{k.e.}\right)\rho'+\left(h_s'+k.e.'\right)\overline{\rho}\right\}dV-\frac{\partial}{\partial t}\iiint_{C.V.}p'\,dV\\
&\qquad\qquad+\iint_{C.S.}\overline{\rho}\left(\overline{h}_s+\overline{k.e.}\right)\vec{V}'\circ\hat{n}\,dS\\
&\qquad\qquad+\iint_{C.S.}\left\{\left(\overline{h}_s+\overline{k.e.}\right)\rho'+\left(h_s'+k.e.'\right)\overline{\rho}\right\}\overline{\vec{V}}\circ\hat{n}\,dS\\
&\quad=\left(-\sum_l h_{f,l}(\dot{M}_l)'\right)+\left\{(\dot{H}_s+\dot{K}.E.)'_{injector}-(\dot{H}_s+\dot{K}.E.)'_{nozzle}\right\}\\
&\quad\equiv\tilde{S}_{energy}
\end{aligned}\qquad\textbf{(3-18)}$$

where,

$$(\dot{Q}_{chem})'\equiv-\sum_l h_{f,l}(\dot{M}_l)'\qquad\textbf{(3-19)}$$

$$
\begin{aligned}
(\dot{H}_s + \dot{K}.E.)'_{injector} &\equiv -\iint_{C.S.,s3} \overline{\rho}\left(\overline{h}_s + \overline{k.e.}\right)\vec{V}' \circ \hat{n}\, dS \\
&\quad - \iint_{C.S.,s3} \left\{\left(\overline{h}_s + \overline{k.e.}\right)\rho' + \left(h'_s + k.e.'\right)\overline{\rho}\right\}\overline{\vec{V}} \circ \hat{n}\, dS \\
(\dot{H}_s + \dot{K}.E.)'_{nozzle} &\equiv \iint_{C.S.,s4} \overline{\rho}\left(\overline{h}_s + \overline{k.e.}\right)\vec{V}' \circ \hat{n}\, dS \\
&\quad + \iint_{C.S.,s4} \left\{\left(\overline{h}_s + \overline{k.e.}\right)\rho' + \left(h'_s + k.e.'\right)\overline{\rho}\right\}\overline{\vec{V}} \circ \hat{n}\, dS
\end{aligned}
\tag{3-20}
$$

For simplicity, the control surface description *"C.S."* in the integrals on the LHS of the Eqs. (2-1), (3-17), and (3-18) denotes the control surfaces s1 and s2 only (i.e., it does not include control surfaces s3 and s4 (see Figure 35)). Since it is assumed that no external force in tangential direction (i.e., $\hat{x}_1$ direction) is present, i.e., $\left(\sum \vec{F}_{external,\hat{x}_1}\right)' = \vec{0}$, it follows that the acoustic source term in the small-perturbation momentum equation in $\hat{x}_1$ direction (i.e., Eq. (3-17) above) is also zero, i.e., $\tilde{S}_{force,\hat{x}_1} = \vec{0}$.

Notably, the terms on the LHS of the above equations describe the acoustic motions with the presence of a (tangential) mean flow while the terms on the right hand side (RHS) of these equations describe the effects of the "sources" and "sinks" that add and remove acoustic energy from the acoustic field, respectively. These "sources" and "sinks" include the acoustic energy supplied by the combustion process and the acoustic energy added and removed from the system by the injectors and the exhaust nozzles, respectively.

As shown in Section A.1.4., Eqs. (2-1), (3-17), and (3-18) can be manipulated to obtain the following integral form of the non-homogeneous wave equation:

$$\begin{aligned}\frac{1}{\bar{a}^2}\iiint_{C.V.}\frac{D}{Dt}\frac{D}{Dt}p'dV-\iiint_{C.V.}\nabla\circ\nabla p'dV \\ =\frac{D}{Dt}\tilde{S}_{mass} \\ -\nabla\circ\left\{\tilde{S}_{force,\hat{x}_1}-\overline{\vec{V}}\cdot\tilde{S}_{mass}\right\} \\ +\frac{\gamma-1}{\bar{a}^2}\frac{D}{Dt}\left\{\tilde{S}_{energy}-(\bar{h}_s+\overline{k.e.})\tilde{S}_{mass}-\overline{\vec{V}}\circ\left(\tilde{S}_{force,\hat{x}_1}-\overline{\vec{V}}\cdot\tilde{S}_{mass}\right)\right\}\end{aligned} \tag{3-21}$$

where,

$$\frac{D}{Dt}=\frac{\partial}{\partial t}+\overline{\vec{V}}\circ\nabla \tag{3-22}$$

$$\begin{aligned}\tilde{S}_{mass}&=\dot{M}'_{injector}-\dot{M}'_{nozzle} \\ \tilde{S}_{force,\hat{x}_1}&=\vec{0} \\ \tilde{S}_{energy}&=(\dot{Q}_{chem})'+\left\{(\dot{H}_s+\dot{K}.E.)'_{injector}-(\dot{H}_s+\dot{K}.E.)'_{nozzle}\right\}\end{aligned} \tag{3-23}$$

The LHS of Eq. (3-21) is the integral form of the wave equation with mean flow ($\overline{\vec{V}}$), and the RHS describes the effects of the acoustic sources, $\tilde{S}_{mass}$, $\tilde{S}_{force,\hat{x}_1}$, and $\tilde{S}_{energy}$, that amplify/damp the oscillations within the combustion region. These acoustic sources describe the effects of the in/out flows through the injector and exhaust nozzle, respectively, and the chemical reactions, and are described in Eq. (3-23) above (with the definitions in Eqs. (3-19) and (3-20)). The term $(\dot{Q}_{chem})'$ describes the chemical heat release perturbation. The terms $\dot{M}'_{injector}$ and $(\dot{H}_s+K\dot{.}E.)'_{injector}$ are the perturbed mass flow rate and energy flux of the fuel/oxidizer mixture "inflow" through the injector, respectively, and the terms $\dot{M}'_{nozzle}$ and $(\dot{H}_s+K\dot{.}E.)'_{nozzle}$ are the perturbed mass flow rate and energy flux of the gaseous combustion products "outflow" through the exhaust nozzle, respectively; see Eq. (3-16), Eq. (3-20), and Figure 35.

As discussed in Section 3.1.1. and described in Figure 34, the CI problem in the annular combustor will be investigated by solving the non-homogeneous wave equation with mean flow ($\vec{\bar{V}}$), i.e., Eq. (3-21), in the “no combustion” regions and “combustion” regions separately and then matching the obtained solutions at the interfaces between these regions. The solutions of Eq. (3-21) in the “no combustion” and “combustion” regions are described in the following Sections 3.2.1. and 3.2.2., respectively.

3.2.1. Acoustic Waves Propagations in the “No Combustion” Regions

Since there are no combustion processes and no in/out flows through injectors and exhaust nozzles in the “no combustion” regions, see Figure 34, all the acoustic source terms on the RHS of Eq.(3-21) are zero in these regions, yielding the following integral form of the homogeneous wave equation that describes the acoustics in these regions:

$$\frac{1}{\bar{a}^2}\iiint_{C.V.}\frac{D}{Dt}\frac{D}{Dt}p'dV-\iiint_{C.V.}\nabla\circ\nabla p'dV=0 \tag{3-24}$$

Assuming that the oscillations are one-dimensional (in the tangential direction), the solutions of Eq. (3-24) are given by the following expressions [20-22]:

$$\begin{aligned} &f(x-(\bar{a}+\bar{V})\cdot t)=const\\ &g(x+(\bar{a}-\bar{V})\cdot t)=const \end{aligned} \tag{3-25}$$

where, f and g are the clockwise and counterclockwise moving waves, respectively. These acoustic waves, f and g, are shown as the right and the left going waves, respectively, as they cross the left and right boundaries of the combustion region in the top schematics in Figure 34 and Figure 35. The acoustic pressure and velocity are related to f and g by the following expressions [20-22]:

$$\begin{aligned} &p'=f(x-(\bar{a}+\bar{V})\cdot t)+g(x+(\bar{a}-\bar{V})\cdot t)\\ &v'=\frac{1}{\bar{\rho}\,\bar{a}}f(x-(\bar{a}+\bar{V})\cdot t)-\frac{1}{\bar{\rho}\,\bar{a}}g(x+(\bar{a}-\bar{V})\cdot t) \end{aligned} \tag{3-26}$$

While the acoustic waves propagate in the "no combustion" regions without change in amplitude, their propagation velocities are affected by the tangential mean flow $\bar{V}$. The propagation velocities of the right going waves f (f_1, f_2) and the left going waves g (g_1, g_2) are $\bar{a}+\bar{V}$ and $\bar{a}-\bar{V}$, respectively, see Eq. (3-25).

Using the following normalization expressions:

$$\hat{p}' = \frac{p'}{\bar{p}}, \quad \hat{v}' = \frac{u'}{\bar{a}}, \quad \hat{f} = \frac{f}{\bar{p}}, \quad \hat{g} = \frac{g}{\bar{p}} \qquad \textbf{(3-27)}$$

the solutions of Eqs. (3-25) and (3-26) can be expressed in the following form:

$$\begin{aligned} &\hat{f}(x-(\bar{a}+\bar{V})\cdot t) = const \\ &\hat{g}(x+(\bar{a}-\bar{V})\cdot t) = const \end{aligned} \qquad \textbf{(3-28)}$$

$$\begin{aligned} &\hat{p}' = \hat{f}(x-(\bar{a}+\bar{V})\cdot t) + \hat{g}(x+(\bar{a}-\bar{V})\cdot t) \\ &\hat{v}' = \frac{1}{\gamma}\hat{f}(x-(\bar{a}+\bar{V})\cdot t) - \frac{1}{\gamma}\hat{g}(x+(\bar{a}-\bar{V})\cdot t) \end{aligned} \qquad \textbf{(3-29)}$$

Equations (3-28) and (3-29) above describe the acoustic waves motions in the "no combustion" region and will be used to determine the properties of the waves, f_1 and g_2, (see Figure 35) that enter the concentrated "combustion" region. These waves, f_1 and g_2, will be used by the equations that describe the processes taking place within the concentrated "combustion" region (described in the next section) to determine the properties of the waves, g_1 and f_2, that leave the concentrated "combustion" region.

3.2.2. Interaction between the Combustion Process and the Acoustic Waves in the "Combustion" Regions

The physics of the acoustically compact combustion region are described by Eq. (3-21). It describes the acoustic waves' interactions with the combustion process, the in/out flows through the injector and exhaust nozzle, and the mean flow. The LHS of Eq. (3-21) describes acoustics of the system, and the RHS describes the source terms that generate or remove acoustic energy from the oscillations [32-34].

To predict the effect of these acoustic sources and the mean flow upon the acoustic oscillations, the following expressions were substituted into the LHS of Eq. (3-21).

$$
\begin{aligned}
&p' = f + g\,; \quad p'_1 = f_1 + g_1\,, \quad p'_2 = f_2 + g_2 \\
&v' = \frac{1}{\bar{\rho}\,\bar{a}}(f - g)\,; \quad v'_1 = \frac{1}{\bar{\rho}\,\bar{a}}(f_1 - g_1)\,, \quad v'_2 = \frac{1}{\bar{\rho}\,\bar{a}}(f_2 - g_2)
\end{aligned}
\tag{3-30}
$$

Next, the values of the integrals on the LHS of the equation were evaluated in the limit when the width of the combustion region goes to zero; i.e., $\Delta x \to 0$. This procedure is justified because the combustion region was assumed to be acoustically compact; i.e., $k\Delta x \ll 1$ [21, 22, 31]. The details of this analysis are described in Section A.2. (see Eq. (A-85)) where the following equation is derived:

$$
\begin{aligned}
&\left(\frac{\bar{a} - \bar{V}}{\bar{a}^2}\right)\left\{f_2(t) - f_1(t)\right\} + \left(\frac{\bar{a} + \bar{V}}{\bar{a}^2}\right)\left\{g_1(t) - g_2(t)\right\} \\
&\quad = \left(\frac{\gamma - 1}{\bar{a}^2}\right)\left[\frac{\tilde{S}_{energy}}{A} - (\bar{h}_s + \overline{k.e.})\frac{\tilde{S}_{mass}}{A} - \bar{\vec{V}} \circ \left(-\bar{\vec{V}}\,\frac{\tilde{S}_{mass}}{A}\right) + \frac{\bar{a}^2}{\gamma - 1}\,\frac{\tilde{S}_{mass}}{A}\right]
\end{aligned}
\tag{3-31}
$$

Equation (3-31) shows that the "unknown" waves, g_1 and f_2, that leave the combustion region depend upon the "known" waves, f_1 and g_2, that enter the combustion region and the acoustic sources on the RHS that describe the processes within the combustion region that add/remove acoustic energy from the oscillations.

Since the combustion region is acoustically compact and the acoustic sources on the RHS of Eq. (3-31) are monopole sources [21, 33, 34], the acoustic pressure across the combustion region is continuous, implying that the pressures at the surfaces s1 and s2 are the same. However, the acoustic velocity is not continuous because the heat added by the combustion process and the mass and energy added/removed by the in/out flows produce an acoustic velocity jump across the "combustion source" [21, 22]. Thus, the variation of the acoustic pressure across the combustion region is described by the following expressions:

$$\begin{aligned} &p_1'(t) = p_2'(t) \\ &f_1(t) + g_1(t) = f_2(t) + g_2(t) \end{aligned} \qquad \textbf{(3-32)}$$

Equations (3-31) and (3-32) can then be solved to determine the two unknowns g_1 and f_2 (i.e., the outgoing acoustic waves).

It is shown in Section A.2. (see Eq. (A-89)) that substituting the expressions for the acoustic source terms, $\tilde{S}_{mass}$ and $\tilde{S}_{energy}$ in Eq. (3-23), into the RHS of Eq. (3-31) yields the following expression:

$$\begin{aligned} &\left(\frac{\bar{a}-\bar{V}}{\bar{a}^2}\right)\{f_2(t) - f_1(t)\} + \left(\frac{\bar{a}+\bar{V}}{\bar{a}^2}\right)\{g_1(t) - g_2(t)\} \\ &\quad = \left(\frac{\gamma-1}{\bar{a}^2}\right)\frac{1}{A}\left[(\dot{Q}_{chem})' + (S_{injector})' - (S_{nozzle})'\right] \end{aligned} \qquad \textbf{(3-33)}$$

where,

$$\begin{aligned} (S_{injector})' = {} & (\dot{H}_s + \dot{K}.E.)'_{injector} - (\bar{h}_s + \overline{k.e.})\dot{M}'_{injector} \\ & + \left(\frac{\bar{a}^2}{\gamma-1}\right)\dot{M}'_{injector} + \bar{\vec{V}} \circ \bar{\vec{V}}\dot{M}'_{injector} \end{aligned} \qquad \textbf{(3-34)}$$

$$\begin{aligned} (S_{nozzle})' = {} & (\dot{H}_s + \dot{K}.E.)'_{nozzle} - (\bar{h}_s + \overline{k.e.})\dot{M}'_{nozzle} \\ & + \left(\frac{\bar{a}^2}{\gamma-1}\right)\dot{M}'_{nozzle} + \bar{\vec{V}} \circ \bar{\vec{V}}\dot{M}'_{nozzle} \end{aligned} \qquad \textbf{(3-35)}$$

As noted before, the RHS of Eq. (3-33) describes the acoustic sources produced by the chemical reactions $(\dot{Q}_{chem})'$, the inflow through the injector $(S_{injector})'$, and the outflow through the exhaust nozzle $(S_{nozzle})'$. To solve Eqs. (3-32) and (3-33) and determine the relationships between the “unknown” outgoing acoustic waves, g_1 and f_2, and the “given” incoming acoustic waves, f_1 and g_2, (from the no combustion region), the acoustic source terms need to be calculated.

As discussed above, the nozzle has been assumed to be short and choked, implying that $M = 1$ at the throat, and that the distance from the combustion chamber to the nozzle throat is much shorter than the acoustic wavelength. Since the time scale of the short nozzle is much shorter than the time scale of the acoustic motions, the flow in the nozzle can be assumed to be quasi-steady. In this case, the stagnation conditions in the combustion region (with $M = 1$ at the nozzle throat) determine the mass flow rate and energy flux through the nozzle [35].

These stagnation conditions can be expressed in terms of the acoustic pressure and velocity inside the combustion region. Since the combustion region is assumed to be acoustically compact, the acoustic pressure inside the region is the same as the acoustic pressures on the surface s1 and s2; see the red dashed line in Figure 36. On the other hand, since the acoustic velocity across the region is discontinuous, the velocity inside the region is assumed to be the average of the velocities on the surfaces s1 and s2; see the blue dashed line in Figure 36.

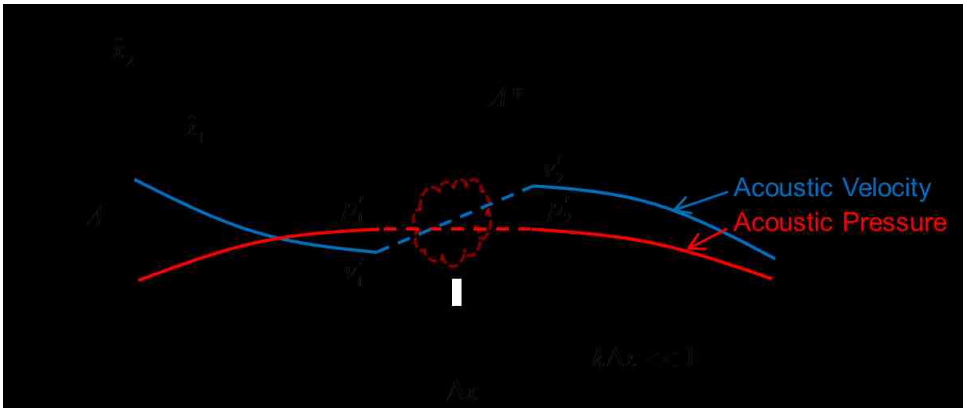

Figure 36. Description of the acoustically compact combustion region having a constant acoustic pressure and an acoustic velocity jump.

Thus, the acoustic pressure and velocity inside the combustion region can be expressed in terms of the acoustic properties at the control surface s1 and s2 as shown below:

$$\begin{aligned} p' &= f_1 + g_1 = f_2 + g_2 \\ v' &= \frac{v'_1 + v'_2}{2} = \frac{1}{2}\frac{1}{\bar{\rho}\,\bar{a}}\{(f_1 - g_1) + (f_2 - g_2)\} \end{aligned} \tag{3-36}$$

The above discussed, short-choked, nozzle assumptions were used to model the flow through the exhaust nozzle, which has been shown to "act" as a source/sink term (i.e., $(S_{nozzle})'$) in the derived equations (i.e., Eqs. (3-33) and (3-35)). Specifically, the exhaust nozzle affects the physics of the problem by allowing acoustic energy to be convected and radiated through the nozzle and be reflected back into the no combustion region, see Eqs. (3-33) and (3-35). The development of the model that describes the effect of a short-choked exhaust nozzle is presented in detail in Section A.3.1.

As shown in Section A.3.1. (see Eq. (A-130)), using the expression for the exhaust nozzle source/sink, $(S_{nozzle})'$, Eqs. (3-32) through (3-36) can be solved to obtain the following expressions for the outgoing waves, g_1 and f_2, in terms of the incoming waves, f_1 and g_2 and the source/sink terms that drive/damp the acoustic oscillations within the combustion region:

$$\begin{aligned} \begin{Bmatrix} f_2 \\ g_1 \end{Bmatrix} &= \frac{1}{1+\varepsilon_{\overline{M}}} \left(\frac{1}{2} \left(\frac{\gamma-1}{\bar{a}} \right) \frac{1}{A} \right) \left((\dot{Q}_{chem})' + (S_{injecor})' \right) \begin{Bmatrix} 1 \\ 1 \end{Bmatrix} \\ &+ \frac{1}{1+\varepsilon_{\overline{M}}} \begin{bmatrix} 1 & -\varepsilon_{\overline{M}} \\ -\varepsilon_{\overline{M}} & 1 \end{bmatrix} \begin{Bmatrix} f_1 \\ g_2 \end{Bmatrix} + \frac{\varepsilon_{\overline{M}} \overline{M}}{1+\varepsilon_{\overline{M}}} \begin{bmatrix} -1 & 1 \\ -1 & 1 \end{bmatrix} \begin{Bmatrix} f_1 \\ g_2 \end{Bmatrix} \end{aligned} \qquad \textbf{(3-37)}$$

where,

$$\begin{aligned} \varepsilon_{\overline{M}} &= \left(\frac{1}{2} \left(\frac{\gamma-1}{\bar{a}} \right) \frac{1}{A} \right) \\ &\cdot \overline{(\dot{Q}_{ref})} \left(\frac{c_p \overline{T}}{\bar{h}_s + \frac{1}{2} \overline{V}^2} \right) \left(\frac{3\gamma-1}{2} + \left(\frac{\gamma+1}{2} \right) \frac{\frac{1}{2}(\gamma-1)\overline{M}^2}{\left(1 + \frac{1}{2}(\gamma-1)\overline{M}^2 \right)} \right) \left(\frac{1}{\gamma} \right) \frac{1}{\bar{p}} \end{aligned} \qquad \textbf{(3-38)}$$

$$\overline{(\dot{Q}_{ref})} = \overline{(\dot{Q}_{chem})} + \overline{(\dot{H}_s + \dot{K}.E.)}_{injector} = \overline{(\dot{H}_s + \dot{K}.E.)}_{nozzle} \qquad \textbf{(3-39)}$$

The parameter, $\varepsilon_{\overline{M}}$, in Eqs. (3-37) and (3-38) describes the effect by the exhaust nozzle. As shown in Section *A.3.1.4.*, the parameter, $\varepsilon_{\overline{M}}$, is a non-dimensional number. Also, using the assumptions that the nozzle throat area, A^*, is much smaller than the cross sectional area of the annular combustor, A, (i.e., $\frac{A^*}{A} \ll 1$) and that the tangential mean flow is subsonic (i.e., $\overline{M} < 1$), it can be shown that $\varepsilon_{\overline{M}} \ll 1$, implying that $\varepsilon_{\overline{M}}\overline{M} \ll 1$; see the discussions in Section *A.3.1.4.* It, thus, follows that

$$\begin{aligned} 0 &< \varepsilon_{\overline{M}} << 1 \\ 0 &< \varepsilon_{\overline{M}} \overline{M} << 1 \end{aligned} \qquad \textbf{(3-40)}$$

Using the above order of magnitudes expressions, the following relationships can be derived:

$$\begin{aligned}\frac{1}{1+\varepsilon_{\overline{M}}} &= 1-\varepsilon_{\overline{M}}+\frac{1}{2}\varepsilon_{\overline{M}}^{2}\cdots \approx 1-\varepsilon_{\overline{M}}\\ \frac{\varepsilon_{\overline{M}}}{1+\varepsilon_{\overline{M}}} &= \varepsilon_{\overline{M}}(1-\varepsilon_{\overline{M}}+\frac{1}{2}\varepsilon_{\overline{M}}^{2}\cdots) \approx \varepsilon_{\overline{M}}\end{aligned} \qquad \textbf{(3-41)}$$

Finally, substituting the above expressions into Eq. (3-37) yields the following, simplified, expressions for the outgoing waves, g_1 and f_2:

$$\begin{aligned}\begin{Bmatrix} f_2 \\ g_1 \end{Bmatrix} &= \left(\frac{1}{2}\left(\frac{\gamma-1}{\bar{a}}\right)\frac{1}{A}\right)\left((\dot{Q}_{chem})'+(S_{injecor})'\right)\begin{Bmatrix} 1 \\ 1 \end{Bmatrix}\\ &+(1-\varepsilon_{\overline{M}})\begin{bmatrix} 1 & 0 \\ 0 & 1 \end{bmatrix}\begin{Bmatrix} f_1 \\ g_2 \end{Bmatrix}-\varepsilon_{\overline{M}}\begin{bmatrix} 0 & 1 \\ 1 & 0 \end{bmatrix}\begin{Bmatrix} f_1 \\ g_2 \end{Bmatrix}-(\varepsilon_{\overline{M}}\overline{M})\begin{bmatrix} 1 & -1 \\ 1 & -1 \end{bmatrix}\begin{Bmatrix} f_1 \\ g_2 \end{Bmatrix}\end{aligned} \qquad \textbf{(3-42)}$$

Applying the normalization expressions in Eq. (3-27) to the above equation, the following relationship between the acoustic waves entering and leaving the compact combustion region can be obtained.

$$\begin{aligned}\begin{Bmatrix} \hat{f}_2 \\ \hat{g}_1 \end{Bmatrix} &= \left(\left(\frac{1}{2}\left(\frac{\gamma-1}{\bar{a}}\right)\frac{1}{A}\right)\frac{(\overline{\dot{Q}_{ref}})}{\bar{p}}\right)\left((\hat{\dot{Q}}_{chem})'+(\hat{S}_{injecor})'\right)\begin{Bmatrix} 1 \\ 1 \end{Bmatrix}\\ &+(1-\varepsilon_{\overline{M}})\begin{bmatrix} 1 & 0 \\ 0 & 1 \end{bmatrix}\begin{Bmatrix} \hat{f}_1 \\ \hat{g}_2 \end{Bmatrix}-\varepsilon_{\overline{M}}\begin{bmatrix} 0 & 1 \\ 1 & 0 \end{bmatrix}\begin{Bmatrix} \hat{f}_1 \\ \hat{g}_2 \end{Bmatrix}-(\varepsilon_{\overline{M}}\overline{M})\begin{bmatrix} 1 & -1 \\ 1 & -1 \end{bmatrix}\begin{Bmatrix} \hat{f}_1 \\ \hat{g}_2 \end{Bmatrix}\end{aligned} \qquad \textbf{(3-43)}$$

where,

$$(\hat{\dot{Q}}_{chem})' = \frac{(\dot{Q}_{chem})'}{(\overline{\dot{Q}_{ref}})} = \frac{1}{(\overline{\dot{Q}_{ref}})}\left(-\sum_{l} h_{f,l}(\dot{M}_l)'\right) \qquad \textbf{(3-44)}$$

$$\begin{aligned}(\hat{S}_{injector})' = \frac{(S_{injector})'}{(\overline{\dot{Q}_{ref}})} = \frac{1}{(\overline{\dot{Q}_{ref}})}\Big\{&(\dot{H}_s+\dot{K}.E.)'_{injector}-(\bar{h}_s+\overline{k.e.})\dot{M}'_{injector}\\ &+\left(\frac{\bar{a}^2}{\gamma-1}\right)\left(1+(\gamma-1)\overline{M}^2\right)\dot{M}'_{injector}\Big\}\end{aligned} \qquad \textbf{(3-45)}$$

Equation (3-43) provides a relationship between the unknown outgoing waves, $\hat{g}_1$ and $\hat{f}_2$, and the known incoming waves, $\hat{f}_1$ and $\hat{g}_2$. The incoming waves, $\hat{f}_1$ and $\hat{g}_2$, are given by Eq. (3-28) that describes the acoustic waves propagation in the no combustion regions. The outgoing waves, $\hat{g}_1$ and $\hat{f}_2$, are the "unknown" of the problem and are determined by the model equations (i.e., Eqs. (3-43), (3-44), and (3-45)) that describe the processes taking place within the combustion region.

Notably, the term $\varepsilon_{\bar{M}}$ in Eq. (3-43) describes the effect by the exhaust nozzle. Since the term $\varepsilon_{\bar{M}}$ is always greater than zero (see Eq. (3-40)), the acoustic oscillations in the combustion region are damped by the exhaust nozzle as indicated by the minus sign in front of the term $\varepsilon_{\bar{M}}$ in Eq. (3-43). Also, when an acoustic wave interacts with the exhaust nozzle, reflected and transmitted waves are generated.

The term $(\hat{S}_{injector})'$ in Eq. (3-43) describes the acoustic driving/damping by the mass and energy fluxes (i.e., sensible enthalpy and kinetic energy) transported through the injector (see the definition of $(\hat{S}_{injector})'$, Eq. (3-45)). Since the inflow through the injector depends on the injection system, the small-perturbations of the mass flow rate, the sensible enthalpy flux, and the kinetic energy flux can be related to the operating conditions of the injection system (i.e., the fuel and oxidizer, mass flow rate, temperature, pressure, fuel/oxidizer ratio, flow velocities, etc.), which can be used to calculate $(\hat{S}_{injector})'$ using Eq. (3-45).

The term $(\hat{\dot{Q}}_{chem})'$ in Eq. (3-43) describes the acoustic driving/damping by the combustion process heat release perturbation. As shown in Eq. (3-44), this heat release perturbation depends on the perturbation of the rate of change of the chemical compositions, which is due to the reaction rate perturbation. Since this reaction rate perturbation depends on the flow condition within the combustion region, it is undoubtedly affected by the acoustic oscillations in the combustor.

Briefly, the system of equations, Eqs. (3-43), (3-44), and (3-45), describes the driving and damping of the oscillations in the "combustion" region. The processes involve the arrived waves f_1 and g_2 at the concentrated combustion region, their amplification and damping by the chemical reactions and the in/out flows through the injector and exhaust nozzle, and the generation of the outgoing waves g_1 and f_2.

In summary the developed model equations consist of equations describing the physics in the "no combustion" and "combustion" regions; see the list in Section A.4. in APPENDIX A.

3.3. Numerical Solutions of the Developed Model Equations

The developed model was numerically solved to validate the model and investigate the effects of the combustion process, injector and exhaust nozzle flows, and the tangential mean flow upon the characteristics of tangential CIs.

The method of characteristics [23, 25, 36] was used to calculate the acoustic waves' behavior in the "no combustion" region (see Eqs. (3-28) and (3-29)), and a numerical algorithm [26] was used to solve the equations that simulate the interactions between the acoustic waves and the processes taking place in the "combustion" region (see Eqs. (3-43), (3-44), and (3-45)).

Acoustic waves propagating in the counterclockwise and clockwise directions in the "no combustion" regions enter/leave the combustion regions. Upon entering a "combustion" region, these waves affect the physical/chemical processes taking place there, while being affected by the processes taking place in the combustion region. At each "time step" of the numerical calculation, "separate" solutions describing the waves entering and leaving the “no combustion” and “combustion” regions are obtained and “matched” at the interfaces between these regions. These numerical simulations were performed using the following sequence of steps:

i. At the start of the numerical simulation, an initial condition (e.g., the presence of a travelling or standing wave oscillations) is set in the entire computational domain of the combustor; i.e., the incoming (f_1 and g_2) and outgoing (g_1 and f_2) waves in the “combustion” region and the acoustic pressure and velocity in the “no combustion” region.

ii. In the “no combustion” region, the acoustic waves propagations are determined using Eqs. (3-28) and (3-29). The outgoing waves, g_1 and f_2 at the present time step t leave the “combustion” region and propagate into the adjacent “no combustion” regions at the next time step $t + \Delta t$. The acoustic waves in the “no combustion” region at the present time step t arrive at the boundaries of the “combustion region” at the next time step $t + \Delta t$; i.e., the incoming waves, f_1 and g_2 (see Figure 35) enter the “combustion” region at the next time step $t + \Delta t$.

iii. The model equations that describe the processes within the concentrated “combustion” region (i.e., Eqs. (3-43), (3-44), and (3-45)) are solved to determine the effects of the acoustic sources there (generated by the combustion process, injector, and exhaust nozzle) upon the waves entering this “combustion” region from the “no combustion” region. Specifically, these solutions determine how the waves entering the “combustion” region, f_1 and g_2 (which are provided by the solutions of the “no combustion” region in *step ii*), are modified as they pass through the “combustion” region. These solutions determine the properties of the outgoing waves, g_1 and f_2, that enter the adjacent “no combustion” regions at the next time step $t + \Delta t$.

iv. These steps determine the solutions at the next time step; i.e., the acoustic waves (f_1, g_2, g_1, and f_2) at the “combustion” region and the acoustic waves in the “no combustion” region. The above described solution approach (i.e., *step ii* ~ *step iii*) is repeated at each time step to determine the time dependence of the solutions.

Some of the results obtained using this approach are described in the remainder of this section. They describe the effects of the basic driving/damping processes that control the investigated CIs. They also show that the presence and direction of the tangential component of the mean flow critically affect the characteristics of spinning tangential instabilities, [37-39].

3.3.1. Utilized Numerical Simulations

To investigate the dependence of tangential CIs upon design parameters and operating conditions, the developed model was numerically solved to determine the characteristics of tangential CIs in annular combustors with and without the presence of a tangential component of the mean flow assuming that combustion occurred in a single combustion region having a single injector, a single exhaust nozzle, and a single concentrated chemical reaction region, as shown in Figure 37. These computations were repeated using different assumptions about the conditions within the combustion region (e.g., with/without the effects by the exhaust nozzle, the combustion process, and the tangential mean flow) and using different models to describe the unsteady combustion process.

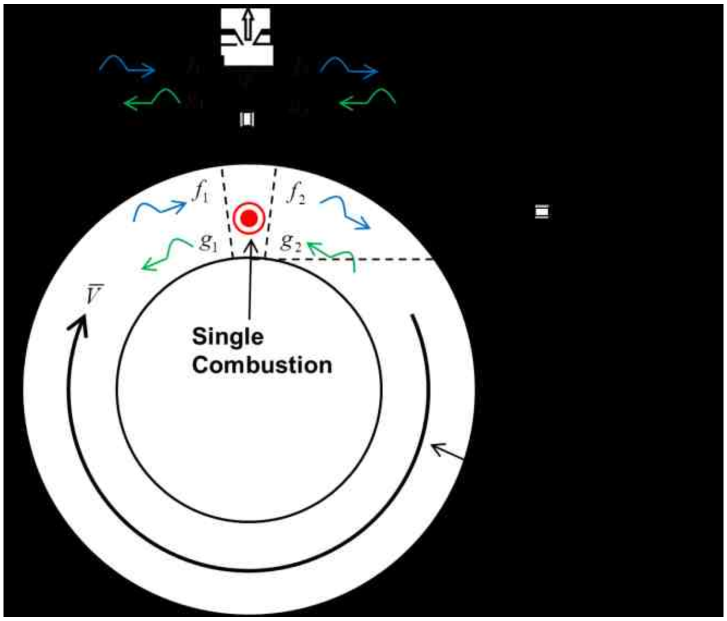

Figure 37. A schematic of an annular combustor with a single concentrated combustion region.

Since the characteristics of tangential acoustic waves in large radius of curvature annular combustors could be approximated by the behavior of one-dimensional acoustic waves, the investigated annular combustor was approximated by a one-dimensional straight duct, as shown in Figure 38. In order to simulate the wave propagations in the closed annular tube, the boundaries of the straight domain were virtually linked; i.e., the right going waves leaving the domain through the right boundary enter the domain through the left boundary, and the left going waves leaving through the left boundary enter the domain through the right boundary. To perform the numerical computations, the straight domain was discretized uniformly, and the concentrated combustion region was located at the point, $i_{combustion}$, shown on the bottom of Figure 38.

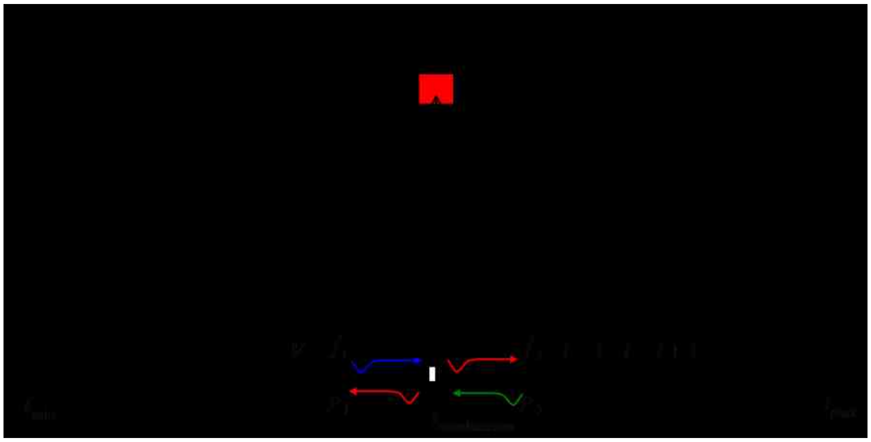

Figure 38. Computational domain for the numerical simulation of one-dimensional annular combustor with a single combustion region.

3.3.2. Exhaust Nozzle Damping

3.3.2.1. Exhaust Nozzle Damping Without a Tangential Mean Flow

In this section, the results of a study of the effect of an exhaust nozzle upon acoustic waves in an annular combustor without a tangential mean flow are discussed. To meet this objective, the model equations that accounted for the effect of the exhaust nozzle only were numerically solved. Specifically, it was assumed that the oscillatory heat release by chemical reactions was zero and that there were no fluctuations in the inlet flow through the injector. Consequently, the following values of the model parameters:

$$\overline{M} = 0,\ \ \varepsilon_{\overline{M}} = 0.1 << 1,\ \ (\hat{\dot{Q}}_{chem})' = 0,\ \ (\hat{S}_{injector})' = 0 \qquad \textbf{(3-46)}$$

were substituted into the model equations; i.e., Eqs. (3-28), (3-29), (3-43), (3-44), and (3-45). It was also assumed that a traveling wave propagating from left to right was initially (i.e., at $t = 0$) present in the combustor and that the exhaust nozzle was located at the center of the combustor as shown in Figure 38.

Figure 39 describes the calculated spatial dependence of the acoustic pressures in the annular combustor at several time steps. To trace the evolution of these waves, the pressure maxima at different time steps were connected by blue dashed lines that describe the wave front motion. The figures on the left in Figure 39 show the evolution of the waves shortly after an initial travelling wave was introduced into the combustor. It shows that initially the wave is a travelling at the speed of sound from left to right, the propagation direction of the initial disturbance. The figures on the right in Figure 39 show the behavior of the wave a long time thereafter (i.e., 18.75 cycles later; one period of the oscillations equals 1 in this example). The plots on the right show that after some time has elapsed, the initially travelling wave has transformed into a standing wave whose pressure node is aligned with the location of the exhaust nozzle.

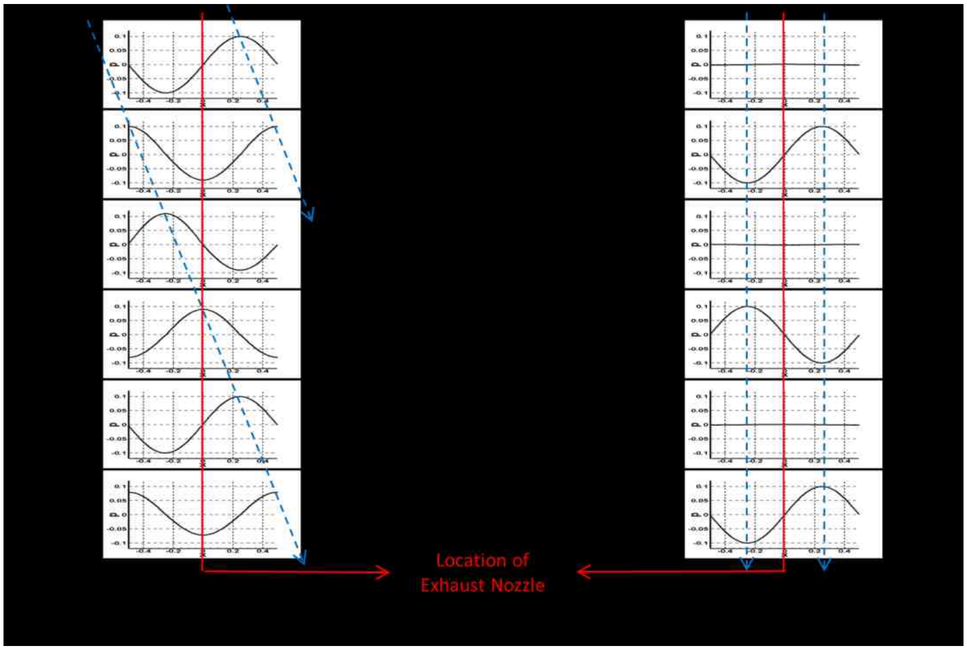

Figure 39. Result of a numerical simulation investigating the effect of the exhaust nozzle flow upon an "initial" travelling wave in an annular combustor in the absence of a tangential mean flow.

The result above shows that in the absence of a tangential mean flow, an initially spinning wave, rotating at the speed of sound, gradually transforms itself into a standing wave. The initial travelling wave excited the oscillations in the combustion region that generated the mass flow rate and the energy flux fluctuations through the exhaust nozzle, which interacted with the oscillations in the combustor. The expressions describing the interactions of the acoustic waves with the exhaust nozzle can be derived by substituting $(\hat{\dot{Q}}_{chem})' = 0$ and $(\hat{S}_{injector})' = 0$ into the "combustion" region model equations, i.e., Eq. (3-43), which yields the following expressions:

$$\begin{aligned} \hat{f}_2 &= \hat{f}_1 - \varepsilon_{\overline{M}}(\hat{f}_1 + \hat{g}_2) - (\varepsilon_{\overline{M}}\overline{M})(\hat{f}_1 - \hat{g}_2) \\ \hat{g}_1 &= \hat{g}_2 - \varepsilon_{\overline{M}}(\hat{g}_2 + \hat{f}_1) - (\varepsilon_{\overline{M}}\overline{M})(\hat{f}_1 - \hat{g}_2) \end{aligned} \qquad \textbf{(3-47)}$$

The above equations show that when only a right going wave $\hat{f}_1$ arrives at the combustion region (i.e., $\hat{g}_2 = 0$), the amplitude of the transmitted wave $\hat{f}_2$ is smaller than that of the incoming wave (i.e., $\hat{f}_2 = \hat{f}_1 - \varepsilon_{\overline{M}}(1 + \overline{M})\hat{f}_1 < \hat{f}_1$). Equation (3-47) also shows that the interaction of the incident wave $\hat{f}_1$ with the exhaust nozzle generates a reflected wave $\hat{g}_1$ (i.e., $\hat{g}_1 = -\varepsilon_{\overline{M}}(1 + \overline{M})\hat{f}_1$) that propagates in the opposite direction (i.e., leftward); notably, the reflected wave $\hat{g}_1$ is 180° out of phase with respect to the incident wave $\hat{f}_1$, as $\hat{g}_1$ and $\hat{f}_1$ have opposite signs. It should be also noted that the effect of the tangential mean flow on the interaction between the exhaust nozzle and the acoustic waves in the combustion region is described by the last term in Eqs. (3-47) and (3-43), which is very small because $\varepsilon_{\overline{M}}\overline{M}$ is even smaller than $\varepsilon_{\overline{M}}$ (i.e., $\varepsilon_{\overline{M}}\overline{M} < \varepsilon_{\overline{M}} \ll 1$). Notably, this term was zero in this example because it has been assumed that there was no tangential mean flow in the annular combustor, thus requiring that $\overline{M} = 0$ and $\varepsilon_{\overline{M}}\overline{M} = 0$.

The discussion showed that the interaction of the initial, right going, wave, $\hat{f}_1$, with the exhaust nozzle damped the initial wave and generated a smaller amplitude transmitted wave, $\hat{f}_2$, and a reflected wave, $\hat{g}_1$ having 180° out of phase (with the incident wave $\hat{f}_1$) that propagated in opposite directions. To elucidate the physics of these waves and exhaust nozzle interactions, we will denote the waves involved in this "first" interaction with the exhaust nozzle as $\hat{f}_1(1)$, $\hat{f}_2(1)$, and $\hat{g}_1(1)$. Since there was no mean flow in this example, the damped right going wave and reflected left going wave propagated around the annular combustor at the same speed of sound without experiencing amplitude changes. These waves returned to the combustion region and interacted with the exhaust nozzle for a "second" time. At the "second" interaction with the exhaust nozzle, the right going wave $\hat{f}_1(2)$ arrived at the combustion region with an amplitude $\hat{f}_1(2) = \hat{f}_2(1) = \hat{f}_1(1) - \varepsilon_{\bar{M}}\hat{f}_1(1)$ and the arriving left going wave $\hat{g}_2(2)$ had an amplitude $\hat{g}_2(2) = \hat{g}_1(1) = -\varepsilon_{\bar{M}}\hat{f}_1(1)$. After completing the "second" interaction with the exhaust nozzle, the amplitudes of the outgoing right going and left going waves were: $\hat{f}_2(2) = \hat{f}_1(1) - \varepsilon_{\bar{M}}\hat{f}_1(1) - \varepsilon_{\bar{M}}\left(\hat{f}_1(1) - 2\varepsilon_{\bar{M}}\hat{f}_1(1)\right)$ and $\hat{g}_1(2) = -\varepsilon_{\bar{M}}\hat{f}_1(1) - \varepsilon_{\bar{M}}\left(\hat{f}_1(1) - 2\varepsilon_{\bar{M}}\hat{f}_1(1)\right)$, respectively, see Eq. (3-47) above. An examination of the above expressions shows that the interactions of the waves with the exhaust nozzle damped the larger amplitude, right going, waves and amplified the smaller amplitude, (180° out of phased), left going waves. Consequently, the amplitudes of the right going and left going waves decreased and increased, respectively, as they continued to interact with the exhaust nozzle. Eventually, the amplitudes of the right and left going waves became equal and a standing wave was established in the combustor. Notably, as the results on the right of Figure 39 show, the pressure node of the resulting “final” standing wave field is aligned with the exhaust nozzle (depicted as red line at center of the combustor) because the magnitudes of the amplitudes of the incoming right and left going waves were the same but had “opposite” signs. These two waves exactly “cancel one another” at the resulting, standing wave, pressure node where the exhaust nozzle is located; i.e., $p' = 0$ at the exhaust nozzle. When the pressure node of the standing wave in the combustor was aligned with the exhaust nozzle axis, the flow fluctuations through the exhaust nozzle stopped and the exhaust nozzle could no longer affect the standing wave acoustic field in the combustor.

Figure 40 describes the time dependence of the right and left going waves and the acoustic pressure waveform at a specific location in the annular combustor. It shows that interactions of the waves with the exhaust nozzle damped the right going wave (described by blue curve) and amplified the left going wave (described by green curve) until their amplitudes was equal to one another and a standing wave acoustic field was established in the combustor. As discussed above, the pressure node of the resulting standing wave was aligned with the location of the exhaust nozzle (i.e., $p' = 0$ at the exhaust nozzle), and the exhaust nozzle stopped affecting the acoustic waves in the annular combustor.

Notably, Figure 40 shows that the amplitude of the acoustic pressure at the indicated location (described by the black curve) remains constant throughout the duration of the process that results in the transition of the initial travelling wave into a final standing wave as shown in Figure 39 above. This observation may (erroneously) suggest that the interaction of the exhaust nozzle with the acoustic oscillations did not damp the acoustic oscillations in the combustor, which is not the case. The acoustic field produced by the “initial” disturbance (near $t \approx 0$) consisted mostly of a right going travelling wave, while the acoustic field during the “final” period (i.e., near $t \approx 20$) was a standing wave acoustic field that consisted of right and left going waves having equal amplitudes. In order to investigate whether the acoustic oscillations in the combustor were damped by the exhaust nozzle during the transition from a travelling wave field into a standing wave field having the same amplitude, the “acoustic energy” of the initial and final oscillations in the combustor were evaluated.

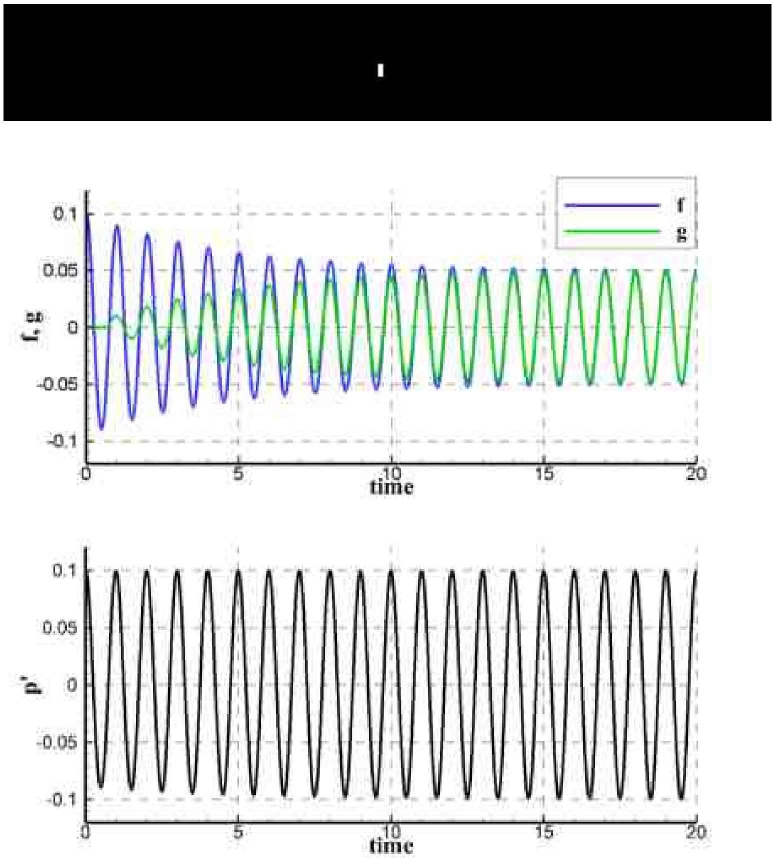

Figure 40. The right going wave, the left going wave, and the acoustic pressure in the annular combustor (at x=0.25, see the figure on the top).

In order to clearly demonstrate the exhaust nozzle “damping” effect, the “time averaged acoustic energies” [20, 21] of the oscillations in the annular combustor at the initial state (i.e., oscillations described on the left in Figure 39) and at the final state after the transition to standing wave oscillations (i.e., oscillations described on the right in Figure 39) were calculated and compared each other. The time averaged acoustic energy, W_{av}, in a one-dimensional duct of length, L, is shown as below:

$$W_{av} = \frac{1}{T}\int_0^T \int_0^L \left(\frac{1}{2}\overline{\rho}\, v'^2 + \frac{1}{2}\frac{p'^2}{\overline{\rho}\,\overline{a}^2} \right) dxdt \tag{3-48}$$

where, W_{av}: time averaged acoustic energy in a one-dimensional duct
T : period of the oscillations
L : length of the one-dimensional duct

The time averaged acoustic energy of the "initial" right going acoustic wave in the annular combustor, $W_{av,initial}$, having the normalized acoustic pressure amplitude, $\hat{P}_{initial} = 0.1$, can be calculated by integrating Eq. (3-48) as following.

$$W_{av,initial} = \frac{\left|P_{initial}\right|^2}{2\overline{\rho}\,\overline{a}^2} L = \frac{\overline{p}^2 L}{2\overline{\rho}\,\overline{a}^2}\left|\hat{P}_{initial}\right|^2 = 0.01\left(\frac{\overline{p}^2 L}{2\overline{\rho}\,\overline{a}^2}\right) \tag{3-49}$$

where, $P_{initial}$: amplitude of the initial acoustic wave; $p'_{initial} = \mathrm{Re}[P_{initial} e^{-i\omega t}]$
$\hat{P}_{initial}$: normalized amplitude; $\hat{p}'_{initial} = \mathrm{Re}[\hat{P}_{initial} e^{-i\omega t}]$
$\hat{p}'_{initial} = p'_{initial} / \overline{p}$; $\hat{P}_{initial} = P_{initial} / \overline{p}$

After a sufficient time of the transition, the time averaged acoustic energy of the "final" standing wave acoustic field in the annular combustor, $W_{av,final}$, having the normalized acoustic pressure amplitude, $\hat{P}_{final} = 0.1$, can be also calculated using Eq. (3-48) as following.

$$W_{av,final} = \frac{\left|P_{final}\right|^2}{4\overline{\rho}\,\overline{a}^2} L = \frac{\overline{p}^2 L}{4\overline{\rho}\,\overline{a}^2}\left|\hat{P}_{final}\right|^2 = \frac{0.01}{2}\left(\frac{\overline{p}^2 L}{2\overline{\rho}\,\overline{a}^2}\right) \tag{3-50}$$

As shown in Eqs. (3-49) and (3-50), the acoustic energy in the annular combustor after the transition into the “final” standing wave acoustic field is smaller than that of the “initial” right going wave (i.e., $W_{av,final} < W_{av,initial}$), and it indicates that the acoustic energy was lost (or discharged) through the exhaust nozzle. Thus, the exhaust nozzle “damps” the acoustic oscillations (energy) in the combustor.

To further investigate the effect of the exhaust nozzle upon tangential CIs in an annular combustor, the above described calculation was repeated for the case when the initial disturbance in the annular combustor was a standing wave acoustic oscillation, assuming that all other parameters that describe the combustor’s operation was equal to those used in the above example, see Eq. (3-46). It was also assumed that the pressure node and anti-node of the initial standing wave acoustic oscillation were not aligned with the location of the exhaust nozzle. The result of this computation is described in Figure 41 where the spatial dependences of the initial disturbance at different times shortly after the introduction of the disturbance into the combustor are shown on the left, and the spatial dependences of the oscillations at later times (18.75 cycles later; one period of the oscillations equals 1 in this example) are shown on the right. The vertical red lines on the left and right of Figure 41 describe the location of the exhaust nozzle. In order to trace the evolution of the standing wave, the maxima of the oscillations (i.e., the acoustic pressure anti-nodes) at different time steps were connected by blue dashed lines.

The figures on the left of Figure 41 show the evolution of the initial, standing wave disturbance shortly after it was introduced into the combustor. It shows that initially the pressure node of the standing wave disturbance was not aligned with the exhaust nozzle (i.e., its location is identified by the vertical red line). The figures on the left of Figure 41 also show that the anti-node of the initial standing wave disturbance, which had a value of 0.2, was located slightly to the left of the location of the exhaust nozzle. The figures on the right of Figure 41 show that during a period of 18.75 cycles the standing wave acoustic oscillation “shifted” to a position at which its pressure node was aligned with the location of the exhaust nozzle (i.e., as denoted by the vertical red line). Furthermore, the calculations show that the exhaust nozzle damped the initial disturbance, reducing its amplitude to a value of 0.14. Interestingly, these two examples (shown in Figure 39 and Figure 41) show that in the absence of a tangential mean flow component in the annular combustor, initially travelling or standing acoustic wave disturbances are damped by the exhaust nozzle until “final” standing wave acoustic oscillations, whose pressure node is aligned with the location of the exhaust nozzle, are established in the combustor.

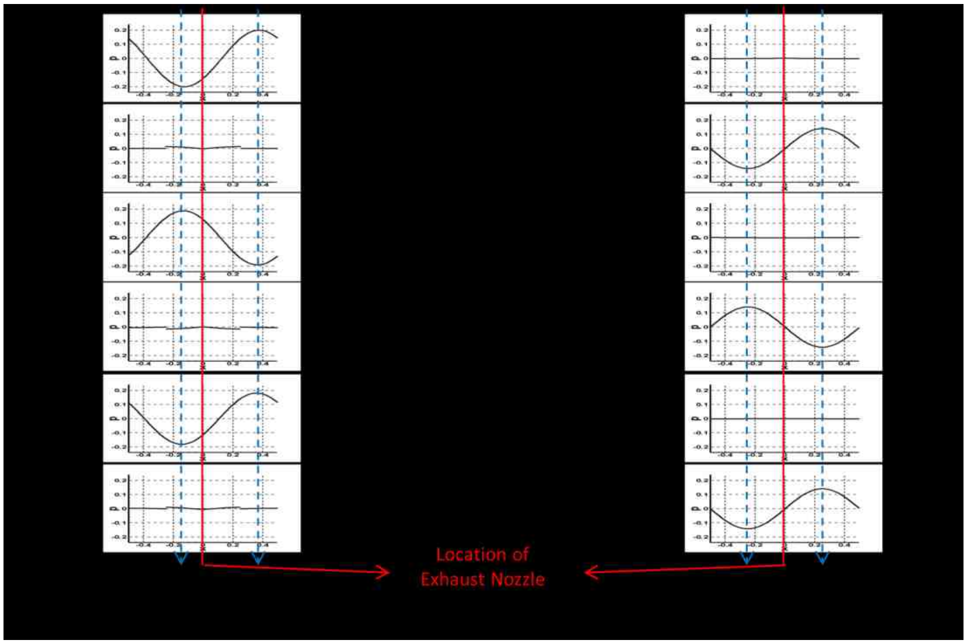

Figure 41. Result of a numerical simulation investigating the effect of the exhaust nozzle flow upon an “initial” standing wave in the annular combustor in the absence of a tangential mean flow.

To gain insight that control the wave phenomena discussed above and described in Figure 41, it was assumed that when the "initial" standing wave was introduced into the combustor, the right and left going waves, $\hat{f}_1(1)$ and $\hat{g}_2(1)$, respectively, arrive at the combustion region and "first" interact with the exhaust nozzle, and generate the outgoing waves, $\hat{f}_2(1)$ and $\hat{g}_1(1)$. These waves propagate at the same speed of sound around the annular combustor and return to the combustion region where they interact again with the exhaust nozzle. These processes are repeated and at the "n-th" interaction of the incoming waves, $\hat{f}_1(n)$ and $\hat{g}_2(n)$, with the exhaust nozzle, the outgoing waves, $\hat{f}_2(n)$ and $\hat{g}_1(n)$, are generated. The latter can be expressed in the following form (using Eq. (3-47)):

$$\begin{aligned} \hat{f}_2(n) &= \hat{f}_1(n) - \varepsilon_{\overline{M}}(\hat{f}_1(n) + \hat{g}_2(n)) \\ \hat{g}_1(n) &= \hat{g}_2(n) - \varepsilon_{\overline{M}}(\hat{g}_2(n) + \hat{f}_1(n)) \end{aligned} \tag{3-51}$$

Using the expressions for the travelling acoustic waves provided in Eq. (3-51) above, the acoustic pressure in the combustion region (i.e., the exhaust nozzle) can be expressed in the following form (using Eq. (3-36)):

$$\begin{aligned} \hat{p}'(n) &= \hat{f}_1(n) + \hat{g}_1(n) = \hat{f}_2(n) + \hat{g}_2(n) \\ &= (1 - \varepsilon_{\overline{M}})(\hat{f}_1(n) + \hat{g}_2(n)) \end{aligned} \tag{3-52}$$

The fact that the outgoing right going wave $\hat{f}_2(n)$ and left going wave $\hat{g}_1(n)$ propagate around the annular combustor and return to the combustion region as incoming right going wave $\hat{f}_1(n+1)$ and left going wave $\hat{g}_2(n+1)$, respectively, can be mathematically expressed as follows:

$$\begin{aligned} \hat{f}_1(n+1) &= \hat{f}_2(n) \\ \hat{g}_2(n+1) &= \hat{g}_1(n) \end{aligned} \tag{3-53}$$

At the “(n+1)-th” interaction between the acoustic waves and the exhaust nozzle, the relationships between the incoming and outgoing waves are described by the following expressions:

$$\begin{aligned} \hat{f}_2(n+1) &= \hat{f}_1(n+1) - \varepsilon_{\overline{M}}(\hat{f}_1(n+1) + \hat{g}_2(n+1)) \\ \hat{g}_1(n+1) &= \hat{g}_2(n+1) - \varepsilon_{\overline{M}}(\hat{g}_2(n+1) + \hat{f}_1(n+1)) \end{aligned} \qquad \textbf{(3-54)}$$

At this “(n+1)-th” interaction, the acoustic pressure in the combustion region (and at the exhaust nozzle) can be expressed as follows:

$$\begin{aligned} \hat{p}'(n+1) &= \hat{f}_1(n+1) + \hat{g}_1(n+1) = \hat{f}_2(n+1) + \hat{g}_2(n+1) \\ &= (1-\varepsilon_{\overline{M}})(\hat{f}_1(n+1) + \hat{g}_2(n+1)) \\ &= (1-\varepsilon_{\overline{M}})(1-\varepsilon_{\overline{M}})(\hat{f}_1(n) + \hat{g}_2(n)) \end{aligned} \qquad \textbf{(3-55)}$$

By comparing Eq. (3-52) and Eq. (3-55), it can be shown that the magnitude of the acoustic pressure oscillations at the exhaust nozzle gradually decrease as the interactions between the acoustic waves and the exhaust nozzle are repeated. In fact, using Eqs. (3-52) and (3-55) it can be shown that

$$\hat{p}'(n+1) = (1-\varepsilon_{\overline{M}})\hat{p}'(n) \qquad \textbf{(3-56)}$$

Applying Eq. (3-56) above to the acoustic pressure oscillations at the “n-th” interaction and the “initial” acoustic pressure oscillations results in the following relationship:

$$\hat{p}'(n) = (1-\varepsilon_{\overline{M}})^n \hat{p}'(0) = \hat{p}'(0)e^{\ln(1-\varepsilon_{\overline{M}})n} \approx \hat{p}'(0)e^{-\varepsilon_{\overline{M}}n} \qquad \textbf{(3-57)}$$

Also, by expressing the argument (i.e., the variable of interaction number, “n”) in Eq. (3-57) above in terms of the time variable, “t”, the exponentially decaying “amplitude” of the acoustic oscillations in the combustion region (i.e., at the exhaust nozzle) can be expressed as follows:

$$\hat{p}'(t) \approx \hat{p}'(0)e^{-\varepsilon_{\overline{M}}(\bar{a}/L)t} \qquad \textbf{(3-58)}$$

The above Eqs. (3-56), (3-57), and (3-58) show that the acoustic pressure at the exhaust nozzle keeps decreasing exponentially until, eventually, it becomes zero and a pressure node of the standing wave is established at the exhaust nozzle.

Figure 41 shows that the exhaust nozzle damps the oscillations in the combustion region until the standing wave reaches its “equilibrium” state, when its pressure node is adjusted to the location of the exhaust nozzle. In this case, the exhaust nozzle damping reduced the amplitude of the initial standing wave disturbance from 0.2 to 0.14 (see Figure 41).

We also investigated the time evolution of an initial standing wave disturbance whose pressure anti-node was aligned with the location of the exhaust nozzle by numerically solving the model equations (i.e., Eqs. (3-28), (3-29), (3-43), (3-44), and (3-45)), assuming that all other parameters that describe the combustor’s operation was equal to those used in the previously discussed examples, see Eq. (3-46). Figure 42 describes the results of this calculation. It shows that the initial standing wave acoustic oscillation was damped until its amplitude eventually became zero; the amplitude was reduced from 0.2 to 0.003 as shown in the figures on the left and right in Figure 42.

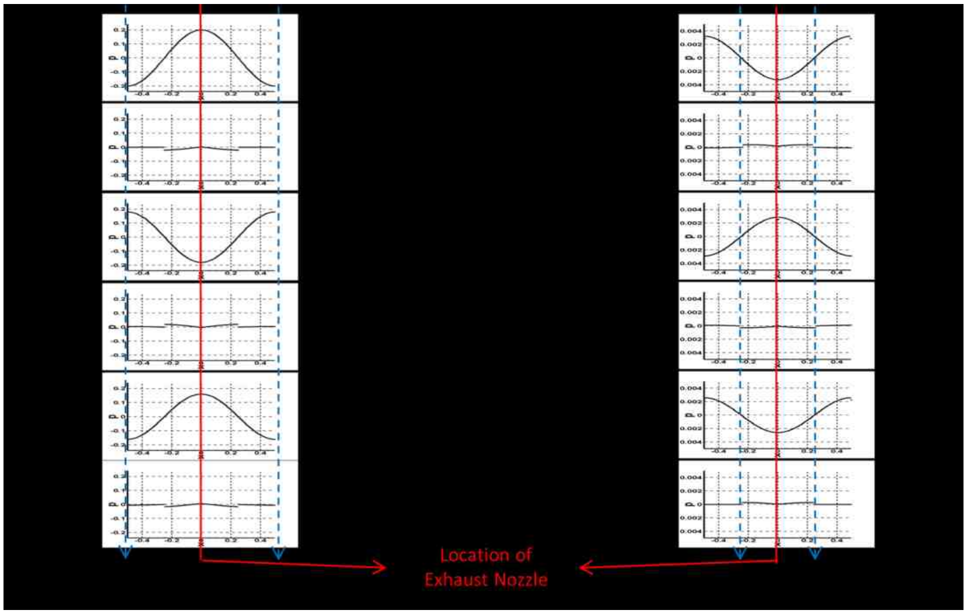

Figure 42. Result of a numerical simulation investigating the effect of the exhaust nozzle flow upon an "initial" standing wave in the annular combustor in the absence of a tangential mean flow; the pressure anti-node of the initial standing wave was located at the exhaust nozzle.

In order to investigate the effect of the location of the exhaust nozzle relative to the acoustic pressure node and anti-node of the initial standing wave oscillations upon the exhaust nozzle "damping" effect, the above described calculation was repeated using a "series" of standing waves initial conditions whose pressure nodes were located at different distances from the location of the exhaust nozzle. In all the cases, the initial standing waves oscillations in the annular combustor were damped as their pressure nodes moved toward the location of the exhaust nozzle.

Figure 43 describes the dependence of the "initial" (described by the blue solid line) and "final" (described by the red dashed line) standing waves' amplitudes upon the distance between the initial disturbance's pressure node and the location of the exhaust nozzle; where this distance was measured in the wavelength, λ of the oscillations. Figure 43 shows that the damping of the initial standing wave disturbance increased as the distance between its pressure node and the exhaust nozzle increased. As discussed above, Figure 43 also shows that complete damping of the initial disturbance occurred when this distance was $\frac{1}{4}\lambda$ and the initial disturbance's pressure anti-node was aligned with the location of the exhaust nozzle. Notably, when this distance was zero and the initial disturbance's pressure node was aligned with the exhaust nozzle location, damping of the initial disturbance did not occur (see Figure 43), and the initial disturbance was not affected by the exhaust nozzle. This occurred because the initial disturbance did not excite flow fluctuations through the exhaust nozzle because the exhaust nozzle was aligned with the wave's pressure node (i.e., $p' = 0$) and, thus, was not exposed to pressure fluctuations.

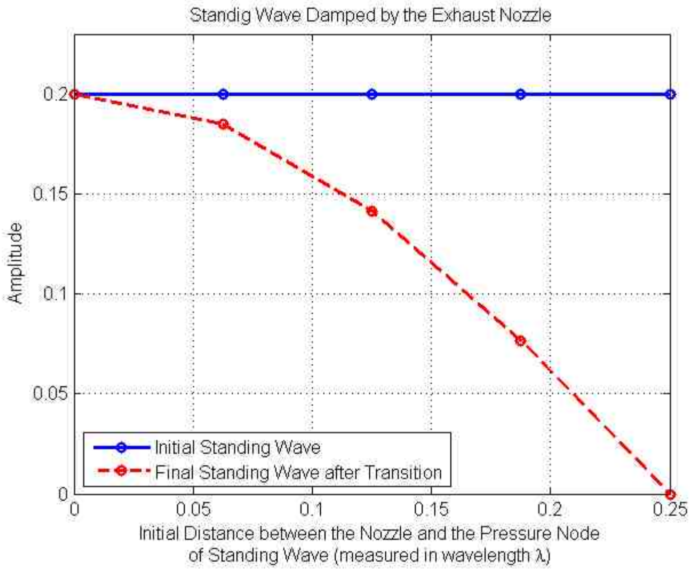

Figure 43. Damping of the "initial" standing wave oscillations in the annular combustor by the exhaust nozzle in the absence of a tangential mean flow; the effect of the location of the exhaust nozzle relative to the structure of the "initial" standing wave on the amount of damping.

3.3.2.2. Effect of a Tangential Mean Flow upon the Exhaust Nozzle Damping

In this section, the results of a study of the effect of an exhaust nozzle upon acoustic waves in an annular combustor in the presence of a tangential mean flow are discussed. When a tangential mean flow, $\bar{V}$, is present in the annular combustor, the propagation velocities of the right going wave and the left going wave are $\bar{V} + \bar{a}$ and $\bar{V} - \bar{a}$, respectively; see Figure 37 and Figure 38. Consequently, when right and left going waves leave the combustion region after interacting with the exhaust nozzle they do not return to the combustion region (i.e., exhaust nozzle) at the same time, as was the case when we studied these interactions earlier assuming that there was no tangential mean flow in the annular combustor. In addition, the dependences of the model equation (i.e., Eq. (3-43)) and its parameter $\varepsilon_{\bar{M}}$ (i.e., Eq. (3-38)) upon the tangential mean flow Mach number, $\bar{M}$, indicate that the interactions of the exhaust nozzle with the oscillations inside the combustor is affected by the tangential mean flow.

In order to investigate the effect of the presence of a tangential mean flow component on the interactions of the acoustic waves with the exhaust nozzle, the above described calculations were repeated assuming that a tangential mean flow component was present in the annular combustor and that all the other operating conditions were the same with the previous cases (these are described in the examples discussed in Section *3.3.2.1.* whose results are shown in Figure 39 through Figure 43). Specifically, it was assumed that the oscillatory heat release by chemical reactions was zero and that there were no fluctuations in the inlet flow through the injector. The same exhaust nozzle parameter $\varepsilon_{\bar{M}}$ was used while assuming that the tangential mean flow Mach number was not zero. Specifically, the following model parameters were employed:

$$\overline{M} = 0.1, \quad \varepsilon_{\overline{M}} = 0.1 << 1, \quad (\hat{\dot{Q}}_{chem})' = 0, \quad (\hat{S}_{injector})' = 0 \qquad \textbf{(3-59)}$$

It was also assumed that the exhaust nozzle was located at the center of the annular combustor as was assumed in the solved examples in Section *3.3.2.1.*; see Figure 38. It was also assumed that the initial conditions (i.e., the acoustic oscillations in the combustor at $t = 0$), consisted of either a traveling acoustic wave that propagated from left to right with a velocity that equals the sum of the mean flow velocity and the speed of sound or a standing acoustic wave that was convected by the tangential mean flow.

The results of these computations are described in Figure 44 and Figure 45 where the spatial dependences of the initial disturbance at different time instants shortly after the introduction of the disturbance into the combustor are shown on the left, and the corresponding spatial dependences at different time instants after some time has elapsed (about 18.77 cycles later; one period of the oscillations equals 1 in this example) are shown on the right. The plots on the left of Figure 44 show that an initial travelling wave disturbance propagated to the right at a speed that equals the sum of the speed of sound and the (tangential) mean flow velocity. In this case, the initial travelling wave disturbance was “completely” damped until its amplitude eventually became zero (in this example, the amplitude of the initial wave was reduced from 0.1 to ~0.01, as shown in the figures on the right). The plots on the left of Figure 45 show that an initial, standing, acoustic wave disturbance moved slowly to the right, suggesting that it was convected by the tangential mean flow velocity. As in the case of an initial travelling wave disturbance, the plots on the right side show that the initial standing wave disturbance was also “completely” damped to nearly zero amplitude (in this example, the amplitude of the initial standing wave disturbance was reduced from 0.2 to 0.014).

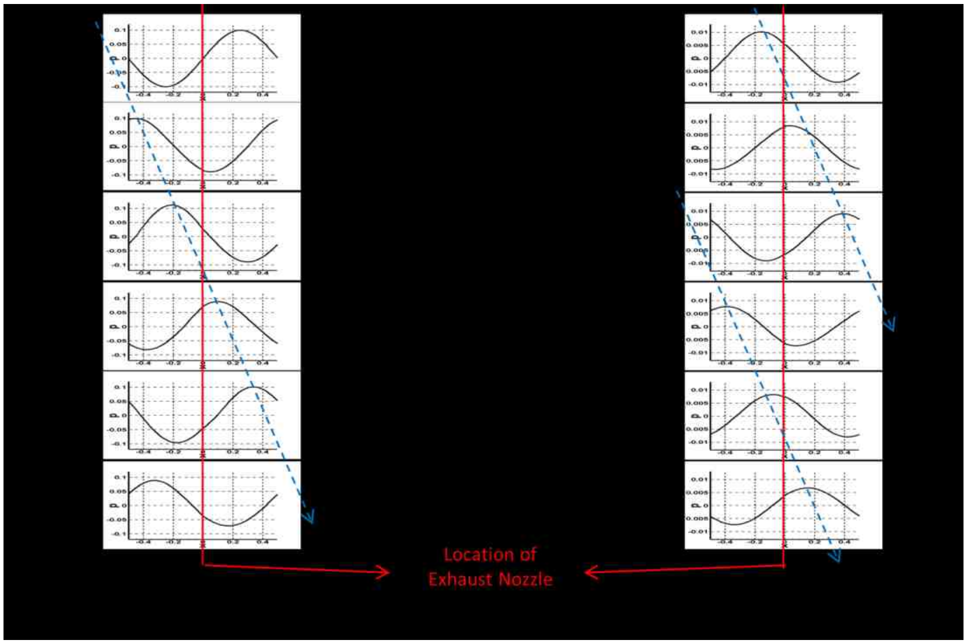

Figure 44. Result of a numerical simulation investigating the effect of the exhaust nozzle flow upon an "initial" travelling wave in the annular combustor in the presence of a tangential mean flow.

The two examples described in Figure 44 and Figure 45 show that in the presence of a tangential mean flow component in the annular combustor, initially travelling or standing acoustic wave disturbances are "completely" damped by the exhaust nozzle (essentially reducing their amplitudes to zero). Since in these examples the right and left going waves had different propagation velocities due to the presence of a tangential mean flow, the transmitted and reflected waves leaving the combustion region, after their interaction with the exhaust nozzle, did not return to the combustion region at the same time, and the repeated interactions of these "pair" of waves with the exhaust nozzle did not occur (which is different from the previous examples in the absence of the tangential mean flow in Section *3.3.2.1.*). Therefore, the transition from the initial travelling wave disturbance to "final" standing wave oscillations did not occur. Similarly, the pressure node of an initial standing wave disturbance did not move toward the location of the exhaust nozzle when the tangential mean flow was present in the annular combustor.

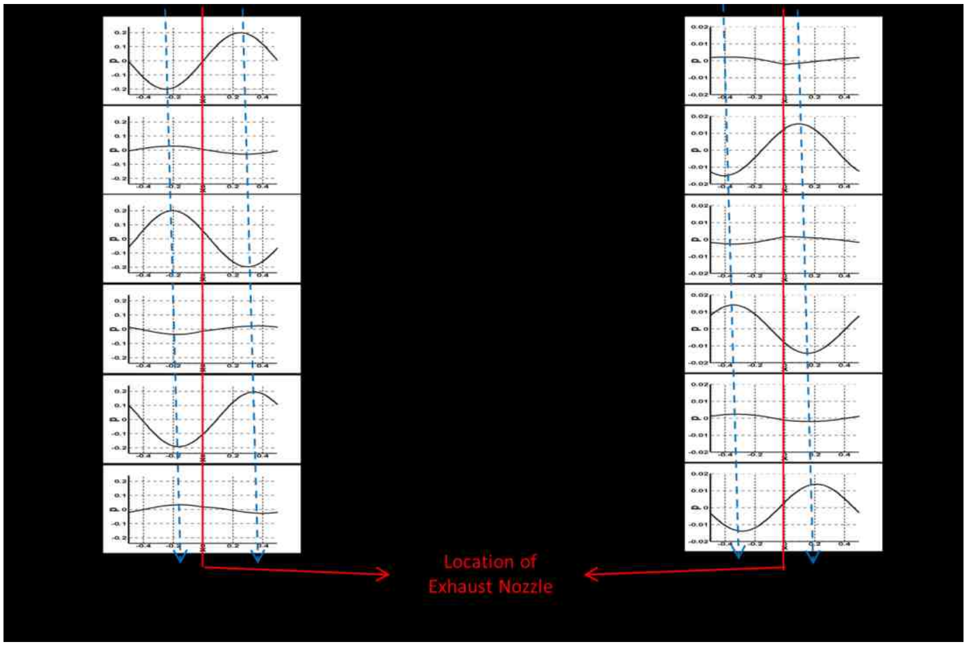

Figure 45. Result of a numerical simulation investigating the effect of the exhaust nozzle flow upon an "initial" standing wave in the annular combustor in the presence of a tangential mean flow.

However, as shown in the model equation (Eq. (3-43)) and in the previous examples described in Figure 39 through Figure 43, some of the acoustic energy of the waves in the combustor was lost through the exhaust nozzle (via sound radiation and convection by the flow through the exhaust nozzle) until the oscillations in the combustion region were completely damped. Thus, in the presence of a tangential mean flow in the annular combustor, initial travelling or standing acoustic wave disturbances are completely damped by the exhaust nozzle.

It should be also noted that additional studies, whose details are not reported here, showed that when the exhaust nozzle parameter, $\varepsilon_{\overline{M}}$, was increased, the exhaust nozzle "damping" also increased. This was accompanied by increased damping and amplification of the transmitted and reflected waves leaving the “combustion region”, respectively. Also, as the exhaust nozzle parameter, $\varepsilon_{\bar{M}}$, was increased in the absence of a tangential mean flow, the transition period from an initial travelling wave disturbance to a “final” standing wave oscillation whose pressure node is aligned with the exhaust nozzle became shorter.

3.3.3. Driving of Combustion Instabilities by a Pressure Dependent Combustion Process

In this section, the results of a study of the effect of the characteristics of the unsteady combustion process upon the stability of an annular combustor operating with and without a tangential mean flow are discussed.

This required that the dependence of the perturbed heat release by the combustion process (i.e., $(\hat{\dot{Q}}_{chem})'$) upon the conditions in the combustion region be modeled. In this study, we used an empirical model used in related previous studies [1, 40], that used the following expression to describe the dependence of the chemical heat release perturbation $(\hat{\dot{Q}}_{chem})'$ upon the mean velocity and the velocity and pressure perturbations in the combustion region:

$$(\hat{\dot{Q}}_{chem})' = k_p \cdot \hat{p}' + k_v \cdot \left(\left| \hat{\bar{V}} + \hat{v}' \right| - \left| \hat{\bar{V}} \right| \right) \qquad \textbf{(3-60)}$$

The terms k_p and k_v in Eq. (3-60) above are empirical constants that “relate” the chemical heat release perturbation to the acoustic pressure and velocity perturbations in the combustion region; i.e., $\hat{p}'$ and $\hat{v}'$. Notably, the acoustic pressure and velocity, $\hat{p}'$ and $\hat{v}'$, in the “combustion” region can be obtained using the following equations, which are obtained from Eq. (3-36):

$$
\begin{aligned}
&\hat{p}' = \hat{f}_1 + \hat{g}_1 = \hat{f}_2 + \hat{g}_2 \\
&v' = \frac{v_1' + v_2'}{2} = \frac{1}{2\gamma}\left\{(\hat{f}_1 - \hat{g}_1) + (\hat{f}_2 - \hat{g}_2)\right\}
\end{aligned}
\qquad \textbf{(3-61)}
$$

Notably, the second term in the expression for $(\hat{\hat{Q}}_{chem})'$ in Eq. (3-60) describes the effect of the tangential mean flow on the interaction between the combustion process and the acoustic waves in the combustion region.

First, the stability of the annular combustor was studied assuming that the combustion process heat release (i.e., $(\hat{\hat{Q}}_{chem})'$ in Eq. (3-60)) only depended upon the pressure oscillations in the combustion region (i.e., $\hat{p}'$) while neglecting the effects of the mean and perturbed velocity components (described by the second term on the RHS of Eq. (3-60)) upon the combustor stability. Furthermore, to investigate the effect of the pressure dependence of the combustion process, it was assumed that the empirical constant k_p was a large number, thus assuring that the heat addition process that drives the instability is much larger than the damping provided by the exhaust nozzle (which is discussed in Section 3.3.2.). This assumption was used because the exhaust nozzle parameter, $\varepsilon_{\bar{M}}$, cannot be set to zero because it also describes the "steady state" operation of the combustor. It can be set, however, to have a non-zero, but small value; see discussions in Section 3.2.2. and Section *A.3.1.4.*, and Eqs. (A-125) and (A-126). Therefore, instead of using zero valued exhaust nozzle parameter $\varepsilon_{\bar{M}}$, the empirical constant k_p was assumed to be large to allow the study of the effect of the pressure dependence of the combustion process.

3.3.3.1. Combustor Stability in the Absence of a Tangential Mean Flow

The stability of the annular combustor under the conditions discussed in the previous section and when there is no tangential mean flow in the annular combustor was studied by numerically solving the derived model equations (i.e., Eqs. (3-28), (3-29), (3-43), (3-44), (3-45), and (3-60)). This solution was obtained by also assuming that the flow through the injector did not interact with the oscillations in the combustor. To satisfy these assumptions, the following model parameters were employed:

$$\overline{M} = 0, \ \ \varepsilon_{\overline{M}} = 0.1 << 1, \ \ k_p = 1.8, \ \ k_v = 0, \ \ (\hat{S}_{injector})' = 0 \tag{3-62}$$

It was also assumed that a traveling wave propagating from left to right was initially (i.e., at $t = 0$) present in the annular combustor and that the concentrated combustion region was located at the center of the combustor as shown in Figure 38.

Figure 46 describes the calculated spatial dependence of the acoustic pressures in the annular combustor at several time steps. As was done in the examples presented in Section 3.3.2., the wave fronts motions are described by blue dashed lines, and the plots on the left of Figure 46 show the evolution of the waves shortly after the initial travelling wave disturbance was introduced into the combustor. These plots show that the initial disturbance is travelling at the speed of sound from left to right, the propagation direction of the initial disturbance. The plots on the right of Figure 46 show the characteristics of the waves some time thereafter (specifically, 23.60 cycles later; one period of the oscillations equals 1 in this example). They show that the wave front is stationary, indicating that the initially travelling wave has settled into a standing wave. These plots also show that the amplitude of the initial disturbance increased from an initial travelling wave amplitude of 0.1 to a standing wave amplitude of 2.3 after ~24 cycles. Notably, the pressure anti-node of the developed standing wave was aligned with the location of the combustion region. This is described by the plots of the standing acoustic wave pressure profiles on the right in Figure 46 whose pressure maxima/minima are aligned with the red vertical line that describes the location of the combustion region.

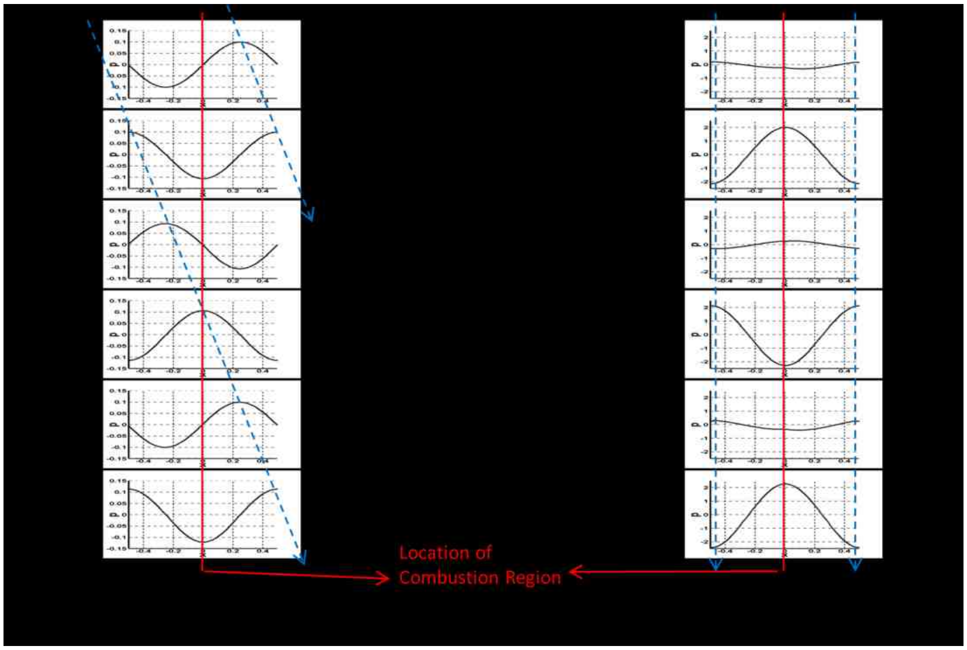

Figure 46. Result of a numerical simulation investigating the effect of the combustion (pressure dependence) upon an "initial" travelling wave in the annular combustor in the absence of a tangential mean flow.

The result presented in Figure 46 above shows that in the absence of a tangential mean flow, an initially spinning wave, rotating at the speed of sound, gradually transforms itself into a standing wave. Figure 46 also shows that the amplitude of the oscillation in the annular combustor increased in time due to the driving provided by the pressure dependent combustion process heat addition. In fact, the time dependence of the combustor's oscillations depends upon the difference between the damping provided by the exhaust nozzle and the driving provided by the combustion process. Specifically, the amplitude of the combustor oscillations increases/decreases when the combustion process driving is larger/smaller than the exhaust nozzle's damping, respectively.

In the discussed example, the initial travelling wave disturbance excited oscillations in the combustion region that affected the combustion process that produced interactions between the combustion process and acoustic oscillations, which "pumped" acoustic energy from the combustion process into the oscillations. In fact, using the derived model equation (i.e., Eq. (3-43)) and the assumed combustion model (i.e., Eqs. (3-60) and (3-62)), it can be shown that a combustion process amplifies the oscillations in the combustor. These equations show that when only a right going wave $\hat{f}_1$ arrives at the combustion region (i.e., $\hat{g}_2 = 0$), the amplitude of the transmitted wave $\hat{f}_2$ is larger than that of the incoming wave (i.e., $\hat{f}_2 > \hat{f}_1$) and a reflected wave $\hat{g}_1$ is generated. In this case, the reflected wave $\hat{g}_1$ is in phase with the incoming wave $\hat{f}_1$ (because $\hat{g}_1$ has the same sign with $\hat{f}_1$), while in the examples investigating the effect of exhaust nozzle (described in Section 3.3.2.), the reflected wave is 180° out of phase with the incoming wave.

Thus, the interaction of the initial, right going wave, $\hat{f}_1$, with the combustion process (which only depends upon the pressure in the combustion region) amplified the initial wave and generated a larger amplitude transmitted wave, $\hat{f}_2$, and a reflected wave, $\hat{g}_1$ that is in phase with the incident wave $\hat{f}_1$. Notably, since the combustion process is a monopole acoustic source and the combustion region is acoustically compact (i.e., $k\Delta x \ll 1$), the acoustic pressure across the combustion region is continuous; i.e., $\hat{p}'_1 = \hat{p}'_2$ (see Eq. (3-32)). When the initial, right going wave, $\hat{f}_1$, arrives at the combustion region, this acoustic pressure "continuity" can be expressed in terms of the incoming and outgoing right and left going waves as $\hat{f}_1 + \hat{g}_1 = \hat{f}_2$, since initially there is no left going wave (i.e., $\hat{g}_2 = 0$) entering the combustion region. Thus, the combustion driving at this instant increases the amplitude of the incident wave $\hat{f}_1$ by an amount equal to the difference between the incident and transmitted right going waves $\hat{f}_1$ and $\hat{f}_2$, (i.e., by $\hat{f}_2 - \hat{f}_1$). In additions, the combustion process supplies the energy needed to generate the reflected, left going wave $\hat{g}_1$. Notably, equal amounts of energy are added to the generation of $\hat{g}_1$ and amplification of $\hat{f}_1$; i.e., $\hat{g}_1 = \hat{f}_2 - \hat{f}_1$. Since there was no mean flow in the annular combustor, the amplified right going wave and reflected left going wave propagated at the same speed of sound around the annular combustor without experiencing amplitude changes. These waves returned to the combustion region at the same time, after propagating once around the annular combustor, and interacted again with the combustion process there. This interaction, again, added the same amount of acoustic energy to the outgoing right and left going waves through the amplification and reflection processes. These propagation/amplification processes continued until, "eventually", a standing wave having a larger amplitude (than the initial disturbance) was established in the annular combustor. Notably, the results on the right of Figure 46 show that the pressure anti-node of the resulting standing wave field after the passage of 23.60 cycles was centered in the combustion region (depicted as red line at the center of the combustor) because the incoming right and left going waves have the same amplitudes and signs (phases) at the combustion region and each has been amplified by the same amount by the combustion process. Since the location of the pressure anti-node coincided with the location of the combustion process, the driving provided by the combustion process was maximized according to the well-known Rayleigh Criterion [41, 42]. It should be also noted that the amplitude of the oscillations in Figure 46 continuously increased with time. This is a well-known feature of linear stability problems (which include all the examples discussed so far) whose instabilities' amplitudes grow to infinity if left unchecked.

The results presented in Figure 46 clearly show that the combustion process driving increases the amplitude of the combustor's oscillation, thus increasing their acoustic energy. The amount of energy added to the oscillations may be determined by comparing the "time averaged acoustic energies" of the oscillations in the annular combustor when the "initial" travelling wave disturbance was excited in the combustor (described by the plots on the left of Figure 46) and the "amplified", standing wave oscillations at a later time of $t \approx 24$ (described by the plots on the right of Figure 46). These time averaged acoustic energies were calculated and compared to each other following the approach presented in Section *3.3.2.1*. The time averaged acoustic energy of the "initial" right going travelling wave in the annular combustor, $W_{av,initial}$, having a normalized acoustic pressure amplitude, $\hat{P}_{initial} = 0.1$, can be calculated using the following expression:

$$W_{av,initial} = \frac{\left|P_{initial}\right|^2}{2\bar{\rho}\,\bar{a}^2} L = \frac{\bar{p}^2 L}{2\bar{\rho}\,\bar{a}^2}\left|\hat{P}_{initial}\right|^2 = 0.01\left(\frac{\bar{p}^2 L}{2\bar{\rho}\,\bar{a}^2}\right) \qquad \textbf{(3-63)}$$

As time passed, the initial travelling wave disturbance has transformed itself into a standing acoustic wave whose time averaged acoustic energy, $W_{av,t\approx 24}$, is calculated below at time $t \approx 24$, when the normalized amplitude of the standing wave oscillations was equal to $\hat{P}_{t\approx 24} = 2.3$.

$$W_{av,t\approx 24} = \frac{\left|P_{t\approx 24}\right|^2}{4\bar{\rho}\,\bar{a}^2} L = \frac{\bar{p}^2 L}{4\bar{\rho}\,\bar{a}^2}\left|\hat{P}_{t\approx 24}\right|^2 = \frac{2.3^2}{2}\left(\frac{\bar{p}^2 L}{2\bar{\rho}\,\bar{a}^2}\right) = 2.645\left(\frac{\bar{p}^2 L}{2\bar{\rho}\,\bar{a}^2}\right) \qquad \textbf{(3-64)}$$

Comparing Eqs. (3-63) and (3-64) shows that the acoustic energy in the annular combustor after the transition into the standing wave acoustic field is larger than that of the "initial" right going wave (i.e., $W_{av,t\approx 24} > W_{av,initial}$), indicating that acoustic energy was supplied by the combustion process to the oscillations.

Figure 47 describes the time dependence of the right and left going waves and the acoustic pressure in the annular combustor at location $x = -0.5$ as shown on the top and bottom of the figure. Figure 47 shows that the amplitudes of the right going wave (the blue curve) and the left going wave (the green curve) increased in time. These plots also show that the amplitudes of the two oppositely propagating waves approached one another as time increased, thus establishing a standing wave within the annular combustor. Notably, the pressure anti-node of this standing wave was located at the combustion region, and the acoustic pressure amplitude in the combustor exponentially increased with time as described in the acoustic pressure plots in Figure 47. The exponential pressure growth is due to the fact that the driving of the oscillations by the combustion process was larger in this example than the damping provided by the exhaust nozzle, and both are linearly related to the local pressure oscillations, as shown by Eqs. (3-43) and (3-60).

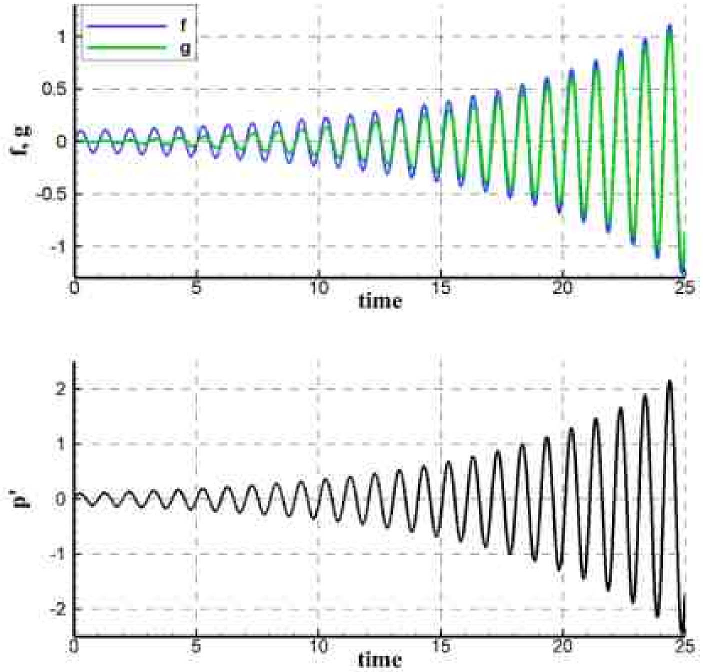

Figure 47. The right going wave, the left going wave, and the acoustic pressure in the annular combustor (at x=-0.5, see the figure on the top).

To further investigate the effect of this combustion process upon tangential CIs in an annular combustor, the above described calculation was repeated for the case when the initial disturbance in the annular combustor was a standing wave acoustic oscillation, assuming that all other parameters that describe the combustor's operation were kept the same as in the above example, see Eq. (3-62). It was also assumed that neither the pressure node nor the anti-node of the initial standing wave disturbance were located at the combustion region. The results of this computation are described in Figure 48 where the spatial dependences of the initial disturbance at different time instants shortly after the introduction of the disturbance into the combustor are shown on the left, and the developed wave behaviors at later times (i.e., 23.60 cycles later; one period of the oscillations equals 1 in this example) are shown on the right.

The figures on the left of Figure 48 show the evolution of the initial, standing wave disturbance shortly after it was introduced into the combustor. It shows that initially the pressure anti-node of the standing wave disturbance was not located at combustion region (designated by the vertical red line). The plots on the left of Figure 48 also show that the anti-node of the initial standing wave disturbance, which had a value of 0.2, was located slightly to the left of the location of the combustion region. The figures on the right of Figure 48 show that during a period of 23.60 cycles the standing wave acoustic oscillation “shifted” to a position at which its pressure anti-node was aligned with the location of the combustion region (designated by the vertical red line). Furthermore, the calculations show that the combustion process amplified the initial standing wave disturbance, increasing its initial amplitude of 0.2 to a value of 3.0.

These two examples whose behaviors are described in Figure 46 and Figure 48 show that in the absence of a tangential mean flow component in the annular combustor, initially travelling or standing acoustic wave disturbances were amplified by the pressure dependent combustion process in a manner that eventually establishes standing wave acoustic oscillations having their pressure anti-nodes at the combustion region. As expected, the amplitudes of these standing wave oscillations continuously increased with time.

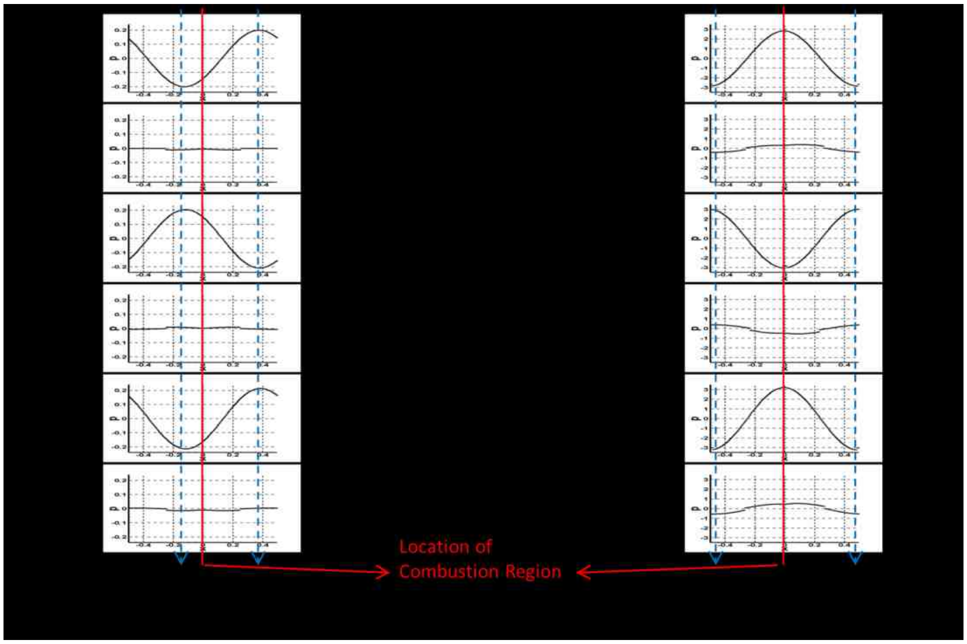

Figure 48. Result of a numerical simulation investigating the effect of the combustion (pressure dependence) upon an "initial" standing wave in the annular combustor in the absence of a tangential mean flow.

Similar to the case of an initial travelling wave disturbance, when a standing wave disturbance was initially introduced into the annular combustor, it generated right and left going waves that entered the combustion region and were amplified there through their interaction with the pressure dependent combustion process, see Eqs. (3-43), (3-60), and (3-62)), resulting in amplified outgoing waves. Notably, both waves were amplified by the same amount as they passed through the combustion region. These amplified, outgoing, right and left going waves propagated at the same speed of sound, since there was no tangential mean flow in the combustor, without experiencing amplitude changes. They returned to the combustion region and interacted again with the combustion process at the same time. These processes continued until, "eventually", a standing wave with a larger amplitude was established in the annular combustor. Notably, the pressure anti-node of the "resulting" standing wave was located at the combustion region (designated by red line at center of the combustor), as shown on the right of Figure 48. The amplitude of this wave would continue to increase as long as the acoustic pressure oscillations were not zero in the combustion region because of the pressure dependence of the combustion process driving, see Eqs. (3-60) and (3-62). If left unchecked, the amplitude of these oscillations would reach (mathematically, but not realistically) an infinite value.

3.3.3.2. Effect of a Tangential Mean Flow upon the Combustor Stability

This section discusses the results of a study that investigated the effect of the presence of a tangential mean flow component upon the investigated annular combustor stability. As discussed in Section *3.3.2.2.*, when a tangential mean flow is present in the annular combustor, the right and left going waves that leave the combustion region, after interacting with the combustion process, propagate in opposite directions in the annular combustor with different propagation velocities; i.e., the velocities of the right and left going waves are $\bar{V} + \bar{a}$ and $\bar{V} - \bar{a}$, respectively. Consequently, these waves do not return to the combustion region at the same time.

In order to investigate the effect of a tangential mean flow upon the combustor stability when the combustion process driving only depends upon the pressure oscillations, the calculations described in the previous sections were repeated assuming that a tangential mean flow was present in the annular combustor. As was the case with the examples described in Section *3.3.3.1.* and Figure 46 and Figure 48, it was assumed that there were no fluctuations present in the inlet flow through the injector and that the effects of the exhaust nozzle damping and combustion process driving were described by the same parameters $\varepsilon_{\overline{M}}$ and k_p, respectively. However, since the presence of a tangential mean flow needed to be accounted for, the investigated stability problem is described by the following set of model parameters:

$$\overline{M} = 0.1,\ \ \varepsilon_{\overline{M}} = 0.1 << 1,\ \ k_p = 1.8,\ \ k_v = 0,\ \ (\hat{S}_{injector})' = 0 \qquad \textbf{(3-65)}$$

As in the examples discussed in Section *3.3.3.1.*, it was also assumed that the combustion region was located at the center of the annular combustor and that the computational domain of the investigated annular combustor is described in Figure 38. Additionally, the investigated initial conditions were assumed to be either a traveling acoustic wave that propagated from left to right with a velocity that was equal to the sum of the mean flow velocity and the speed of sound, and a standing acoustic wave that was convected by the tangential mean flow.

The numerical solutions of these problems are described in Figure 49 and Figure 50 where the spatial dependence of the initial disturbance at different instants of time shortly after the introduction of the initial disturbance into the combustor are shown on the left, and the spatial dependence of the oscillations at later times (about 18.77 cycles later; one period of the oscillations equals 1 in this example) are shown on the right. The plots of the left and right of Figure 49 show that the wave fronts propagated to the right at a speed that was equal to the sum of the speed of sound and the tangential mean flow velocity throughout the process, and that the amplitude of the travelling wave increased from 0.1 to ~0.3 during the investigated time period.

Figure 50 describes the behavior of the combustor's oscillations when the initial disturbance was a standing acoustic wave. It shows that the ensuing combustion instability also behaved as a standing acoustic wave that was convected from left to right with the velocity of the tangential mean flow. Figure 50 also shows that the amplitude of the combustor oscillations continuously increased due to their driving by the pressure dependent combustion process. Specifically, the amplitude of the oscillations increased from an initial value of 0.2 to ~0.74 during the investigated time period.

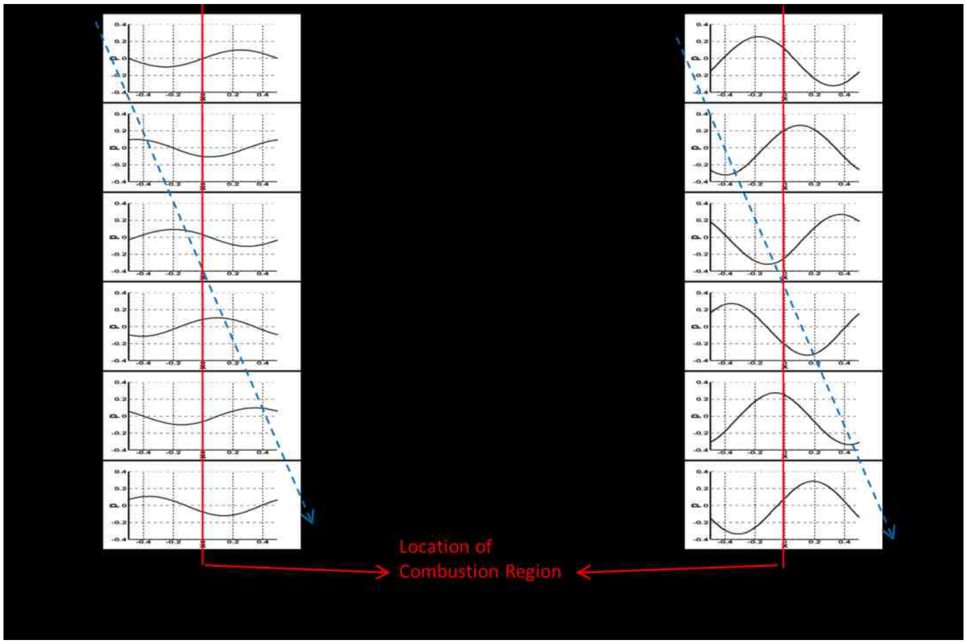

Figure 49. Result of a numerical simulation investigating the effect of the pressure dependent combustion process upon an "initial" travelling wave in the annular combustor in the presence of a tangential mean flow.

The result presented in Figure 49 shows that in the presence of a tangential mean flow, an initial *travelling wave* disturbance develops into a *travelling wave* CI, and Figure 50 shows that an initially *standing wave* disturbances develops into a *standing wave* type CI. In both cases, the initial disturbances were amplified by the pressure dependent combustion process. Interestingly, the presence of the tangential mean flow modified the characteristics of the resulting instability. For example, when an initial travelling wave disturbance was introduced into the annular combustor in the absence of a tangential mean flow, the disturbance was "transformed" into a standing wave CI whose pressure anti-node was located at the combustion region. On the other hand, when a tangential mean flow was present in the annular combustor, an initial travelling wave disturbance developed into a travelling wave CI. Also, in the absence of a tangential mean flow, an initial standing wave disturbance “developed” into a standing wave CI whose pressure anti-node stabilized at the combustion region. Such a pressure anti-node was not located at the combustion region when a tangential mean flow was present in the annular combustor.

The above discussed differences in behavior of the initial disturbances in the presence and absence of a tangential mean flow is due to the differences in the velocities of the right and left going waves that leave the combustion region after interacting with the combustion process there. Since the right and left going waves have different propagation velocities in the presence of a tangential mean flow, these (transmitted and reflected) outgoing waves did not return to the combustion region at the same time, and the repeated interactions between these pairs of waves and the combustion process after each traverse of the annular combustor did not occur “in phase”, which prevented the establishment of a standing wave acoustic pressure anti-node at the combustion region. This behavior differs from that observed when a tangential mean flow was absent in the annular combustor (discussed in Section *3.3.3.1.*) and the right and left going waves propagated around the combustor at the same speed and arrived at the combustion region “in phase”, resulting in the establishment of a standing wave pressure anti-node there.

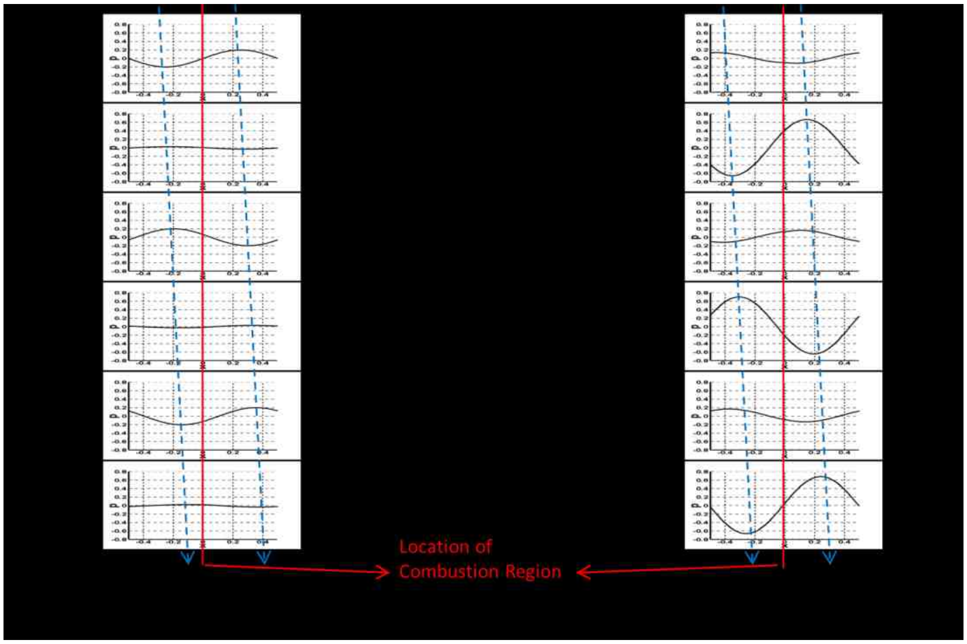

Figure 50. Result of a numerical simulation investigating the effect of the combustion (pressure dependence) upon an "initial" standing wave in the annular combustor in the presence of a tangential mean flow.

In summary, the examples presented in this section show that as long as the driving by the pressure dependent combustion process was larger than the damping provided by the exhaust nozzle, initial disturbances were amplified and exponentially increased in amplitude with time, unless nonlinear processes that limited this growth were present. Furthermore, if the driving by this combustion process increased by increasing the pressure dependence parameter k_p (see Eqs. (3-60) and (3-65)), the growth rate of the amplitude of the combustor oscillations also increased. It was also shown that the characteristics of the resulting CIs strongly depend on whether a tangential mean flow was present in the annular combustor.

3.3.4. Driving of Combustion Instabilities by a Combustion Process Nonlinearly Depended upon the Velocity

In Section 3.3.3., the results of a study of the effect of a pressure (only) dependent combustion process upon the stability of an annular combustor are reported. In this section, the results of a study of the effects of nonlinear dependence of the combustion process upon the tangential mean velocity component and perturbed velocity with and without the presence of a tangential mean flow in the annular combustor are presented.

The examples solved in this section assumed the dependence of the perturbed heat release by the combustion process, $(\hat{\dot{Q}}_{chem})'$, upon the acoustic pressure and velocity, $\hat{p}'$ and $\hat{v}'$, in the combustion region is described by the empirical relationship shown in Eq. (3-60). To investigate the effect of the acoustic velocity dependence of the combustion process (which is the second term on the RHS of Eq. (3-60)) upon the combustor stability, the magnitudes of the parameters describing the exhaust nozzle damping (i.e., $\varepsilon_{\bar{M}}$) and the acoustic pressure dependent combustion process (i.e., k_p) were adjusted, so that the effect of the driving by the pressure dependent combustion process nearly cancelled the effect of the exhaust nozzle damping to produce a scenario in which the driving by the acoustic velocity dependent combustion process could be clearly observed.

3.3.4.1. Combustor Stability in the Absence of a Tangential Mean Flow

The effect of the acoustic velocity dependence of the combustion process upon the acoustic waves in an annular combustor without a tangential mean flow was investigated, by numerically solving Eqs. (3-28), (3-29), (3-43), (3-44), (3-45), and (3-60). As described above, the parameters describing the driving by the pressure dependent component of the combustion process and the exhaust nozzle damping were adjusted in the model equations so that the effects of these two processes nearly cancelled one another. When this was accomplished, the amplitude of the oscillations in the annular combustor slowly increased or decreased. In addition, it was assumed that the combustion process depends upon the acoustic velocity oscillation in the combustion region and that there were no fluctuations in the inlet flow through the injector. Consequently, the following model parameters were employed:

$$\overline{M} = 0, \ \ \varepsilon_{\overline{M}} = 0.1 << 1, \ \ k_p = 0.7, \ \ k_v = 1.0, \ \ (\hat{S}_{injector})' = 0 \qquad \textbf{(3-66)}$$

It was also assumed that a traveling wave propagating from left to right was initially (i.e., at $t = 0$) present in the annular combustor and that the concentrated combustion region was located at the center of the combustor as shown in Figure 38.

Figure 51 describes the calculated spatial dependence of the acoustic pressures in the annular combustor at several time steps. The wave front motion, described by blue dashed lines on the left of Figure 51, describes the evolution of the waves shortly after the initial travelling wave was introduced into the combustor. It shows that initially the wave travelled at the speed of sound from left to right, the propagation direction of the initial disturbance. The figures on the right of Figure 51 show the behavior of the wave a long time thereafter (i.e., 28.75 cycles later; one period of the oscillations equals 1 in this example). They show that the wave profile is no longer sinusoidal, exhibiting the presence of higher frequency oscillations.

The result in Figure 51 shows that in the absence of a tangential mean flow, an initially travelling wave disturbance, propagating at the speed of sound, gradually transforms itself into a nonlinear waveform oscillation having higher frequency components. When there is no tangential mean flow in the annular combustor, i.e., $\bar{V} = 0$ and $\bar{M} = 0$, the velocity dependence of the combustion process can be expressed by $(\hat{\hat{Q}}_{chem})' \propto k_v \cdot |\hat{v}'|$, which is obtained by substituting $\bar{V} = 0$ into the second term of the RHS of Eq. (3-60). In this example, the initial travelling wave disturbance excited velocity oscillations in the combustion region (i.e., $\hat{v}'$) that affected the combustion process via the relationship, $(\hat{\hat{Q}}_{chem})' \propto k_v \cdot |\hat{v}'|$. Since it can be shown that the (most dominant) frequency of oscillations in the term $k_v \cdot |\hat{v}'|$ equals twice frequency of the velocity oscillation $\hat{v}'$ in the combustion region, the combustion process generates acoustic waves in the combustion region with twice the frequency of the initial disturbance. It follows the combustion process must generate oscillations in the annular combustor that have a component that oscillates with twice the frequency of the initial disturbance. Figure 51 shows that the initial disturbance in the annular combustor at $\mathrm{t} = 0$ has two local minima/maxima (as shown in the figure at $\mathrm{t} = 0$ on the left), and that the oscillation at $\mathrm{t} = 28.75$ has four local minima/maxima (as shown in the figure at $\mathrm{t} = 28.75$ on the right), which confirms the above discussed expectation that the assumed velocity dependence of the combustion process would produce an oscillation in the combustor with twice the frequency of the initial disturbance.

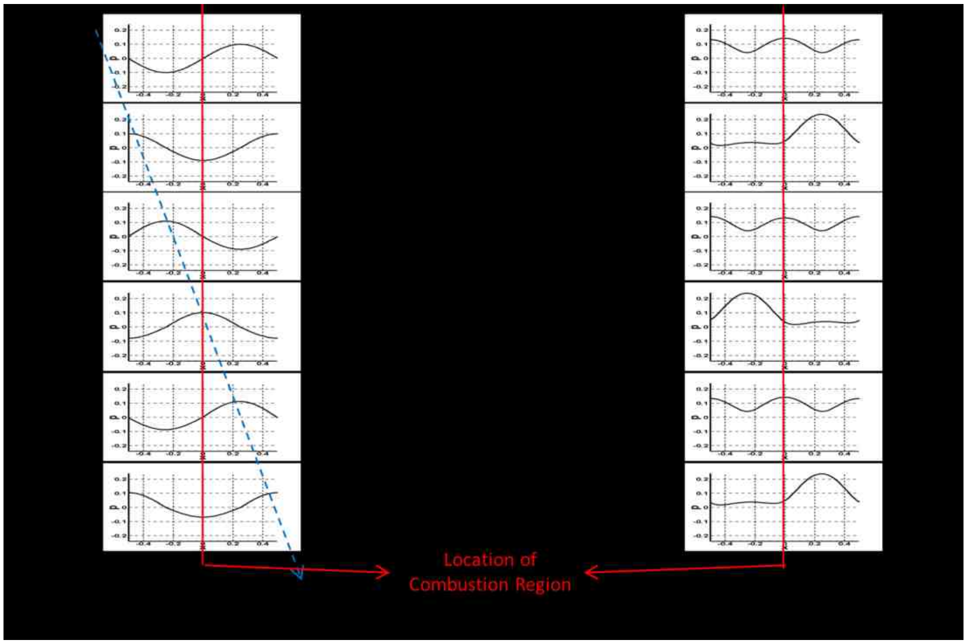

Figure 51. Result of a numerical simulation investigating the effect of the acoustic velocity dependence of the combustion process upon an "initial" travelling wave disturbance in the annular combustor in the absence of a tangential mean flow.

3.3.4.2. Combustor Stability in the Presence of a Tangential Mean Flow

In this section, the results of a study of the effects of the presence of a tangential mean flow component in the annular combustor and a combustion heat release perturbation that depends upon both the tangential mean flow velocity and the acoustic velocity perturbation (see Eq. (3-60)) are presented. This problem was investigated by numerically solving Eqs. (3-28), (3-29), (3-43), (3-44), (3-45), and (3-60).

As one done in the example discussed in Section *3.3.4.1.* above, the parameters describing the amplification of the waves by the pressure dependent component of the combustion driving process and their damping by the exhaust nozzle were chosen so that these two effects nearly cancelled one another and had a negligible effect upon the growth/decay of the combustion oscillations. It was also assumed that the combustion process depends upon the acoustic velocity oscillations in the combustion region and that there is a tangential mean flow moving in the clockwise direction in the annular combustor, as shown in Figure 37 (which also appears as a mean flow moving from left to right near the combustion region shown in Figure 38). It was also assumed that there were no fluctuations in the inlet flow through the injector, and that the following parameters described the investigated problem:

$$\overline{M} = 0.15, \;\; \varepsilon_{\overline{M}} = 0.1 << 1, \;\; k_p = 0.7, \;\; k_v = 1.0, \;\; (\hat{S}_{injector})' = 0 \qquad \textbf{(3-67)}$$

To start the numerical simulation, it was assumed that a standing acoustic wave that was convected by the tangential mean flow was initially (i.e., at $t = 0$) present in the combustor and that the concentrated combustion region was located at the center of the annular combustor, as shown in Figure 38.

The solutions describing the spatial dependence of the acoustic pressures in the combustor at several time steps are shown in Figure 52, where the blue dashed lines indicate the positions of the wave fronts at different times. The figures on the left describe the behavior of the initial disturbance. It shows that the initially “introduced” standing acoustic wave is moving slowly to the right, indicating that the initial disturbance is being convected by the tangential mean flow velocity. The figures on the right show the behavior of the disturbance some time thereafter. They indicate that the wave fronts are propagating to the right at a speed that equals the sum of the speed of sound and the tangential mean flow velocity.

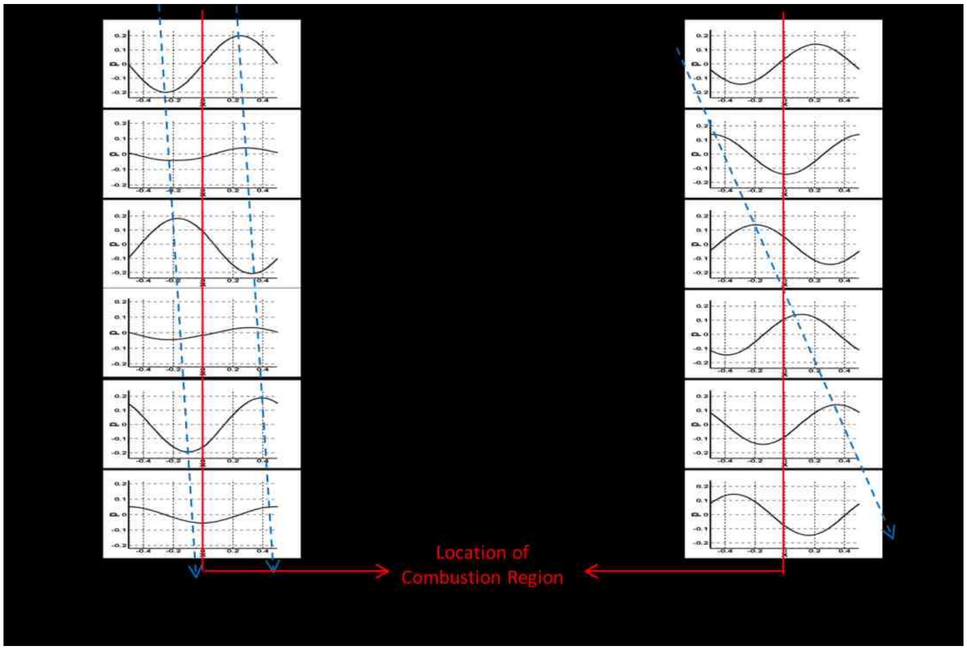

Figure 52. Result of a numerical simulation investigating the effect of a tangential mean flow and the acoustic velocity dependence of the combustion process upon an “initial” standing wave disturbance in the annular combustor.

This solution shows that when a tangential mean flow component is present in the combustor, an initially standing wave disturbance that is being convected by the tangential mean flow gradually transforms itself into a spinning wave that rotates around the annular combustor with a velocity that equals the sum of the mean flow velocity and the speed of sound. Notably, this behavior is consistent with observations made in relatively recent experimental studies [37-39] that showed that the direction of spin of tangential CIs coincided with the direction of the mean tangential flow in the combustor.

As noted earlier, this simulation assumed that the chemical heat release perturbation, $(\hat{\dot{Q}}_{chem})'$, depends upon the acoustic pressure and velocity fluctuations, $\hat{p}'$ and $\hat{v}'$, in the combustion region, as described in Eq. (3-60). It is particularly noteworthy that the expression describing the dependence of this chemical heat release on the tangential mean flow and acoustic velocity, i.e., $(\hat{\dot{Q}}_{chem})' \propto k_v \cdot \left(\left|\hat{\bar{V}} + \hat{v}'\right| - \left|\hat{\bar{V}}\right|\right)$, amplifies and damps the right and the left going waves, respectively, as they pass through the combustion region. For example, when a (positive valued) right going wave, $\hat{f}$, alone arrives at the combustion region, its acoustic velocity is also positive, (i.e., $\hat{v}' = \hat{f}/\gamma$, see Eq. (3-27) for normalized expressions), and the chemical heat release term depending upon the tangential mean flow and acoustic velocity is also positive; i.e., $\left(\hat{\dot{Q}}_{chem}\right)' \propto k_v \cdot \left(\left|\hat{\bar{V}} + \hat{v}'\right| - \left|\hat{\bar{V}}\right|\right) \approx k_v \cdot \hat{f}/\gamma$. On the other hand, when a (positive valued) left going wave, $\hat{g}$ alone arrives at the combustion region, its acoustic velocity is negative (i.e., $\hat{v}' \approx -\hat{g}/\gamma$), resulting in a negative chemical heat release term; i.e., $\left(\hat{\dot{Q}}_{chem}\right)' \propto k_v \cdot \left(\left|\hat{\bar{V}} + \hat{v}'\right| - \left|\hat{\bar{V}}\right|\right) \approx -k_v \cdot \hat{g}/\gamma$. Thus, the presence of a tangential mean flow in the above expression amplifies the wave whose propagation direction is aligned with the mean flow direction and damps the wave that moves in the opposite direction. This dependence produces a travelling wave whose propagation direction is aligned with the direction of the tangential mean flow. This behavior will be discussed in detail later in this section.

Figure 53 describes the time dependence of the magnitudes of the right and left going waves and the acoustic pressure in the annular combustor at location $x = 0.25$ shown on the top of the figure. It shows that the right going wave (the blue curve) that propagated in the direction of the tangential mean flow and the left going wave (the green curve) that propagated in the direction opposite to that of the tangential mean flow were amplified and damped, respectively, by the velocity dependent "part" of the combustion process. These complex, nonlinear, interactions between the initial standing wave disturbance that was initially convected by the tangential mean flow and the combustion process resulted in the gradual transition of the initial standing wave disturbance into a spinning wave CI that propagated in the tangential mean flow direction at a speed that was equal to the sum of the speed of sound and the (tangential) mean flow velocity (after $t \approx 25$).

While the spatial dependence of the acoustic pressures in the combustor at several time steps (shown in Figure 52) and the right and left going waves at one location (shown in the middle of Figure 53) show the gradual transition from the initial standing wave disturbance into a spinning wave CI, the acoustic pressure at a location $x = 0.25$ (the black curve in Figure 53) shows irregularly varying amplitude during this transition.

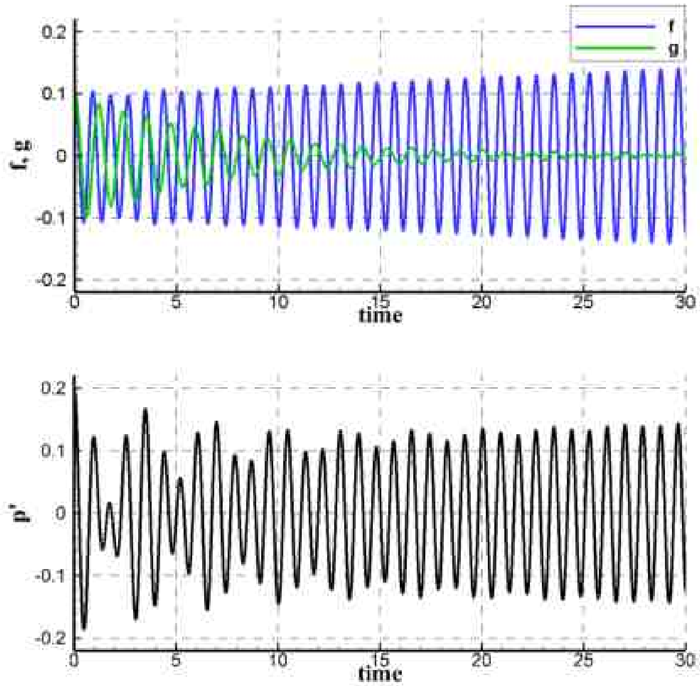

Figure 53. The right going wave, the left going wave, and the acoustic pressure in the annular combustor (at x=0.25, see the figure on the top).

To further elucidate the manner in which a combustion process that depends upon the acoustic velocity and the tangential mean flow velocity causes a transition from an initial standing wave disturbance into a spinning wave CI, it was assumed that the combustor oscillations were only driven by a combustion process heat release that is described by the expression, $(\hat{\hat{Q}}_{chem})' \propto k_v \cdot \left(\left|\hat{\hat{V}} + \hat{v}'\right| - \left|\hat{\hat{V}}\right|\right)$, and that the flows through the injector and exhaust nozzle did not fluctuate.

This problem is described in Figure 54. The top of the figures shows that when a sinusoidal right going wave f_1 arrives at the combustion region, its interaction with the combustion process there generates the outgoing right and left going waves (i.e., f_2, g_1).

Figure 54 also shows the spatial dependence of the acoustic pressure and velocity of the right going wave as it arrive at the combustion region just below the top of the figure. Additionally, the figure includes descriptions of the time dependence of the acoustic waves at the combustion region. It shows that when the magnitude of the acoustic velocity is smaller than the magnitude of the mean flow velocity, the fluctuating flow velocity experienced by the combustion processes (i.e., $\left(\left|\hat{\bar{V}} + \hat{v}'\right| - \left|\hat{\bar{V}}\right|\right)$) is also sinusoidal and “in phase” with the acoustic pressure oscillations of the incoming right going wave, as also shown in Figure 54. Consequently, the driving of the acoustic oscillations provided by the heat release process described by $(\hat{\dot{Q}}_{chem})' \propto k_v \cdot \left(\left|\hat{\bar{V}} + \hat{v}'\right| - \left|\hat{\bar{V}}\right|\right)$) is also sinusoidal and “in phase” with the oscillations of the incoming right going wave f_1. Because of this “in phase” driving by the combustion process, the incident right going wave f_1 is amplified and a larger amplitude, transmitted, right going wave f_2 is generated (i.e., $f_2 > f_1$). This amplified transmitted right going wave f_2 propagates into the “no combustion” region of the closed annular tube (see Figure 37). It returns to the “combustion” region, after one passage through the annular combustor, where it is amplified again by its interaction with the combustion process. Thus, the right going waves (propagating in the tangential mean flow direction) are amplified by the velocity dependent combustion process as they repeatedly move around the annular combustor and enter the combustion region.

The interaction of the combustion process with the right going wave f_1 also generates a reflected left going wave g_1 that propagates into the “no combustion” region of the annular combustor and returns to the combustion region again as an incoming left going wave g_2.

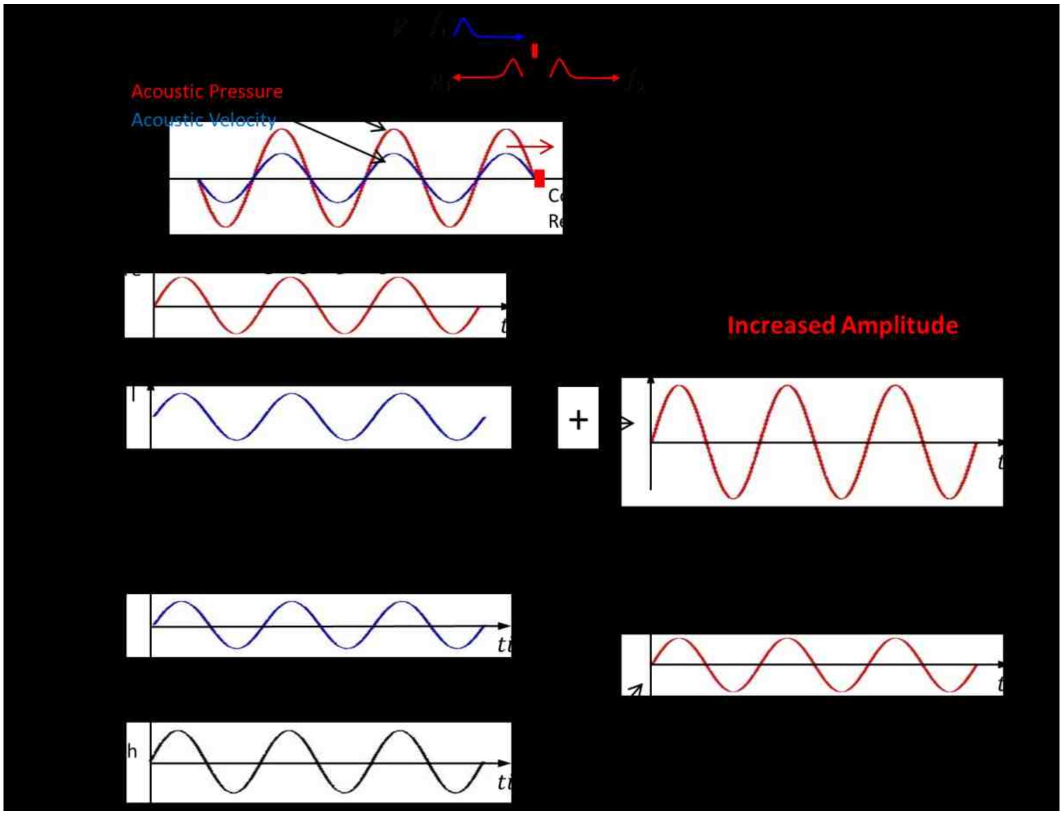

Figure 54. Amplification of the right going waves by the combustion process that depends upon the acoustic velocity and the tangential mean flow velocity.

Its behavior is described in Figure 55, where the top schematic shows that when a sinusoidal left going wave g_2 arrives at the combustion region, its interaction with the combustion process generates outgoing (reflected) right and (transmitted) left going waves, f_2 and g_1, respectively. In this case, the fluctuating flow velocity experienced by the combustion process (i.e., $\left(\left|\hat{\bar{V}} + \hat{v}'\right| - \left|\hat{\bar{V}}\right|\right)$) is sinusoidal but "out of phase" with the acoustic pressure oscillations of the incoming left going wave because the acoustic pressure and velocity of left going waves are "out of phase" with each other as shown in Figure 55. The driving of the acoustic oscillations provided by the combustion process heat release, described by $(\hat{\bar{Q}}_{chem})' \propto k_u \cdot \left(\left|\hat{\bar{V}} + \hat{v}'\right| - \left|\hat{\bar{V}}\right|\right)$, is also "out of phase" with the incoming left going wave g_2. This produces “out of phase” interactions between the pressure oscillations of the incoming wave g_2 and the combustion process heat addition oscillations that damp the incident left going wave g_2, thus generating a lower amplitude transmitted left going wave g_1 (i.e., $g_1 < g_2$). This damped, transmitted, left going wave g_1 propagates into the “no combustion” region of the annular combustor and returns to the combustion region, after propagating once around the annular combustor, where it is damped again by the combustion process. Thus, the left going waves (whose propagation directions are opposite to the direction of the tangential mean flow) are damped at every passage through the combustion region.

In this example, in spite of the fact that no incoming right going wave was initially present in the combustor, a reflected right going wave f_2 was generated by the interaction of the left going incident wave g_2 with the combustion process. Although the reflected right going wave f_2 may be initially small, its subsequent travel around the annular combustor and interactions with the velocity dependent combustion process would amplify this right going wave by the above described process (also described in Figure 54).

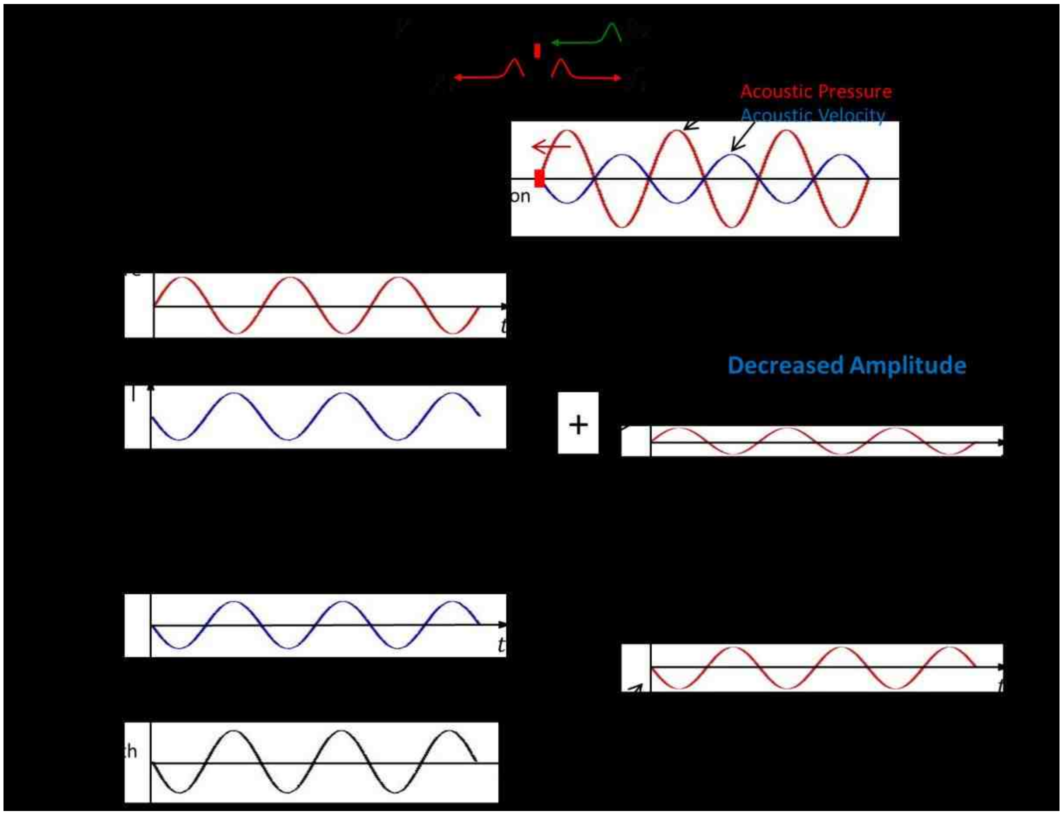

Figure 55. Damping of the left going waves by the combustion process that depends upon the acoustic velocity and the tangential mean flow velocity.

The above discussion indicates that the chosen dependence of the combustion process upon the acoustic velocity and the tangential mean flow velocity causes right going waves to be gradually amplified and left going wave to be gradually damped as they repeatedly propagate around the annular combustor and pass through the combustion region. When an initial standing wave disturbance is introduced into the combustor, its components consist of equal amplitude right and left going waves that propagate in opposite directions around the annular combustor. As they repeatedly interact with the combustion process, the right going wave is gradually amplified and the left going wave is gradually damped until it finally disappears. Thus, an initial standing wave oscillation gradually transforms itself into the travelling wave propagating in the direction of the tangential mean flow. As stated above, this behavior is consistent with the experimental results of recent studies, [37-39]. To the best of this writer's knowledge, this analysis and discussion provide the first known (and plausible) explanation of the causes of this behavior.

3.3.5. Summary of Chapter 3's Results

The main results obtained in this chapter's studies are summarized in the two tables below. Table 1 below summarizes the dependence of the exhaust nozzle and combustion process upon local state variables and the manner in which they affect the oscillations.

Table 1 Effects of the exhaust nozzle and combustion in the developed model

	Exhaust Nozzle		**Combustion Process**	
Dependence	p' in the combustion region	v' in the combustion region	p' in the combustion region	v' in the combustion region
Functional Dependence on State Variables	$\sim p'$	$\sim \bar{V} v'$	$\sim p'$	$\sim \lvert \bar{V} + v' \rvert - \lvert \bar{V} \rvert$
Effects	○ Damps the oscillations ○ Reflects incident waves	○ Selectively Damps waves propagating in $\bar{M}$ direction ○ Reflects incident waves ○ Effects are small	○ Amplifies the oscillations ○ Reflects incident waves	○ Amplifies waves propagating in $\bar{M}$ direction ○ Damps waves propagating in the opposite direction ○ Reflects incident waves
Controlling Parameter	$\varepsilon_{\bar{M}}$	$\varepsilon_{\bar{M}} \bar{M}$ (small)	k_p	k_v

On the other hand, Table 2 below summarizes the dependence of the exhaust nozzle and combustion process upon local state variables and the manner in which they affect CIs in annular combustors.

Table 2 Summary of the Effects of Exhaust Nozzle and Combustion Process on the Behavior of the Combustion Instabilities

	Exhaust Nozzle		**Combustion Process**	
Dependence	p'	v'	p'	v'
No Mean flow ($\bar{M} = 0$)	○ Damps the oscillations ○ Forms a standing wave acoustic field (STDG) ○ Forms a pressure node at the Exhaust Nozzle ○ TRVL* → STDG ○ STDG* → STDG	○ No effect ○ Because $\varepsilon_{\bar{M}}\bar{M} = 0$	○ Amplifies the oscillations ○ Forms a standing wave acoustic field (STDG) ○ The STDG has a pressure anti-node at the Combustion Region ○ TRVL → STDG ○ STDG → STDG	○ Generates higher frequency modes ○ By $\sim\lvert v'\rvert$ term ○ $\sim\lvert\bar{V} + v'\rvert - \lvert\bar{V}\rvert = \sim\lvert v'\rvert$ with $\bar{V} = 0$
With Mean flow (small $\bar{M}$)	○ Damps the oscillations ○ TRVL → decay ○ STDG → decay	○ Effects are small ○ $\varepsilon_{\bar{M}}\bar{M} < \varepsilon_{\bar{M}}$	○ Amplifies the oscillations ○ TRVL → grow ○ STDG → grow	○ Selective Amplification of waves propagating in the $\bar{M}$ direction ○ Selective Damping of waves propagating in the opposite direction ○ Forms a spinning CI moving in the $\bar{M}$ direction (TRVL) ○ STDG → TRVL ○ TRVL→ TRVL

TRVL*: travelling wave acoustic field STDG*: standing wave acoustic field

CHAPTER 4.

ACCOMPLISHMENTS AND RECOMMANDATIONS

The objective of this study was to develop an *active control approach* that allows small-scale rigs to simulate *longitudinal* and *tangential* combustion instabilities (CIs) in full-scale engines. The following tasks were accomplished in this study:

- Developed a *real time, active, acoustic boundary control approach* that enables simulation of acoustic environments within a full-scale engine in a small-scale rig in *real time*.
- Developed and demonstrated a small-scale, cold flow, rig that can simulate *longitudinal (axial)* acoustic oscillations that are encountered in full-scale (i.e., longer) tubes. Specifically, it was shown that the developed, actively controlled, small-scale, rig can simulate *travelling* and *standing acoustic waves* oscillations that are encountered in longer tubes or full-scale engines.
- To allow implementation of the ACS, developed a *real time wave separation algorithm* that determines the properties of the *right and left going waves* in the actively controlled small-scale rig from two acoustic pressure measurements, using the *method of characteristics*.
- Developed a theoretical model that describes the characteristics of *tangential* CIs in an annular combustor when a tangential mean flow is present in the combustor. This model can be used to determine the actively controlled acoustic boundary conditions (BCs) that must be generated in *real time* in a small-scale rig that simulates *tangential* CIs in full-scale engines.

- Utilized the above described model to study the effects of the exhaust nozzle, combustion process, and tangential mean flow component upon the characteristics of *tangential* CIs in an annular combustor using numerical calculations.
- Demonstrated that the *presence* and direction of the mean tangential flow critically affect the characteristics of *tangential* CIs due to the nonlinear dependence of the combustion process upon the acoustic velocity and the tangential mean flow. It has been shown that when a tangential mean flow component is present in the annular combustor, an initially standing wave disturbance gradually transforms itself into a *spinning* wave that rotates around the annular combustor in the direction of the tangential mean flow component. This finding is in agreement with previous experimental observations that have not been explained to date.

The following are a few suggestions for follow up studies that would improve the capabilities for simulating full-scale engines CIs in small-scale rigs:

- As discussed in Chapter 2, modify the developed actively controlled small-scale rig to be able to simulate any section of the wavelength of the unstable oscillations in the full-scale engine. This could be done by replacing the driving actuator (i.e., speaker) on the left side of the rig with a second ACS and a control actuator. This would allow an actively controlled, small-scale, rig to investigate the processes taking place at any location within an unstable, full-scale, engine.
- Improve the developed *real time wave separation module* and *simulation module* by providing them with capabilities for accounting for the effects of the temperature dependence of the speed of sound and the presence of an axial mean flow component.

- Modify the developed, cold flow, small-scale, rig to allow the presence of a mean, axial, flow component whose Mach number would be equal to that of the mean flow in full-scale engines. A schematic of the proposed setup is shown in Figure 12 below. It shows the "full-scale" engine on top and the proposed "small-scale" rig on the bottom. The schematic of the small-scale rig shows that its driving and actively controlled actuators (speakers) will be most likely installed on the side walls of the rig to allow the mean flow to enter and leave the rig.

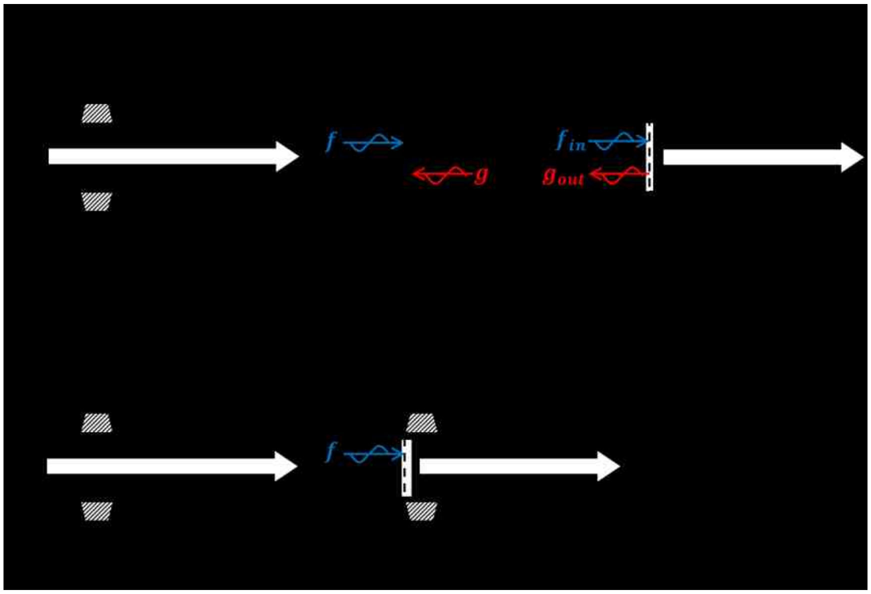

Figure 56. Schematics of the "full-scale" engine having a real exhaust nozzle to allow the presence of an axial mean flow (top) and the actively controlled "small-scale" rig (bottom).

- Investigate the applications into real combustion systems; e.g., high temperature and temperature variations induced by the combustion process, the mean flow from the fuel injector to the exhaust nozzle, the acoustic waves propagations in three-dimensional domain of the combustor, and the power of the actuator to excite and control the large amplitude oscillations in the combustor need to be considered.

APPENDIX A.

DERIVATION OF A MODEL DESCRIBING TANGENTIAL COMBUSTION INSTABILITIES IN AN ANNULAR COMBUSTOR

A.1. A Non-Homogeneous Wave Equation with Mean Flow

As discussed in CHAPTER 3, in order to develop the model of the combustion instabilities (especially, tangential or spinning CIs) in an annular combustor (shown in Figure 34), the following physical processes need to be considered:

i. The acoustic waves propagations and reflections in the “no combustion” regions in the annular combustor with presence of mean flow; see Figure 34.

ii. The interactions between the combustion processes (and the injectors and exhaust nozzles flows) and the acoustic waves at the “combustion” regions with presence of mean flow; see Figure 34 and Figure 35 in CHAPTER 3.

For the applicability to the real time active control system (ACS), the model must be simple to achieve short calculation time, yet capable of describing the physics controlling the behavior of the CI (i.e., the physical processes *i.* and *ii.* discussed above). To account these physical processes, the development of the model was started from the general conservation equations for reacting flow. These conservation equations were reduced by a first order small perturbation approximation, and the resulted small-perturbation equations were combined into a non-homogeneous wave equation with mean flow having acoustic sources by the chemical reaction and the in/out flows through the injector and exhaust nozzle. The solutions of this non-homogeneous wave equation were obtained for the "no combustion" regions and the "combustion" regions with further approximations (e.g., acoustically compact "combustion" regions, quasi-steady exhaust nozzles, subsonic tangential mean flow Mach number, etc.). These solutions composes the model of tangential or spinning CIs in the annular combustor, and will be numerically calculated separated for the "combustion" regions and the "no combustion" regions and matched at the interfaces between the regions, when applying to the real time ACS.

Among the procedures of the development of the model, this section describes the derivation of the non-homogeneous wave equation with mean flow from the general conservation equations for reacting flow.

A.1.1. General Conservation Equations for Mass, Momentum, Energy, and Species

As discussed in CHAPTER 3, we start the development of the model by considering the following, general, three-dimensional, integral form of the conservation equations for a reacting flow [30, 31]:

Mass:

$$0 = \frac{\partial}{\partial t}\iiint_{C.V.} \rho \, dV + \iint_{C.S.} \rho \vec{V} \circ \hat{n} \, dS \tag{3-1}$$

Momentum:

$$\sum \vec{F}_{external} = \frac{\partial}{\partial t}\iiint_{C.V.} \rho \vec{V} \, dV + \iint_{C.S.} \left(\rho \vec{V}\right)\vec{V} \circ \hat{n} \, dS + \iint_{C.S.} p \, \hat{n} \, dS \tag{3-2}$$

where, $\sum \vec{F}_{external}$ is the sum of the external forces acting on the control volume.

Energy:

$$\dot{Q}_{external} - \dot{W}_s = \frac{\partial}{\partial t}\iiint_{C.V.} e\,\rho\,dV + \iint_{C.S.} e\,\rho\,\vec{V}\circ\hat{n}\,dS + \iint_{C.S.} p\,\vec{V}\circ\hat{n}\,dS \qquad \textbf{(3-3)}$$

where, $\dot{Q}_{external}$ is the external heat added to the control volume; $\dot{W}_s$ is the shaft work; $e = u + p.e. + k.e.$ where u, $p.e.$, and $k.e.$ are the internal energy per unit mass, the potential energy per unit mass, and the kinetic energy per unit mass, respectively.

Species:

$$\dot{M}_l = \frac{\partial}{\partial t}\iiint_{C.V.} Y_l\,\rho\,dV + \iint_{C.S.} Y_l\,\rho\,\vec{v}_l\circ\hat{n}\,dS \qquad \textbf{(3-4)}$$

where, $\dot{M}_l$ is the mass production rate of species l in the control volume; i.e., $\dot{M}_l = \iiint_{C.V.} \dot{m}_l'''dV = \iiint_{C.V.} MW_l\,\dot{\omega}_l\,dV$

where MW_l is the molecular weight of species l; $\dot{\omega}_l$ is the molar production rate of species l per unit volume. Additionally, $\vec{v}_l = \vec{V} + \vec{V}_{l,diffusion}$ is the velocity of species l and $\vec{V}$ and $\vec{V}_{l,diffusion}$ are the mass averaged flow velocity and the diffusion velocity of species l, respectively.

A.1.2. Small Perturbation Approximations up to First-Order

Next, we derive the mean and small-perturbation conservation equations. We assume that all the properties can be expressed as a sum of a steady state property and a small-perturbation; e.g., $p = \bar{p} + p'$, $\rho = \bar{\rho} + \rho'$, … where $\frac{p'}{\bar{p}}, \frac{\rho'}{\bar{\rho}}, \ldots \ll 1$. The assumed expressions for the properties are then substituted into the above conservation equations, Eqs. (3-1), (3-2), (3-3), and (3-4). Using the steady state conservation equations (i.e., Eqs. (A-1), (A-2), (A-3), and (A-4) shown below), the small-perturbation equations (i.e., Eqs. (A-5), (A-6), (A-7), and (A-8) shown below) are separated out.

Steady state conservation equations or Mean equations:

Mass:
$$0=\frac{\partial}{\partial t}\iiint_{C.V.}\overline{\rho}\,dV+\iint_{C.S.}\overline{\rho}\,\overline{\vec{V}}\circ\hat{n}\,dS \tag{A-1}$$

Mom.:
$$\overline{\left(\sum\vec{F}_{external}\right)}=\frac{\partial}{\partial t}\iiint_{C.V.}\overline{\rho}\,\overline{\vec{V}}\,dV+\iint_{C.S.}\left(\overline{\rho}\,\overline{\vec{V}}\right)\overline{\vec{V}}\circ\hat{n}\,dS+\iint_{C.S.}\overline{p}\,\hat{n}\,dS \tag{A-2}$$

Energy:
$$\overline{(\dot{Q}_{external})}=\frac{\partial}{\partial t}\iiint_{C.V.}\overline{h}_t\,\overline{\rho}\,dV-\frac{\partial}{\partial t}\iiint_{C.V.}\overline{p}\,dV+\iint_{C.S.}\left(\overline{h}_t\,\overline{\rho}\right)\overline{\vec{V}}\circ\hat{n}\,dS \tag{A-3}$$

Species:
$$\overline{(\dot{M}_l)}=\frac{\partial}{\partial t}\iiint_{C.V.}\overline{Y}_l\,\overline{\rho}\,dV+\iint_{C.S.}\overline{Y}_l\,\overline{\rho}\,\overline{\vec{v}}_l\circ\hat{n}\,dS \tag{A-4}$$

Small-perturbation conservation equations:

Mass:
$$0=\frac{\partial}{\partial t}\iiint_{C.V.}\rho'\,dV+\iint_{C.S.}\overline{\rho}\,\vec{V}'\circ\hat{n}\,dS+\iint_{C.S.}\rho'\,\overline{\vec{V}}\circ\hat{n}\,dS \tag{A-5}$$

Mom.:
$$\begin{aligned}\left(\sum\vec{F}_{external}\right)'=&\frac{\partial}{\partial t}\iiint_{C.V.}\overline{\rho}\,\vec{V}'\,dV+\iint_{C.S.}p'\,\hat{n}\,dS\\&+\frac{\partial}{\partial t}\iiint_{C.V.}\rho'\,\overline{\vec{V}}\,dV\\&+\iint_{C.S.}\left(\overline{\rho}\,\vec{V}'+\rho'\,\overline{\vec{V}}\right)\overline{\vec{V}}\circ\hat{n}\,dS+\iint_{C.S.}\left(\overline{\rho}\,\overline{\vec{V}}\right)\vec{V}'\circ\hat{n}\,dS\end{aligned} \tag{A-6}$$

Energy:
$$\begin{aligned}(\dot{Q}_{external})'=&\frac{\partial}{\partial t}\iiint_{C.V.}\left(\overline{h}_t\,\rho'+h_t'\,\overline{\rho}\right)dV-\frac{\partial}{\partial t}\iiint_{C.V.}p'\,dV\\&+\iint_{C.S.}\left(\overline{h}_t\,\overline{\rho}\right)\vec{V}'\circ\hat{n}\,dS+\iint_{C.S.}\left(\overline{h}_t\,\rho'+h_t'\,\overline{\rho}\right)\overline{\vec{V}}\circ\hat{n}\,dS\end{aligned} \tag{A-7}$$

Species:
$$\begin{aligned}(\dot{M}_l)'=&\frac{\partial}{\partial t}\iiint_{C.V.}\left(Y_l'\,\overline{\rho}+\overline{Y}_l\,\rho'\right)dV\\&+\iint_{C.S.}\overline{Y}_l\,\overline{\rho}\,\vec{v}_l'\circ\hat{n}\,dS+\iint_{C.S.}\left(Y_l'\,\overline{\rho}+\overline{Y}_l\,\rho'\right)\overline{\vec{v}}_l\circ\hat{n}\,dS\end{aligned} \tag{A-8}$$

The total enthalpy (and formation and sensible enthalpy) per mass and kinetic energy per mass terms also need to be considered.

$$h_t = h + k.e. \tag{A-9}$$

$$h = h_f + h_s \tag{A-10}$$

$$k.e. = \frac{1}{2}\vec{V} \circ \vec{V} \tag{A-11}$$

Equation (A-9) describes the total enthalpy when potential energy per mass, $p.e.$, is negligible. With applying the small-perturbation approximation to the Eqs. (A-9), (A-10), and (A-11) as discussed above, the following mean (or steady state) and small-perturbation equations are obtained.

<u>Mean total enthalpy, enthalpy (of the mixture), and kinetic energy per mass:</u>

$$\bar{h}_t = \bar{h} + \overline{k.e.} \tag{A-12}$$

$$\bar{h} = \bar{h}_f + \bar{h}_s \tag{A-13}$$

$$\overline{k.e.} = \frac{1}{2}\bar{\vec{V}} \circ \bar{\vec{V}} \tag{A-14}$$

<u>Small-perturbation total enthalpy, enthalpy (of the mixture), and kinetic energy per mass:</u>

$$h_t' = h' + k.e.' \tag{A-15}$$

$$h' = h_f' + h_s' \tag{A-16}$$

$$k.e.' = \bar{\vec{V}} \circ \vec{V}' \tag{A-17}$$

For Eqs. (A-13) and (A-16), the mean and small-perturbation formation and sensible enthalpies for the mixture, $\bar{h}_f$, h'_f, $\bar{h}_s$, and h'_s, also need to be considered. The formation enthalpy and the sensible enthalpy of the mixtures can be expressed in terms of the specific heat, $c_{p,l}$, and the mixture ratio (mass fraction), Y_l, of the species l, as following.

$$h_f = \sum_l h_{f,l} \cdot Y_l \tag{A-18}$$

$$h_s = \sum_l \int_{T_{ref}}^{T} c_{p,l} \cdot Y_l \, dT \tag{A-19}$$

Equations (A-18) and (A-19) are expressed as a sum of (mean) steady state properties and small-perturbation properties with neglecting higher order terms.

$$\bar{h}_f + h'_f = \sum_l h_{f,l} \cdot \bar{Y}_l + \sum_l h_{f,l} \cdot Y'_l \tag{A-20}$$

$$\bar{h}_s + h'_s = \sum_l \int_{T_{ref}}^{\bar{T}} c_{p,l} \cdot \bar{Y}_l \, dT + \sum_l \int_{\bar{T}}^{\bar{T}+T'} c_{p,l}(\bar{T}) \cdot \bar{Y}_l \, dT + \sum_l \int_{T_{ref}}^{\bar{T}} c_{p,l} \cdot Y'_l dT \tag{A-21}$$

Where, the higher order term, e.g., $\sum_l \int_{\bar{T}}^{\bar{T}+T'} c_{p,l}(T) \cdot \bar{Y}_l \, dT$, is neglected. The third term in Eq. (A-21), $\sum_l \int_{T_{ref}}^{\bar{T}} c_{p,l} \cdot Y'_l dT$, describes the small-perturbation sensible enthalpy of the mixture by the chemical composition perturbation. Even though this term is a first order term, but its magnitude is small comparing the other terms. In this study, the specific heat, $c_{p,l}$, assumed to have similar values for all the species, as shown below; cf. this assumption is similar to the Zeldovich's assumption [30, 31].

$$\begin{aligned} &c_{p,l} \cong c_{p,m} \text{ for the species } l \text{ and } m,\ l \neq m \\ &c_{p,l} \cong c_{p,mix} \equiv c_p \end{aligned} \tag{A-22}$$

Using the above assumption and the definition of the mixture ratio (mass fraction), the third term in Eq. (A-21) is neglected as shown below.

$$\sum_l \int_{T_{ref}}^{\bar{T}} c_{p,l} \cdot Y'_l dT \cong \int_{T_{ref}}^{\bar{T}} c_p dT \cdot \sum_l Y'_l = 0 \qquad \because \sum_l Y'_l = 0 \tag{A-23}$$

Matching the mean and small-perturbation terms in Eqs. (A-20) and (A-21), the mean and small-perturbation formation enthalpies and sensible enthalpies for the mixture are obtained as following.

Mean formation enthalpy and sensible enthalpy for the mixture:

$$\bar{h}_f = \sum_l h_{f,l} \cdot \bar{Y}_l \tag{A-24}$$

$$\begin{aligned} \bar{h}_s &= \sum_l \int_{T_{ref}}^{\bar{T}} c_{p,l} \cdot \bar{Y}_l \, dT \\ &\cong \sum_l \int_{T_{ref}}^{\bar{T}} c_p \cdot \bar{Y}_l \, dT \approx \int_{T_{ref}}^{\bar{T}} c_p \, dT \end{aligned} \tag{A-25}$$

Small-perturbation formation enthalpy and sensible enthalpy for the mixture:

$$h'_f = \sum_l h_{f,l} \cdot Y'_l \tag{A-26}$$

$$\begin{aligned} h'_s &= \sum_l \int_{\bar{T}}^{\bar{T}+T'} c_{p,l}(\bar{T}) \cdot \bar{Y}_l \, dT \\ &\cong \sum_l \int_{\bar{T}}^{\bar{T}+T'} c_p(\bar{T}) \cdot \bar{Y}_l \, dT \approx c_p(\bar{T})T' \equiv c_p T' \end{aligned} \tag{A-27}$$

In this study, thermally perfect gas assumption was used.

$$p = \rho R T \tag{A-28}$$

Substituting $p = \bar{p} + p'$, $\rho = \bar{\rho} + \rho'$, and $T = \bar{T} + T'$ into Eq. (A-28) and neglecting higher order terms by $\frac{p'}{\bar{p}}, \frac{\rho'}{\bar{\rho}}, \frac{T'}{\bar{T}} \ldots \ll 1$, the following mean and small-perturbation equation of state are obtained.

Mean state equation of state:

$$\bar{p} = \bar{\rho} R \bar{T} \tag{A-29}$$

Small-perturbation equation of state:

$$T' = \frac{p'}{\bar{\rho} R} - \frac{\bar{T}}{\bar{\rho} R} \rho' \tag{A-30}$$

A.1.3. Separation of the Heat Release by Chemical Reaction

The mean (or steady state) energy equation, Eq. (A-3), and small-perturbation energy equations, Eq. (A-7), account the chemical reaction by combustion processes. For example, in the equations, the total enthalpy terms, $\overline{h_t}$ and h'_t, contain the formation enthalpy terms, $\overline{h_f}$ and h'_f, these terms are affected by the chemical compositions change due to chemical reactions; see Eqs. (A-24) and (A-26). However, the effects (e.g., the chemical compositions change and the heat release) by the chemical reactions are not expressed explicitly, and the derivation of a non-homogeneous wave equation is not simple.

In order to express the thermal and kinetic behaviors (involved by the sensible enthalpies and the kinetic energy terms) on the LHS (non-source side) and the chemical reaction phenomena (involved by the formation enthalpies and chemical compositions) on the RHS (source side) in the non-homogeneous wave equation, the terms related to the chemical reactions need to be separated. In order to separate the terms affected by the chemical reaction, the mean (or steady state) species equation, Eq. (A-4), and the small-perturbation species equation, Eq. (A-8), can be used. By multiplying the formation enthalpy of the species l, $h_{f,l}$, to the mean and small-perturbation species equations, Eqs. (A-4) and (A-8), and summing these equations for all the species using the below relationship (i.e., Eq. (A-31) below), the following equations are obtained; see Eqs. (A-32) and (A-34) shown below.

$$\sum_l Y_l = 1\,,\ \ \sum_l \bar{Y}_l = 1\,,\ \ \sum_l Y_l' = 0 \tag{A-31}$$

$$\sum_l h_{f,l}\,\overline{(\dot{M}_l)} = \frac{\partial}{\partial t}\iiint_{C.V.} \bar{\rho}\,\bar{h}_f\,dV + \iint_{C.S.} \bar{\rho}\,\bar{h}_f\,\bar{\vec{V}} \circ \hat{n}\,dS + \overline{(h_{flxdiff})} \tag{A-32}$$

$$\text{where, } \overline{(h_{flxdiff})} = \iint_{C.S.} \bar{\rho}\left(\sum_l h_{f,l}\,\bar{Y}_l\,\overline{\vec{V}_{l,diffusion}}\right) \circ \hat{n}\,dS \approx 0 \tag{A-33}$$

$$\begin{aligned}\sum_l h_{f,l}(\dot{M}_l)' = {} & \frac{\partial}{\partial t}\iiint_{C.V.}\left(h_f'\bar{\rho} + \bar{h}_f\rho'\right)dV \\ & + \iint_{C.S.} \bar{\rho}\,\bar{h}_f\vec{V}' \circ \hat{n}\,dS + \iint_{C.S.} \bar{\rho}\,h_f'\bar{\vec{V}} \circ \hat{n}\,dS \\ & + \iint_{C.S.} \rho'\,\bar{h}_f\bar{\vec{V}} \circ \hat{n}\,dS + (h_{flxdiff})'\end{aligned} \tag{A-34}$$

$$\text{where, }\quad \begin{aligned}(h_{flxdiff})' = {} & \iint_{C.S.} \bar{\rho}\left(\sum_l h_{f,l}\,\bar{Y}_l\,\vec{V}'_{l,diffusion}\right) \circ \hat{n}\,dS \\ & + \iint_{C.S.} \bar{\rho}\left(\sum_l h_{f,l}\,Y_l'\overline{\vec{V}_{l,diffusion}}\right) \circ \hat{n}\,dS \\ & + \iint_{C.S.} \rho'\left(\sum_l h_{f,l}\,\bar{Y}_l\,\overline{\vec{V}_{l,diffusion}}\right) \circ \hat{n}\,dS \approx 0\end{aligned} \tag{A-35}$$

Where, in this study, it is assumed that diffusion velocities, $\bar{\vec{V}}_{l,diffusion}$ and $\vec{V}'_{l,diffusion}$ are negligible as in Eq. (3-4) or that the diffusion related terms, $\overline{(h_{flxdiff})}$ and $(h_{flxdiff})'$, in Eqs. (A-33) and (A-35) are negligible.

The above equations have similar forms with the mean and small-perturbation energy equations; compare Eq. (A-32) with the mean energy equation (i.e., Eq. (A-3)), and compare Eq. (A-34) with the small-perturbation energy equation (i.e., Eq. (A-7)). By subtracting Eq. (A-32) from Eq. (A-3), the following equation is obtained.

Mean (steady state) energy equation with heat release by chemical reaction:

$$\text{Energy:}\quad \overline{(\dot{Q}_{external})} - \sum_{l} h_{f,l}\overline{(\dot{M}_{l})} + \overline{(h_{flxdiff})}$$

$$= \frac{\partial}{\partial t}\iiint_{C.V.} \bar{\rho}\left(\bar{h}_s + \overline{k.e.}\right)dV - \frac{\partial}{\partial t}\iiint_{C.V.} \bar{p}\; dV + \iint_{C.S.} \bar{\rho}\left(\bar{h}_s + \overline{k.e.}\right)\bar{\vec{V}} \circ \hat{n}\; dS \qquad \textbf{(A-36)}$$

where, $\overline{(h_{flxdiff})} \approx 0$

Also, subtracting Eq. (A-34) from Eq. (A-7) results in the following expression.

Small-perturbation energy equation with heat release by chemical reaction:

$$\text{Energy:}\quad (\dot{Q}_{external})' - \sum_{l} h_{f,l}(\dot{M}_{l})' + (h_{flxdiff})'$$

$$= \frac{\partial}{\partial t}\iiint_{C.V.} \left\{\left(\bar{h}_s + \overline{k.e.}\right)\rho' + \left(h_s' + k.e.'\right)\bar{\rho}\right\}dV - \frac{\partial}{\partial t}\iiint_{C.V.} p'\; dV \qquad \textbf{(A-37)}$$

$$+ \iint_{C.S.} \bar{\rho}\left(\bar{h}_s + \overline{k.e.}\right)\vec{V}' \circ \hat{n}\; dS + \iint_{C.S.} \left\{\left(\bar{h}_s + \overline{k.e.}\right)\rho' + \left(h_s' + k.e.'\right)\bar{\rho}\right\}\bar{\vec{V}} \circ \hat{n}\; dS$$

where, $(h_{flxdiff})' \approx 0$

In Eq. (A-36), the mean (or steady state) heat release by the chemical composition change is shown as $-\sum_l h_{f,l}\overline{(\dot{M}_l)}$, and in Eq. (A-37), the small-perturbation heat release by the chemical composition change is shown as $-\sum_l h_{f,l}(\dot{M}_l)'$. As shown in Eqs. (A-36) and (A-37), these terms affected by chemical reactions are separated and explicitly written on the source side of the equations; i.e., in these expressions, the LHSs. Notably, Eqs. (A-36) and (A-37) also have similar forms of the mean and small-perturbation energy equations, Eqs. (A-3) and (A-7), respectively.

A.1.4. Separation of Acoustic Motions and In/Out Flows through Injectors and Exhaust Nozzles

The control volume of combustion region consists of 4 control surfaces; see Figure 35 in CHAPTER 3. Through the control surfaces s1 and s2 (oriented in $\hat{x}_1$ direction), the acoustic waves interact with the combustion processes. Through the control surfaces s3 and s4 (oriented in $\hat{x}_2$ direction), i.e., the injector (s3) and the exhaust nozzle (s4), the fuel/oxidizer mixture is introduced and the product gas is discharged. The terms describing the in/out flows through the inlet (injector) and outlet (exhaust nozzle) can be separated and expressed as source terms of the conservation equations; see the mean and small-perturbation conservation equations of mass (Eqs. (A-1) and (A-5)), momentum (Eqs. (A-2) and (A-6)), and energy (Eqs. (A-36) and (A-37)).

Also, as shown in Figure 35, the acoustic motions occur in $\hat{x}_1$ direction, and the acoustic velocity and tangential mean flow are in $\hat{x}_1$ direction. On the other hand, the in/out flows through the injector and exhaust nozzle are in $\hat{x}_2$ direction and do not transport the $\hat{x}_1$ directional momentum. Thus, the mean (or steady state) momentum equation, Eq. (A-2), and the small-perturbation momentum equation, Eq. (A-6), can be written separately as the $\hat{x}_1$ component mean and small-perturbation momentum equations describing acoustic motions and the $\hat{x}_2$ component momentum equations describing the injector and exhaust nozzle flows.

By applying the expressions of the medium properties (i.e., the mean (steady state) properties describing the acoustic motions) and the expressions of the mean in/out flows through the injector and exhaust nozzle, the mean (steady state) conservation equations for mass (Eq. (A-1)), momentum (Eq. (A-2)), and energy (Eq. (A-36) with separation of the heat release by the chemical reaction) are manipulated as following.

<u>Mean (steady state) conservation equations with separation of acoustics and sources:</u>

Mass:

$$\overline{\dot{M}}_{nozzle} - \overline{\dot{M}}_{injector} = 0 \tag{A-38}$$

where,
$$\begin{aligned} \overline{\dot{M}}_{injector} &= -\iint_{C.S.,s3} \bar{\rho}\,\overline{\vec{V}} \circ \hat{n}\, dS \\ \overline{\dot{M}}_{nozzle} &= \iint_{C.S.,s4} \bar{\rho}\,\overline{\vec{V}} \circ \hat{n}\, dS \end{aligned} \tag{A-39}$$

Momentum in $\hat{x}_1$ direction (or tangential direction):

$$\overline{\left(\sum \vec{F}_{external,\hat{x}_1}\right)} = \iint_{C.S.,s1\&s2} \bar{p}\,\hat{n}\, dS \tag{A-40}$$

where, $\overline{\left(\sum \vec{F}_{external,\hat{x}_1}\right)} = \vec{0}$, i.e., no support force in $\hat{x}_1$ direction

Energy:

$$\overline{(\dot{Q}_{external})} - \sum_l h_{f,l}\overline{(\dot{M}_l)} = \overline{(\dot{H}_s + \dot{K}.E.)}_{nozzle} - \overline{(\dot{H}_s + \dot{K}.E.)}_{injector} \tag{A-41}$$

where, $\overline{(\dot{Q}_{external})} = 0$, i.e., adiabatic condition

$$\overline{(\dot{Q}_{chem})} \equiv -\sum_l h_{f,l}\overline{(\dot{M}_l)} \tag{A-42}$$

$$\begin{aligned} \overline{(\dot{H}_s + \dot{K}.E.)}_{injector} &= -\iint_{C.S.,s3} \bar{\rho}\left(\bar{h}_s + \overline{k.e.}\right)\overline{\vec{V}} \circ \hat{n}\, dS \\ \overline{(\dot{H}_s + \dot{K}.E.)}_{nozzle} &= \iint_{C.S.,s4} \bar{\rho}\left(\bar{h}_s + \overline{k.e.}\right)\overline{\vec{V}} \circ \hat{n}\, dS \end{aligned} \tag{A-43}$$

In the above equations, the time derivative (i.e., $\frac{\partial}{\partial t}(\cdot)$) terms are disappeared because of applying mean (steady state) properties. Since the medium properties (mean properties) in the control surface s1 and s2 are same, the mass, momentum and energy fluxes across the control surfaces s1 and s2 are cancelled each other and disappeared in the equations. As shown in the above equations, the steady state of the system is maintained by the mean (steady state) in/out flows through the injector and exhaust nozzle. Equation (A-38) describes that the mass flux in through the injector and the mass flux out through the exhaust nozzle are balanced. Equation (A-40) describes that there is no support force in $\hat{x}_1$ direction and the mean (steady state) pressures at the control surfaces s1 and s2 are the same. Equation (A-41) describes the energy conservation at the steady state; i.e., the total enthalpy flux flows in to the combustion region through the injector, it is consumed by the chemical reactions, and the remaining total enthalpy flux flows out from the combustion region through the exhaust nozzle. The mean (steady state) heat release by the mean chemical composition change is defined by the term, $(\overline{\dot{Q}_{chem}})$, shortly the mean (or steady state) chemical heat release; see Eq. (A-42).

Also, by separating the acoustic motions and the injector and exhaust nozzle flows in the small-perturbation conservation equations for mass (Eq. (A-5)), momentum (Eq. (A-6)), and energy (Eq. (A-37) with separation of the heat release by the chemical reaction), the following equations are obtained.

Small-perturbation conservation equations with separation of acoustics and sources:

Mass:

$$\begin{aligned}&\frac{\partial}{\partial t}\iiint_{C.V.}\rho'\,dV+\iint_{C.S.}\bar{\rho}\,\vec{V}'\circ\hat{n}\,dS+\iint_{C.S.}\rho'\,\overline{\vec{V}}\circ\hat{n}\,dS\\&=\dot{M}'_{injector}-\dot{M}'_{nozzle}\equiv\tilde{S}_{mass}\end{aligned}\qquad\textbf{(A-44)}$$

where, $\dot{M}'_{injector}=-\iint_{C.S.,s3}\bar{\rho}\,\vec{V}'\circ\hat{n}\,dS-\iint_{C.S.,s3}\rho'\,\overline{\vec{V}}\circ\hat{n}\,dS$

$$\dot{M}'_{nozzle}=\iint_{C.S.,s3}\bar{\rho}\,\vec{V}'\circ\hat{n}\,dS+\iint_{C.S.,s3}\rho'\,\overline{\vec{V}}\circ\hat{n}\,dS\qquad\textbf{(A-45)}$$

Momentum in $\hat{x}_1$ direction (i.e., tangential direction):

$$\begin{aligned}&\frac{\partial}{\partial t}\iiint_{C.V.}\bar{\rho}\,\vec{V}'\,dV+\iint_{C.S.}p'\,\hat{n}\,dS+\frac{\partial}{\partial t}\iiint_{C.V.}\rho'\,\overline{\vec{V}}\,dV\\&\qquad+\iint_{C.S.}\left(\bar{\rho}\,\vec{V}'+\rho'\,\overline{\vec{V}}\right)\overline{\vec{V}}\circ\hat{n}\,dS+\iint_{C.S.}\left(\bar{\rho}\,\overline{\vec{V}}\right)\vec{V}'\circ\hat{n}\,dS\\&=\left(\sum\vec{F}_{external,\hat{x}_1}\right)'\equiv\tilde{S}_{force,\hat{x}_1}\end{aligned}\qquad\textbf{(A-46)}$$

where, $\left(\sum\vec{F}_{external,\hat{x}_1}\right)'=\vec{0}$, i.e., no support force in $\hat{x}_1$ direction

Energy:

$$\begin{aligned}&\frac{\partial}{\partial t}\iiint_{C.V.}\left\{\left(\bar{h}_s+\overline{k.e.}\right)\rho'+\left(h_s'+k.e.'\right)\bar{\rho}\right\}dV-\frac{\partial}{\partial t}\iiint_{C.V.}p'\,dV\\&\qquad+\iint_{C.S.}\bar{\rho}\left(\bar{h}_s+\overline{k.e.}\right)\vec{V}'\circ\hat{n}\,dS\\&\qquad+\iint_{C.S.}\left\{\left(\bar{h}_s+\overline{k.e.}\right)\rho'+\left(h_s'+k.e.'\right)\bar{\rho}\right\}\overline{\vec{V}}\circ\hat{n}\,dS\\&=(\dot{Q}_{external})'+\left(-\sum_{l}h_{f,l}(\dot{M}_l)'\right)+\left\{(\dot{H}_s+\dot{K}.E.)'_{injector}-(\dot{H}_s+\dot{K}.E.)'_{nozzle}\right\}\\&\equiv\tilde{S}_{energy}\end{aligned}\qquad\textbf{(A-47)}$$

where, $(\dot{Q}_{external})'=0$, i.e., adiabatic condition

$$(\dot{Q}_{chem})'\equiv-\sum_{l}h_{f,l}(\dot{M}_l)'\qquad\textbf{(A-48)}$$

$$
\begin{aligned}
(\dot{H}_s + \dot{K}.E.)'_{injector} &= -\iint_{C.S.,s3} \overline{\rho}\left(\overline{h_s} + \overline{k.e.}\right)\vec{V}' \circ \hat{n}\, dS \\
&\quad - \iint_{C.S.,s3} \left\{\left(\overline{h_s} + \overline{k.e.}\right)\rho' + \left(h_s' + k.e.'\right)\overline{\rho}\right\}\overline{\vec{V}} \circ \hat{n}\, dS \\
(\dot{H}_s + \dot{K}.E.)'_{nozzle} &= \iint_{C.S.,s4} \overline{\rho}\left(\overline{h_s} + \overline{k.e.}\right)\vec{V}' \circ \hat{n}\, dS \\
&\quad + \iint_{C.S.,s4} \left\{\left(\overline{h_s} + \overline{k.e.}\right)\rho' + \left(h_s' + k.e.'\right)\overline{\rho}\right\}\overline{\vec{V}} \circ \hat{n}\, dS
\end{aligned}
\tag{A-49}
$$

Where, for simplicity, the control surface $C.S.$ in the integrals on the LHS of the Eqs. (A-44), (A-46), and (A-47) denotes the control surface s1 and s2 (see Figure 35). As shown in the above equations, the terms describing the acoustic motions are on the LHS, and the source terms by the combustion processes and the in/out flows through the injector and exhaust nozzle are on the RHS. The heat release perturbation by the chemical composition change is defined by the term, $(\dot{Q}_{chem})'$, shortly the small-perturbation chemical heat release; see Eq. (A-48).

Similarly, by applying the expressions of the mean in/out flows through the injector and exhaust nozzle to Eq. (A-32), the following equation is obtained.

<u>Mean energy equation for the heat release by chemical reaction:</u>

$$
\overline{(\dot{Q}_{chem})} = -(\overline{\dot{H}}_f)_{nozzle} + (\overline{\dot{H}}_f)_{injector}
\tag{A-50}
$$

where, $\overline{(\dot{Q}_{chem})} \equiv -\sum_{l} h_{f,l}\overline{(\dot{M}_l)}$

$$
\begin{aligned}
(\overline{\dot{H}}_f)_{injector} &= -\iint_{C.S.,s3} \overline{\rho}\, \overline{h}_f\, \overline{\vec{V}} \circ \hat{n}\, dS \\
(\overline{\dot{H}}_f)_{nozzle} &= \iint_{C.S.,s4} \overline{\rho}\, \overline{h}_f\, \overline{\vec{V}} \circ \hat{n}\, dS
\end{aligned}
\tag{A-51}
$$

Equation (A-50) describes that in the steady state, the chemical energy (i.e., formation enthalpy) is introduced through the injector, the heat is released by the chemical reaction, and remaining chemical energy leaves the combustion region through the exhaust nozzle.

Also, by applying the expressions of the small-perturbation in/out flows through the injector and exhaust nozzle to Eq. (A-34), the following expression is obtained.

Small-perturbation energy equation for the heat release by chemical reaction:

$$(\dot{Q}_{chem})' = -\frac{\partial}{\partial t}\iiint_{C.V.}\left(h'_f\bar{\rho} + \bar{h}_f\rho'\right)dV - (\dot{H}_f)'_{nozzle} + (\dot{H}_f)'_{injector} \qquad \textbf{(A-52)}$$

where, $(\dot{Q}_{chem})' \equiv -\sum_l h_{f,l}(\dot{M}_l)'$

$$\begin{aligned}(\dot{H}_f)'_{injector} &= -\iint_{C.S.s3}\bar{\rho}\,\bar{h}_f\vec{V}'\circ\hat{n}\,dS - \iint_{C.S.s3}\bar{\rho}\,h'_f\overline{\vec{V}}\circ\hat{n}\,dS \\ &\quad -\iint_{C.S.s3}\rho'\,\bar{h}_f\overline{\vec{V}}\circ\hat{n}\,dS \\ (\dot{H}_f)'_{nozzle} &= \iint_{C.S.s4}\bar{\rho}\,\bar{h}_f\vec{V}'\circ\hat{n}\,dS + \iint_{C.S.s4}\bar{\rho}\,h'_f\overline{\vec{V}}\circ\hat{n}\,dS \\ &\quad +\iint_{C.S.s4}\rho'\,\bar{h}_f\overline{\vec{V}}\circ\hat{n}\,dS\end{aligned} \qquad \textbf{(A-53)}$$

A.1.5. Non-Homogeneous Wave Equation with Acoustic Sources by Combustion, Injector Flow, and Exhaust Nozzle Flow

As discussed above, the effects by the combustion processes and the in/out flows through the injector and exhaust nozzle are separated and expressed explicitly as source terms in small-perturbation conservation equations. These resulted small-perturbation equations for mass (Eq. (A-44)), momentum (Eq. (A-46)), and energy (Eq. (A-47)), can be modified into a form of non-homogeneous wave equation having acoustic sources by the combustion process, and the in/out flows through the injector and exhaust nozzle; see Eq. (3-21) in CHAPTER 3.

With defining the following derivative using the tangential mean flow velocity, $\overline{\vec{V}}$,

$$\frac{D}{Dt} = \frac{\partial}{\partial t} + \overline{\vec{V}} \circ \nabla \qquad \textbf{(A-54)}$$

Equation (A-44) can be expressed as following.

$$\frac{D}{Dt} \iiint_{C.V.} \rho' \, dV + \iint_{C.S.} \bar{\rho} \, \vec{V}' \circ \hat{n} \, dS = \tilde{S}_{mass} \qquad \textbf{(A-55)}$$

Multiplying $\overline{\vec{V}}$ on the both sides of Eq. (A-44) and the resulting equation is subtracted from Eq. (A-46).

$$\begin{aligned} \frac{\partial}{\partial t} \iiint_{C.V.} \rho \vec{V}' \, dV + \iint_{C.S.} \left(\bar{\rho} \, \vec{V}' \right) \overline{\vec{V}} \circ \hat{n} \, dS + \iint_{C.S.} p' \, \hat{n} \, dS \\ = \tilde{S}_{force,\widehat{x}_1} - \overline{\vec{V}} \cdot \tilde{S}_{mass} \end{aligned} \qquad \textbf{(A-56)}$$

Using Eq. (A-54), the above equation can also be expressed as following.

$$\frac{D}{Dt} \iiint_{C.V.} \rho \vec{V}' \, dV + \iint_{C.S.} p' \, \hat{n} \, dS = \tilde{S}_{force,\widehat{x}_1} - \overline{\vec{V}} \cdot \tilde{S}_{mass} \qquad \textbf{(A-57)}$$

Subtracting the divergence ($\nabla \circ$) of Eq. (A-57) from the material derivative ($\frac{D}{Dt}$) of Eq. (A-55) results in the following expression.

$$\begin{aligned} \frac{D}{Dt} \left(\frac{D}{Dt} \iiint_{C.V.} \rho' \, dV \right) - \nabla \circ \iint_{C.S.} p' \, \hat{n} \, dS \\ = \frac{D}{Dt} \tilde{S}_{mass} - \nabla \circ \tilde{S}_{force,\widehat{x}_1} + \nabla \circ \left(\overline{\vec{V}} \cdot \tilde{S}_{mass} \right) \end{aligned} \qquad \textbf{(A-58)}$$

By multiplying ($\bar{h}_s + \overline{k.e.}$) on the both sides of Eq. (A-44), taking dot-product on $\overline{\vec{V}}$ on the both sides of Eq. (A-56) with applying Eqs. (A-14) and (A-17), and subtracting these resulting equations from Eq. (A-47), the following expression is obtained.

$$\begin{aligned}\frac{\partial}{\partial t}\iiint_{C.V.} h_s' \,\overline{\rho}\, dV + \iint_{C.S.} h_s' \,\overline{\rho}\, \overline{\vec{V}} \circ \hat{n}\, dS - \frac{\partial}{\partial t}\iiint_{C.V.} p'\, dV - \iint_{C.S.} p' \vec{V}' \circ \hat{n}\, dS \\ = \widetilde{S}_{energy} - \left(\overline{h}_s + \overline{k.e.}\right) \cdot \widetilde{S}_{mass} - \overline{\vec{V}} \circ \left(\widetilde{S}_{force,\hat{x}_1} - \overline{\vec{V}} \cdot \widetilde{S}_{mass}\right)\end{aligned} \qquad \textbf{(A-59)}$$

Using Eq. (A-54), the above equation can also be expressed as following.

$$\begin{aligned}\frac{D}{Dt}\iiint_{C.V.} h_s' \,\overline{\rho}\, dV - \frac{D}{Dt}\iiint_{C.V.} p'\, dV \\ = \widetilde{S}_{energy} - \left(\overline{h}_s + \overline{k.e.}\right) \cdot \widetilde{S}_{mass} - \overline{\vec{V}} \circ \left(\widetilde{S}_{force,\hat{x}_1} - \overline{\vec{V}} \cdot \widetilde{S}_{mass}\right)\end{aligned} \qquad \textbf{(A-60)}$$

Taking the material derivative ($\frac{D}{Dt}$) of Eq. (A-60), applying the expressions for h'_s, Eq. (A-27), and applying the mean and small-perturbation equations of state, Eqs. (A-29) and (A-30), result in the following expression.

$$\begin{aligned}\frac{D}{Dt}\left(\frac{D}{Dt}\iiint_{C.V.} \rho'\, dV\right) - \frac{1}{\overline{a}^2}\frac{D}{Dt}\left(\frac{D}{Dt}\iiint_{C.V.} p'\, dV\right) \\ = -\frac{\gamma - 1}{\overline{a}^2}\frac{D}{Dt}\left\{\widetilde{S}_{energy} - \left(\overline{h}_s + \overline{k.e.}\right) \cdot \widetilde{S}_{mass} - \overline{\vec{V}} \circ \left(\widetilde{S}_{force,\hat{x}_1} - \overline{\vec{V}} \cdot \widetilde{S}_{mass}\right)\right\}\end{aligned} \qquad \textbf{(A-61)}$$

$$\text{where, } \overline{a} = \sqrt{\gamma \frac{\overline{p}}{\overline{\rho}}} = \sqrt{\gamma R \overline{T}} \qquad \textbf{(A-62)}$$

Using Eqs. (A-61) and (A-58), the following expression is obtained.

$$\begin{aligned}\frac{1}{\overline{a}^2}\frac{D}{Dt}\left(\frac{D}{Dt}\iiint_{C.V.} p' dV\right) - \nabla \circ \iint_{C.S.} p'\, \hat{n}\, dS \\ = \frac{D}{Dt}\widetilde{S}_{mass} \\ - \nabla \circ \left\{\widetilde{S}_{force,\hat{x}_1} - \overline{\vec{V}} \cdot \widetilde{S}_{mass}\right\} \\ + \frac{\gamma - 1}{\overline{a}^2}\frac{D}{Dt}\left\{\widetilde{S}_{energy} - (\overline{h}_s + \overline{K.E.})\widetilde{S}_{mass} - \overline{\vec{V}} \circ \left(\widetilde{S}_{force,\hat{x}_1} - \overline{\vec{V}} \cdot \widetilde{S}_{mass}\right)\right\}\end{aligned} \qquad \textbf{(A-63)}$$

By applying Gauss theorem (Eq. (A-64) below),

$$\nabla \circ \iint_{C.S.} p'\, \hat{n}\, dS = \nabla \circ \iiint_{C.V.} \nabla p' dV = \iiint_{C.V.} \nabla \circ \nabla p' dV \qquad \textbf{(A-64)}$$

Eq. (A-63) is expressed as following.

Non-homogeneous wave equation with mean flow having the acoustic sources by combustion process and in/out flows through injector and exhaust nozzle:

$$
\begin{aligned}
&\frac{1}{\bar{a}^2}\iiint_{C.V.}\frac{D}{Dt}\frac{D}{Dt}p'dV-\iiint_{C.V.}\nabla\circ\nabla p'dV\\
&\qquad=\frac{D}{Dt}\tilde{S}_{mass}\\
&\qquad-\nabla\circ\left\{\tilde{S}_{force,\hat{x}_1}-\bar{\vec{V}}\cdot\tilde{S}_{mass}\right\}\\
&\qquad+\frac{\gamma-1}{\bar{a}^2}\frac{D}{Dt}\left\{\tilde{S}_{energy}-(\bar{h}_s+\overline{K.E.})\tilde{S}_{mass}-\bar{\vec{V}}\circ\left(\tilde{S}_{force,\hat{x}_1}-\bar{\vec{V}}\cdot\tilde{S}_{mass}\right)\right\}
\end{aligned}
\qquad \textbf{(A-65)}
$$

where, $\frac{D}{Dt}=\frac{\partial}{\partial t}+\bar{\vec{V}}\circ\nabla$

The LHS is the wave equation with mean flow ($\bar{\vec{V}}$) in integral form, and the RHS has the acoustic sources, $\tilde{S}_{mass}$, $\tilde{S}_{force,\hat{x}_1}$, and $\tilde{S}_{energy}$, that amplify/damp the oscillations within the combustion region.. As defined in Eqs. (A-44), (A-46), and (A-47), these acoustic sources describe the effects of the in/out flows through the injector and exhaust nozzle and the chemical reactions in the combustion region.

A.2. Interactions at the Combustion Region

The source terms in the RHS of the non-homogeneous wave equation, Eq. (3-21) or Eq. (A-65), depend on the oscillations in the combustion region (i.e., the variables on the LHS). For example, the chemical reaction and the out flow through the exhaust nozzle depends on the acoustic oscillations in the combustion region, and in the same time these processes (as acoustic sources) generate and interact with the acoustic waves. In this case, the Green function approach for the solutions of the entire annular combustor is not available [32-34]. However, Eq. (3-21) or Eq. (A-65) could provide the relationship between acoustic waves and combustion processes (with in/out flows through the injector and exhaust nozzle) at the combustion region at a certain instant.

The obtained non-homogeneous wave equation with mean flow having acoustic sources, $\tilde{S}_{mass}$, $\tilde{S}_{force,\hat{x}_1}$, and $\tilde{S}_{energy}$, (i.e., Eq. (3-21) or Eq. (A-65) shown below) is applied to the combustion region.

$$\begin{aligned}
\frac{1}{\bar{a}^2}\iiint_{C.V.}\frac{D}{Dt}\frac{D}{Dt}p'dV - \iiint_{C.V.}\nabla\circ\nabla p'dV \\
&= \frac{D}{Dt}\tilde{S}_{mass} \\
&-\nabla\circ\left\{\tilde{S}_{force,\hat{x}_1} - \bar{\vec{V}}\cdot\tilde{S}_{mass}\right\} \\
&+\frac{\gamma-1}{\bar{a}^2}\frac{D}{Dt}\left\{\tilde{S}_{energy} - (\bar{h}_s + \overline{k.e.})\tilde{S}_{mass} - \bar{\vec{V}}\circ\left(\tilde{S}_{force,\hat{x}_1} - \bar{\vec{V}}\cdot\tilde{S}_{mass}\right)\right\}
\end{aligned}$$

(3-21)

or

(A-65)

where, $\frac{D}{Dt} = \frac{\partial}{\partial t} + \bar{\vec{V}}\circ\nabla$

$$\tilde{S}_{mass} = \dot{M}'_{injector} - \dot{M}'_{nozzle}$$ **(3-23)**

$$\tilde{S}_{force,\hat{x}_1} = \vec{0}$$ or

$$\tilde{S}_{energy} = (\dot{Q}_{chem})' + \left\{ (\dot{H}_s + \dot{K}.\dot{E}.)'_{injector} - (\dot{H}_s + \dot{K}.\dot{E}.)'_{nozzle} \right\}$$ **(A-44)** **(A-46)**

$$(\dot{Q}_{chem})' = -\sum_l h_{f,l} (\dot{M}_l)'$$ **(A-47)** **(A-48)**

By applying $\tilde{S}_{force,\hat{x}_1} = \vec{0}$ (i.e., Eq. (A-46) or (3-17)) and $\nabla \circ \left(\bar{\vec{V}} \cdot \tilde{S}_{mass} \right) = 0$ (because of no gradient in the combustion region) and defining the temporary acoustic source, S_{energy}, for convenience, the above equation is simplified as following.

$$\frac{1}{\bar{a}^2} \iiint_{C.V.} \frac{D}{Dt} \frac{D}{Dt} p' dV - \iiint_{C.V.} \nabla \circ \nabla p' dV = \frac{\gamma - 1}{\bar{a}^2} \frac{D}{Dt} S_{energy} \tag{A-66}$$

where, $$S_{energy} \equiv \tilde{S}_{energy} - (\bar{h}_s + \overline{k.e.}) \tilde{S}_{mass} - \bar{\vec{V}} \circ \left(-\bar{\vec{V}} \cdot \tilde{S}_{mass} \right) + \frac{\bar{a}^2}{\gamma - 1} \tilde{S}_{mass} \tag{A-67}$$

By applying one-dimensional assumption and setting the coordinate x for $\hat{x}_1$ in Figure 35, for simplicity, Eqs. (A-66) and (A-67) are expressed as following.

$$\frac{1}{\bar{a}^2} \int_{\Delta x} \frac{D}{Dt} \frac{D}{Dt} p' A dx - \int_{\Delta x} \frac{\partial}{\partial x} \frac{\partial}{\partial x} p' A dx = \frac{\gamma - 1}{\bar{a}^2} \frac{D}{Dt} S_{energy} \tag{A-68}$$

where, A; the cross sectional area of the annular combustor

$Adx = dV$

$$\frac{D}{Dt} = \frac{\partial}{\partial t} + \bar{V} \frac{\partial}{\partial x} \text{ for 1-D approach with } x \equiv x_1 \tag{A-69}$$

$$S_{energy} \equiv \tilde{S}_{energy} - (\bar{h}_s + \overline{k.e.}) \tilde{S}_{mass} - \bar{V} \cdot \left(-\bar{V} \cdot \tilde{S}_{mass} \right) + \frac{\bar{a}^2}{\gamma - 1} \tilde{S}_{mass} \tag{A-70}$$

Since the acoustic source, S_{energy} describes the effects by the inflow through the injector, outflow through the exhaust nozzle, and the heat by the conversion of the chemical compositions, which are carried by the in/out flows, it does not depend upon the volume of the combustion region and has finite value. The RHS of Eq. (A-68) can be written rigorously using the cross sectional area of the annular combustor, A (see Figure 35), and delta function, $\delta(x - x_0)$, as following.

$$\frac{1}{\bar{a}^2}\int_{\Delta x}\frac{D}{Dt}\frac{D}{Dt}p'Adx - \int_{\Delta x}\frac{\partial}{\partial x}\frac{\partial}{\partial x}p'Adx = \frac{\gamma-1}{\bar{a}^2}\int_{\Delta x}\frac{D}{Dt}\left(\frac{S_{energy}}{A}\right)\delta(x-x_0)Adx \quad \textbf{(A-71)}$$

where, $x_0(=0)$; the location of the combustion region

In order to calculate the first term on the LHS of Eq. (A-71), the definition of the material derivative, $\frac{D}{Dt}$, Eq. (A-69), for one-dimensional approach is applied.

$$\begin{aligned}\int_{\Delta x}\frac{D}{Dt}\frac{D}{Dt}p'Adx &= \int_{\Delta x}\left(\frac{\partial}{\partial t}+\bar{V}\frac{\partial}{\partial x}\right)\left(\frac{\partial}{\partial t}+\bar{V}\frac{\partial}{\partial x}\right)p'Adx \\ &= \int_{\Delta x}\left(\frac{\partial^2}{\partial t^2}+2\bar{V}\frac{\partial^2}{\partial t\partial x}+\bar{V}^2\frac{\partial^2}{\partial x^2}\right)p'Adx \\ &= \int_{\Delta x}\left(\frac{\partial^2 p'}{\partial t^2}+2\bar{V}\frac{\partial^2 p'}{\partial t\partial x}+\bar{V}^2\frac{\partial^2 p'}{\partial x^2}\right)Adx\end{aligned} \quad \textbf{(A-72)}$$

By applying Eq. (A-72) to Eq. (A-71) and integrating Eq. (A-71) over Δx, the following expression is obtained.

$$\begin{aligned}&\frac{1}{\bar{a}^2}\left(\frac{\partial^2 p'}{\partial t^2}A\Delta x + 2\bar{V}\frac{\partial}{\partial t}\left[p'\big|_{x=\frac{\Delta x}{2}+} - p'\big|_{x=\frac{-\Delta x}{2}-}\right]A + \bar{V}^2\left[\frac{\partial p'}{\partial x}\bigg|_{x=\frac{\Delta x}{2}+} - \frac{\partial p'}{\partial x}\bigg|_{x=\frac{-\Delta x}{2}-}\right]A\right) \\ &-\left[\frac{\partial p'}{\partial x}\bigg|_{x=\frac{\Delta x}{2}+} - \frac{\partial p'}{\partial x}\bigg|_{x=\frac{-\Delta x}{2}-}\right]A = \frac{\gamma-1}{\bar{a}^2}\left\{\frac{D}{Dt}\left(\frac{S_{energy}}{A}\right)\right\}A\end{aligned} \quad \textbf{(A-73)}$$

In this study, the combustion region is assumed to be acoustically compact; i.e., $k\Delta x \ll 1$ [21, 22, 31]. Also, it is assumed that the acoustic sources, S_{energy} (or $\tilde{S}_{mass}$ and $\tilde{S}_{energy}$) have no gradient in the combustion region, and behave as monopole acoustic sources [21, 33, 34]. The acoustic pressures at the control surface s1 and s2 are the same.

$$p'\big|_{x=\frac{\Delta x}{2}+} - p'\big|_{x=\frac{-\Delta x}{2}-} = 0 \tag{A-74}$$

With applying the assumption of the acoustically compact combustion region, Eq. (A-74) above, Eq. (A-73) is expressed as below.

$$\frac{1}{\bar{a}^2}\left(\frac{\partial^2 p'}{\partial t^2}\right)A\Delta x + \frac{\bar{V}^2 - \bar{a}^2}{\bar{a}^2}\left[\frac{\partial p'}{\partial x}\bigg|_{x=\frac{\Delta x}{2}+} - \frac{\partial p'}{\partial x}\bigg|_{x=\frac{-\Delta x}{2}-}\right]A = \frac{\gamma - 1}{\bar{a}^2}\left\{\frac{D}{Dt}\left(\frac{S_{energy}}{A}\right)\right\}A \tag{A-75}$$

The acoustic pressures, p', in Eq. (A-75) can be expressed as a sum of the right going wave, f, and the left going wave, g. Since the goal of the derivation of this section is to obtain the relationship between the acoustic waves and the physical processes in the combustion region at a certain instant, the arguments for the acoustic pressure, p', the right going wave, f, and the left going wave, g, are chosen as below.

$$p'(t,x) = f(t - \frac{x}{\bar{a} + \bar{V}}) + g(t + \frac{x}{\bar{a} - \bar{V}}) \tag{A-76}$$

As shown in Figure 35, the right and left going wave, f_1 and g_1, arrives and leaves the control surface s1, which is located at $x = \frac{-\Delta x}{2}-$. Similarly, the right and left going wave, f_2 and g_2, arrives and leaves the control surface s2, which is located at $x = \frac{\Delta x}{2}+$.

$$\begin{aligned} p'\big|_{x=\frac{-\Delta x}{2}-} &= f_1(t - \frac{1}{\bar{a} + \bar{V}}(\frac{-\Delta x}{2}-)) + g_1(t + \frac{1}{\bar{a} - \bar{V}}(\frac{-\Delta x}{2}-)) \\ p'\big|_{x=\frac{\Delta x}{2}+} &= f_2(t - \frac{1}{\bar{a} + \bar{V}}(\frac{\Delta x}{2}+)) + g_2(t + \frac{1}{\bar{a} - \bar{V}}(\frac{\Delta x}{2}+)) \end{aligned} \tag{A-77}$$

Applying Eq. (A-77) above to Eq. (A-75) and cancelling the cross section area, A, of the annular combustor results in the following expression.

$$
\begin{aligned}
&\frac{1}{\bar{a}^2}\left(\frac{\partial^2 p'}{\partial t^2}\right)\Delta x \\
&+\frac{\bar{V}^2-\bar{a}^2}{\bar{a}^2}\left[\frac{-1}{\bar{a}+\bar{V}}\left\{\frac{\partial}{\partial t}f_2\Big(t-\frac{1}{\bar{a}+\bar{V}}\big(\frac{\Delta x}{2}+\big)\Big)-\frac{\partial}{\partial t}f_1\Big(t-\frac{1}{\bar{a}+\bar{V}}\big(\frac{-\Delta x}{2}-\big)\Big)\right\}\right] \\
&+\frac{\bar{V}^2-\bar{a}^2}{\bar{a}^2}\left[\frac{-1}{\bar{a}-\bar{V}}\left\{\frac{\partial}{\partial t}g_1\Big(t+\frac{1}{\bar{a}-\bar{V}}\big(\frac{-\Delta x}{2}-\big)\Big)-\frac{\partial}{\partial t}g_2\Big(t+\frac{1}{\bar{a}-\bar{V}}\big(\frac{\Delta x}{2}+\big)\Big)\right\}\right] \\
&\quad=\frac{\gamma-1}{\bar{a}^2}\left\{\frac{D}{Dt}\left(\frac{S_{energy}}{A}\right)\right\}
\end{aligned}
\tag{A-78}
$$

Since the combustion region is acoustically compact, i.e., $k\Delta x \ll 1$, we can set $\Delta x \rightarrow 0$ for Eq. (A-78). The LHS of the non-homogeneous wave equation (i.e., Eq. (A-65) or Eq. (3-21)) has the wavelength as the length scale, and the size of the combustion is very small and infinitesimal in this length scale. These manipulations results in the following expression:

$$
\begin{aligned}
&\frac{\bar{a}-\bar{V}}{\bar{a}^2}\left\{\frac{\partial}{\partial t}f_2\Big(t-\frac{0+}{\bar{a}+\bar{V}}\Big)-\frac{\partial}{\partial t}f_1\Big(t-\frac{0-}{\bar{a}+\bar{V}}\Big)\right\} \\
&\qquad+\frac{\bar{a}+\bar{V}}{\bar{a}^2}\left\{\frac{\partial}{\partial t}g_1\Big(t+\frac{0-}{\bar{a}-\bar{V}}\Big)-\frac{\partial}{\partial t}g_2\Big(t+\frac{0+}{\bar{a}-\bar{V}}\Big)\right\} \\
&\quad=\frac{\gamma-1}{\bar{a}^2}\left\{\frac{D}{Dt}\left(\frac{S_{energy}}{A}\right)\right\}
\end{aligned}
\tag{A-79}
$$

Since the width of the combustion region goes to zero, $\Delta x \rightarrow 0$, by the above limiting procedure, the locations of the control surface s1 and s2 are at $x = 0-$ and $x = 0+$, respectively. The expressions of the right and left going waves at control surface s1 and s2 can be simplified as following.

$$
\begin{aligned}
f_1\left(t-\frac{0-}{\bar{a}+\bar{V}}\right) &= f_1\left(t-\frac{x}{\bar{a}+\bar{V}}\right)\Bigg|_{x=0-} = f_1(t) \\
g_1\left(t+\frac{0-}{\bar{a}-\bar{V}}\right) &= g_1\left(t+\frac{x}{\bar{a}-\bar{V}}\right)\Bigg|_{x=0-} = g_1(t) \\
f_2\left(t-\frac{0+}{\bar{a}+\bar{V}}\right) &= f_2\left(t-\frac{x}{\bar{a}+\bar{V}}\right)\Bigg|_{x=0+} = f_2(t) \\
g_2\left(t+\frac{0+}{\bar{a}-\bar{V}}\right) &= g_2\left(t+\frac{x}{\bar{a}-\bar{V}}\right)\Bigg|_{x=0+} = g_2(t)
\end{aligned} \tag{A-80}
$$

Using Eq. (A-80), Eq. (A-79) is simplified as below.

$$
\begin{aligned}
&\frac{\bar{a}-\bar{V}}{\bar{a}^2}\left\{\frac{\partial}{\partial t} f_2(t)-\frac{\partial}{\partial t} f_1(t)\right\}+\frac{\bar{a}+\bar{V}}{\bar{a}^2}\left\{\frac{\partial}{\partial t} g_1(t)-\frac{\partial}{\partial t} g_2(t)\right\} \\
&\quad=\frac{\gamma-1}{\bar{a}^2}\left\{\frac{D}{Dt}\left(\frac{S_{energy}}{A}\right)\right\}
\end{aligned} \tag{A-81}
$$

Since it is assumed that the acoustic sources terms have no gradient in the combustion region, the term in the RHS is expressed as following.

$$
\frac{D}{Dt}\left(\frac{S_{energy}}{A}\right)=\frac{\partial}{\partial t}\left(\frac{S_{energy}}{A}\right)+\bar{V}\frac{\partial}{\partial x}\left(\frac{S_{energy}}{A}\right)=\frac{\partial}{\partial t}\left(\frac{S_{energy}}{A}\right) \tag{A-82}
$$

Applying Eq. (A-82) to Eq. (A-81) results in the following expression.

$$
\begin{aligned}
&\frac{\bar{a}-\bar{V}}{\bar{a}^2}\left\{\frac{\partial}{\partial t} f_2(t)-\frac{\partial}{\partial t} f_1(t)\right\}+\frac{\bar{a}+\bar{V}}{\bar{a}^2}\left\{\frac{\partial}{\partial t} g_1(t)-\frac{\partial}{\partial t} g_2(t)\right\} \\
&\quad=\frac{\gamma-1}{\bar{a}^2}\left\{\frac{\partial}{\partial t}\left(\frac{S_{energy}}{A}\right)\right\}
\end{aligned} \tag{A-83}
$$

The both sides of Eq. (A-83) have the time derivative, $\frac{\partial}{\partial t}$, and the properties (i.e., f_1, g_1, f_2, g_2, and S_{energy}) in the equation are all small-perturbation properties and fluctuate about zero. Also, when the source strength is zero, i.e. $S_{energy} = 0$, the acoustic waves are not affected by the processes in the combustion region, i.e., $f_2 = f_1$ and $g_1 = g_2$. It is consistent with the case of the acoustic waves propagations in "no combustion" region; see section 3.2.1. in CHAPTER 3. Removing the time derivative, $\frac{\partial}{\partial t}$ without integral constant from the both sides of Eq. (A-83), the following expression is obtained.

$$\left(\frac{\bar{a}-\bar{V}}{\bar{a}^2}\right)\left\{f_2(t)-f_1(t)\right\}+\left(\frac{\bar{a}+\bar{V}}{\bar{a}^2}\right)\left\{g_1(t)-g_2(t)\right\}=\left(\frac{\gamma-1}{\bar{a}^2}\right)\left\{\left(\frac{S_{energy}}{A}\right)\right\} \qquad \textbf{(A-84)}$$

Applying Eq. (A-67) back to the temporary acoustic source, S_{energy}, in the RHS of the above equation, the following equation is obtained.

$$\begin{aligned}&\left(\frac{\bar{a}-\bar{V}}{\bar{a}^2}\right)\left\{f_2(t)-f_1(t)\right\}+\left(\frac{\bar{a}+\bar{V}}{\bar{a}^2}\right)\left\{g_1(t)-g_2(t)\right\}\\&=\left(\frac{\gamma-1}{\bar{a}^2}\right)\left[\frac{\tilde{S}_{energy}}{A}-(\bar{h}_s+\overline{k.e.})\frac{\tilde{S}_{mass}}{A}-\vec{\bar{V}}\circ\left(-\vec{\bar{V}}\frac{\tilde{S}_{mass}}{A}\right)+\frac{\bar{a}^2}{\gamma-1}\frac{\tilde{S}_{mass}}{A}\right]\end{aligned} \qquad \textbf{(A-85)}$$

where, $\vec{\bar{V}}=\bar{V}\,\hat{x}_1$

Where, in order to avoid confusions when applying $\tilde{S}_{energy}$ and $\tilde{S}_{mass}$ on the RHS of the above equation (which acts in $\hat{x}_2$ direction), the tangential mean flow is expressed as $\vec{\bar{V}}=\bar{V}\hat{x}_1$.

Equation (A-85) describes that the "unknown" outgoing waves, g_1 and f_2, depend upon the "known" incident waves, f_1 and g_2, and the acoustic sources on the RHS that describe the processes taking place within the combustion region.

Since the combustion region is acoustically compact and the acoustic sources on the RHS of Eq. (A-85) are monopole sources [21, 33, 34], the acoustic pressure across the combustion region is continuous and the pressures at the surfaces s1 and s2 are the same. However, the acoustic velocity is not continuous because the heat added by the combustion process and the mass and energy added/removed by the in/out flows produce a discontinuous acoustic velocity jump across the "combustion source" [21, 22].

$$\begin{aligned} &p'_1(t) = p'_2(t) \\ &v'_1(t) \neq v'_2(t) \end{aligned} \tag{A-86}$$

The requirement, $p'_1(t) = p'_2(t)$, (which was also used in Eq. (A-74)) yields the following relationship:

$$f_1(t) + g_1(t) = f_2(t) + g_2(t) \tag{A-87}$$

Notably, Eqs. (A-85) and (A-87) can be solved to determine the two unknowns, the outgoing acoustic waves, g_1 and f_2.

Substituting the definitions of $\tilde{S}_{mass}$ and $\tilde{S}_{energy}$, Eq. (3-23) or Eqs. (A-44), (A-47), and (A-48), into the RHS of Eq. (A-85), yields the following expression.

$$\begin{aligned} &\left(\frac{\bar{a} - \bar{V}}{\bar{a}^2}\right)\left\{f_2(t) - f_1(t)\right\} + \left(\frac{\bar{a} + \bar{V}}{\bar{a}^2}\right)\left\{g_1(t) - g_2(t)\right\} \\ &= \left(\frac{\gamma - 1}{\bar{a}^2}\right)\frac{1}{A}\Big[(\dot{Q}_{chem})' + \left\{(\dot{H}_s + \dot{K}.E.)'_{injector} - (\dot{H}_s + \dot{K}.E.)'_{nozzle}\right\} \\ &\qquad - (\bar{h}_s + \overline{k.e.})\left\{\dot{M}'_{injector} - \dot{M}'_{nozzle}\right\} \\ &\qquad - \bar{\vec{V}} \circ \left(-\bar{\vec{V}}\left\{\dot{M}'_{injector} - \dot{M}'_{nozzle}\right\}\right) \\ &\qquad + \left(\frac{\bar{a}^2}{\gamma - 1}\right)\left\{\dot{M}'_{injector} - \dot{M}'_{nozzle}\right\}\Big] \end{aligned} \tag{A-88}$$

By arranging the terms on the RHS of Eq. (A-88) by the small-perturbation heat release by the chemical reaction, the effects by the injector flow, and the effects by the exhaust nozzle flow, the following expression is obtained.

$$\begin{aligned} &\left(\frac{\bar{a} - \bar{V}}{\bar{a}^2}\right)\left\{f_2(t) - f_1(t)\right\} + \left(\frac{\bar{a} + \bar{V}}{\bar{a}^2}\right)\left\{g_1(t) - g_2(t)\right\} \\ &= \left(\frac{\gamma - 1}{\bar{a}^2}\right)\frac{1}{A}\left[(\dot{Q}_{chem})' + (S_{injector})' - (S_{nozzle})'\right] \end{aligned} \tag{A-89}$$

where,

$$\begin{aligned}(S_{injector})' = {} & (\dot{H}_s + \dot{K}.E.)'_{injector} - (\overline{h}_s + \overline{k.e.})\dot{M}'_{injector} \\ & + \left(\frac{\overline{a}^2}{\gamma - 1} \right) \dot{M}'_{injector} + \overline{\vec{V}} \circ \overline{\vec{V}} \dot{M}'_{injector}\end{aligned} \tag{A-90}$$

$$\begin{aligned}(S_{nozzle})' = {} & (\dot{H}_s + \dot{K}.E.)'_{nozzle} - (\overline{h}_s + \overline{k.e.})\dot{M}'_{nozzle} \\ & + \left(\frac{\overline{a}^2}{\gamma - 1} \right) \dot{M}'_{nozzle} + \overline{\vec{V}} \circ \overline{\vec{V}} \dot{M}'_{nozzle}\end{aligned} \tag{A-91}$$

Where, the RHS of Eq. (A-89) describes the acoustic sources produced by the chemical reaction, $(\dot{Q}_{chem})'$, the inflow through the injector, $(S_{injector})'$, and the outflow through the exhaust nozzle, $(S_{nozzle})'$.

A.3. Effects by the Combustion, Injector Flow, and Exhaust Nozzle Flow

As discussed in A.2. , Eqs. (A-89) and (A-87) describe that the “unknown” outgoing waves, g_1 and f_2, depend upon the “known” incident waves, f_1 and g_2, and the acoustic sources, $(\dot{Q}_{chem})'$, $(S_{injector})'$, and $(S_{nozzle})'$, on the RHS that describe the processes taking place within the combustion region, i.e., the combustion process and the in/out flows through the injector and exhaust nozzle; see Figure 35.

$$\left(\frac{\bar{a}-\bar{V}}{\bar{a}^2}\right)\{f_2(t)-f_1(t)\}+\left(\frac{\bar{a}+\bar{V}}{\bar{a}^2}\right)\{g_1(t)-g_2(t)\} \\ =\left(\frac{\gamma-1}{\bar{a}^2}\right)\frac{1}{A}\left[(\dot{Q}_{chem})'+(S_{injector})'-(S_{nozzle})'\right] \tag{A-89}$$

$$\text{where, } (\dot{Q}_{chem})' \equiv -\sum_l h_{f,l}(\dot{M}_l)' \tag{A-48}$$

$$(S_{injector})' = (\dot{H}_s+\dot{K}.E.)'_{injector}-(\bar{h}_s+\overline{k.e.})\dot{M}'_{injector} \\ +\left(\frac{\bar{a}^2}{\gamma-1}\right)\dot{M}'_{injector}+\bar{\bar{\vec{V}}}\circ\bar{\bar{\vec{V}}}\dot{M}'_{injector} \tag{A-90}$$

$$(S_{nozzle})' = (\dot{H}_s+\dot{K}.E.)'_{nozzle}-(\bar{h}_s+\overline{k.e.})\dot{M}'_{nozzle} \\ +\left(\frac{\bar{a}^2}{\gamma-1}\right)\dot{M}'_{nozzle}+\bar{\bar{\vec{V}}}\circ\bar{\bar{\vec{V}}}\dot{M}'_{nozzle} \tag{A-91}$$

$$f_1(t)+g_1(t)=f_2(t)+g_2(t) \tag{A-87}$$

Equations (A-89) and (A-87) above provide two equations for two unknown, and the outgoing waves, g_1 and f_2, (leaving the combustion region after completing the interactions) can be calculated, when the given incident waves, f_1 and g_2, and the descriptions about the acoustic sources, $(\dot{Q}_{chem})'$, $(S_{injector})'$, and $(S_{nozzle})'$, are provided. The incident waves, f_1 and g_2, are provided by the model of “no combustion” region; see Eqs. (3-27), (3-28), and (3-29) and Section 3.2.1 in CHAPTER 3. In order to calculate the effects by the acoustic sources, the terms, $(\dot{Q}_{chem})'$, $(S_{injector})'$, and $(S_{nozzle})'$, need to be modeled.

A.3.1. Effect by the Out Flow through the Exhaust Nozzle

At first, the model of the out flow through the exhaust nozzle will be developed.

A.3.1.1. Quasi-Steady and Choked Exhaust Nozzle

As discussed in Section 3.2.2 in CHAPTER 3, the exhaust nozzle has been assumed to be short and choked, implying that $M = 1$ at the throat, and the distance from the combustion chamber to the nozzle throat is much shorter than the acoustic wavelength. Since the time scale of the short nozzle is much shorter than the time scale of the acoustic motions, the flow in the nozzle can be assumed to be quasi-steady. In this case, the stagnation conditions in the combustion region (with $M = 1$ at the nozzle throat) determine the mass flow rate and energy flux through the nozzle [35].

The following equations describe the mass flow and sensible enthalpy and kinetic energy flux through the choked nozzle [35].

$$\dot{M}_{nozzle} = \left\{ A^* \sqrt{\frac{\gamma}{R}} \left(\frac{2}{\gamma+1} \right)^{\frac{\gamma+1}{2(\gamma-1)}} \right\} \frac{p_t}{\sqrt{T_t}} \tag{A-92}$$

$$(\dot{H}_s + \dot{K}.\dot{E}.)_{nozzle} = \left\{ A^* \sqrt{\frac{\gamma}{R}} \left(\frac{2}{\gamma+1} \right)^{\frac{\gamma+1}{2(\gamma-1)}} \right\} \frac{p_t}{\sqrt{T_t}} (h_s + k.e.) \tag{A-93}$$

Where, p_t and T_t are the stagnation pressure and temperature and A^* is the area of the throat of the exhaust nozzle; see Figure 34 and Figure 35 in CHAPTER 3.

By defining the following coefficient, k_{nozzle}, and expressing p_t and T_t in terms of mean properties and small-perturbation properties in Eqs. (A-92) and (A-93), the following expressions are obtained; see Eqs. (A-95), (A-96), (A-97), and (A-98) below.

$$k_{nozzle} = \left\{ A^* \sqrt{\frac{\gamma}{R}} \left(\frac{2}{\gamma+1} \right)^{\frac{\gamma+1}{2(\gamma-1)}} \right\} \tag{A-94}$$

The mean (steady state) and the small-perturbation equations of the mass flow through the short and choked nozzle are expressed in Eqs. (A-95) and (A-96) as below.

$$\overline{\dot{M}}_{nozzle} = k_{nozzle} \frac{\overline{p}_t}{\sqrt{\overline{T}_t}} \tag{A-95}$$

$$\dot{M}'_{nozzle} = k_{nozzle} \left(-\frac{1}{2} \frac{\overline{p}_t}{\overline{T}_t^{3/2}} T_t' + \frac{p_t'}{\sqrt{\overline{T}_t}} \right) \tag{A-96}$$

The mean (steady state) and the small-perturbation equations of the sensible enthalpy and kinetic energy flux through the short and choked nozzle are expressed in Eqs. (A-97) and (A-98) as below.

$$\overline{(\dot{H}_s + \dot{K}.\dot{E}.)}_{nozzle} = k_{nozzle} \frac{\overline{p}_t}{\sqrt{\overline{T}_t}} (\overline{h}_s + \overline{k.e.}) \tag{A-97}$$

$$(\dot{H}_s + \dot{K}.E.)'_{nozzle} = k_{nozzle} \left(\frac{(\overline{h}_s + \overline{k.e.})}{\sqrt{\overline{T}_t}} p_t' - \frac{1}{2} \frac{\overline{p}_t}{\overline{T}_t^{3/2}} (\overline{h}_s + \overline{k.e.}) T_t' + \frac{\overline{p}_t}{\sqrt{\overline{T}_t}} c_p T_t' \right) \tag{A-98}$$

The mean (or steady state) energy conservation equations with separation of acoustic motions and acoustic sources by the combustion process (chemical reaction), and the in/out flow through the injector and exhaust nozzle, (i.e., Eqs. (A-41) and (A-42) in A.1.), can be expressed as Eq. (A-99) below.

$$\overline{(\dot{Q}_{external})} - \sum_l h_{f,l} \overline{(\dot{M}_l)} = \overline{(\dot{H}_s + \dot{K}.E.)}_{nozzle} - \overline{(\dot{H}_s + \dot{K}.E.)}_{injector} \tag{A-41}$$

where, $\overline{(\dot{Q}_{external})} = 0$, i.e., adiabatic condition

$$\overline{(\dot{Q}_{chem})} \equiv -\sum_{l} h_{f,l} \overline{(\dot{M}_l)} \tag{A-42}$$

$$\overline{(\dot{Q}_{chem})} = \overline{(\dot{H}_s + \dot{K}.E.)}_{nozzle} - \overline{(\dot{H}_s + \dot{K}.E.)}_{injector} \tag{A-99}$$

Eq. (A-99) is manipulated as following, and the reference energy flux (or heat release) is defined in Eq. (A-100) as below.

$$\begin{aligned} &\overline{(\dot{Q}_{chem})} + \overline{(\dot{H}_s + \dot{K}.E.)}_{injector} = \overline{(\dot{H}_s + \dot{K}.E.)}_{nozzle} \\ &\equiv \overline{(\dot{Q}_{ref})} \end{aligned} \tag{A-100}$$

Using Eqs. (A-97) and (A-100), the coefficient, k_{nozzle}, can be expressed as following.

$$\begin{aligned} k_{nozzle} &= \frac{\overline{(\dot{Q}_{ref})}}{\frac{\bar{p}_t}{\sqrt{\bar{T}_t}}(\bar{h}_s + \overline{k.e.})} \\ &\left(= \frac{\overline{(\dot{Q}_{chem})} + \overline{(\dot{H}_s + \dot{K}.E.)}_{injector}}{\frac{\bar{p}_t}{\sqrt{\bar{T}_t}}(\bar{h}_s + \overline{k.e.})} = \frac{\overline{(\dot{H}_s + \dot{K}.E.)}_{nozzle}}{\frac{\bar{p}_t}{\sqrt{\bar{T}_t}}(\bar{h}_s + \overline{k.e.})} \right) \end{aligned} \tag{A-101}$$

Applying Eq. (A-101) to Eqs. (A-96) and (A-98), the small-perturbation equations of the mass flow and the sensible enthalpy and kinetic energy flux through the quasi-steady and choked nozzle are expressed in Eqs. (A-102) and (A-103) as below.

$$\dot{M}'_{nozzle} = \frac{\overline{(\dot{Q}_{ref})}}{\frac{\bar{p}_t}{\sqrt{\bar{T}_t}}(\bar{h}_s + \overline{k.e.})} \left(-\frac{1}{2}\frac{\bar{p}_t}{\bar{T}_t^{3/2}} T_t' + \frac{p_t'}{\sqrt{\bar{T}_t}} \right) \tag{A-102}$$

$$\begin{aligned} &(\dot{H}_s + \dot{K}.E.)'_{nozzle} \\ &\quad = \frac{\overline{(\dot{Q}_{ref})}}{\frac{\bar{p}_t}{\sqrt{\bar{T}_t}}(\bar{h}_s + \overline{k.e.})} \left(\frac{(\bar{h}_s + \overline{k.e.})}{\sqrt{\bar{T}_t}} p_t' - \frac{1}{2}\frac{\bar{p}_t}{\bar{T}_t^{3/2}}(\bar{h}_s + \overline{k.e.}) T_t' + \frac{\bar{p}_t}{\sqrt{\bar{T}_t}} c_p T_t' \right) \end{aligned} \tag{A-103}$$

The small-perturbation stagnation pressure, p'_t, and temperature, T'_t, in Eqs. (A-102) and (A-103) can be obtained from the small-perturbation properties in the combustion region.

A.3.1.2. Stagnation Properties in the Combustion Region

In order to calculate the fluctuating mass flow rate and enthalpy and kinetic energy flux through the exhaust nozzle (using Eqs. (A-102) and (A-103)), the small-perturbation stagnation pressure, p'_t, and temperature, T'_t, need to be obtained. Using the small-perturbation pressure, temperature, and velocity in the combustion region, the stagnation properties can be calculated.

In order to avoid confusions with the total enthalpy, h_t, by the sum of the formation enthalpy, the sensible enthalpy, and the kinetic energy, the notation $h_{t,s}$ is used for the stagnation enthalpy accounting the sensible enthalpy, h_s, and the kinetic energy, $k.e.$, but not accounting the formation enthalpy, h_f; see Eq. (A-104) below.

$$\begin{aligned} h_t &= h_f + h_{t,s} = h_f + (h_s + k.e.) \\ h_{t,s} &= h_s + k.e. \end{aligned} \quad \textbf{(A-104)}$$

The relationships between the stagnation properties and the state properties are expressed in Eqs. (A-105), (A-106), and (A-107) as shown below [35].

$$h_{t,s} = h_{s,cv} + k.e._{cv} = h_{s,cv} + \frac{1}{2}V_{cv}^2 \quad \textbf{(A-105)}$$

$$T_t = T_{cv}\left(1 + \frac{1}{2}(\gamma - 1)M_{cv}^2\right) \quad \textbf{(A-106)}$$

$$\frac{p_{cv}}{p_t} = \left(\frac{T_{cv}}{T_t}\right)^{\frac{\gamma}{\gamma-1}} \quad \textbf{(A-107)}$$

Where, we define control volume or cavity, *"cv"*, for notating the combustion region in order to avoid confusion; i.e., the properties in the control volume or cavity, *"cv"*, (e.g., p'_{cv}) means the properties in the combustion region (e.g., $p'_{combustion\,region}$). Other required properties, Mach number and speed of sound in the combustion region, are also expressed in Eqs. (A-108) and (A-109) as below.

$$M_{cv} = \frac{V_{cv}}{a_{cv}} \tag{A-108}$$

$$a_{cv} = \sqrt{\gamma R T_{cv}} = \sqrt{\gamma \frac{p_{cv}}{\rho_{cv}}} \tag{A-109}$$

The properties in Eqs. (A-104) ~ (A-109) are expressed in terms of the mean (or steady state) properties and small-perturbation properties, the higher order terms are neglected, and the mean and small-perturbation equations are obtained as below.

Mean and small-perturbation stagnation enthalpy (sensible enthalpy & kinetic energy)

$$\bar{h}_{t,s} = \bar{h}_{s,cv} + \frac{1}{2}\bar{V}_{cv}^{2} \tag{A-110}$$

$$h'_{t,s} = h'_{s,cv} + \bar{V}_{cv} V'_{cv} \tag{A-111}$$

Mean and small-perturbation stagnation temperature

$$\bar{T}_t = \bar{T}_{cv}\left(1 + \frac{1}{2}(\gamma - 1)\bar{M}_{cv}^{2}\right) \tag{A-112}$$

$$T'_t = T'_{cv} + T'_{cv}(\gamma - 1)\bar{M}_{cv}^{2}\frac{V'_{cv}}{\bar{V}_{cv}} \tag{A-113}$$

Mean and small-perturbation Mach number

$$\bar{M}_{cv} = \frac{\bar{V}_{cv}}{\bar{a}_{cv}} \tag{A-114}$$

$$M'_{cv} = \bar{M}_{cv}\left(\frac{V'_{cv}}{\bar{V}_{cv}} - \frac{1}{2}\frac{T'_{cv}}{\bar{T}_{cv}}\right) \tag{A-115}$$

Mean and small-perturbation speed of sound

$$\bar{a}_{cv} = \sqrt{\gamma R \bar{T}_{cv}} \tag{A-116}$$

$$a'_{cv} = \sqrt{\gamma R \bar{T}_{cv}}\left(-\frac{1}{2}\frac{T'_{cv}}{\bar{T}_{cv}}\right) \tag{A-117}$$

$$\frac{a'_{cv}}{\bar{a}_{cv}} = \left(-\frac{1}{2}\frac{T'_{cv}}{\bar{T}_{cv}}\right) \tag{A-118}$$

Mean and small-perturbation expressions for the relationship between pressures and temperatures

$$\frac{\bar{p}_{cv}}{\bar{p}_t} = \left(\frac{\bar{T}_{cv}}{\bar{T}_t}\right)^{\frac{\gamma}{\gamma-1}} \tag{A-119}$$

$$\frac{p'_t}{\bar{p}_t} - \frac{p'_{cv}}{\bar{p}_{cv}} = \left(\frac{\gamma}{\gamma-1}\right)\left(\frac{T'_t}{\bar{T}_t} - \frac{T'_{cv}}{\bar{T}_{cv}}\right) \tag{A-120}$$

In the above equations, Eqs. (A-110) ~ (A-120), the mean and small-perturbation stagnation properties are expressed by the properties in the combustion region (i.e., cavity).

A.3.1.3. Acoustic Source Effects by the Out Flow through the Exhaust Nozzle

As discussed above, the acoustic source effect by the exhaust nozzle flow can be expressed as below; see Eqs. (A-89) and (A-91), that are mentioned in A.2. and in the introduction of A.3. .

$$\begin{aligned}&\left(\frac{\bar{a}-\bar{V}}{\bar{a}^2}\right)\{f_2(t)-f_1(t)\}+\left(\frac{\bar{a}+\bar{V}}{\bar{a}^2}\right)\{g_1(t)-g_2(t)\}\\&\quad=\left(\frac{\gamma-1}{\bar{a}^2}\right)\frac{1}{A}\left[(\dot{Q}_{chem})'+(S_{injector})'-(S_{nozzle})'\right]\end{aligned}\qquad\textbf{(A-89)}$$

$$\begin{aligned}(S_{nozzle})' &= (\dot{H}_s+\dot{K}.E.)'_{nozzle}-(\bar{h}_s+\overline{k.e.})\dot{M}'_{nozzle}\\&\quad+\left(\frac{\bar{a}^2}{\gamma-1}\right)\dot{M}'_{nozzle}+\bar{\vec{V}}\circ\bar{\vec{V}}\dot{M}'_{nozzle}\end{aligned}\qquad\textbf{(A-91)}$$

The small-perturbation mass flow, $\dot{M}'_{nozzle}$ (i.e., Eq. (A-102)), and the sensible energy and kinetic energy flux, $(\dot{H}_s+\dot{K}.E.)'_{nozzle}$ (i.e., Eq. (A-103)), through the exhaust nozzle are applied into the above acoustic source by the exhaust nozzle (i.e., Eq. (A-91)). Then, the stagnation properties in the resulting equation are expressed by the properties in the combustion regions, using Eqs. (A-110) ~ (A-120). These manipulations result in the following expression.

$$\begin{aligned}&(S_{nozzle})'\\&=\overline{(\dot{Q}_{ref})}\left(\frac{c_p\bar{T}_{cv}}{\bar{h}_{s,cv}+\frac{1}{2}\bar{V}_{cv}^2}\right)\left(\frac{3\gamma-1}{2}+\frac{\gamma+1}{2}\frac{\frac{1}{2}(\gamma-1)\bar{M}_{cv}^2}{\left(1+\frac{1}{2}(\gamma-1)\bar{M}_{cv}^2\right)}\right)\left(\frac{1}{\gamma}\frac{p'_{cv}}{\bar{p}_{cv}}+\bar{M}_{cv}^2\frac{v'_{cv}}{\bar{V}_{cv}}\right)\end{aligned}\qquad\textbf{(A-121)}$$

The acoustic source by the exhaust nozzle flow is expressed in terms of the properties in the combustion region, and, for simplicity, omitting the notation, *"cv"*, the acoustic source effects by the exhaust nozzle flow are expressed as following.

$$(S_{nozzle})' = \overline{(\dot{Q}_{ref})}\left(\frac{c_p\bar{T}}{\bar{h}_s + \frac{1}{2}\bar{V}^2}\right)\left(\frac{3\gamma - 1}{2} + \frac{\gamma + 1}{2}\frac{\frac{1}{2}(\gamma - 1)\bar{M}^2}{\left(1 + \frac{1}{2}(\gamma - 1)\bar{M}^2\right)}\right)\left(\frac{1}{\gamma}\frac{p'}{\bar{p}} + \overline{M}^2\frac{v'}{\overline{V}}\right) \quad \textbf{(A-122)}$$

Where, $c_p\bar{T} \neq \bar{h}_s$ in Eq. (A-122) above, and $c_p\bar{T} = \frac{\gamma R\bar{T}}{\gamma - 1} = \frac{\bar{a}^2}{\gamma - 1}$.

A.3.1.4. Further Manipulation of the Effects by the Exhaust Nozzle

In order to further investigate the effects by the out flow through the exhaust nozzle, after combining Eq. (A-89) (describing the interactions between the acoustic waves and the acoustic sources) and Eq. (A-87) (describing the acoustic pressure condition by the assumption of the acoustically compact combustion region), Eq. (A-122) is applied to the resulting equations. These manipulations result in the following expression.

$$f_2 - f_1 = RHS$$
$$g_1 - g_2 = RHS$$

$$RHS = \left(\frac{1}{2}\left(\frac{\gamma - 1}{\bar{a}}\right)\frac{1}{A}\right)\Bigg[(\dot{Q}_{chem})' - \overline{(\dot{Q}_{ref})}\left(\frac{c_p\bar{T}}{\bar{h}_s + \frac{1}{2}\bar{V}^2}\right)\left(\frac{3\gamma - 1}{2} + \frac{\gamma + 1}{2}\frac{\frac{1}{2}(\gamma - 1)\bar{M}^2}{\left(1 + \frac{1}{2}(\gamma - 1)\bar{M}^2\right)}\right)\left(\frac{1}{\gamma}\frac{p'}{\bar{p}} + \overline{M}^2\frac{v'}{\overline{V}}\right) + (S_{injector})'\Bigg] \quad \textbf{(A-123)}$$

Defining the following parameter, $\varepsilon_{\bar{M}}$, in Eq. (A-125) below, the above equation (Eq. (A-123)) can be expressed as following.

$$f_2 - f_1 = RHS$$
$$g_1 - g_2 = RHS$$
$$RHS = \left(\frac{1}{2}\left(\frac{\gamma-1}{\bar{a}}\right)\frac{1}{A}\right)\left((\dot{Q}_{chem})' + (S_{injector})'\right) - \varepsilon_{\bar{M}}\, p' - \varepsilon_{\bar{M}}\, \bar{M}\,(\bar{\rho}\bar{a}v') \qquad \textbf{(A-124)}$$

$$\varepsilon_{\bar{M}} = \left(\frac{1}{2}\left(\frac{\gamma-1}{\bar{a}}\right)\frac{1}{A}\right) \cdot \overline{(\dot{Q}_{ref})}\left(\frac{c_p\bar{T}}{\bar{h}_s + \frac{1}{2}\bar{V}^2}\right)\left(\frac{3\gamma-1}{2} + \left(\frac{\gamma+1}{2}\right)\frac{\frac{1}{2}(\gamma-1)\bar{M}^2}{\left(1+\frac{1}{2}(\gamma-1)\bar{M}^2\right)}\right)\left(\frac{1}{\gamma}\right)\frac{1}{\bar{p}} \qquad \textbf{(A-125)}$$

As shown in Eq. (A-124), the acoustic source effects by the out flow through the exhaust nozzle are expressed in terms of the parameters, $\varepsilon_{\bar{M}}$ and $\varepsilon_{\bar{M}}\bar{M}$, and the acoustic properties in the combustion region, p' and $\bar{\rho}\bar{a}v'$. Where, the parameters, $\varepsilon_{\bar{M}}$ and $\varepsilon_{\bar{M}}\bar{M}$, are non-dimensional, and the acoustic pressure, p', and the term, $\bar{\rho}\bar{a}v'$, have dimensions of acoustic pressures. Also, the acoustic source effect by the out flow through the exhaust nozzle is damping the oscillations; see the minus sign in Eq. (A-124).

By applying Eqs. (A-94) and (A-101) to Eq. (A-125) and expressing stagnation properties in the resulting equation in terms of the properties in the combustion region, the parameter, $\varepsilon_{\bar{M}}$, by Eq. (A-125) is expressed as following.

$$\varepsilon_{\bar{M}} = \frac{1}{2}\left(\frac{A^*}{A}\right)\left(\frac{2}{\gamma+1}\right)^{\frac{\gamma+1}{2(\gamma-1)}}\left(1+\frac{1}{2}(\gamma-1)\bar{M}^2\right)^{\frac{\gamma+1}{2(\gamma-1)}} \cdot \left(\frac{3\gamma-1}{2} + \left(\frac{\gamma+1}{2}\right)\frac{\frac{1}{2}(\gamma-1)\bar{M}^2}{\left(1+\frac{1}{2}(\gamma-1)\bar{M}^2\right)}\right) \qquad \textbf{(A-126)}$$

Notably, Eq. (A-126) above clearly shows that the parameter, $\varepsilon_{\bar{M}}$, is a non-dimensional number.

As shown in Figure 35 in CHAPTER 3, the nozzle throat area, A^*, is much smaller than the cross sectional area of the annular combustor, A, i.e., $A^* \ll A$. By applying $\frac{A^*}{A} \ll 1$ to Eq. (A-126) and investigating the magnitudes of the each factors, it can be deduced that the parameter, $\varepsilon_{\overline{M}}$, is a small number, i.e., $\varepsilon_{\overline{M}} \ll 1$. Since it is assumed that the tangential mean flow is subsonic, i.e., $\overline{M} < 1$, the parameter, $\varepsilon_{\overline{M}}\overline{M}$, is also a small number, i.e., $\varepsilon_{\overline{M}}\overline{M} \ll 1$.

$$\begin{aligned} &0 < \varepsilon_{\overline{M}} << 1 \\ &0 < \varepsilon_{\overline{M}}\overline{M} << 1 \end{aligned} \qquad \textbf{(A-127)}$$

As shown on the RHS of each equation in Eq. (A-124), the effect by the exhaust nozzle flow depends on the acoustic pressure and velocity inside the combustion region. Since the combustion region is assumed as an acoustically compact zone, the acoustic pressure inside the region is the same as the acoustic pressures on the surface s1 and s2. On the other hand, since the acoustic velocity across the region is discontinuous, the velocity inside the region is assumed to be the average of the velocities on the surfaces s1 and s2; see Figure 36 in CHAPTER 3. These oscillations inside the combustion region in terms of the acoustic waves arriving/leaving the combustion region are expressed in the following relationships, Eq. (A-128), as below.

$$\begin{aligned} &p' = f_1 + g_1 = f_2 + g_2 \\ &v' = \frac{v_1' + v_2'}{2} = \frac{1}{2}\frac{1}{\overline{\rho}\,\overline{a}}\{(f_1 - g_1) + (f_2 - g_2)\} \end{aligned} \qquad \textbf{(A-128)}$$

Applying Eq. (A-128) to Eq. (A-124) results in the following system of equations of two unknowns (i.e., the outgoing waves, f_2 and g_1 from the combustion region) and two knowns (i.e., the incident waves, f_1 and g_2 to the combustion region) with the acoustic sources by chemical reaction, $(\dot{Q}_{chem})'$, the inflow through the injector, $(S_{injector})'$, and the outflow through the exhaust nozzle in terms of $\varepsilon_{\overline{M}}$.

$$
\begin{aligned}
&(1+\varepsilon_{\overline{M}}+\varepsilon_{\overline{M}}\overline{M}\frac{1}{2})f_2-\varepsilon_{\overline{M}}\overline{M}\frac{1}{2}g_1 \\
&\qquad=\left(\frac{1}{2}\left(\frac{\gamma-1}{\bar{a}}\right)\frac{1}{A}\right)\left((\dot{Q}_{chem})'+(S_{injecor})'\right) \\
&\qquad\quad+(1-\varepsilon_{\overline{M}}\overline{M}\frac{1}{2})f_1+(-\varepsilon_{\overline{M}}+\varepsilon_{\overline{M}}\overline{M}\frac{1}{2})g_2 \\
&(1+\varepsilon_{\overline{M}}-\varepsilon_{\overline{M}}\overline{M}\frac{1}{2})g_1+\varepsilon_{\overline{M}}\overline{M}\frac{1}{2}f_2 \\
&\qquad=\left(\frac{1}{2}\left(\frac{\gamma-1}{\bar{a}}\right)\frac{1}{A}\right)\left((\dot{Q}_{chem})'+(S_{injector})'\right) \\
&\qquad\quad+(-\varepsilon_{\overline{M}}-\varepsilon_{\overline{M}}\overline{M}\frac{1}{2})f_1+(1+\varepsilon_{\overline{M}}\overline{M}\frac{1}{2})g_2
\end{aligned}
\tag{A-129}
$$

In the above system of equations, i.e., Eq. (A-129), the unknowns are on the LHS and the knowns are on the RHS. Eq. (A-129) can be solved and expressed in a matrix form:

$$
\begin{aligned}
\begin{Bmatrix} f_2 \\ g_1 \end{Bmatrix} &= \frac{1}{1+\varepsilon_{\overline{M}}}\left(\frac{1}{2}\left(\frac{\gamma-1}{\bar{a}}\right)\frac{1}{A}\right)\left((\dot{Q}_{chem})'+(S_{injecor})'\right)\begin{Bmatrix} 1 \\ 1 \end{Bmatrix} \\
&\quad+\frac{1}{1+\varepsilon_{\overline{M}}}\begin{bmatrix} 1 & -\varepsilon_{\overline{M}} \\ -\varepsilon_{\overline{M}} & 1 \end{bmatrix}\begin{Bmatrix} f_1 \\ g_2 \end{Bmatrix}+\frac{2(\varepsilon_{\overline{M}}\overline{M}\frac{1}{2})}{1+\varepsilon_{\overline{M}}}\begin{bmatrix} -1 & 1 \\ -1 & 1 \end{bmatrix}\begin{Bmatrix} f_1 \\ g_2 \end{Bmatrix}
\end{aligned}
\tag{A-130}
$$

Since the parameter, $\varepsilon_{\overline{M}}$, is a small number as discussed above (see Eq. (A-127)), the following approximation is available.

$$
\begin{aligned}
&\varepsilon_{\overline{M}} << 1,\ \varepsilon_{\overline{M}}\overline{M} << 1 \\
&\frac{1}{1+\varepsilon_{\overline{M}}} = 1-\varepsilon_{\overline{M}}+\frac{1}{2}\varepsilon_{\overline{M}}^2\cdots \approx 1-\varepsilon_{\overline{M}} \\
&\frac{\varepsilon_{\overline{M}}}{1+\varepsilon_{\overline{M}}} = \varepsilon_{\overline{M}}(1-\varepsilon_{\overline{M}}+\frac{1}{2}\varepsilon_{\overline{M}}^2\cdots) \approx \varepsilon_{\overline{M}}
\end{aligned}
\tag{A-131}
$$

Using Eq. (A-131), Eq. (A-130) can be further simplified as below:

$$\begin{Bmatrix} f_2 \\ g_1 \end{Bmatrix} = \left(\frac{1}{2}\left(\frac{\gamma-1}{\bar{a}}\right)\frac{1}{A}\right)\left((\dot{Q}_{chem})' + (S_{injecor})'\right)\begin{Bmatrix}1\\1\end{Bmatrix} + (1-\varepsilon_{\bar{M}})\begin{bmatrix}1&0\\0&1\end{bmatrix}\begin{Bmatrix}f_1\\g_2\end{Bmatrix} - \varepsilon_{\bar{M}}\begin{bmatrix}0&1\\1&0\end{bmatrix}\begin{Bmatrix}f_1\\g_2\end{Bmatrix} - 2(\varepsilon_{\bar{M}}\bar{M}\frac{1}{2})\begin{bmatrix}1&-1\\1&-1\end{bmatrix}\begin{Bmatrix}f_1\\g_2\end{Bmatrix} \tag{A-132}$$

Using the following expressions for normalization:

$$\hat{p}' = \frac{p'}{\bar{p}},\ \ \hat{v}' = \frac{u'}{\bar{a}},\ \ \hat{f}_1 = \frac{f_1}{\bar{p}},\ \ \hat{f}_2 = \frac{f_2}{\bar{p}},\ \ \hat{g}_1 = \frac{g_1}{\bar{p}},\ \ \hat{g}_2 = \frac{g_2}{\bar{p}}$$
$$(\hat{\dot{Q}}_{chem})' = \frac{(\dot{Q}_{chem})'}{\overline{(\dot{Q}_{ref})}},\ \ (\hat{S}_{injector})' = \frac{(S_{injector})'}{\overline{(\dot{Q}_{ref})}} \tag{A-133}$$

where, $\overline{(\dot{Q}_{ref})} \equiv \overline{(\dot{Q}_{chem})} + \overline{(\dot{H}_s + \dot{K}.E.)}_{injector} = \overline{(\dot{H}_s + \dot{K}.E.)}_{nozzle}$ **(A-100)**

the approximated solutions of the outgoing waves, f_2 and g_1, from the combustion region given in Eqs. (A-132) can be expressed in the following expressions:

$$\begin{Bmatrix} \hat{f}_2 \\ \hat{g}_1 \end{Bmatrix} = \left(\left(\frac{1}{2}\left(\frac{\gamma-1}{\bar{a}}\right)\frac{1}{A}\right)\frac{\overline{(\dot{Q}_{ref})}}{\bar{p}}\right)\left((\hat{\dot{Q}}_{chem})' + (\hat{S}_{injecor})'\right)\begin{Bmatrix}1\\1\end{Bmatrix} + (1-\varepsilon_{\bar{M}})\begin{bmatrix}1&0\\0&1\end{bmatrix}\begin{Bmatrix}\hat{f}_1\\\hat{g}_2\end{Bmatrix} - \varepsilon_{\bar{M}}\begin{bmatrix}0&1\\1&0\end{bmatrix}\begin{Bmatrix}\hat{f}_1\\\hat{g}_2\end{Bmatrix} - 2(\varepsilon_{\bar{M}}\bar{M}\frac{1}{2})\begin{bmatrix}1&-1\\1&-1\end{bmatrix}\begin{Bmatrix}\hat{f}_1\\\hat{g}_2\end{Bmatrix} \tag{A-134}$$

Or,

$$\begin{Bmatrix} \hat{f}_2 \\ \hat{g}_1 \end{Bmatrix} = \left(\frac{\varepsilon_{\bar{M}}}{C_{\bar{M}}}\right)\left((\hat{\dot{Q}}_{chem})' + (\hat{S}_{injecor})'\right)\begin{Bmatrix}1\\1\end{Bmatrix} + (1-\varepsilon_{\bar{M}})\begin{bmatrix}1&0\\0&1\end{bmatrix}\begin{Bmatrix}\hat{f}_1\\\hat{g}_2\end{Bmatrix} - \varepsilon_{\bar{M}}\begin{bmatrix}0&1\\1&0\end{bmatrix}\begin{Bmatrix}\hat{f}_1\\\hat{g}_2\end{Bmatrix} - 2(\varepsilon_{\bar{M}}\bar{M}\frac{1}{2})\begin{bmatrix}1&-1\\1&-1\end{bmatrix}\begin{Bmatrix}\hat{f}_1\\\hat{g}_2\end{Bmatrix} \tag{A-135}$$

where,

$$\varepsilon_{\bar{M}} = \left(\frac{1}{2}\left(\frac{\gamma-1}{\bar{a}}\right)\frac{1}{A}\right) \cdot \overline{(\dot{Q}_{ref})}\left(\frac{c_p\bar{T}}{\bar{h}_s + \frac{1}{2}\bar{V}^2}\right)\left(\frac{3\gamma-1}{2} + \left(\frac{\gamma+1}{2}\right)\frac{\frac{1}{2}(\gamma-1)\bar{M}^2}{\left(1+\frac{1}{2}(\gamma-1)\bar{M}^2\right)}\right)\left(\frac{1}{\gamma}\right)\frac{1}{\bar{p}} \tag{A-125}$$

$$C_{\overline{M}} = \left(\frac{c_p \overline{T}}{\overline{h}_s + \frac{1}{2}\overline{V}^2} \right) \left(\frac{3\gamma - 1}{2} + \left(\frac{\gamma + 1}{2} \right) \frac{\frac{1}{2}(\gamma - 1)\overline{M}^2}{\left(1 + \frac{1}{2}(\gamma - 1)\overline{M}^2 \right)} \right) \left(\frac{1}{\gamma} \right) \qquad \textbf{(A-136)}$$

Eq. (A-134) or (A-135) provides a relationship between the unknown outgoing waves, $\hat{g}_1$ and $\hat{f}_2$, and the known incoming waves, $\hat{f}_1$ and $\hat{g}_2$. The incoming waves $\hat{f}_1$ and $\hat{g}_2$, are given by Eq. (3-28) (in Section 3.2.1 in CHAPTER 3) that describes the acoustic propagations in the no combustion regions. The outgoing waves, $\hat{g}_1$ and $\hat{f}_2$, are "unknown" and are calculated by this model equation that describes the processes taking place within the combustion region. Notably, the term $\varepsilon_{\overline{M}}$ in Eqs. (A-134) and (A-135) describes the effect by the exhaust nozzle. Since the term $\varepsilon_{\overline{M}}$ is always greater than zero (see Eq. (A-127)), the acoustic oscillations are damped by the exhaust nozzle interaction; i.e., $\varepsilon_{\overline{M}} > 0$ and $\hat{f}_2 < \hat{f}_1$, $\hat{g}_1 < \hat{g}_2$ when $(\hat{\dot{Q}}_{chem})' = 0$ and $(\hat{S}_{injector})' = 0$, as shown in Eq. (3-43).

A.3.2. Effect by the In Flow through the Injector

The term, $(\hat{S}_{injector})'$, in Eqs. (A-134) and (A-135) describes the acoustic driving/damping by the mass and energy fluxes (i.e., sensible enthalpy and kinetic energy) through the injector. With the definition of the Mach number of the tangential mean flow, $\overline{M} = \frac{\overline{V}}{\overline{a}}$, the definition the acoustic source by the inflow through the injector, $(\hat{S}_{injector})'$, Eq. (A-90) can be written as following.

$$(\hat{S}_{injector})' = \frac{(S_{injector})'}{(\overline{\dot{Q}_{ref}})} = \frac{1}{(\overline{\dot{Q}_{ref}})}\Big\{(\dot{H}_s + \dot{K}.E.)'_{injector} - (\bar{h}_s + \overline{k.e.})\dot{M}'_{injector} + \left(\frac{\bar{a}^2}{\gamma - 1}\right)\left(1 + (\gamma - 1)\bar{M}^2\right)\dot{M}'_{injector}\Big\} \qquad \textbf{(A-137)}$$

Since the inflow through the injector depends on the injection system, the small-perturbation mass flow rate and the sensible enthalpy and kinetic energy flux can be given by the operation conditions of the injection (or fuel and oxidizer supply) system (e.g., mass flow, temperature, fuel/oxidizer, flow velocity, etc.)

A.3.3. Effect by the Chemical Reaction (Combustion Process)

The term, $(\hat{\dot{Q}}_{chem})'$, in Eqs. (A-134) and (A-135) describes the driving/damping by the chemical heat release perturbation, and in this study it has been assumed to have the following linear dependence upon the acoustic pressure and velocity [1]:

$$(\hat{\dot{Q}}_{chem})' = k_p \cdot \hat{p}' + k_v \cdot \left(\left| \hat{\bar{V}} + \hat{v}' \right| - \left| \hat{\bar{V}} \right| \right) \qquad \textbf{(A-138)}$$

A.3.4. Interactions between the Acoustic Waves and the Acoustic Sources in the Combustion Region

The system of equations, Eq. (A-134) (or Eq. (A-135)), Eq. (A-137), and Eq. (A-138), describe the driving and damping of the oscillations in the "combustion" region. They essentially describe:

(i) The arrival of the waves f_1 and g_2 at the concentrated combustion region.

(ii) The amplification/damping of these waves by the chemical reactions and the in/out flows through the injector and exhaust nozzle.

(iii) The dependence of the sources by these processes upon the oscillations in the region.

(iv) The generation of the waves g_1 and f_2, that leave the combustion region and enter the “no combustion” regions.

The equation set of the developed model consists of equations in the “no combustion” and “combustion” regions, ant it is listed in A.4. .

A.4. Equation Set of the Developed Model

The equation set of the developed model with tangential mean flow are arranged in this section. For the case of subsonic tangential mean flow, $\overline{M} < 1$ and short and choked nozzle, the term $\varepsilon_{\overline{M}}$ in the following equation set is a small number; i.e., $\varepsilon_{\overline{M}} \ll 1$. The following equation set is simplified equations using $\varepsilon_{\overline{M}} \ll 1$.

A.4.1. Normalization of the Properties

All properties are normalized by the definitions in Eq. (A-139).

$$\begin{aligned}
&\hat{p}' = \frac{p'}{\overline{p}}, \quad \hat{v}' = \frac{u'}{\overline{a}}, \\
&\hat{f}_1 = \frac{f_1}{\overline{p}}, \quad \hat{f}_2 = \frac{f_2}{\overline{p}}, \quad \hat{g}_1 = \frac{g_1}{\overline{p}}, \quad \hat{g}_2 = \frac{g_2}{\overline{p}} \\
&(\hat{\dot{Q}}_{chem})' = \frac{(\dot{Q}_{chem})'}{\overline{(\dot{Q}_{ref})}}, \quad (\hat{S}_{injector})' = \frac{(S_{injector})'}{\overline{(\dot{Q}_{ref})}}
\end{aligned} \tag{A-139}$$

A.4.2. Interactions in the "Combustion" Region

$$\begin{aligned}
\begin{Bmatrix} \hat{f}_2 \\ \hat{g}_1 \end{Bmatrix} = &\left(\left(\frac{1}{2}\left(\frac{\gamma-1}{\overline{a}}\right)\frac{1}{A}\right)\frac{\overline{(\dot{Q}_{ref})}}{\overline{p}}\right)\left((\hat{\dot{Q}}_{chem})' + (\hat{S}_{injecor})'\right)\begin{Bmatrix} 1 \\ 1 \end{Bmatrix} \\
&+ (1-\varepsilon_{\overline{M}})\begin{bmatrix} 1 & 0 \\ 0 & 1 \end{bmatrix}\begin{Bmatrix} \hat{f}_1 \\ \hat{g}_2 \end{Bmatrix} - \varepsilon_{\overline{M}}\begin{bmatrix} 0 & 1 \\ 1 & 0 \end{bmatrix}\begin{Bmatrix} \hat{f}_1 \\ \hat{g}_2 \end{Bmatrix} - 2(\varepsilon_{\overline{M}}\overline{M}\,\frac{1}{2})\begin{bmatrix} 1 & -1 \\ 1 & -1 \end{bmatrix}\begin{Bmatrix} \hat{f}_1 \\ \hat{g}_2 \end{Bmatrix}
\end{aligned} \tag{A-140}$$

$$\varepsilon_{\overline{M}} = \left(\frac{1}{2}\left(\frac{\gamma-1}{\overline{a}}\right)\frac{1}{A}\right)$$

$$\cdot\overline{(\dot{Q}_{ref})}\left(\frac{c_p\overline{T}}{\overline{h}_s+\frac{1}{2}\overline{V}^2}\right)\left(\frac{3\gamma-1}{2}+\left(\frac{\gamma+1}{2}\right)\frac{\frac{1}{2}(\gamma-1)\overline{M}^2}{\left(1+\frac{1}{2}(\gamma-1)\overline{M}^2\right)}\right)\left(\frac{1}{\gamma}\right)\frac{1}{\overline{p}}$$

or,

$$\varepsilon_{\overline{M}} = \frac{1}{2}\left(\frac{A^*}{A}\right)\left(\frac{2}{\gamma+1}\right)^{\frac{\gamma+1}{2(\gamma-1)}}\left(1+\frac{1}{2}(\gamma-1)\overline{M}^2\right)^{\frac{\gamma+1}{2(\gamma-1)}} \tag{A-141}$$

$$\cdot\left(\frac{3\gamma-1}{2}+\left(\frac{\gamma+1}{2}\right)\frac{\frac{1}{2}(\gamma-1)\overline{M}^2}{\left(1+\frac{1}{2}(\gamma-1)\overline{M}^2\right)}\right)$$

$\varepsilon_{\overline{M}} << 1$ and $\overline{M} < 1$

$$(\hat{\dot{Q}}_{chem})' = k_p \cdot \hat{p}' + k_v \cdot \left(\left|\hat{\overline{V}} + \hat{v}'\right| - \left|\hat{\overline{V}}\right|\right) \tag{A-142}$$

$$(\hat{S}_{injector})' = \frac{(S_{injector})'}{\overline{(\dot{Q}_{ref})}} = \frac{1}{\overline{(\dot{Q}_{ref})}}\left\{(\dot{H}_s + \dot{K}.\dot{E}.)'_{injector} - (\overline{h}_s + \overline{k.e.})\dot{M}'_{injector}\right.$$

$$\left. + \left(\frac{\overline{a}^2}{\gamma-1}\right)\left(1+(\gamma-1)\overline{M}^2\right)\dot{M}'_{injector}\right\} \tag{A-143}$$

Eqs. (A-140), (A-142), and (A-143) describe the interactions between acoustic waves and physical processes in the combustion region (chemical reactions, in/out flows through the injector and exhaust nozzle) with the mean flow.

where, $\hat{p}' = \hat{f}_1 + \hat{g}_1 = \hat{f}_2 + \hat{g}_2$

$$\hat{v}' = \frac{\hat{v}_1' + \hat{v}_2'}{2} = \frac{1}{\gamma}\frac{1}{2}\left\{(\hat{f}_1 - \hat{g}_1) + (\hat{f}_2 - \hat{g}_2)\right\} \tag{A-144}$$

$$(\dot{Q}_{chem})' = -\sum_l h_{f,l}(\dot{M}_l)' \tag{A-145}$$

$$\overline{(\dot{Q}_{chem})} = -\sum_l h_{f,l}\overline{(\dot{M}_l)}$$

$$\overline{(\dot{Q}_{ref})} = \overline{(\dot{Q}_{chem})} + \overline{(\dot{H}_s + \dot{K}.E.)}_{injector} = \overline{(\dot{H}_s + \dot{K}.E.)}_{nozzle} \quad \textbf{(A-146)}$$

$$\overline{(\dot{Q}_{chem})} = -(\overline{\dot{H}}_f)_{nozzle} + (\overline{\dot{H}}_f)_{injector} \quad \textbf{(A-147)}$$

A.4.3. Acoustic Waves in the "No Combustion" Region

$$\begin{aligned} &\hat{f}(x-(\overline{a}+\overline{V})\cdot t) = const \\ &\hat{g}(x+(\overline{a}-\overline{V})\cdot t) = const \end{aligned} \quad \textbf{(A-148)}$$

$$\begin{aligned} &\hat{p}' = \hat{f}(x-(\overline{a}+\overline{V})\cdot t) + \hat{g}(x+(\overline{a}-\overline{V})\cdot t) \\ &\hat{v}' = \frac{1}{\gamma}\hat{f}(x-(\overline{a}+\overline{V})\cdot t) - \frac{1}{\gamma}\hat{g}(x+(\overline{a}-\overline{V})\cdot t) \end{aligned} \quad \textbf{(A-149)}$$

Eqs. (A-148) and (A-149) describe the acoustic waves propagations affected by the mean flow outside the combustion region.

REFERENCES

1. Crocco, L. and Cheng, S.-I., *Theory of combustion instability in liquid propellant rocket motors*. AGARDograph ;. 1956, Published for and on behalf of the Advisory Group for Aeronautical Research and Development North Atlantic Treaty Organization by Butterworths Scientific Publications: London.

2. Lieuwen, T.C. and Yang, V., *Combustion instabilities in gas turbine engines : operational experience, fundamental mechanisms and modeling*. Progress in astronautics and aeronautics ;, ed. T.C. Lieuwen and V. Yang. 2005, American Institute of Aeronautics and Astronautics: Reston, VA.

3. Lieuwen, T.C., *Experimental Investigation of Limit-Cycle Oscillations in an Unstable Gas Turbine Combustor.* Journal of Propulsion and Power, 2002. **18**(1): p. 61-67.

4. Tim, L. and Ben, Z., *Experimental investigation of limit cycle oscillations in an unstable gas turbine combustor*, in *38th Aerospace Sciences Meeting and Exhibit*. 2000, American Institute of Aeronautics and Astronautics.

5. Sutton, G.P., *History of Liquid Propellant Rocket Engines in the United States.* Journal of Propulsion and Power, 2003. **19**(6): p. 978-1007.

6. Jun, C., Fumitaka, I., Bassam, M., Samir, T., Yi-Huan, K., and San-Mou, J., *Gas Turbine Single Annular Combustor Sector: Combustion Dynamics*, in *48th AIAA Aerospace Sciences Meeting Including the New Horizons Forum and Aerospace Exposition*. 2010, American Institute of Aeronautics and Astronautics.

7. John, B., David, L., and Robert, F., *Characterization of a Single Swirl-Coaxial Injector in a Sub-Scale Combustor*, in *46th AIAA/ASME/SAE/ASEE Joint Propulsion Conference & Exhibit*. 2010, American Institute of Aeronautics and Astronautics.

8. Hermsmeyer, H., Prade, B., Gruschka, U., Schmitz, U., Hoffmann, S., and Krebs, W., *V64.3A Gas Turbine Natural Gas Burner Development.* ASME Turbo Expo 2002: Power for Land, Sea, and Air, 2002. **1**: p. 689-695.

9. Lefebvre, A.H., *Gas turbine combustion*. 2nd ed. ed. 1999, Taylor & Francis: Philadelphia.

10. Guicking, D. and Karcher, K., *Active Impedance Control for One-Dimensional Sound.* Journal of Vibration, Acoustics Stress and Reliability in Design, 1984. **106**(3): p. 393-396.

11. Bothien, M.R., Moeck, J.P., and Paschereit, C.O. *Impedance Tuning of a Premixed Combustor Using Active Control*. in *ASME Turbo Expo 2007: Power for Land, Sea, and Air*. 2007. Montreal, Canada.

12. Bothien, M.R., Moeck, J.P., and Paschereit, C.O., *Active control of the acoustic boundary conditions of combustion test rigs.* Journal of Sound and Vibration, 2008. **318**(4–5): p. 678-701.

13. Moeck, J., Bothien, M., and Paschereit, C., *An Active Control Scheme for Tuning Acoustic Impedances*, in *13th AIAA/CEAS Aeroacoustics Conference (28th AIAA Aeroacoustics Conference)*. 2007, American Institute of Aeronautics and Astronautics.

14. Guicking, D. and Lorenz, E., *An Active Sound Absorber With Porous Plate.* Journal of Vibration, Acoustics Stress and Reliability in Design, 1984. **106**(3): p. 389-392.

15. Yaoyu, L., Chiu, G.T.C., and Mongeau, L.G. *Dual-driver standing wave tube: acoustic impedance matching with robust repetitive control*. in *American Control Conference, 2002. Proceedings of the 2002*. 2002.

16. Chung, J.Y. and Blaser, D.A., *Transfer function method of measuring in-duct acoustic properties. I. Theory.* The Journal of the Acoustical Society of America, 1980. **68**(3): p. 907-913.

17. Chung, J.Y. and Blaser, D.A., *Transfer function method of measuring in-duct acoustic properties. II. Experiment.* The Journal of the Acoustical Society of America, 1980. **68**(3): p. 914-921.

18. Heideman, M., Johnson, D., and Burrus, C., *Gauss and the history of the fast fourier transform.* IEEE ASSP Magazine, 1984. **1**(4): p. 14-21.

19. Cooley, J.W. and Tukey, J.W., *An algorithm for the machine calculation of complex Fourier series.* Mathematics of Computation, 1965. **19**(90): p. 297-297.

20. L.E. Kinsler, A.R.F., A.B. Coppens and J.V. and Sanders, *Fundamentals of acoustics*. 4th ed. ed, ed. L.E. Kinsler. 2000, Wiley: New York.

21. Pierce, A.D., *Acoustics : an introduction to its physical principles and applications*. McGraw-Hill series in mechanical engineering. 1981, McGraw-Hill Book Co.: New York.

22. Morse, P.M.C. and Ingard, K.U., *Theoretical acoustics*. 1968: McGraw-Hill.

23. Thomas, J.W., *Numerical partial differential equations*. 1995, New York: New York : Springer.

24. Hoffmann, K.A., *Computational fluid dynamics*. 3rd ed.. ed, ed. S.T. Chiang and K.A. Hoffmann. 1998, Wichita, Kan.: Wichita, Kan. : Engineering Education System.

25. Tannehill, J.C., *Computational fluid mechanics and heat transfer*. 2nd ed. ed. Series in computational and physical processes in mechanics and thermal sciences, ed. D.A. Anderson and R.H. Pletcher. 1997, Taylor & Francis: Washington, DC.

26. Faires, J.D., *Numerical methods*. 3rd ed.. ed, ed. R.L. Burden. 2003, Pacific Grove, CA: Pacific Grove, CA : Thomson/Brooks/Cole.

27. Paschereit, C.O., Gutmark, E., and Weisenstein, W., *Excitation of Thermoacoustic Instabilities by Interaction of Acoustics and Unstable Swirling Flow.* AIAA Journal, 2000. **38**(6): p. 1025-1034.

28. O'Connor, J. and Lieuwen, T., *Disturbance Field Characteristics of a Transversely Excited Burner.* Combustion Science and Technology, 2011. **183**(5): p. 427-443.

29. Acharya, V., Malanoski, M., Aguilar, M., and Lieuwen, T., *Dynamics of a Transversely Excited Swirling, Lifted Flame: Flame Response Modeling and Comparison With Experiments.* Journal of Engineering for Gas Turbines and Power, 2014. **136**(5): p. 051503.

30. Turns, S.R., *An introduction to combustion : concepts and applications*. 2nd ed. ed. McGraw-Hill series in mechanical engineering. 2000, WCB/McGraw-Hill: Boston.

31. Williams, F.A., *Combustion theory : the fundamental theory of chemically reacting flow systems*. 2nd ed.. ed. 1985, Menlo Park, Calif.: Menlo Park, Calif. : Benjamin/Cummings Pub. Co.

32. Strahle, W.C., *On combustion generated noise.* Journal of Fluid Mechanics, 1971. **49**(2): p. 399-414.

33. Strahle, W.C., *Combustion noise.* Progress in Energy and Combustion Science, 1978. **4**(3): p. 157-176.

34. Lighthill, M.J., *On Sound Generated Aerodynamically. I. General Theory.* Proceedings of the Royal Society of London. Series A, Mathematical and Physical Sciences, 1952. **211**(1107): p. 564-587.

35. John, J.E.A., *Gas dynamics*. 2nd ed.. ed. 1984, Englewoods Cliffs, N.J.: Englewoods Cliffs, N.J. : Prentice Hall.

36. Shu, C.-W., *Essentially non-oscillatory and weighted essentially non-oscillatory schemes for hyperbolic conservation laws*, in *Advanced Numerical Approximation of Nonlinear Hyperbolic Equations: Lectures given at the 2nd Session of the*

Centro Internazionale Matematico Estivo (C.I.M.E.) held in Cetraro, Italy, June 23–28, 1997, A. Quarteroni, Editor. 1998, Springer Berlin Heidelberg: Berlin, Heidelberg. p. 325-432.

37. Oleksandr, B., Eugene, L., Dmitriy, S., Michalis, H., and Ben, Z., *Rotational Traveling of Tangential Wave in LRE Combustor Simulator*, in *46th AIAA Aerospace Sciences Meeting and Exhibit*. 2008, American Institute of Aeronautics and Astronautics.

38. Feiler, C.E. and Heidmann, M.F., *Evaluation of tangential velocity effects on spinning transverse combustion instability*. 1966, NASA Lewis Research Center; Cleveland, OH, United States.

39. Feiler, C.E., Heidmann, M.F., and Povinelli, L.A., *Experimental investigation of transverse-mode solid-propellant combustion instability in a vortex burner*. 1966, NASA Lewis Research Center; Cleveland, OH, United States.

40. Dowling, A. and Stow, S., *Acoustic analysis of gas turbine combustors.* Journal of Propulsion and Power, 2003. **19**(5): p. 751-764.

41. Rayleigh, *The Explanation of Certain Acoustical Phenomena.* Nature, 1878. **18**(455): p. 319-321.

42. Rayleigh, J.W.S., *The theory of sound*. 2d ed. rev. and enl.. ed, ed. R.B. Lindsay. 1945, New York: New York, Dover.